Numerical Analysis and Laboratory Test of Concrete Jacking Pipes

by

Jian-Qing Zhou

A thesis submitted for the
Degree of Doctor of Philosophy
at the University of Oxford

Linacre College

Trinity Term, 1998

Numerical Analysis and Laboratory Test of Concrete Jacking Pipes

Jian-Qing Zhou
Linacre College, University of Oxford

A thesis submitted for the Degree of Doctor of Philosophy.
Trinity Term, 1998.

ABSTRACT

Pipe jacking is a trenchless construction technique for the installation of underground pipelines. Although pipe jacking is widely used, fundamental research is still needed to understand fully the factors affecting the process and to prevent unexpected failure. With the time and financial limitation, it is difficult to explore all aspects of these factors with experiments; and it is also difficult to study them by analytical methods because of the complexity of the problem. This thesis describes the use of the finite element technique to study the pipe performance under different environments and the laboratory tests of several different joint designs.

The emphasis of the current research is on the performance of the concrete pipes during jacking under working conditions and to seek possible improvements in the design of pipes and pipe joints by numerical modelling. In the finite element modelling, a simplified two-dimensional model is used for a preliminary study, then the analyses are carried out with three-dimensional models A, B and C representing a complete pipe, a pipe with surrounding soil and a symmetric three-pipe system respectively. Several factors affecting the pipe performance have been examined, for example, the properties of the packing material, the stiffness of the surrounding soil, the misalignment angle at the pipe joint, and the interaction between the pipe and surrounding soil.

The numerical results show that the misalignment of the pipeline is the dominating factor inducing both tensile stresses and localized compressive stresses in the concrete pipe, especially with a high misalignment angle which results in separation between the packing material and the pipe. The packing materials with high Poisson's ratio and high stiffness also induce higher tensile stresses in the pipe, and the influence of the Poisson's ratio is significant. Under 'diagonal' loading, both the stiffness of the surrounding soil and the interaction between the pipe and the surrounding soil have a significant effect on the stresses within the concrete pipe. Under 'edge' loading, the greatest potential damage is at the pipe joint due to the tensile stresses in the hoop direction; while under 'diagonal' loading, the damage is most likely the cracking on the external surface of the pipe along a line connecting the two diagonal loaded corners. The results also show that the Australian model gives somewhat good prediction about the maximum normal stress and the diametrical contact width at pipe joint.

Based on the numerical results, several different joint designs for improving the pipe strength have been proposed and tested in the laboratory. Both the laboratory tests and the back analyses suggest that the local reinforcement and the local prestressed band at the pipe joint will improve the pipe strength.

CONTENTS

Acknowledgements

This research is the outcome of much effort and encouragement from many interested parties. First of all, I wish to express my sincere thanks to Dr H. J. Burd and Dr G.W.E. Milligan for their excellent supervision and guidance during the course of this study.

The financial support from EPRSC for a research assistantship in Oxford University and part of my admission fee from the Pipe Jacking Association are gratefully acknowledged.

I would like to thank Professor G. T. Houlsby for his kindness to let me use his program OXMESH and 2CAN for the mesh generation and stress contours in the preliminary study. I would also like to thank Professor D. R. Hayhurst at UMIST to allow me to use the computer facilities in his research group to produce the stress contours in this thesis.

My thanks also go to Dr C. E. Augarde, Dr G. Liu and Dr C. L. Ngo-Tran for the co-operation in updating the finite element program, OXFEM, to its three-dimensional version, Mr R. C. Sawala for his assistance during the laboratory test. The Civil Engineering Research Group at Oxford provided an enjoyable atmosphere to work and study as one of its members. The friendship of other members of the group was and will be a continuing source of inspiration in my life.

Finally, I would like to thank my wife, Cui-Ling, and my daughter, Wen-Qian, for their support over many years. Without their encouragement, it is impossible for me to finish this thesis after away from the university over a year.

Nomenclature

a	Initial packing material thickness
Δa	Compression of the pipe joint
Δa_p	Compression of the packing material
c	Cohesion of soil or interface
$[D]$	Material matrix
E	Young's modulus
E_c	Young's modulus of concrete
E_p	Young's modulus of packing material
Es	Young's modulus of soil
f	Yield function
$f_1 \ldots f_8$	Element shape function
f_c	Compression strength of concrete
f_t	Tensile strength of concrete
g	Plastic potential
G	Shear modulus
G_c	Shear modulus of concrete
G_p	Shear modulus of packing material
I_1, I_2, I_3	Stress invariant
I_c	Second moment of cross-section area of concrete pipe
K_n, K_s	Normal and shear stiffness of interface
$[K]$	Stiffness matrix

L	Pipe length
M	Bending moment at pipe joint
P	Total applied load
$\{P\}$	Vector of applied load
$\{dP\}$	Vector of increments of applied load
q	Intensity of pressure
R	External radius of pipe
$\{R\}$	Vector of unbalanced /residual force
r	Internal radius of pipe
t	Wall thickness of pipe
u,v,w	Displacements
du, dv, dw	Increments of displacements
$\{U\}$	Vector of displacements
$\{dU\}$	Vector of displacement increments
x,y,z	Co-ordinates of a node / point in Cartesian system
r,θ,z	Co-ordinates of a node / point in cylindrical system
Z	Diametrical contact width at pipe joint
β	Angular deflection at pipe joint
β_c	Angular deflection of concrete pipe at pipe joint
β_p	Angular deflection of packing material at pipe joint
γ	Shear strain
ε	Normal strain
$\{\varepsilon\}$	Vector of strains

$\{d\varepsilon\}$	Vector of strain increments
σ	Normal stress
σ_{max}	Maximum normal stress at pipe joint
$\{\sigma\}$	Vector of stresses
$\{d\sigma\}$	Vector of stress increments
$\sigma_1, \sigma_2, \sigma_3$	Principal stresses
$\sigma_x, \sigma_y, \sigma_z$	Normal stresses in Cartesian co-ordinate system
τ	Shear stress
$\tau_{xy}, \tau_{xy}, \tau_{xy}$	Shear stresses in Cartesian co-ordinate system
ϕ	Frictional angle of soil or interface
ψ	Dilation angle of soil or interface
μ	Poisson's ratio
μ_c	Poisson's ratio of concrete
μ_p	Poisson's ratio of packing material
μ_s	Poisson's ratio of soil
ξ, η	Isoparametric co-ordinates of a node / point

CHAPTER 1 INTRODUCTION AND BACKGROUND

1.1 PIPE JACKING

Pipe jacking is a trenchless technique for installing underground pipelines by jacking specially designed pipes through the ground from a thrust pit to a receiving pit. Pipes are advanced using hydraulic power packs located in the thrust pit as the ground in front of the pipeline is mined. Excavation can be carried out within a shield using either pneumatic tools or a tunnel boring machine, depending on ground condition and cost. The spoil is transported along the pipeline to the surface. Corrections to the alignment of the pipes are made using hydraulic rams in the shield in conjunction with frequent surveying to fixed reference points. The technique is illustrated in Figure 1.1.

Pipe jacking offers the benefits of non-disruptive construction coupled with a unique one-pass lining without need for temporary ground support or secondary lining. Pipe jacking is now available under most types of ground condition, from hard rock to highly unstable silts and sands with high water table (Pipe Jacking Association 1995a, Thomson 1993, Sharp and Turner 1989). It offers considerable advantages over the traditional open-cut methods (Read 1986, Kosowatz 1987, Thomson 1993). Besides minimising surface disruption to the public and the environment, the risk of settlement is far less and the inherent strength of monolithic linings almost eliminates the risk of damage to existing utilities from further adjacent excavations. Moreover, it offers excellent flow characteristics with a smooth internal finish and lends itself easily to mechanised excavation. A summary of the conditions in which pipe jacking is a competitive alternative to other forms of primary lining is given by Craig and Muir Wood (1978). The main disadvantage of this method is its limitation to access the jacking front, which may result in heavy cost if unexpected failure happens (Shullock 1982).

The pipe jacking technique is thought to have first been used in Roman times. The first records of pipe jacking jobs were for installations done in the USA between 1896 and 1900 for the Northern Pacific Railroad Company (Moss 1993, Thomson 1993). Gradually it became standard practice for a number of railroad companies to jack cast iron pipes under rail tracks. By the late 1920s, concrete pipes were being used. Pipe sizes ranged from 750mm to 2400mm in diameter. Records reveal that working methods were similar to a simple hand-mined jacking job of today. Excavation was mainly by shovel and pick, helped by pneumatic clay spades in tougher soil with air hammers to break out boulders (Thomson 1993).

Prior to World War II, the pipe jacking technique was used on an isolated basis in various countries, among them the UK, Germany and Japan (Moss 1993, Thomson 1993, Anon 1978). In the earlier stage, pipe jacking covered mainly the man-entry size and was used for short lengths of tunnel. It was usually used for sections of pipelines under embankment, roads and railways, where open cut methods would be particular uneconomic because of the need to keep traffic moving continuously. Likewise there had been many occasions when the method had been used for small sections of long tunnels that passed below buildings. With the improvements in techniques and the application of modern technology, for example, the introduction of mechanised excavation and computerised laser guidance, pipe jacking may be used for long distance driving and different pipe sizes from 100mm up to very much larger diameter as an alternative to open-cut methods either for direct economy or for less disturbances at the surface (Moss 1993). Pipe jacking now became one of the popular methods to install underground pipelines in many countries (Wang 1982, Anon 1987, Roisin 1989, Pau et al 1993, Liao and Cheng 1996). The basic principles of the technique have been presented in detail by the American Concrete Pipe Association (1960), Richardson (1970), Hough (1974) and Thomson (1993). To improve the quality of pipe jacking, the British Pipe Jacking Association published notes giving guidance on design and practice (Pipe Jacking Association 1981, 1986, 1995a and 1995b).

The renewed interest in pipe jacking is a natural consequence of the needs of the market. Throughout the Western World a massive replacement programme was put underway to make good war-damaged networks and to meet the demands of rising living standards. Many of the pipelines had to be installed under busy roads and railways and at depths where open-cut was impracticable. Pipe jacking offered a solution which allowed short crossings to be made in a way that is safe, as well as economical. To cope with different ground conditions and to meet the varying needs of authorities in different countries, new methods were devised and equipment improved.

Recently, the pipe jacking technique developed very rapidly. Advances in technology have been particularly significant in Japan and Germany. The computerised laser guidance was widely used to reduce the pipeline misalignment (Lock 1988). Pipe jacking techniques can now be used at great depths below ground and in unstable ground conditions (Sharp and Turner 1989, Pipe Jacking Association 1995a) and pipes can be pushed along a curved line if needed (Wallis 1984, Nomura al et 1985). Pipe jacking over a very long distance was reported in Germany (Remmer 1995, Lauritzsen et al 1996). To deal with the larger diameter pipes and long lengths of thrust, lubrication along the pipeline and intermediate jacking stations were introduced to reduce the jacking forces (Jones 1990, Washbourne 1986, Durden 1982, Pipe Jacking Association 1995a and 1995b).

1.2 CONCRETE JACKING PIPES AND PIPE JOINTS

The most common pipe used in pipe jacking is concrete pipe, although different pipes have been used in practice, such as steel pipe, plastic pipe and clay pipe. The choice of the pipe can be influenced by diameter, length of drive and by ground condition (Pipe Jacking Association 1995a and 1995b). The concrete pipes used for pipe jacking were usually man-entry diameters from 900mm to 3000mm, in compliance with British Standard 5911: Part

120:1989. Pipes are generally available in lengths between 1.2 and 2.5 metres and are designed such that the jacking forces may be transmitted along the pipeline without damage to the joint. The fundamental requirements of the jacking pipes are as following (Thomson 1993):

- Resistance to internal and external corrosion
- Capacity to withstand static and dynamic loading
- Good flow characteristics
- Satisfactory whole-life costs

Precast concrete pipes are generally cast in manufacturers' works and transported to site by road. The pipes are manufactured by centrifugal spinning or vertical casting using concrete with a 28 day characteristic cube strength greater than 60MPa. Spirally wound reinforcement spot welded to longitudinal steel to form internal and external cages are often used to prevent damage during the temporary handling and installation stages.

The key part of a pipe is the pipe joint. The functional requirements of a joint on a jacked pipe are adapted from Clarke (1968):

(1) It should be designed to permit angular and axial movement large enough to tolerate maximum displacement likely to occur without damage or loss of watertightness.

(2) It should be designed to withstand the force applied during installation without detrimental damage.

(3) It should remain efficient throughout its working life.

(4) It should be simple to make and dismantle in the limited space of the jacking thrust pit.

Traditional jacked pipe joints in the United Kingdom have been an in wall spigot and socket as shown in Figure 1.2(a). Disquiet in the industry about the performance of the in wall joint and its ability to transmit longitudinal loads has led to the introduction of new joint details. The most often used of the new joints is shown in Figure 1.2(b), the steel collar joint.

The main reason for its introduction is the belief that jacking load may be better transmitted through the centre of the jacked pipe wall rather than at its edges. An increase of available end area may improve the pipe's jacking load carrying capacity.

Limited research has been carried out to ascertain the performance of the pipe with the steel collar joint. Milligan and Ripley (1989), and Boot and Husein (1991) suggested the use of packing material with low Poisson's ratio and low stiffness to improve the stress distribution on the pipe / packing interface. To improve the current understanding and to improve the pipe design, some more research on this subject should be done. In general, it is believed that the performance of the concrete pipe is mainly affected by:

- Properties of the packing material
- Properties of the concrete pipe and the joint type
- Properties of the surrounding soil
- Interaction between the pipe and the surrounding soil
- Pipeline misalignment at the pipe joint

1.3 THE NEED FOR RESEARCH AND OXFORD RESEARCH

Although pipe jacking has widely been used in many countries, many factors affecting the performance of such tunnels are still not clear. To improve the current understanding, more research is still needed, for example the stress distribution patterns and stress localization within the pipe due to pipeline misalignment. The need for research in several areas was first reported by Kirkland (1982) when he stated the need for researchers to establish more scientific facts of the pipe jacking. The Construction Industries Research and Information Association (CIRIA) then undertook a review of pipe jacking and published a Technical Note 112 (Craig 1983), which recommended that the following areas required research:

- Friction loads in different ground conditions

- Characteristics of joints and joint packing materials
- Effects of cyclic loading on pipes
- Effects of lubrications in reducing friction
- Development of a site investigation test to predict friction forces

As a result of increasing interest in the prediction and control of ground movements due to tunnelling, the measurement of ground movements and pressures has now been included within the list of objectives.

Following the recommendation and support of the Pipe Jacking Association (PJA) and the CIRIA, Oxford Research in pipe jacking began from 1986 and has now been in progress for over twelve years. Project one, from 1986 to 1989, involved laboratory testing of model concrete pipes and a number of common joint materials (Ripley 1989, Milligan and Ripley 1989). This research emphasised the need for suitable packing material at pipe joints along with careful control of pipeline alignment, and the superiority of steel banded butt joints to in wall spigot and socket joints for the transmission of large jacking forces. Project two, from 1989 to 1992, involved the monitoring of field behaviour of concrete pipes at full scale during pipe jacking on five active construction sites (Norris 1992, Milligan and Norris 1991, and Norris and Milligan 1992). Project two has obtained some important results from the field monitoring on pipeline alignment, tunnel stability, pipe-soil interface behaviour, pipe stress and ground movement (Milligan and Norris 1993a, Milligan and Norris 1993b, Milligan and Norris 1995, Milligan and Norris 1996).

Project three and project four were carried out after the success of the first two projects. The former involved a continuation of the site monitoring with a somewhat different emphasis and the latter mainly involved a numerical modelling of concrete pipe jacking to which this thesis refers. After identifying some possible design improvements from the numerical analysis and laboratory testing in the current research, further testing on these designs was carried out with prototype concrete pipes in project five (Holt et al 1997). Project five confirmed the effect of local reinforcement and local prestressing on the improvement of pipe strength. Holt et al (1997) also found that the pipe's capacity was improved with one external prestressed steel band and that two external prestressed bands at the pipe joint would reduce the pipe's capacity. (The pipes used in this experiment were prototype pipes with butt-jointed incorporating steel collar.)

1.4 STRESSES / STRAINS IN THE PIPE

1.4.1 EXPERIMENTAL STUDY

To examine the performance of the concrete pipe in pipe jacking, Ripley (1989) carried out some laboratory tests with small scaled model pipes under both 'edge' and 'diagonal' loading conditions. The misalignment angle in the tests was provided by yokes. The strains at the middle length of the pipe were measured with strain gauges. The results showed that under 'edge' loading the strains were localized in the loaded region and the pipes failed at the pipe joint region. Under 'diagonal' loading high tensile strains existed on the external surface of the pipe and the pipes failed due to the cracking on the external surface along the line between the two loaded corners. In his research, some sand chamber tests were also carried out. In these tests, two concrete pipes were placed in the sand chamber with an initial misalignment angle between them. No packing material was used. The results showed that all the pipes came to an aligned position during the test instead of remaining in a misalignment position. The results were not consistent for different tests. Ripley (1989) concluded: 'The complexity and interaction of various loads applied to the pipe during this test series and the pipes constantly changing their orientation means that strain data from the various tests was not suitable for worthwhile comparisons between tests'.

Husein (1989), Boot and Husein (1991) examined the performance of the vitrified clay pipes in pipe jacking from the in-air testing and in-soil testing of a two pipe and packing system as shown in Figures 1.3 and 1.4 respectively. From the in-air test, it was concluded that pipe failure was caused by tensile hoop strains in the joint region. The strains in the pipe were similar in the case of misalignment angle $\beta = 0.5^0$ and 1.0^0, which conflicted with the analytical theory (Haslem 1996, Concrete Pipe Association of Australia 1983). Strain distributions in the pipe were largely affected by the pipe end geometry under pure axial load and by the hoop geometry with pipeline misalignment. The prime attribute of a packing material was the ability to redistribute stress concentrations by compressing in a mechanically stable manner over a required level of deformation. For the in-soil tests, the results are not consistent. Husein pointed out: '... this has eventually led to serious concern regarding the validity of the strain gauge results ' and the possible reason was that '... it is suspected that defects in the jacking surface geometry may have seriously affected the strain results '.

1.4.2 NUMERICAL ANALYSIS

Husein (1989) also did numerical analysis by using the program ABAQUS. The analysis was mainly limited to his experimental model. In his in-air numerical model, the analyses were carried out with both 20-node brick elements and 8-node thick shell elements as shown in Figures 1.5 and 1.6 (due to the symmetric condition just a quarter of the system was used in this analysis). The interface elements were used to model the interaction between the pipe and the packing material. The initial position of the packer was determined so that a joint opening of 1^0 was obtained (0.5^0 in the analysis due to symmetric condition). The hoops were simulated by isoparametric beam elements and the contact between the pipe and the hoop was also modelled by interface elements.

The clay pipe was assumed elastic in the analysis. The packers were assumed to be elastic with the same Poisson's ratio as that of the clay pipe. The results (the strains on the internal and external pipe surface at the cross section of 20mm from the joint) showed good agreement with this experimental data ($\beta = 0.5^0$). The axial strains were localized in the contact region (near the pivot) and the hoop strains showed periodic patterns along the line of r = constant with high maximum tensile values. The analysis was also extended to model different hoop geometries. In this analysis, the packers were modelled by a hyperelastic model (linear and with different Young's modulus at different stress stages). The actual Poisson's ratio was used for Chipboard and Medite fibreboard, and a value of 0.45 was used for Elastomer and LDPE. The results showed that hoop geometry had a great effect on the strains within the pipe, and that a packing material with a low Poisson's ratio (Chipboard) performs better than those with higher Poisson's ratio.

The in-soil (sand) numerical model consisted of one layer of brick elements of soil and the in-air model with shell elements but different misalignment angles. Again, the clay pipe and the packer were assumed to be linear elastic and to have the same value of Poisson's ratio. The interaction between the pipe and soil, and between the soil and fixed boundary were also simulated by interface elements. Lateral pressure was applied to model the pressure from the air bag in the laboratory tests. The soil (sand) was assumed to be linearly elastic because of the failure of convergence for both non-linear elastic and elastic-plastic soil models. 'The obtained final results were not as predicted ' as pointed out by Husein (1989). The numerical model was then modified, which included using non-linear springs to replace the interface between the soil and the fixed boundary, and using different soil stiffness at different regions according to radial stress variation. However, the results from this modified model showed significant tensile stresses on the pipe-soil interface. At last, two numerical techniques were used for further modification of this numerical model, that is, an initial strain in the packing material and a small stiffness for soil in the tensile zone. The results showed that the effect of the ground passive pressure was significant. Unfortunately, the results were still not satisfactory and there were discrepancies and conflicts between the numerical results and the experimental data.

The in-air numerical model in this research clearly showed the effectiveness of the finite element method. However, the numerical analysis was mainly a back analysis of this experimental data. The effect of the misalignment angle was not examined in this numerical analysis. Due to the significant effect of the hoop geometry, it is difficult to apply the results to fully explain the pipe behaviour in practice. Clearly, a numerical model with surrounding soil is needed. Unfortunately, due to the high non-linearity, the finite element mesh in this in-soil model was too coarse to obtain satisfactory results. To examine the behaviour of the pipe, more research is needed, for example, a parametric study of the influence of pipeline misalignment and the interaction between the pipe and surrounding soil.

1.5 PIPE JACKING LOADS

Jacking load is the force required to advance the complete pipeline forward, which depends on face resistance to penetration of the shield and the frictional force along the pipeline. It is important that jacking forces can be accurately predicted in practice to enable the operation to be designed appropriately. The amount of resistance encountered at the face depends upon ground conditions and the measures required to support the face. In hand drives it is solely due to the cutting edge resistance of the jacking shield and the friction acting on the external surface of the shield (Thomson 1993, Auld 1982). In machine drives the face pressure required to support the ground should also be taken into account. The principal factors affecting the jacking force include (Pipe Jacking Association 1995b, Rogers and Yonan 1992, Norris 1992, Ripley 1989, Thomson 1993):

- Resistance at the excavation face
- Type of soil and its variation along the pipeline
- Length, diameter and self-weight of the jacking pipes
- Depth of overburden and surface surcharge
- Amount of overcut during excavation

- Use of lubrication and intermediate jacking station
- Misalignment of the pipeline
- Jacking around curves
- Frequency and duration of stoppages

Whilst it is difficult to accurately assess the frictional force acting on the pipeline theoretically, pipe jacking contractors have, after years of experience, derived empirical values. The frictional forces usually fall between 0.5 and 2.5 tonnes per square metre of the external circumferential area of the pipe. Typical values of frictional forces for different ground conditions are given in Table 1.1 (Craig 1983):

Table 1.1 Typical values of frictional resistance

Soil type	Frictional resistance (kPa)
Rock	2 to 3
Boulder clay	5 to 18
Firm clay	5 to 20
Wet sand	10 to 15
Silt	5 to 20
Dry loose sand	25 to 45
Fill	up to 45

To predict the frictional force, Auld (1982) presented an analysis for a pipe driven through a cohesionless material, in which the soil was assumed to collapse onto the pipe and to exert radial pressure around its circumference. In this model, it was assumed there was no change of the vertical and horizontal soil stress with the change of the depth below ground level. The frictional force (F) per unit length is derived as following:

$$F = \pi R (\sigma_v + \sigma_h) \tan \phi_l \qquad (1.5.1)$$

Where R is the external radius of the pipe, σ_v and σ_h are the vertical and horizontal soil stress, ϕ_I is the angle of friction between the pipe and the soil. Ripley (1989) modified this model to include the change of the soil stress with the changing depth:

$$F = \pi R \, (\sigma_{vc} + \sigma_{hc}) \tan \phi_I \tag{1.5.2}$$

Where σ_{vc} and σ_{hc} are the vertical and horizontal soil stress at the depth of the pipe centre. This model seems to overestimate the frictional force when comparing with experimental data (Norris 1992) possibly due to the overcut in practice.

Haslem (1986) studied the behaviour of pipe jacks in London Clay and proposed a model to estimate the frictional force in cohesive soil. The model was based on the behaviour of an elastic cylinder resting in a cylindrical void in an elastic continuum. The frictional force is given by:

$$F = \alpha \, S_u \, b \tag{1.5.3}$$

Where α is the adhesion factor commonly used in pile skin-frictional formulae, S_u is the undrained shear strength of soil, b is the contact width. However, this model was found to underestimate the frictional force when comparing the measured data, possibly due to the soil collapsing onto the pipe in practice. O'Reilly and Rogers (1987) used a similar technique to predict the frictional force in clay and rock (sandstone). The equation for frictional force in their model is as follows:

$$F = \frac{W_p \tan \phi_1}{\cos \psi_1} \tag{1.5.4}$$

Where W_p is the weight of pipe per unit length. ψ_I is the offset angle of reaction from vertical. The model produced a good fit to the available data for pipejacks through rock. For pipejacks in clay, the model also gave an underestimate of frictional force. Laboratory tests were carried out to assess the contact area between pipes and clay. The results from experimental data confirmed a need to account for plastic behaviour of clay and the effect of time.

1.6 LOAD TRANSFER AT PIPE JOINTS

The distribution of load transferred across the pipe joint is mainly determined by the pipeline misalignment and the properties of the packing material used. The Concrete Pipe Association of Australia (1983) published a theory based on a linear stress approach and material properties as shown in Figure 1.7. In this model, the normal stress was assumed to be linearly distributed over the contact area on the joint. The stresses were constant in the pipe along the pipe length and in the packer throughout its thickness, and had the same distribution pattern as that on the interface. The axial strain in the pipe and the packer were linearly related to the normal stress at the joint, which in turn resulted in linear distributed deformation of the pipe and packer at the joint. The expression for joint misalignment angle β is given as follows:

$$\tan \beta = a\, \sigma_{max} \,/\, (E_j Z) \qquad (1.6.1)$$

$$E_j = (a\, t\, E_c\, E_p) \,/\, (a\, t\, E_c + L\, t_j\, E_p) \qquad (1.6.2)$$

Where a is the thickness of the packer, σ_{max} is the maximum normal stress on the joint, Z is the diametrical contact width as shown in Figure 1.7, L is the length of the pipe, E_c and E_p are the Young's modulus of the concrete and the packer respectively, t and t_j are the thickness of the pipe wall and the wall thickness at the joint. The Australian model has widely been adopted for its simplicity (Pipe Jacking Association 1995a).

To extend the Australian model to include the tensile stresses, Haslem (1996) proposed a flexible pipe model in which the stress distribution at the joint and the deformation of the packing material were the same as in the Australian model. However, the pipes were assumed to sustain tensile stresses and suffer uniform pressure and bending moment due to the eccentric jacking load at the joint. Moreover, it was assumed that the end of the pipes remained plane during bending and that the bending moment was constant along the two pipe halves adjacent to the joint. The misalignment angle of the pipeline β consisted of the angular deformation of the compressed packer (β_p) and the sum of the angular deflections (β_c) due to the bending of the two halves of the pipe abutting the joint:

$$\beta = \beta_p + 2\beta_c \tag{1.6.3}$$

Where:

$$\beta_p = a\,\sigma_{max} / (E_p\, Z) \tag{1.6.4}$$

$$\beta_c = \frac{M L}{2 E_c I_c} \tag{1.6.5}$$

Where M is the bending moment due to the eccentric jacking load, and $I_c = \pi (R^4 - r^4) / 4$ is the second moment of area of the cross-section of the concrete pipe.

Another model to deal with the load transfer at the joint was proposed by Hornung et al (1987). In this model, no allowance was made for pipe elasticity and only the material properties of the packing material and orientation of the pipe were considered (Ripley 1989). In practice, there is also shear stress at the pipe joint (Norris 1992). However, due to its complicated nature, the shear stress is assumed to be zero in all these analytical models.

1.7 SCOPE OF THE CURRENT RESEARCH

Previous research (Norris 1992, Ripley 1989) suggested that concrete pipes could be under 'edge' loading or 'diagonal' loading conditions due to the misalignment of the pipeline as shown in Figure 1.8 and 1.9 respectively. Under 'edge' loading, pipes usually failed at the joint due to cracking with plane pipe and spalling with reinforced pipe (Ripley 1989, Holt et al 1997). Under 'diagonal' loading, failure of the pipes could be due to cracking on the external surface of the pipe along a line between the two loaded corners (Ripley 1989).

However, the failure model for concrete and the mechanism of the reinforcements are complex and beyond the scope of the current project. In the current research, the emphasis is on the pipe performance under working conditions without reinforcement (except for the back analysis in Chapter 9) and to seek possible improvement on the design of pipe and pipe joint. The study is concentrated on the influence of the properties of the packing material, the properties of the pipe and the surrounding soil, and the misalignment angle at the pipe joint. Under the working condition, it is assumed that:

- Interface gaps may occur between the pipe and the surrounding soil
- Packing material may lose contact with the pipe over some area at the pipe joint
- Soil may yield
- Concrete pipe stays elastic

To assess the influence of different factors on the performance of the concrete pipe, stresses under working conditions are used as an indicator of safety against cracking failure. Concrete usually fails under tension due to the low tensile strength. The tensile strength reduces if accompanied by high principal compressive stress but remains the same under biaxial tension (Neville 1981, Jiang and Feng 1991). In this project, the results of the numerical analysis are used to identify the most probable damage zones of tension, and are interpreted by the most tensile principal stresses (the maximum principal stresses) and the most compressive principal stresses (the minimum principal stresses) within the concrete pipe.

This thesis starts with literature reviews in Chapter 1. Chapter 2 describes some developments of the finite element model used in the research. A two-dimensional preliminary study is discussed in Chapter 3. The simplified plane strain model in Chapter 3 is mainly used to obtain numerical experience of the use of interface elements and the non-linear solution procedure. Chapter 4 discusses the three-dimensional analysis using numerical model A, a single small scaled model pipe. The emphasis in Chapter 4 is on the effect of the load distribution and the thickness of pipe wall. The analysis using numerical model B, a full scale pipe with surrounding soil, is described in Chapter 5. The parametric studies with this model are the interaction between the pipe and the surrounding soil due to the pipeline misalignment and the effect of the soil stiffness. A symmetric three-pipe system (three concrete pipes with two pipe joints and packing materials) is presented in Chapter 6. The analysis with this model is focused on the influence of the properties of the packing material and the influence of the pipeline misalignment. In Chapter 7, the deformation, the maximum normal stress and the diametric contact width at the pipe joint are discussed and compared with the data from the Australian model and Haslem's (1996) flexible pipe model. Chapter 8 describes the laboratory tests of improvements of pipe joint design. The numerical back analysis of the laboratory tests is discussed in Chapter 9. Finally, a summarisation of the research in this project and a few recommendations of future work are given in Chapter 10.

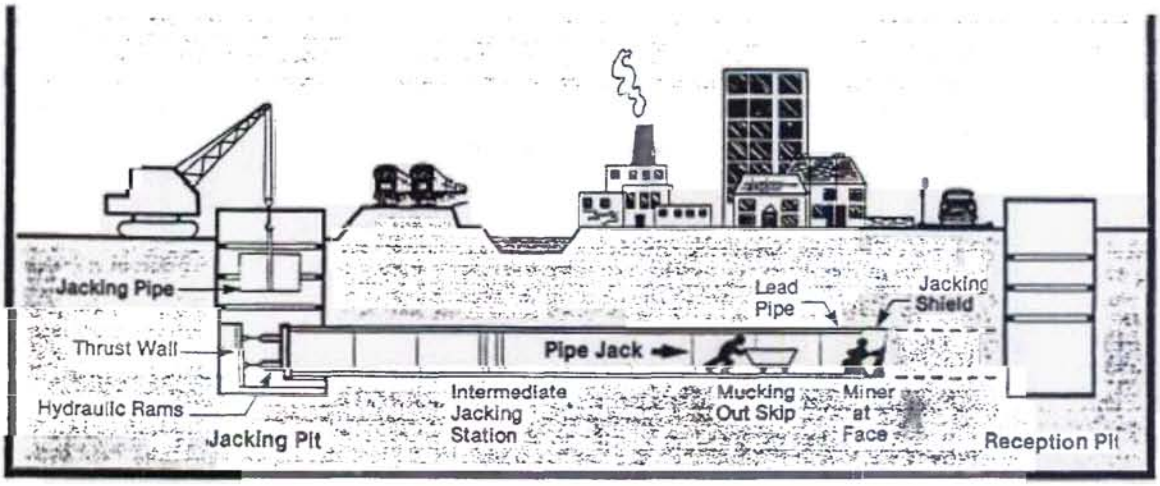

Figure 1.1 A typical arrangement of jacking equipment

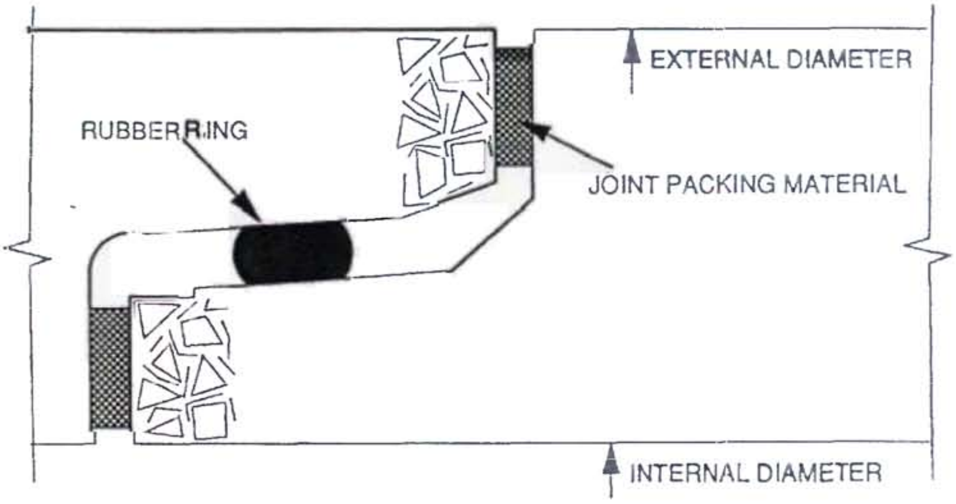

a) IN WALL SPIGOT AND SOCKET JOINT

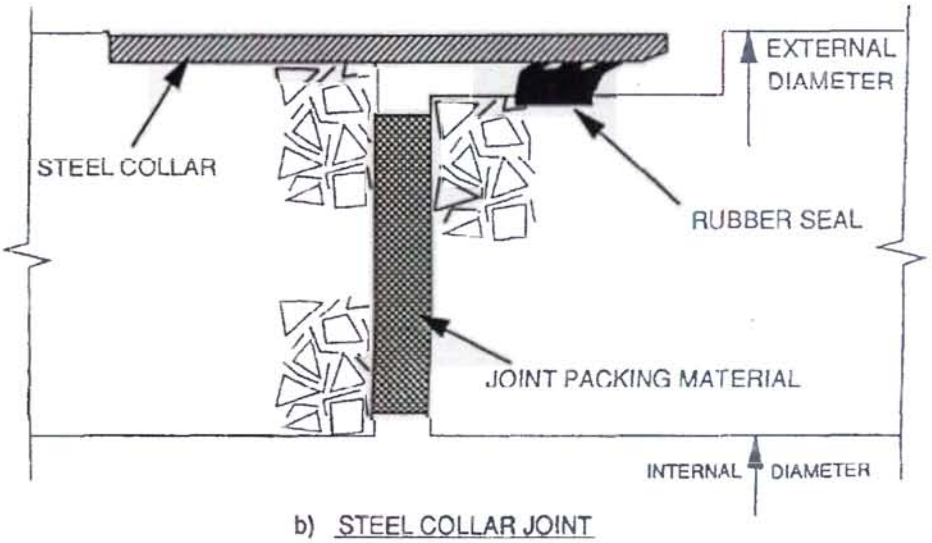

b) STEEL COLLAR JOINT

Figure 1.2 Types of pipe joint common in Britain

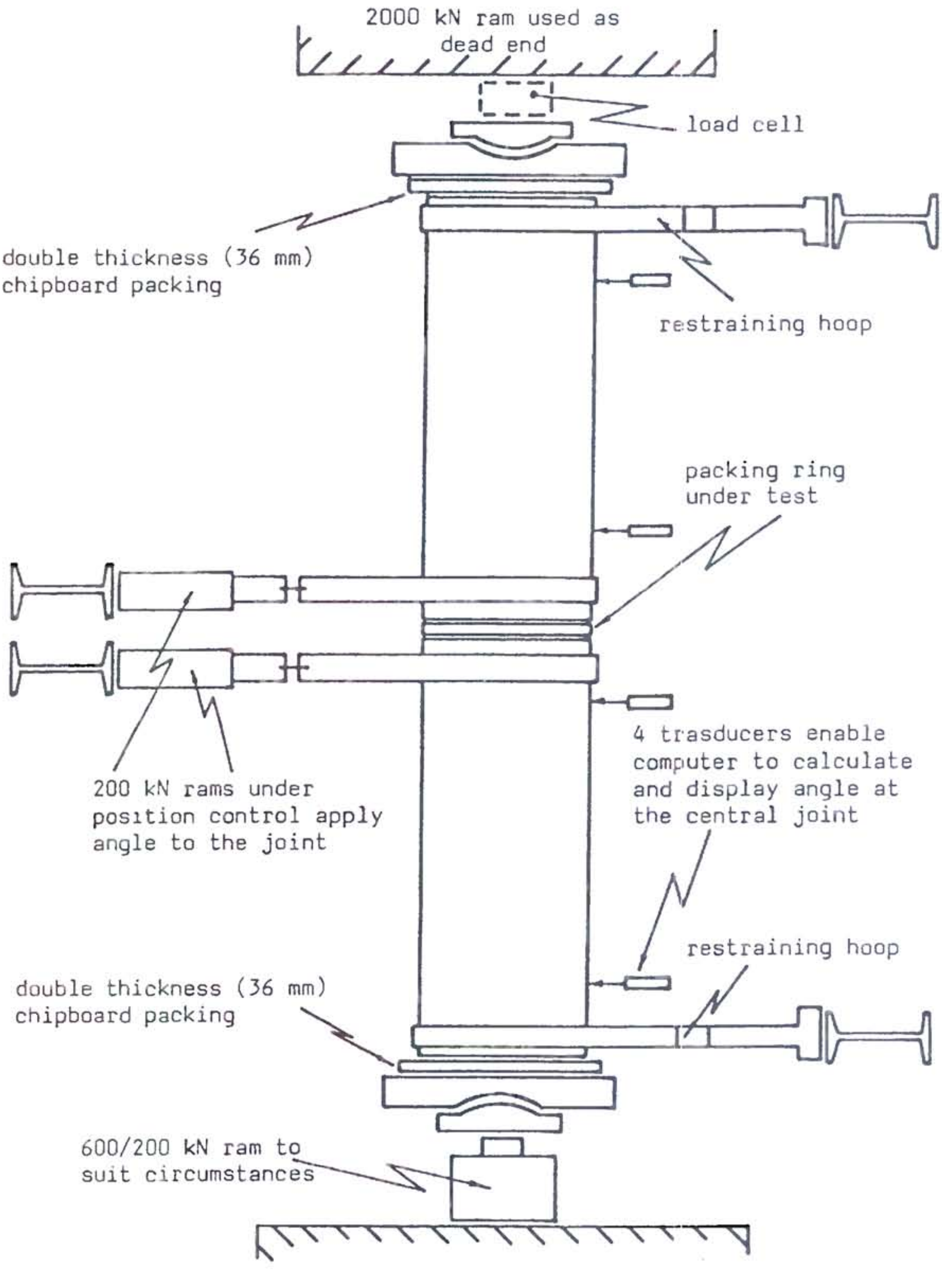

Figure 1.3 Apparatus in Husein's (1989) in-air test

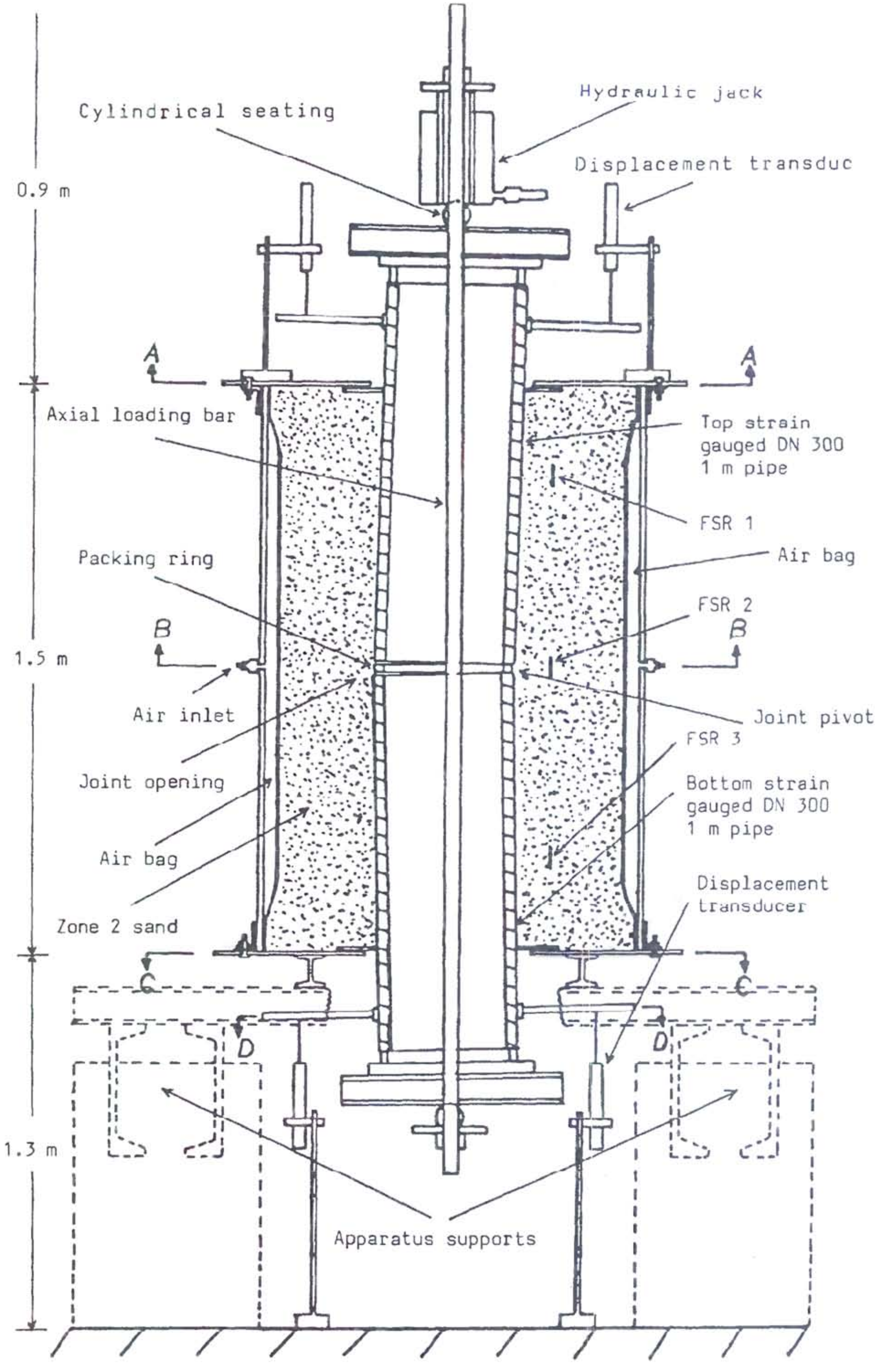

Figure 1.4 Apparatus in Husein's (1989) in-soil test

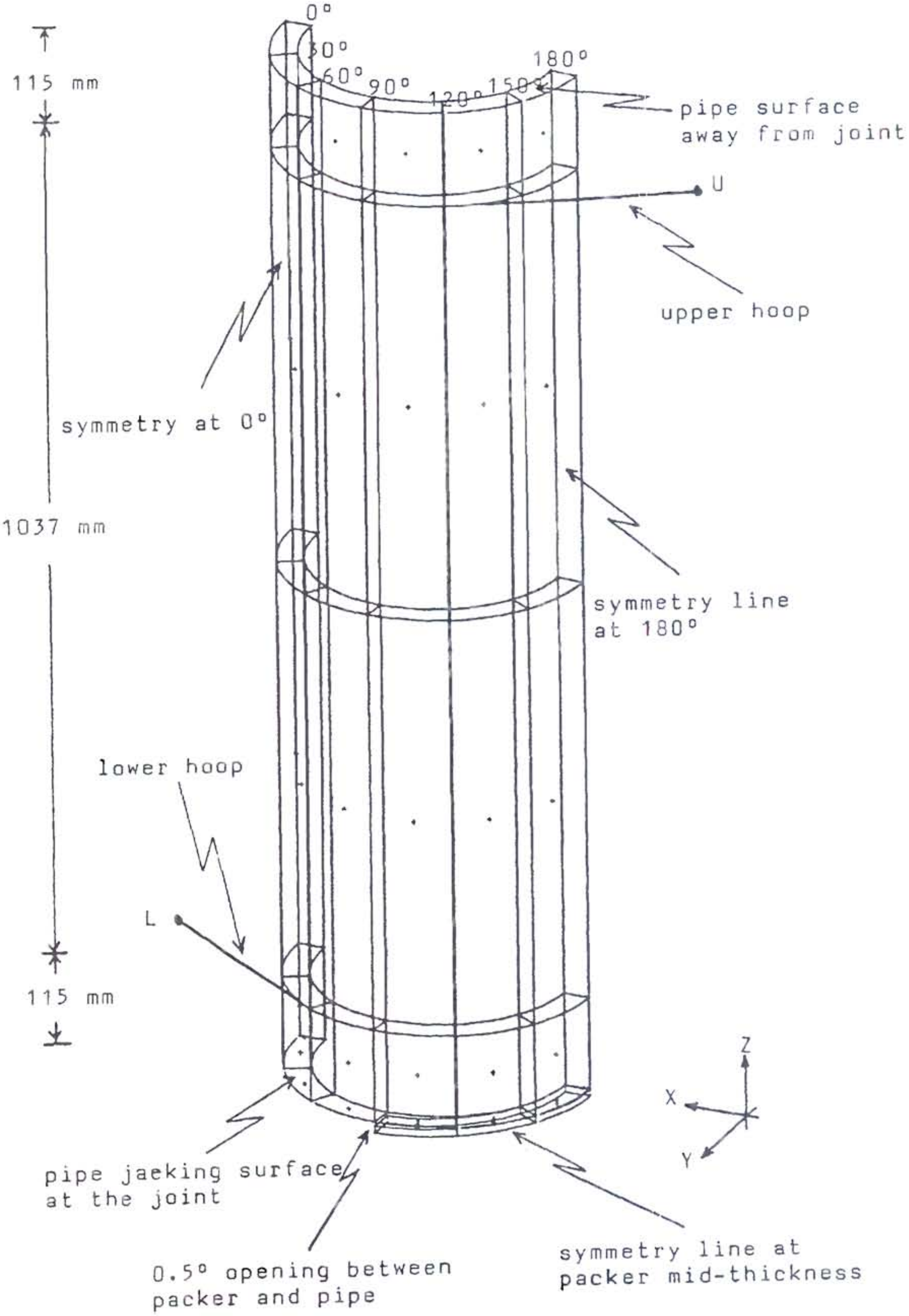

Figure 1.5 Numerical in-air model with brick elements (From Husein 1989)

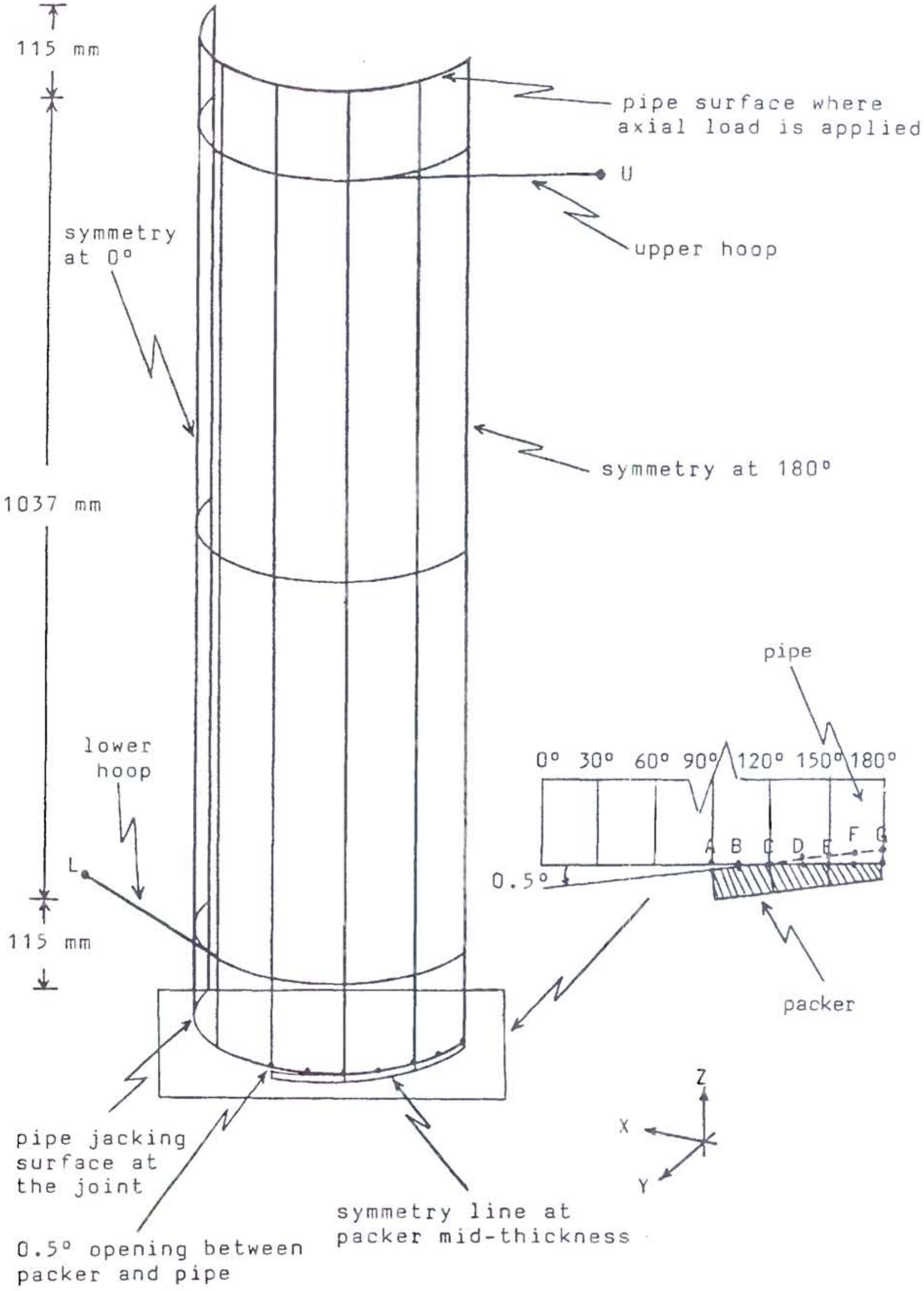

Figure 1.6 Numerical in-air model with shell elements (From Husein 1989)

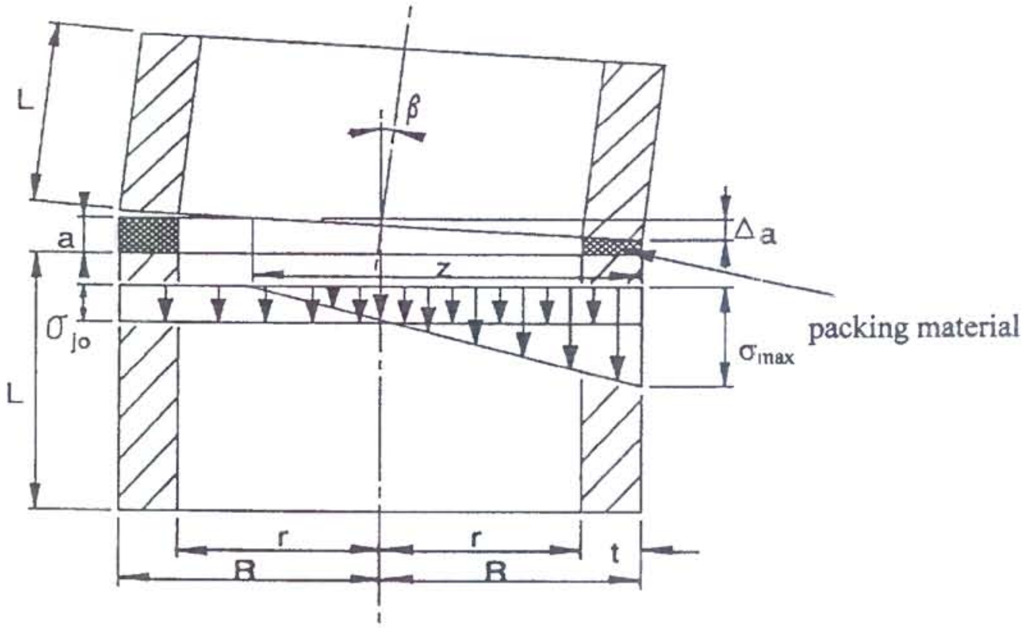

Figure 1.7 Australian model for stress distribution at joint

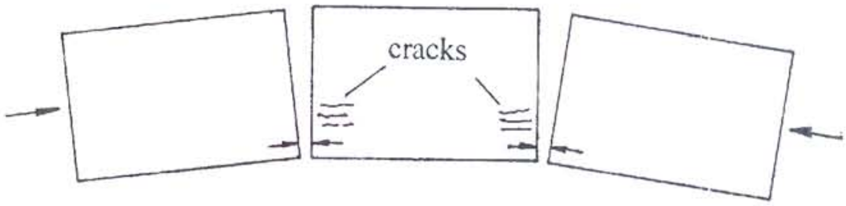

Figure 1.8 A typical edge loading condition

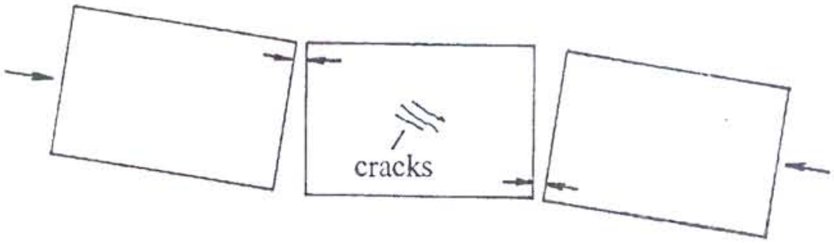

Figure 1.9 A typical diagonal loading condition

CHAPTER 2 DEVELOPMENT OF FINITE ELEMENT MODEL

2.1 INTRODUCTION

In the current research, the behaviour of the jacking pipe and pipe joint are investigated using the finite element method. The finite element program FEPS (Zhou 1997) was mainly used in the research except in Chapter 3 where the program OXFEM (Burd 1996) was used for two-dimensional analysis. FEPS is a finite element package designed to carry out stress analysis with various element types and simple elastic perfectly-plastic material models. The program consists of multiple co-ordinate systems including a cylindrical system which is useful in the current research since pipes are regular structures in this co-ordinate system. The program has various loading input modules especially the non-uniform traction module which can be used to model the non-uniform load at a pipe joint due to pipeline misalignment.

This Chapter describes the development of the finite element model. Mesh generation in the current research is discussed in Section 2.2. Section 2.3 describes the formulation of a two-dimensional interface element and the Mohr-Coulomb frictional model, which play an important role in the research to model the interaction between the concrete pipe and the surrounding soil. A concrete model, modified Matsuoka model, and curved bar elements used to model reinforcements in concrete are discussed in Sections 2.4 and 2.5 respectively. Finally, several solution procedures are presented in Section 2.6.

2.2 MESH GENERATION PROGRAM -- DATAIN

In finite element analysis, the first step is to divide the domain of a structure into many subdomains described as mesh generation. For a simple test example, it is easy to do it by hand. However, automatic mesh generation is always necessary for complex structures, especially for three-dimensional ones, because of the large amount of data.

Some finite element packages have automatic mesh generation, others use a commercial mesh generation package. In the current research project, the main structures are concrete pipes which are regular structures in a cylindrical co-ordinate system. Furthermore, the stress distributions on some surfaces in a cylindrical co-ordinate system, such as surfaces with r=constant or θ=constant, are usually needed. It may be convenient if the program can deal with a cylindrical system. As a result, a program, DATAIN, was developed for mesh generation in this research. It is simple and effective. A finite element mesh of a pipe with 3375 nodes and 2496 elements is shown in Figure 2.1. The mesh has five different mesh sizes in the θ direction and seven mesh sizes in the z direction. The input data of DATAIN for this mesh is given in Table 2.1. It is clearly seen that the input data is very simple.

2.3 INTERACTION BETWEEN STRUCTURES

To understand the behaviour of the jacking pipe and the pipe joint, one of the main aspects to be investigated is the interaction between the concrete pipe and the surrounding soil, and between the concrete pipe and the packing material. For this purpose, a few two-dimensional interface elements (embedded in three-dimensional continuum) and an interface material model were implemented into the program and are discussed in Sections 2.3.1 and 2.3.2 respectively.

2.3.1 TWO-DIMENSIONAL INTERFACE ELEMENT

The use of interface elements is one of the common methods to study the interaction between structures because it is compatible with other element types and provides a convenient way to extract the stresses on the interface in the finite element solution (Burd 1986, Beer 1985, Burd and Brocklehurst 1992, Adhikary and Dysin 1998, Ngo-Tran 1996). A two-dimensional interface element is shown in Figure 2.2 with two layers, the upper layer and the lower layer, and four pairs of nodes. Within each pair, the nodes have independent degrees of freedom but share the same co-ordinate position. It should be pointed out that the element formulation described in this section can also easily be used to derive other interface elements with different shapes and different number of nodes, such as a quadrilateral element with 8 pairs of nodes, triangular element with 3 pairs of nodes and triangular element with 6 pairs of nodes. In fact, these interface elements have all been implemented into the program with little extra effort. For simplicity, the interface element with four pairs of nodes is used to demonstrate the element formulation as follows (similar formulations have been used by Beer (1985) and Ngo-Tran (1996)):

The formulation of the element is based on an isoparametric approach. Following the conventional isoparametric approach, the element is mapped into a rectangular element on the isoparametric plane as shown in Figure 2.3. The co-ordinates of a point in the element are related to the nodal co-ordinates by functions of isoparametric co-ordinates ξ and η:

$$\begin{aligned} x &= f_1 x_1 + f_2 x_2 + f_3 x_3 + f_4 x_4 \\ y &= f_1 y_1 + f_2 y_2 + f_3 y_3 + f_4 y_4 \qquad (2.3.1) \\ z &= f_1 z_1 + f_2 z_2 + f_3 z_4 + f_4 z_4 \end{aligned}$$

where x, y and z are co-ordinates at a point in the element, x_i, y_i and z_i are the co-ordinates of the node i. f_i are shape functions defined in isoparametric co-ordinates ξ and η and listed bellow:

$$\begin{aligned} f_1 &= (1 - \xi)(1 - \eta)/4 \\ f_2 &= (1 + \xi)(1 - \eta)/4 \qquad (2.3.2) \\ f_3 &= (1 + \xi)(1 + \eta)/4 \\ f_4 &= (1 - \xi)(1 + \eta)/4 \end{aligned}$$

The strain increments at a point (ξ, η) within the element are defined as the increments of the relative displacements between the upper layer and the lower layer of the element:

$$
\begin{aligned}
d\gamma_1 &= du_e^{+} - du_e^{-} \\
d\gamma_2 &= dv_e^{+} - dv_e^{-} \qquad (2.3.3) \\
d\varepsilon_n &= dw_n^{+} - dw_n^{-}
\end{aligned}
$$

Where $d\gamma_1$ and $d\gamma_2$ are shear strain increments in the direction of $\mathbf{e}_1$ and $\mathbf{e}_2$, $d\varepsilon_n$ is the normal strain increment in the $\mathbf{n}$ direction; du_e , dv_e and dw_n are the displacement increments at the point (ξ,η) on the surface in the direction of $\mathbf{e}_1$, $\mathbf{e}_2$ and $\mathbf{n}$ respectively; and the symbol '+' and '-' denote the upper and lower layer of the element. $\mathbf{e}_1$, $\mathbf{e}_2$ and $\mathbf{n}$ are unit vectors of a local system as shown in Figure 2.2, which are calculated as follows (Spiegel 1959):

$$
\begin{aligned}
\mathbf{e}_1^* &= \{ \frac{\partial x}{\partial \xi} \ \frac{\partial y}{\partial \xi} \ \frac{\partial z}{\partial \xi} \}^{\mathrm{T}} \\
\mathbf{n}^* &= \mathbf{e}_1^* \times \{ \frac{\partial x}{\partial \eta} \ \frac{\partial y}{\partial \eta} \ \frac{\partial z}{\partial \eta} \}^{\mathrm{T}} \\
\mathbf{e}_1 &= \begin{Bmatrix} e_{11} \\ e_{12} \\ e_{13} \end{Bmatrix} = \mathbf{e}_1^* / | \mathbf{e}_1^* | \qquad (2.3.4) \\
\mathbf{n} &= \begin{Bmatrix} e_{31} \\ e_{32} \\ e_{33} \end{Bmatrix} = \mathbf{n}^* / | \mathbf{n}^* | \\
\mathbf{e}_2 &= \begin{Bmatrix} e_{21} \\ e_{22} \\ e_{23} \end{Bmatrix} = \mathbf{n} \times \mathbf{e}_1
\end{aligned}
$$

Where e_{ij} i,j=1,2,3, are direction cosines of the local system, $| \mathbf{n}^* |$ is the norm of the vector $\mathbf{n}^*$, T denotes transposition and × denotes vector cross product operator (Spiegel 1959).

From Figure 2.2, the displacement increments in the direction of $\mathbf{e}_1$, $\mathbf{e}_2$ and $\mathbf{n}$ at a point (ξ,η) can be related to those in the x, y and z direction at the same point following the conventional displacement transformation between different co-ordinate systems:

$$\begin{Bmatrix} du_e^- \\ dv_e^- \\ dw_n^- \end{Bmatrix} = [\,C\,] \begin{Bmatrix} du^- \\ dv^- \\ dw^- \end{Bmatrix} \tag{2.3.5}$$

Where du_e^-, dv_e^- and dw_n^- are displacement increments at the point (ξ,η) in the direction of $\mathbf{e}_1$, $\mathbf{e}_2$ and $\mathbf{n}$ on the lower layer of the element; du^-, dv^- and dw^- are displacement increments in the x, y and z direction at the same point on the lower layer. The displacement increments on the upper layer have a similar relationship. [C] is the matrix of direction cosines between the global and the local co-ordinate system defined as follow (Spiegel 1959):

$$[\,C\,] = \begin{bmatrix} e_{11} & e_{12} & e_{13} \\ e_{21} & e_{22} & e_{23} \\ e_{31} & e_{32} & e_{33} \end{bmatrix} \tag{2.3.6}$$

In the finite element solution, the final parameters to be solved are the increments of the nodal displacements. So a relationship between the displacement increments at a point and the increments of nodal displacements is needed. The displacement increments on the lower layer in co-ordinate system (x, y, z) at a point are related to the increments of nodal displacements in a similar way as the co-ordinates:

$$\begin{aligned} du^- &= f_1\,du_1 + f_2\,du_2 + f_3\,du_3 + f_4\,du_4 \\ dv^- &= f_1\,dv_1 + f_2\,dv_2 + f_3\,dv_3 + f_4\,dv_4 \\ dw^- &= f_1\,dw_1 + f_2\,dw_2 + f_3\,dw_3 + f_4\,dw_4 \end{aligned} \tag{2.3.7}$$

Where du_i, dv_i and dw_i are the displacement increments at node i in the x, y and z direction. The relationship between the displacement increments at a point and the nodal displacement increments on the upper layer is similar.

Combining equation set (2.3.1) to (2.3.7), a relationship between the strain increments and the increments of the nodal displacements is obtained:

$$\{\,d\varepsilon\,\} = [\,B\,]\,\{\,dU\,\} \tag{2.3.8}$$

Where $\{ dU \} = \{ du_1 \ dv_1 \ dw_1 \ du_2 \ dv_2 \ dw_2 \ \dots \ du_8 \ dv_8 \ dw_8 \}^T$ is the vector of the increments of the nodal displacements, and $\{ d\varepsilon \} = \{ d\gamma_1 \ d\gamma_2 \ d\varepsilon_n \}^T$ is the vector of strain increments. The geometric matrix [B] is derived as follow:

$$[\,B\,] = [\,C\,][\,-F \quad F\,] \tag{2.3.9}$$

$$[\,F\,] = \begin{bmatrix} f_1 & 0 & 0 & f_2 & 0 & 0 & & f_4 & 0 & 0 \\ 0 & f_1 & 0 & 0 & f_2 & 0 & \dots & 0 & f_4 & 0 \\ 0 & 0 & f_1 & 0 & 0 & f_2 & & 0 & 0 & f_4 \end{bmatrix} \tag{2.3.10}$$

The element stiffness matrix is obtained by following the conventional approach (Zienkiewicz 1977):

$$\begin{aligned} [\,K\,] &= \iint_S [\,B\,]^T [\,D\,][\,B\,]\, ds \\ &= \int_{-1}^{1}\int_{-1}^{1} [\,B\,]^T [\,D\,][\,B\,]\, J\, d\xi\, d\eta \end{aligned} \tag{2.3.11}$$

Where [K] is the element stiffness matrix; S is the element domain and [D] is the material matrix which is discussed in detail in Section 2.3.2. $J = |\,\mathbf{n}^*|$ is the Jacobian determinant of co-ordinates transformation between the global co-ordinate system (x, y, z) and the isoparametric co-ordinate system (ξ, η).

2.3.2 THE MOHR-COULOMB FRICTIONAL MODEL

For the interface element discussed in Section 2.3.1, the stress increments are assumed to be related linearly to the strain increments within the element when the interface is elastic (Goodman et al. 1968, Burd 1986, Beer 1985, Burd and Brocklehurst 1992, Ngo-Tran 1996) and the constitutive equation is:

$$\{ d\sigma \} = [\,D\,]\{ d\varepsilon \} \tag{2.3.12}$$

Where $\{ d\sigma \} = \{ d\tau_1 \; d\tau_2 \; d\sigma_n \}^T$ is the vector of stress increments in the direction of $\mathbf{e}_1$, $\mathbf{e}_2$ and **n**; $\{ d\varepsilon \}$ is the vector of strain increments defined in Section 2.3.1 and $[D]$ is the elastic material matrix defined as follows:

$$[D] = \begin{bmatrix} K_s & 0 & 0 \\ 0 & K_s & 0 \\ 0 & 0 & K_n \end{bmatrix} \tag{2.3.13}$$

K_n and K_s are the normal stiffness and the shear stiffness of the interface. Here the shear stiffness is assumed to be the same in both $\mathbf{e}_1$ and $\mathbf{e}_2$ direction.

As in most elastic-plastic problems, the interface is assumed to yield when the stresses satisfy the Mohr-Coulomb criterion:

$$\begin{aligned} f &= \tau^2 - (c - \sigma_n \tan\varphi)^2 \\ &= (\tau_1^2 + \tau_2^2) - (c - \sigma_n \tan\varphi)^2 = 0 \end{aligned} \tag{2.3.14}$$

Where f is the yield function; σ_n, τ, τ_1 and τ_2 are the normal stress, total shear stress, shear stress in the $\mathbf{e}_1$ and $\mathbf{e}_2$ direction; c and φ are the cohesion and the angle of friction assigned to the interface. For the case of plastic material behaviour, the plastic strain increments are derived from a plastic potential which is assumed to have a similar form as the yield function:

$$\{ d\varepsilon_p \} = \lambda \left\{ \frac{\partial g}{\partial \sigma} \right\} \tag{2.3.15}$$

$$\begin{aligned} g &= \tau^2 - (c_1 - \sigma_n \tan\psi)^2 \\ &= (\tau_1^2 + \tau_2^2) - (c_1 - \sigma_n \tan\psi)^2 \end{aligned} \tag{2.3.16}$$

Where $\{ d\varepsilon_p \}$ is the vector of the plastic strain increments; λ is a factor of proportionality determined by the consistency condition; g is plastic potential; ψ is the dilation angle assigned to the interface and the cohesion parameter $c_1 = c + \sigma_n (\tan\psi - \tan\varphi)$ is obtained by setting $f = g$ at the current stress state as shown in Figure 2.4.

The constitutive equation between the stress increments and the strain increments can be obtained by following the conventional procedure (Zienkiewicz 1977) as in most elastic-plastic problems:

$$\{ d\sigma \} = [D_{ep}] \{ d\varepsilon \} \tag{2.3.17}$$

Where $[D_{ep}]$ is the elastic-plastic material matrix derived as following:

$$\left[D_{ep}\right] = [D] - \frac{[D] \left\{\frac{\partial g}{\partial \sigma}\right\} \left\{\frac{\partial f}{\partial \sigma}\right\}^{T} [D]}{\left\{\frac{\partial f}{\partial \sigma}\right\}^{T} [D] \left\{\frac{\partial g}{\partial \sigma}\right\}} \tag{2.3.18}$$

$$\left\{\frac{\partial f}{\partial \sigma}\right\}^{T} = \{ \tau_1 \quad \tau_2 \quad (c - \sigma_n \tan\varphi) \tan\varphi \ \} \tag{2.3.19}$$

$$\left\{\frac{\partial g}{\partial \sigma}\right\}^{T} = \{ \tau_1 \quad \tau_2 \quad (c_1 - \sigma_n \tan\psi) \tan\psi \ \} \tag{2.3.20}$$

2.3.3 UPDATE OF DISPLACEMENTS, STRAINS AND STRESSES

In elastic-plastic problems, a finite element solution is usually obtained step-by-step using an incremental method. The increments of the nodal displacements are solved in each step and then the nodal displacements, strains and stresses are updated as following:

$$\begin{aligned} &\{ U \} = \{U_0\} + \{ dU \} \\ &\{ d\varepsilon \} = [B] \{ dU \} \\ &\{\varepsilon \} = \{\varepsilon_0 \} + \{ d\varepsilon \} \\ &\{ d\sigma \} = \int \left[D_{ep}\right] d\varepsilon \\ &\{\sigma \} = \{\sigma_0 \} + \{ d\sigma \} \end{aligned} \tag{2.3.21}$$

Where $\{ U \}$, $\{U_0\}$ and $\{ dU \}$are the current nodal displacements, the nodal displacement at end of previous step and the increments of nodal displacements in the current step; $\{\varepsilon \}$, $\{\varepsilon_0\}$

and $\{d\varepsilon\}$ are the current strains, the strains at end of previous step and the increments of strains in the current step; $\{\sigma\}$and $\{\sigma_0\}$ are the current stresses and the stresses at end of previous step. $\{d\sigma\}$ is the increments of stresses in the current step, which is obtained by numerical integration in analysis (Burd 1986).

If the stress state is still elastic (that is $f < 0$), the calculation moves to the next step. As in most elastic-plastic models, if the stress state is in the plastic zone ($c - \sigma_n \tan\varphi > 0$ and $f \geq 0$), the stresses should be projected back on the initial yield surface as shown in Figure 2.5 because the model discussed here is an elastic perfectly-frictional model (no hardening effect). To project the stresses back on the yield surface, many return algorithms have been developed (Simo and Taylor 1985, Krieg and Krieg 1977, Schreyer et al 1979, Ortiz et al 1983, Oritiz and Simo 1986). The closest point projection algorithm (Burd 1986) is adopted in the current research, in which the return direction is always normal to the yield surface.

In the current research, the concrete pipe can separate from the surrounding soil or from the packing material due to pipeline misalignment. The gap plays an important role in the pipe performance because the gap changes the stress distribution significantly in its adjacent region. In order to take the influence of the gap into consideration, the interface model here consists of a gap zone ($c - \sigma_n \tan\varphi \leq 0$) as shown in Figure 2.5. Whenever the stress state at a point enters into this gap zone, it is assumed that the two layers of the interface element separate at this point and a gap exists between them. Then the stresses and the stiffness of the element at this point are set to zero according to the nature of the gap (for the purpose of numerical stability , the stiffness is set to a very small value in analysis). In the current research, loading is applied monotonically; so there is no global unloading. However, the gap can be closed ($\varepsilon_n \leq 0$) due to local unloading. When the gap is closed, the element stiffness at this point recovers completely at once and the stresses are updated as follows:

$$\varepsilon_n = \varepsilon_{n0} + d\varepsilon_n$$
$$t = \varepsilon_n \, / \, d\varepsilon_n \qquad (2.3.22)$$
$$\{ d\sigma \} = t \, [D] \, \{ d\varepsilon \}$$
$$\{\sigma\} = \{\sigma_0\} + \{ d\sigma \} = \{d\sigma\}$$

Where ε_n, ε_{n0} and $d\varepsilon_n$ are the normal strain, the normal strain at end of previous step and the increment of the normal strain in the current step as defined in Section 2.3.1; t is the proportional time after the gap is closed within the step, that is, $\varepsilon_{n0} + (1 - t) \, d\varepsilon_n = 0$. The total stresses are equal to the increments of the stress because the stresses at the end of previous step $\{\sigma_0\}$ are zero within the gap.

2.3.4 EXAMPLE ANALYSIS

After implementing the interface element and the interface model into the program, two examples have been analysed to verify the program. The first example is shown in Figure 2.6 with two very stiff blocks and an interface between them. Just one 8-node brick element is used for each block and one quadrilateral interface element with four pairs of nodes for the interface. In order to examine the behaviour of the interface, the two blocks are considered as rigid with a high Young's modulus E = 10^{11}MPa and a zero Poisson's ratio $\mu = 0$. For the interface, the material constants are assigned with a normal stiffness K_n = 2000MPa /mm, a shear stiffness K_s = 1000MPa /mm, a friction angle $\varphi = 26.57^0$, a dilation angle $\psi = 26.57^0$ and a zero cohesion parameter c = 0. The lower block is fixed at the bottom. In the analysis, a uniform vertical displacement δ_1 = -0.1mm was first applied at the top of the upper block, then another uniform displacement δ_2 = 0.2mm was applied on the left surface of the upper block as shown in the figure. The analysis was carried out using the modified Euler iteration scheme (Burd 1986). One step was used for the first calculation stage with the given displacement at the top since the interface was in an elastic state and 100 steps were used in the second stage with the given displacement on the left surface. The results are shown in Figure 2.7.

From the figure, it is clear that at end of the first stage (point A in Figure 2.7) the stresses are linearly related to the given displacement ($\sigma_n = K_n \delta_1$). When the displacement δ_2 was applied on the left surface of the top block, the shear stress increases linearly step by step with a constant normal stress until the theoretical yield point B and then the stresses increase along the yield surface as would be expected.

Another example with two quadrilateral interface elements is shown in Figure 2.8 to examine the gap behaviour of the interface. The two blocks are again considered as rigid with the same material constants used in the first example and two brick elements were used for each block in the analysis. The lower block is also fixed at the bottom. The material constants of the interface are the same as those in the first example. In this example, a linearly distributed vertical displacement was first applied on the top of the upper block to form a gap at the left side of the interface, then an uniform displacement was applied to the top to close the gap. The analysis was again carried out using a modified Euler iteration procedure. There were 200 steps for both the first and the second calculation stage. The stresses at the Gauss point A, B, C and D on the interface are shown in Figure 2.9.

Figure 2.9 shows that in the calculation stage one, the stresses at point A and B are zero because there is a gap between the two blocks and that the normal stresses at point C and D increase linearly with the applied displacement but at different rates since the applied displacement is different at point C and D. In the second calculation stage, the normal stresses at point C and D increase with the applied uniform displacement at the same rate. The normal stress at point B is zero at first and then increases linearly with the given displacement after the gap at this point is closed. The gap at point A is closed at a late stage, so the normal stress at this point is zero for most of the calculation. For this simple example, a closed form solution of the stresses on the interface can be obtained, that is, $\tau = 0$, $\sigma_n = K_n \varepsilon_n$ when $\varepsilon_n < 0$ and $\sigma_n = 0$ when $\varepsilon_n > 0$. Clearly, the numerical results in Figure 2.9

are the same as the closed form solution. This means that the interface element and the interface model have successfully been implemented into the program.

2.4 NUMERICAL MODEL OF CONCRETE

2.4.1 LITERATURE REVIEW

Concrete is a complex composite material mainly used to undertake compressive load. The behaviour of concrete is complex. Experimental tests show that concrete behaves in a non-linear manner (Jiang and Feng 1991, Neville 1981). Figure 2.10 shows a typical stress-strain relationship of concrete under uniaxial load. In the compression region, several numerical models have been developed to express this curve. One of them proposed by Hognestad (Bangash 1989) is as follows:

$$\frac{\sigma}{f_c} = 2\frac{\varepsilon}{\varepsilon_0}\left(1 - \frac{\varepsilon}{\varepsilon_0}\right) \qquad \text{for } 0 < \varepsilon < \varepsilon_0$$

$$\frac{\sigma}{f_c} = 1 - \left(\frac{\varepsilon - \varepsilon_0}{\varepsilon_c - \varepsilon_0}\right) \qquad \text{for } \varepsilon_0 < \varepsilon < \varepsilon_c \qquad (2.4.1)$$

Where σ and ε are stress and strain respectively, f_c is the compressive strength, ε_0 is the strain at peak compressive stress f_c, and ε_c is the ultimate strain. In the tension region, the strain-stress relationship can approximately be expressed by a bi-linear line.

For the behaviour of concrete under biaxial stress, much research work has been done. Numerous formulations on the constitutive relations have been developed (Kupfer and Gerstle 1973, Chen and Chen 1975, Neville 1981) The expressions are generally divided into different regions, say compression-compression, tension-compression and tension-tension region. Most of the formulations are similar with some deviations in the region near the equal biaxial compressive stress state. A typical biaxial stress interaction curve is shown in Figure 2.11. It can be seen from the figure that biaxial tensile strength is no different from uniaxial tensile strength; under biaxial compression, the compression strength for σ_1 increases with the compressive stress σ_3 and reaches its maximum at about $\sigma_3 / \sigma_1 = 0.5$; and in the tension-compression region, the tensile (compressive) strength decreases approximately linearly when the compressive (tensile) stress increases.

However, there are many examples in the design of concrete when a satisfactory explanation of the ultimate strength behaviour can only be achieved if the concrete is considered to be subjected to a three-dimensional stress state. To treat these problems, many models have been developed in the three-dimensional stress state from the simple one-parameter model to very the complicated eight-parameter model, such as Boswell and Chen (1987), de Boer and Dresenkamp (1989). One typical three-dimensional concrete model is shown in Figure 2.12. Other commonly used models include Mohr-Coulomb model, Drucker-Prager model, William three-parameter model, Ottoson model and William five parameter model (Jiang and Feng 1991).

After the discussion above, it is known that the numerical model for concrete is usually complex in order to model the behaviour of concrete properly. However, some important properties of concrete may be stated as following:

(1) Tensile strength is much weaker than compressive strength by about $\frac{1}{8}$ to $\frac{1}{14}$.

(2) Concrete has limited ductility at both tension and compression failure, i.e., concrete will either crush or crack instead of flowing after reaching failure.

(3) The stress-strain relationship is generally non-linear. However, when the stress is below 40-60% of the ultimate stress, the relationship is almost linear elastic.

(4) Hydrostatic pressure has significant influence on discontinuity and failure of concrete.

(5) The failure curve of stress is a smooth non-circular closed curve in the deviatoric plane and changes from nearly triangular to nearly circular with increasing hydrostatic pressure.

2.4.2 FORMULATION OF THE MODIFIED MATSUOKA MODEL

One of the successful soil models, the Matsuoka model (Matsuoka 1976, Burd 1986), is modified here to include tensile strength in order to simulate concrete under compression. This model has the advantage that it is simple and there is no singularity on its yield surface except the origin, and that its parameters have engineering significance and are easily measured. The modified model is also used to model soils with cohesion in this research.

The modified Matsuoka model is illustrated in Figure 2.13 and its yield function can be written as (Matsuoka 1976, Burd 1986):

$$f = I_3^* \, \zeta - I_1^* \, I_2^* \tag{2.4.2}$$

$$\zeta = 9 + 8 \tan\varphi \tag{2.4.3}$$

Where the parameter φ is the frictional angle and I_i^* are defined as follows:

$$\begin{aligned}
I_1^* &= \sigma_1^* + \sigma_2^* + \sigma_3^* \\
&= \sigma_x^* + \sigma_y^* + \sigma_z^* \\
I_2^* &= \sigma_1^* \sigma_2^* + \sigma_2^* \sigma_3^* + \sigma_1^* \sigma_3^* \\
&= \sigma_x^* \sigma_y^* + \sigma_y^* \sigma_z^* + \sigma_x^* \sigma_z^* + \tau_{xy}^{\,2} + \tau_{xz}^{\,2} + \tau_{yz}^{\,2} \\
I_3^* &= \sigma_1^* \sigma_2^* \sigma_3^* \\
&= \sigma_x^* \sigma_y^* \sigma_z^* + 2\, \tau_{xy} \tau_{xz} \tau_{yz} - \sigma_x^* \tau_{yz}^{\,2} - \sigma_y^* \tau_{xz}^{\,2} - \sigma_z^* \tau_{xy}^{\,2} \\
\sigma_i^* &= \sigma_i + M \qquad \text{i=1, 2, 3, } x, y, z
\end{aligned} \tag{2.4.4}$$

σ_1 etc. are principal stresses and σ_x, τ_{xy} etc. are the conventional stresses defined in Cartesian co-ordinate system (Timoshenko and Goodier 1970). M is a material constant which can be derived from the uniaxial tensile strength f_t or from the cohesion parameter c as shown in Figure 2.13(b) by assuming that under uniaxial tension a material reaches its tensile strength and its shear strength at the same time:

$$\begin{aligned}
M &= c \,/ \tan\varphi \\
&= \frac{f_t}{2}\left(1 + \frac{1}{\sin\varphi}\right)
\end{aligned} \tag{2.4.5}$$

The plastic potential of this model is assumed to have the same form of the yield function but with different material parameters:

$$g = J_3^* \zeta^* - J_1^* J_2^* \qquad (2.4.6)$$

$$\zeta^* = 9 + 8 \tan\psi \qquad (2.4.7)$$

Where ψ is the dilation angle of the model and similarly J_i^* are defined as follows:

$$\begin{aligned}
J_1^* &= \overline{\sigma_1} + \overline{\sigma_2} + \overline{\sigma_3} \\
&= \overline{\sigma_x} + \overline{\sigma_y} + \overline{\sigma_z} \\
J_2^* &= \overline{\sigma_1}\,\overline{\sigma_2} + \overline{\sigma_2}\,\overline{\sigma_3} + \overline{\sigma_1}\,\overline{\sigma_3} \\
&= \overline{\sigma_x}\,\overline{\sigma_y} + \overline{\sigma_y}\,\overline{\sigma_z} + \overline{\sigma_x}\,\overline{\sigma_z} + \tau_{xy}^2 + \tau_{xz}^2 + \tau_{yz}^2 \qquad (2.4.8) \\
J_3^* &= \overline{\sigma_1}\,\overline{\sigma_2}\,\overline{\sigma_3} \\
&= \overline{\sigma_x}\,\overline{\sigma_y}\,\overline{\sigma_z} + 2\,\tau_{xy}\tau_{xz}\tau_{yz} - \overline{\sigma_x}\,\tau_{yz}^2 - \overline{\sigma_y}\,\tau_{xz}^2 - \overline{\sigma_z}\,\tau_{xy}^2 \\
\overline{\sigma_i} &= \sigma_i + M^* \qquad i=1, 2, 3, x, y, z
\end{aligned}$$

The parameter M^* is determined by setting $f = g$ at the current stress state as shown in Figure 2.13(b).

Under elastic stress state, the constitutive equation is the usual elastic material matrix:

$$\{ d\sigma \} = [D] \{ d\varepsilon \} \qquad (2.4.9)$$

Where $\{ d\sigma \} = \{ d\sigma_x \; d\sigma_y \; d\sigma_z \; d\tau_{yz} \; d\tau_{xz} \; d\tau_{xy} \}^T$ and $\{ d\varepsilon \} = \{ d\varepsilon_x \; d\varepsilon_y \; d\varepsilon_z \; d\gamma_{yz} \; d\gamma_{xz} \; d\gamma_{xy} \}^T$ are the vector of the stress increments and the vector of the strain increments. $[D]$ is the elastic material matrix defined as:

$$[D] = \frac{E(1-\mu)}{(1+\mu)(1-2\mu)} \begin{bmatrix} 1 & \frac{\mu}{1-\mu} & \frac{\mu}{1-\mu} & 0 & 0 & 0 \\ \frac{\mu}{1-\mu} & 1 & \frac{\mu}{1-\mu} & 0 & 0 & 0 \\ \frac{\mu}{1-\mu} & \frac{\mu}{1-\mu} & 1 & 0 & 0 & 0 \\ 0 & 0 & 0 & \frac{1-2\mu}{2(1-\mu)} & 0 & 0 \\ 0 & 0 & 0 & 0 & \frac{1-2\mu}{2(1-\mu)} & 0 \\ 0 & 0 & 0 & 0 & 0 & \frac{1-2\mu}{2(1-\mu)} \end{bmatrix} \qquad (2.4.10)$$

Where E and μ are Young's modulus and Poisson's ratio of a material.

When the stress state is plastic, an elastic-plastic material matrix can be obtained following the similar procedure in Section 2.3.2 for the interface model. Again, equation (2.3.18) is used to obtain the elastic-plastic material matrix $[\ D_{ep}\ ]$ with $[\ D\ ]$ defined in equation (2.4.10) and $\left\{\frac{\partial f}{\partial \sigma}\right\}$, $\left\{\frac{\partial g}{\partial \sigma}\right\}$ defined as follows:

$$\left\{\frac{\partial f}{\partial \sigma}\right\} = \left\{\begin{array}{l} \varsigma\,(\sigma_y^*\sigma_z^* - \tau_{yz}^2) - I_1^*\,(\sigma_y^* + \sigma_z^*) - I_2^* \\ \varsigma\,(\sigma_x^*\sigma_z^* - \tau_{xz}^2) - I_1^*\,(\sigma_x^* + \sigma_z^*) - I_2^* \\ \varsigma\,(\sigma_x^*\sigma_y^* - \tau_{xy}^2) - I_1^*\,(\sigma_x^* + \sigma_y^*) - I_2^* \\ 2\varsigma\,(\tau_{xz}\tau_{xy} - \sigma_x^*\tau_{yz}) + 2\tau_{yz} I_1^* \\ 2\varsigma\,(\tau_{xy}\tau_{yz} - \sigma_y^*\tau_{xz}) + 2\tau_{xz} I_1^* \\ 2\varsigma\,(\tau_{yz}\tau_{xz} - \sigma_z^*\tau_{xy}) + 2\tau_{xy} I_1^* \end{array}\right\} \qquad (2.4.11)$$

$$\left\{\frac{\partial g}{\partial \sigma}\right\} = \begin{Bmatrix} \varsigma^{*}\ (\overline{\sigma_{y}}\,\overline{\sigma_{z}} - \tau_{yz}^{2}) - J_{1}^{*}\,(\overline{\sigma_{y}} + \overline{\sigma_{z}}\ ) - \ J_{2}^{*} \\ \varsigma^{*}\ (\overline{\sigma_{x}}\,\overline{\sigma_{z}} - \tau_{xz}^{2}) - J_{1}^{*}\,(\overline{\sigma_{x}} + \overline{\sigma_{z}}\ ) - \ J_{2}^{*} \\ \varsigma^{*}\ (\overline{\sigma_{x}}\,\overline{\sigma_{y}} - \tau_{xy}^{2}) - J_{1}^{*}\,(\overline{\sigma_{x}} + \overline{\sigma_{y}}\ ) - \ J_{2}^{*} \\ 2\varsigma^{*}\ (\tau_{xz}\,\tau_{xy} - \overline{\sigma_{x}}\,\tau_{yz}) + 2\tau_{yz}\,J_{1}^{*} \\ 2\varsigma^{*}\ (\tau_{xy}\,\tau_{yz} - \overline{\sigma_{y}}\,\tau_{xz}) + 2\tau_{xz}\,J_{1}^{*} \\ 2\varsigma^{*}\ (\tau_{yz}\,\tau_{xz} - \overline{\sigma_{z}}\,\tau_{xy}) + 2\tau_{xy}\,J_{1}^{*} \end{Bmatrix} \qquad (2.4.12)$$

The element stiffness matrix can be calculated in the similar way as that of the interface element in Section 2.3.

For updating the displacements, strains and stresses, the approach discussed in Section 2.3.3 is also used in this model. When the stress state is in the plastic zone, the stresses are projected back on the yield surface using the closest point projection algorithm (Burd 1986, Simo and Taylor 1985, Krieg and Krieg 1977). When the stress state enters the crack zone (the most tensile principal stress $\sigma_I \geq M$) as shown in Figure 2.13(b), the stresses are proportionally put back to the yield surface to avoid singularity in calculation. This means that the modified Matsuoka model cannot simulate crack behaviour of a material. To deal with cracking, a more complex material model is needed, which is out of the scope of the current research.

2.4.3 EXAMPLE ANALYSIS

An example has been analysed to verify the implementation of the modified Matsuoka model. The example is a block with four elements as shown in Figure 2.14. The block is simply supported at the bottom. The material constants are the Young's modulus E = 10GPa, Poisson's ratio μ = 0.2, friction angle $\varphi = 26.57^0$, dilation angle $\psi = 26.57^0$ and uniaxial tensile strength f_t = 6MPa. Two cases have been examined. In the first case, a uniform displacement is applied at the top of the block as shown in Figure 2.14. The analysis was carried out with modified Euler iteration scheme and 200 steps were used. The results are shown in Figure 2.15(a). The figure shows that the magnitude of the stress σ_z increases linearly with the applied displacement until the theoretical compression yield limit (-15.71MPa) at point A. Afterwards the stress takes a constant value of the yield limit except a small deviation in the region of point A. This means that the numerical results are almost the same as the theoretical solution except for a small disturbance in the region of the yield point A.

In the second case, another uniform displacement is applied on the top but in the opposite direction as shown in the figure. The results are shown in Figure 2.15(b). Again the magnitude of the stress σ_z increases linearly with the applied displacement until the theoretical tensile yield limit (that is, the uniaxial tensile strength 6MPa) at point B. After the yield point, the stress is constant (6MPa) since the model includes neither any hardening parameter nor cracking behaviour. Again, the numerical results are the same as the theoretical solution for this simple example. The results from this example suggest that the modified Matsuoka model has correctly been implemented in the program and works well.

2.5 NUMERICAL MODEL OF REINFORCEMENT

The model discussed in Section 2.4 is for plain concrete under compression. Due to low concrete tensile strength, cracking usually exists in the tension region within concrete structures. To increase the tensile strength of concrete structures, reinforcements are usually used. With cracking in the tension region and with reinforcements, the behaviour of the concrete is different and more complicated. However, as pointed out in Chapter 1, the research in this project is focused on the pipe behaviour under working conditions. The complex cracking behaviour of concrete is out of the scope of this thesis.

In this Section, first, a brief literature review about cracking and reinforcements in concrete is presented. Then a formulation of curved bar elements used as reinforcements is discussed. Finally, two validating examples of the bar elements are presented.

2.5.1 LITERATURE REVIEW

To treat the crack, two distinct models, the discrete-cracking model and the smeared-cracking model, have been developed. The smeared-cracking model treats cracking as distributed cracks on the continuum level. Since this model does not require the knowledge of a crack direction in advance nor the change of topology of an element mesh, it is more commonly used nowadays (Vidosa al et 1991a and 1991b, Morcos and Jorhovde 1992). One of the simple procedures for the smeared-cracking model is to let the strength in direction of maximum stress vanish suddenly at the detection of a crack. Bazant (1976) pointed out that this simple model introduces a fictitious dependence on the size of finite element meshes. Afterwards, many more accurate models have been developed by introducing the concept of linear fracture mechanics (Bazant and Cedolin 1979), or by introducing non-linear mechanics concepts (Hillerborg et at 1976, Yamaguchi and Chen 1990).

The steel reinforcement in concrete is usually considered uniformly distributed within the element with uniaxial stiffness following the bar direction. Moreover, to obtain the constitutive law (one local co-ordinate should be in the bar direction), the strain increments in the reinforcement are usually assumed to be the same as those in the concrete and the stress increments are assumed to be the sum of the stress increments in the concrete and in the reinforcement (Owen et al 1983, Lin and Scordelis 1975). The behaviour of the reinforced concrete with cracks is derived by combining the reinforcement constitutive law and the smeared-cracking model (Frantzeskakis and Theillout 1989, Bazant and Gambarova 1980, Bazant and Tsubaki 1980).

Another method to model the reinforcement is to take the concrete and the reinforcement as two different materials. The bond between the concrete and the reinforcement is considered to be perfect. In analysis, the reinforcement is treated as a separate bar element carrying only axial stress. The volume of the bar may be ignored when dealing with the concrete. The bar elements will be put at an appropriate position or even embedded within the concrete element (Phillips 1987, Damjanic et al 1987). This way is simple and effective when the amount of reinforcement is small. This method is adopted in this project for the back analysis of the experiment with local steel reinforcements.

2.5.2 CURVED BAR ELEMENTS

A bar element with n nodes is shown in Figure 2.16. The formulation procedure is again based on an isoparametric approach. The element is first mapped into a isoparametric plane as a one-dimensional straight line as shown in Figure 2.17. The co-ordinates at a point in the element are related to nodal co-ordinates as functions of the isoparametric co-ordinate ξ in a similar way as those in the interface element in Section 2.3.1:

$$\begin{aligned} x &= f_1\, x_1 + f_2\, x_2 \;\ldots\; + f_n\, x_n \\ y &= f_1\, y_1 + f_2\, y_2 \;\ldots\; + f_n\, y_n \\ z &= f_1\, z_1 + f_2\, z_2 \;\ldots\; + f_n\, z_n \end{aligned} \tag{2.5.1}$$

Where x, y, z are the co-ordinates at a point within the element; x_i, y_i and z_i are the co-ordinates of node i. f_i, i=1, ... n, are the shape functions defined as follows:

$$f_i = \frac{(\xi - 0)\ldots(\xi - \frac{i-1}{n-1})(\xi - \frac{i+1}{n-1})\ldots(\xi - 1)}{(\frac{i}{n-1} - 0)\ldots(\frac{i}{n-1} - \frac{i-1}{n-1})(\frac{i}{n-1} - \frac{i+1}{n-1})\ldots(\frac{i}{n-1} - 1)} \tag{2.5.2}$$

The displacement increments at a point in the element are derived from the increments of nodal displacement in a similar way as the co-ordinates:

$$
\begin{aligned}
du &= f_1\, du_1 + f_2\, du_2 \; \ldots \; + f_n\, du_n \\
dv &= f_1\, dv_1 + f_2\, dv_2 \; \ldots \; + f_n\, dv_n \\
dw &= f_1\, dw_1 + \mathrm{f}_2\, dw_2 \; \ldots \; + \mathrm{f}_n\, dw_n
\end{aligned}
\tag{2.5.3}
$$

Where du, dv and dw are the displacement increments at a point within the element; du_i, dv_i and dw_i are the increments of the nodal displacements.

The bar element has only axial strain and bears axial force. From Figure 2.16, the axial strain increment at a point within the element can be derived by (Spiegel 1959):

$$
d\varepsilon = \frac{\partial u_\xi}{\partial s} = \frac{\partial u_\xi}{\partial \xi}\frac{\partial \xi}{\partial s} \tag{2.5.4}
$$

Where $d\varepsilon$ is the axial strain increment; u_ξ is the displacement in the $\mathbf{e}_1$ direction at the point; s is the length between the point 1 and the point at ξ along the curved line of the bar element. The $\mathbf{e}_1$ is the unit tangent direction of the curved line at the point ξ and is derived as:

$$
\begin{aligned}
\mathbf{e}_1 &= \{\, \mathrm{e}_{11} \;\; \mathrm{e}_{12} \;\; \mathrm{e}_{13} \,\}^{\mathrm{T}} \\
&= \frac{1}{J}\, \{ \frac{\partial x}{\partial \xi} \;\; \frac{\partial y}{\partial \xi} \;\; \frac{\partial z}{\partial \xi} \}^{\mathrm{T}}
\end{aligned}
\tag{2.5.5}
$$

Where $J = \sqrt{\left(\frac{\partial x}{\partial \xi}\right)^2 + \left(\frac{\partial y}{\partial \xi}\right)^2 + \left(\frac{\partial z}{\partial \xi}\right)^2}$ is the Jacobian determinant of the co-ordinates transformation between the global co-ordinates x, y and z and the isoparametric co-ordinate ξ, e_{1j}. $j=1,2,3$ are the direction cosines.

The axial displacement increment at a point in the $\mathbf{e}_1$ direction can be obtained by projecting the displacement increments du, dv and dw in the x, y and z direction at the same point in this direction as following:

$$
du_\xi = \{\, \mathrm{e}_{11} \;\; \mathrm{e}_{12} \;\; \mathrm{e}_{13} \,\}\, \{\, du \;\; dv \;\; dw \,\}^{\mathrm{T}} \tag{2.5.6}
$$

Where du_ξ is the axial displacement increment at a point within the element; T denotes transposition.

Combining the equation set (2.5.1) to (2.5.6), a relationship between the axial strain increment and the increments of the nodal displacement is obtained as following:

$$d\varepsilon = [\,B\,]\,\{\,dU\,\} \tag{2.5.7}$$

Where $\{\,dU\,\}=\{\,du_1\;\;dv_1\;\;dw_1\;\ldots\;du_n\;\;dv_n\;\;dw_n\,\}^{\mathrm{T}}$ is the vector of the nodal displacement increments. $[\,B\,]$ is the geometric matrix derived as follows:

$$[\,B\,] = \{\,e_{11}\;\;e_{12}\;\;e_{13}\,\}\,[\,F'\,]\,/\,J \tag{2.5.8}$$

$$[\,F'\,] = \begin{bmatrix} f_1' & 0 & 0 & f_2' & 0 & 0 & & f_n' & 0 & 0 \\ 0 & f_1' & 0 & 0 & f_2' & 0 & \ldots & 0 & f_n' & 0 \\ 0 & 0 & f_1' & 0 & 0 & f_2' & & 0 & 0 & f_n' \end{bmatrix} \tag{2.5.9}$$

Where $f_i' = \dfrac{\partial f_i}{\partial \xi}$, i = 1, ... n, are the derivatives of the shape function .

The steel reinforcement bar is assumed to be linearly elastic in the current research. So there is a linear constitutive equation for the axial strain increment and axial stress increment (the axial stress defined in the bar element is the axial force):

$$d\sigma = (\,EA\,)\;d\varepsilon \tag{2.5.10}$$

Where $d\sigma$ and $d\varepsilon$ are the axial stress increment and the axial strain increment; E and A are the Young's modulus of the steel bar and the area of the cross section of the bar respectively. The element stiffness matrix is derived as:

$$\begin{aligned} [\,K\,] &= \int_S (\,EA\,)\,[\,B\,]^{\mathrm{T}}\,[\,B\,]\,\mathrm{d}s \\ &= \int_{-1}^{1} (\,EA\,)\;[\,B\,]^{\mathrm{T}}\,[\,B\,]\,J\,\mathrm{d}\xi \end{aligned} \tag{2.5.11}$$

Where $[\,K\,]$ is the element stiffness matrix; S is the domain of the curved line of the bar element. Four curved bar elements with 2, 3, 4 and 5 nodes have been implemented into the program.

2.5.3 EXAMPLE ANALYSIS

Again, a few benchmark tests have been carried out before the program is used for three-dimensional analysis in this research. The first example is a curved bar over a quarter of a circle with radius r =10mm as shown in Figure 2.18. The bar is simply supported in the radial direction, fixed at one end and subjected to a tensile force of 100N at the other end as shown in the figure. The bar has constant axial stiffness *EA*. The problem is examined with 2-node, 3-node and 5-node bar elements. The results are given in Table 2.2.

The second example is almost the same as the first one except that it is with 7 nodes, as shown in Figure 2.19, instead of 9 nodes as in the first example. The problem is now examined with 2-node, 3-node and 4-node bar elements. The results are given in Table 2.3. From the results in these two tables, it is very clear that the elements have been properly implemented into the program and the accuracy is very good especially for the 3-node and 5-node bar elements.

Table 2.2 results of first example

No. of nodes per element	number of elements	number of Gauss points per element	axial stresses at Gauss points	analytical solution
2	8	1	100.48N	100N
3	4	2	100.00N 100.00N	100N
5	2	4	100.03N 99.98N 99.98N 100.03N	100N

Table 2.3 results of second example

No. of nodes per element	number of elements	number of Gauss points per element	axial stresses at Gauss points	analytical solution
2	6	1	100.86N	100N
3	3	2	100.01N 100.01N	100N
4	2	3	100.98N 98.82N 100.98N	100N

2.6 SOLUTION METHOD

In finite element analysis, solution procedures are usually based on incremental methods, that is, a problem is solved step by step with a small load increment within each step to secure solution accuracy and convergence:

$$[K_n]\{dU_n\} = \{dP_n\} \qquad n = 1, 2, \ldots N$$

$$\{U_n\} = \{U_{n-1}\} + \{dU_n\} \qquad n = 1, 2, \ldots N \qquad (2.6.1)$$

Where N is total calculation steps; $[K_n]$ is overall stiffness matrix in the current calculation step n; $\{U_n\}$, $\{U_{n-1}\}$ and $\{dU_n\}$ are the vector of the nodal displacements at end of step n, the vector of the nodal displacements at end of step n-1 and the increments of the nodal displacements within step n; $\{dP_n\}$ is the vector of applied load increments in step n. The load increment $\{dP_n\}$ may be different from step to step. In general, there is an unbalanced force (residual force) at end of each step. This unbalanced force may be added into the applied load increment in the next step, as discussed in later sections.

In this Section, a few commonly used solution methods, Euler method, modified Euler method and Newton-Raphson method, are reviewed briefly. Then a modified Newton-Raphson method is proposed and discussed in Section 2.6.3. Finally, a validating example is presented.

2.6.1 EULER AND MODIFIED EULER METHOD

A simple solution method is the Euler method in which the equation (2.6.1) is solved step by step and the unbalanced force at end of each step is ignored (Zienkiewicz 1977, Sloan 1981). The Euler method usually obtains a good convergent solution if the load increment in each step is very small. This means that convergence is slow using the Euler method.

To improve accuracy and convergence, a modified Euler method is proposed by Sloan (1981). In this modified Euler method, an unbalanced force is evaluated at the end of each step and is then applied in the next calculation step as a part of the applied load together with the applied load increment when solving the equation (2.6.1):

$$\{ P_n \} = \sum_{i=1}^{n} \{ dP_i \} \tag{2.6.2}$$

$$\{ R_n \} = \sum_{e} \iiint_{\Omega} [B]^T \{\sigma\} dV - \{ P_n \} \tag{2.6.3}$$

$$\{ dP^*_{n+1} \} = \{ dP_{n+1} \} + \{ R_n \} \tag{2.6.4}$$

Where $\{ P_n \}$ and $\{ R_n \}$ are the total applied force and the unbalanced force at end of step n; $\{ dP_i \}$ is the applied load increments in step i; Ω is the domain of element e and the summation is over all elements; $\{ dP_{n+1} \}$ and $\{ dP^*_{n+1} \}$ is the applied load increment and modified applied load increment including the unbalanced force from the previous step in step n+1. This modified Euler method is generally found to be stable and accurate (Sloan 1981, Burd 1986). Both the Euler method and the modified Euler method are available in FEPS.

2.6.2 NEWTON-RAPHSON METHOD

The Newton-Raphson method is another commonly used method for solving non-linear problems. In this method, if a solution at step n-1 has been obtained, the equation (2.6.1) at step n is solved by an iteration procedure to secure a zero (or almost zero) unbalanced force:

$$[K_n]^m \{dV_n\}^m - \{R_n\}^m = \{0\} \qquad m=1,2,3,\ldots$$

$$\{dU_n\}^{m+1} = \{dU_n\}^m + \{dV_n\}^m \tag{2.6.5}$$

$$\{R_n\}^{m+1} = [K_n]^{m+1}\{dU_n\}^{m+1} - \{dP_n\}$$

Where $[K_n]^m$ is the overall stiffness matrix at iteration m within step n; $\{dV_n\}^m$ and $\{R_n\}^m$ are the displacement increments and the unbalanced force at iteration m within step n; $\{dU_n\}^m$ and $\{dU_n\}^{m+1}$ are the total displacement increments at the start and end of iteration m in step n; $\{dP_n\}$ is the applied load increments in step n. The calculation begins with initial values $\{dU_n\}^1 = \{0\}$ and $\{R_n\}^1 = \{dP_n\}$. The analysis proceeds to the next step when the unbalanced force $\{R_n\}^{m+1}$ satisfies a given convergent criterion:

$$|\{R_n\}^{m+1}| \,/\, |\{P_n\}| < \delta_1 \qquad \text{for relative error}$$

or $$|\{R_n\}^{m+1}| < \delta_2 \qquad \text{for absolute error} \tag{2.6.6}$$

Where $\{P_n\}$ is the total applied load by end of step n; δ_1 and δ_2 are two very small given numbers to control solution accuracy.

In the Newton-Raphson method, the overall stiffness matrix $[K_n]^m$ is updated not only for each step but also for each iteration within a step. This will increase computing time. A variant version of the Newton-Raphson method is usually used in which the overall stiffness matrix is updated in each step instead of in each iteration. For simplicity, this variant version is referred as Newton-Raphson method in this research.

2.6.3 MODIFIED NEWTON-RAPHSON METHOD AND INITIAL STIFFNESS METHOD

To improve accuracy, convergence and efficiency of the Newton-Raphson method, a modified Newton-Raphson method is proposed in this research. In the modified formulation, a maximum number of iterations is set up for each step, that is, the iteration in a step will stop when the unbalanced force satisfies a given convergent criterion as shown in equation (2.6.6) or when the iteration number reaches the given maximum number. The unbalanced force at the end of each step, if any, is then added into the next step as a part of the applied load as in equation (2.6.4) in the modified Euler method. Moreover, the overall stiffness matrix [K] is updated only when the unbalanced force at end of a step is larger than a given value:

$$| \{ R_n \}^{m+1} | \; / \; | \{ P_n \} | > \delta_3 \qquad \text{for relative error}$$

$$\text{or} \quad | \{ R_n \}^{m+1} | > \delta_4 \qquad \text{for absolute error} \qquad (2.6.7)$$

Where δ_3 and δ_4 are two given small numbers.

Another common solution method available in the program is a variant version of the initial stiffness method (for simplicity, it is referred to as initial stiffness method in this project). In this method, the initial elastic overall stiffness matrix [K_0] is used throughout the calculation. As in the modified Newton-Raphson method, a maximum iteration number is set up for each step and the unbalanced force at end of each step is added into next step as a part of the applied load.

From the discussion above, it is clear that if the maximum iteration number is set to 1, and δ_3 and δ_4 in equation (2.6.7) are set to zero, the modified Newton-Raphson method becomes the modified Euler method discussed in Section 2.6.1. If δ_3 and δ_4 are set to very large numbers, the modified Newton-Raphson method becomes the initial stiffness method. When the maximum iteration number is set to a very large number with δ_3 and δ_4 set to zero, the modified Newton-Raphson method becomes the Newton-Raphson method (the stiffness matrix is updated in each step). This means that the initial stiffness method, the modified Euler method, and the Newton-Raphson method can all be treated to be an alternative version of the modified Newton-Raphson method.

2.6.4 EXAMPLE ANALYSIS

The example for the modified Matsuoka model in Section 2.4.3 is used here to verify the program after the implementation of the solution methods. The calculation is carried out with the Modified Euler method, the Newton-Raphson method, the modified Newton-Raphson method and the initial stiffness method respectively. All the solution methods give the same results as shown in Figure 2.15. This means that the solution methods are successfully implemented and work properly. For this example, the computing time with the modified Newton-Raphson method and the initial stiffness method is less than those with the modified Euler method and the Newton-Raphson method. To obtain a stable solution, the Newton-Raphson method needs more calculation steps than the other three. However, elastic-plastic problems are complex and the best solution method is usually problem dependent (Zienkiewicz 1977). A detailed evaluation of different solution methods is not the task of this research. In this project, the initial stiffness and the modified Newton-Raphson method seem more stable in the analysis with an interface in Chapter 5.

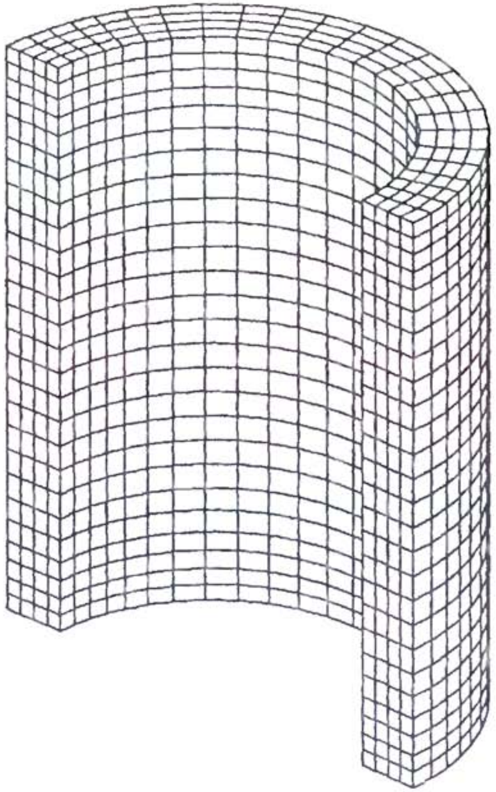

Figure 2.1 A pipe mesh generated by DATAIN

```
! 3D mesh of a pipe
A, 3,  75.,    0.,    0.,
%, 5, 6.25,    0.,    0.,
%, 5,    0.,  5.5,    0.,
%,-2,    0.,  7.0,    0.,
%,-12,   0.,  9.0,    0.,
%,-2,    0.,  7.0,    0.,
%,-4,    0.,  5.5,    0.,
%, 3,    0.,  0.0,   6.5,
%,-2,    0.,  0.0,   7.5,
%,-2,    0.,  0.0,   9.0,
%,-14,   0.,  0.0,   10.,
%,-2,    0.,  0.0,   9.0,
%,-2,    0.,  0.0,   7.5,
%,-2,    0.,  0.0,   6.5,
E,

A, 8,    1 ,  2 ,   7,   6,
        126, 127, 132, 131,
%,  4,   *, 8,    1,
%, 24,   *, 8,    5,
%, 26,   *, 8, 125,
E,
E,
```

Table 2.1 Input data of DATAIN for a pipe mesh

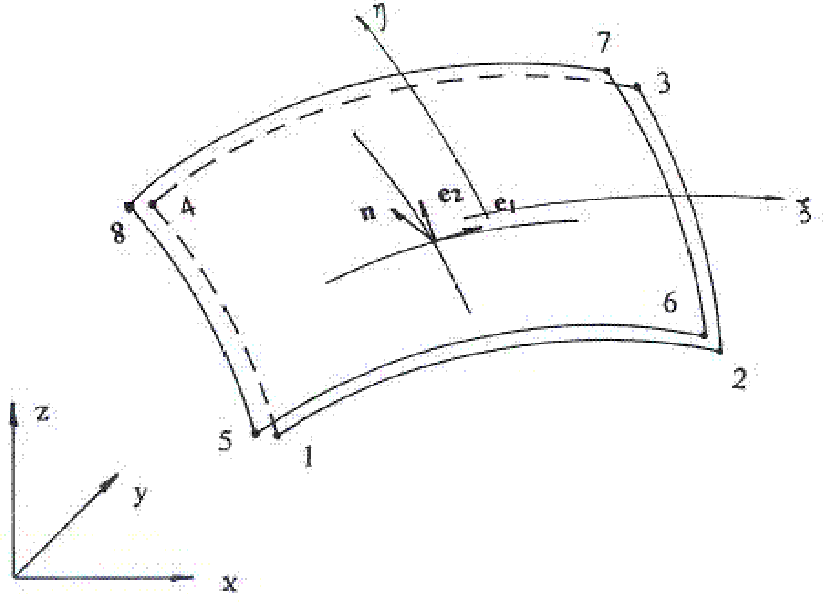

Figure 2.2 A quadrilateral interface element

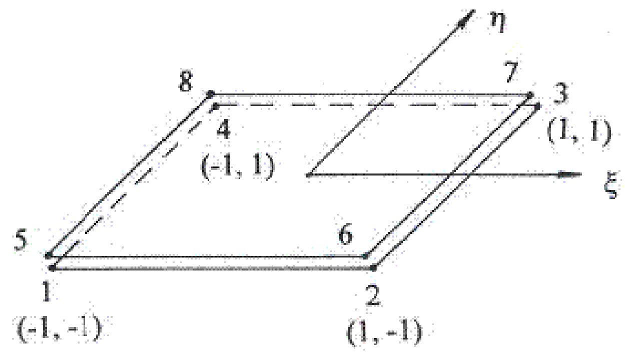

Figure 2.3 Interface element on an isoparametric plane

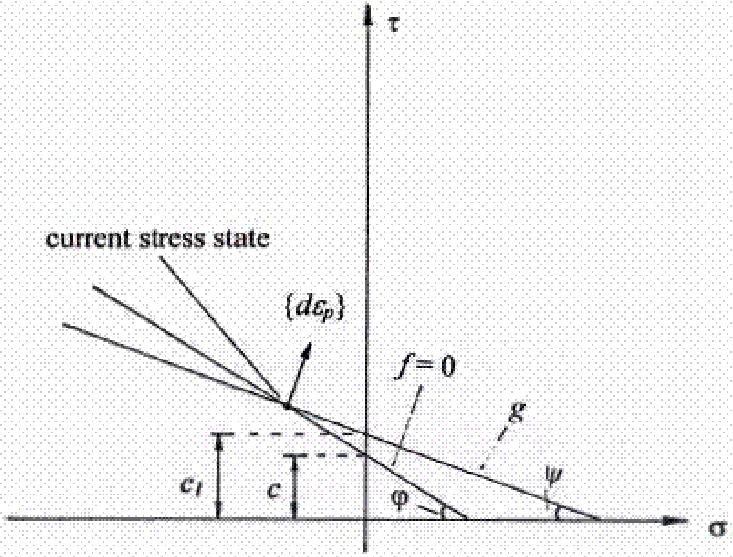

Figure 2.4 Mohr-Coulomb interface model

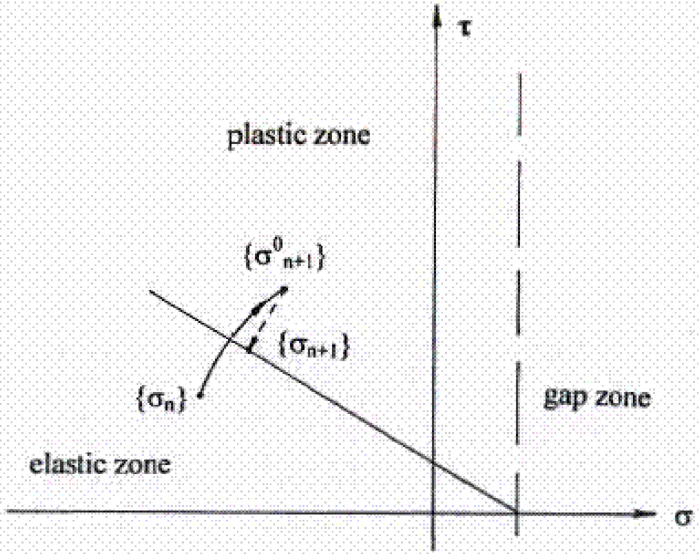

Figure 2.5 Different stress regions in interface model

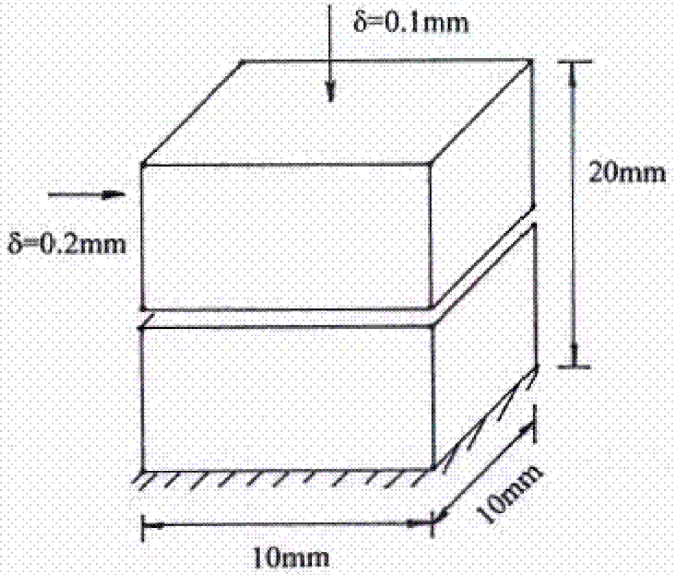

Figure 2.6 An example of interface

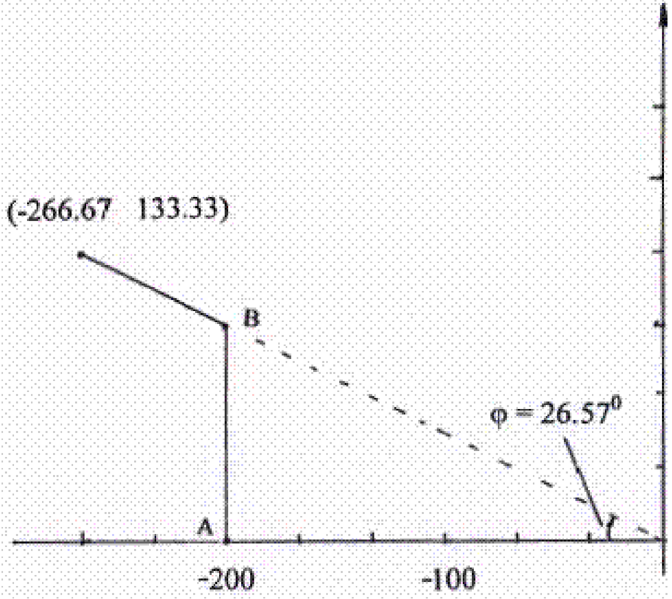

Figure 2.7 Yield behaviour of interface

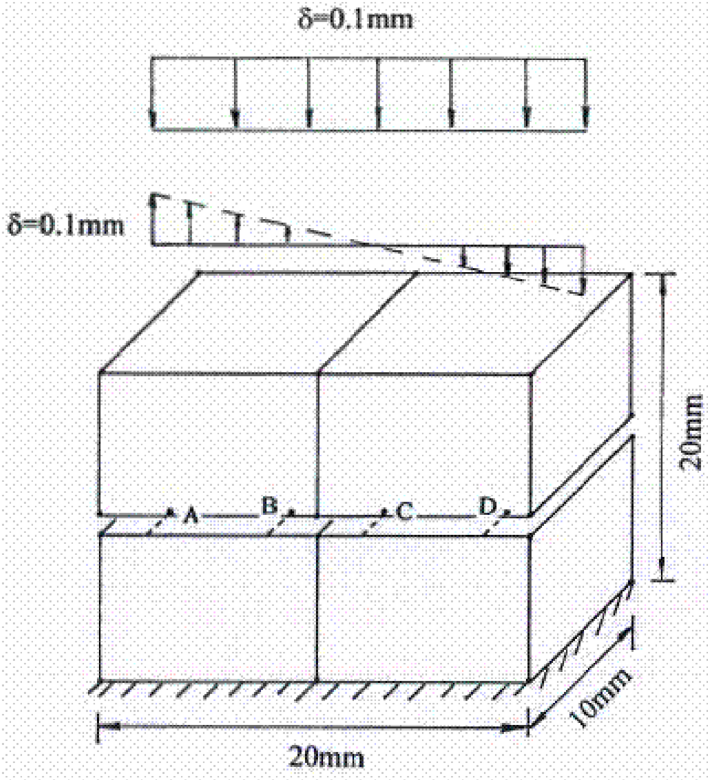

Figure 2.8 An interface with gap

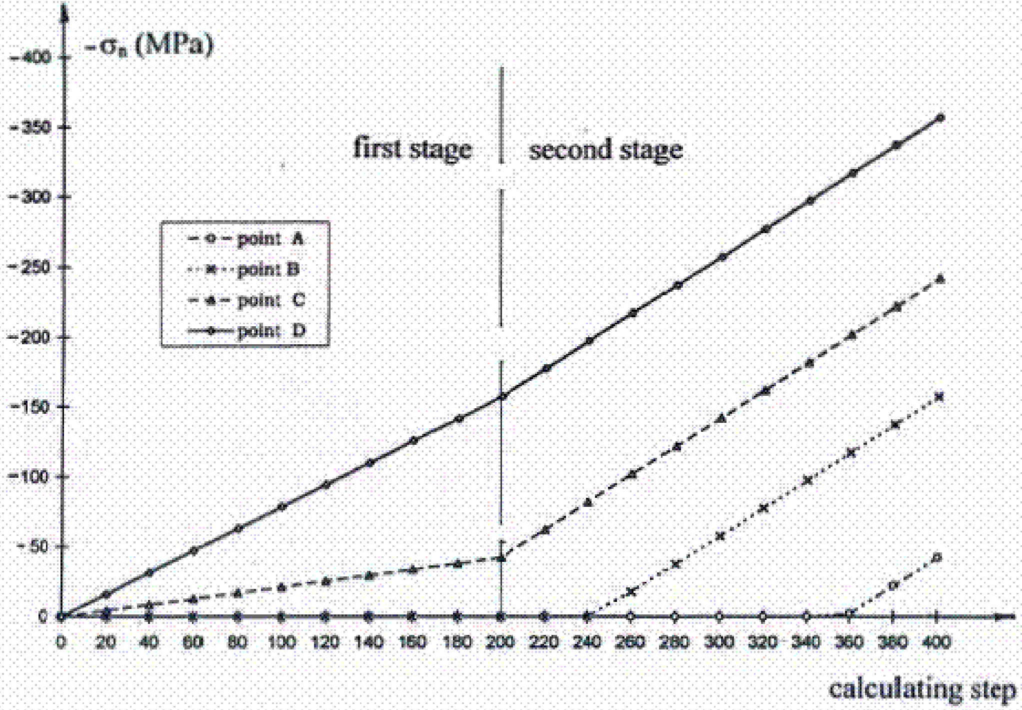

Figure 2.9 Gap behaviour of interface

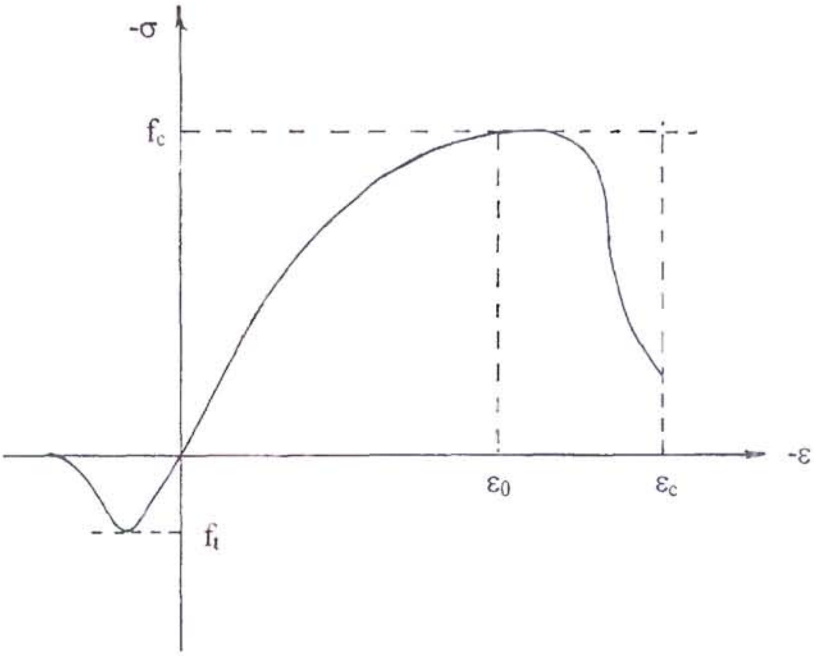

Figure 2.10 A typical uniaxial stress-strain curve for concrete (from Bangash 1989)

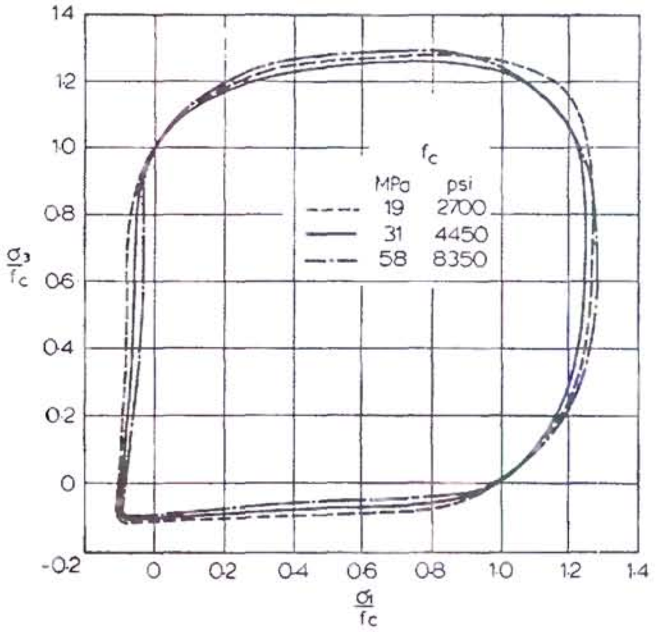

Figure 2.11 A typical biaxial stress interaction in concrete model (from Neville 1981)

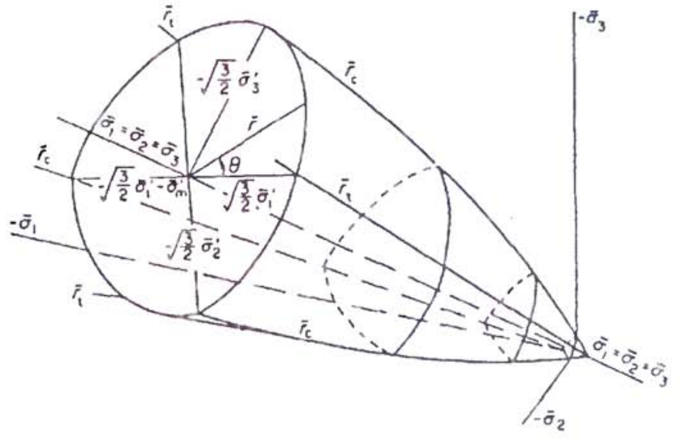

Figure 2.12 A typical three-dimensional concrete model (from Boswell and Chen 1987)

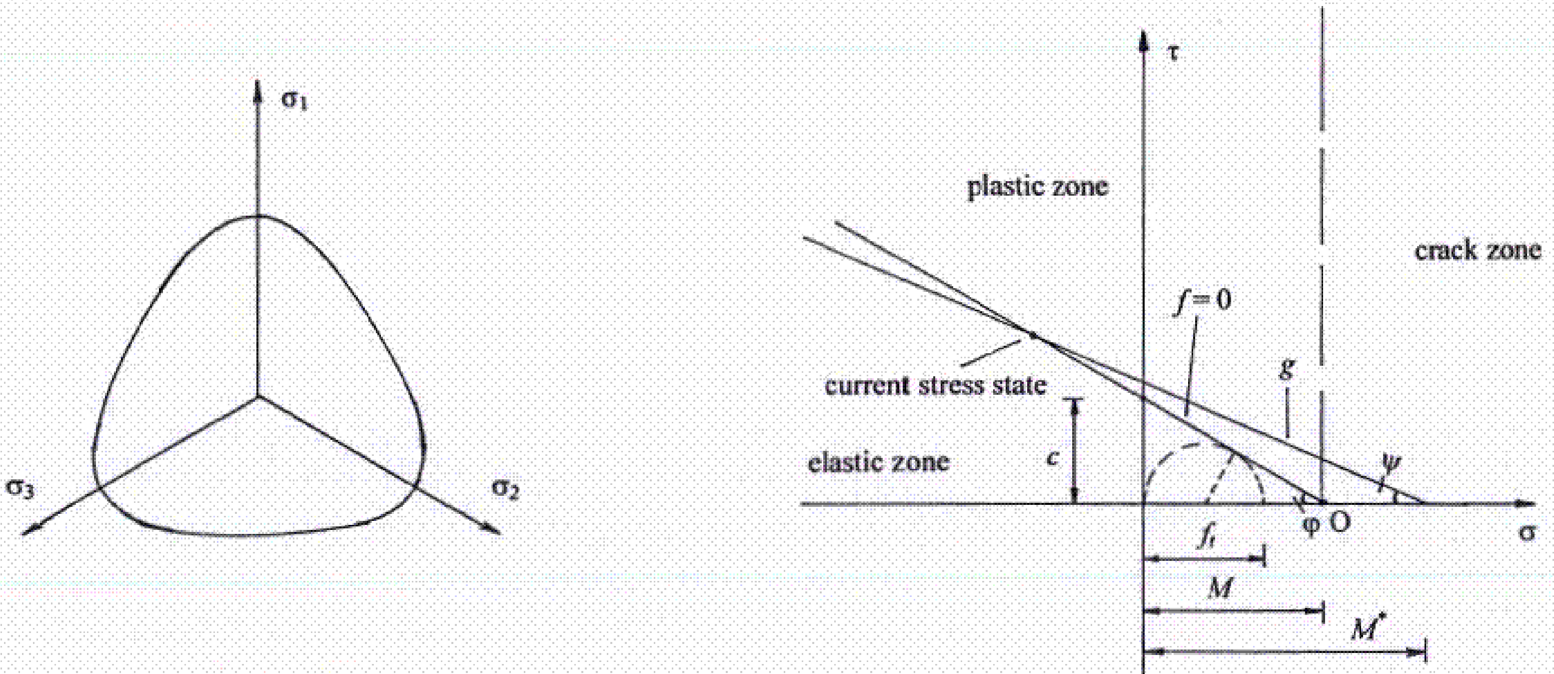

(a) Yield surface

(b) Relationship between c, f_t, M and M^*

Figure 2.13 Modified Matsuoka model

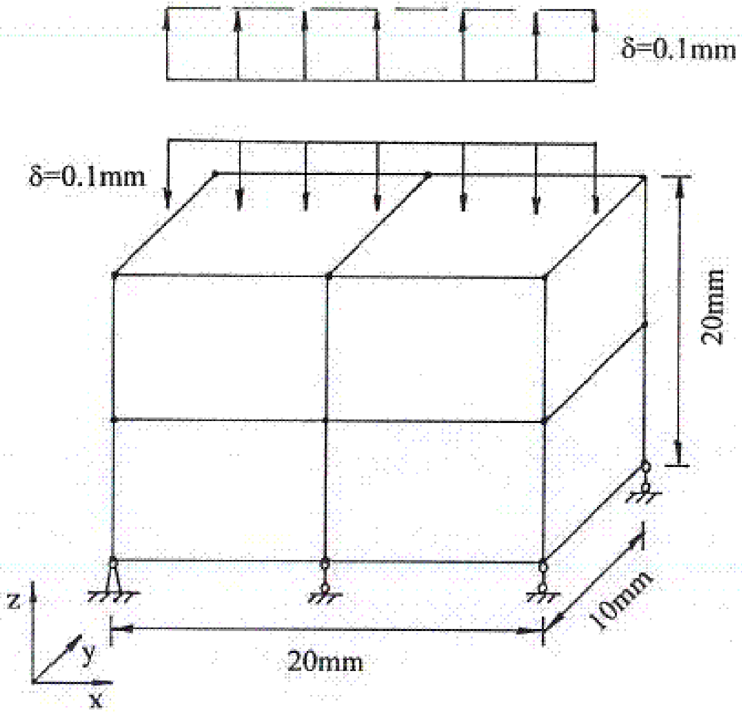

Figure 2.14 An example for modified Matsuoka model

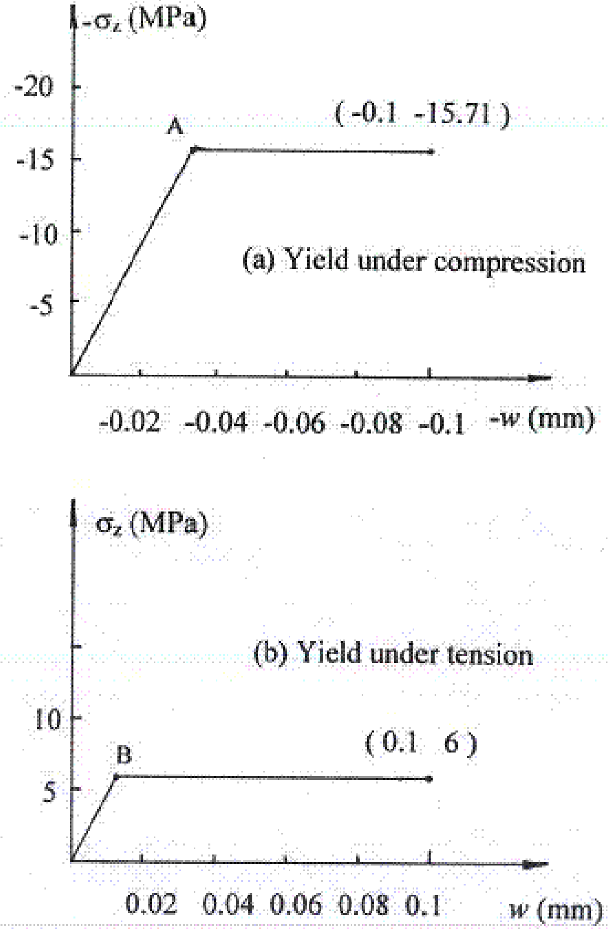

Figure 2.15 Stress yield behaviour in modified Matsuoka model

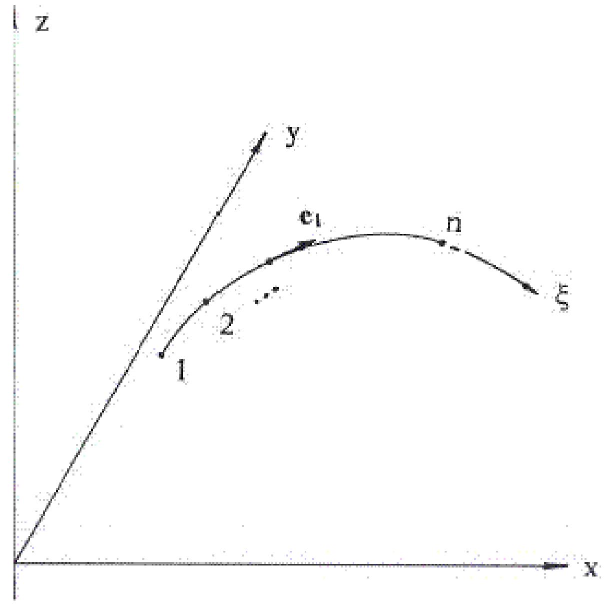

Figure 2.16 Curved bar element

Figure 2.17 Bar element on an isoparametric plane

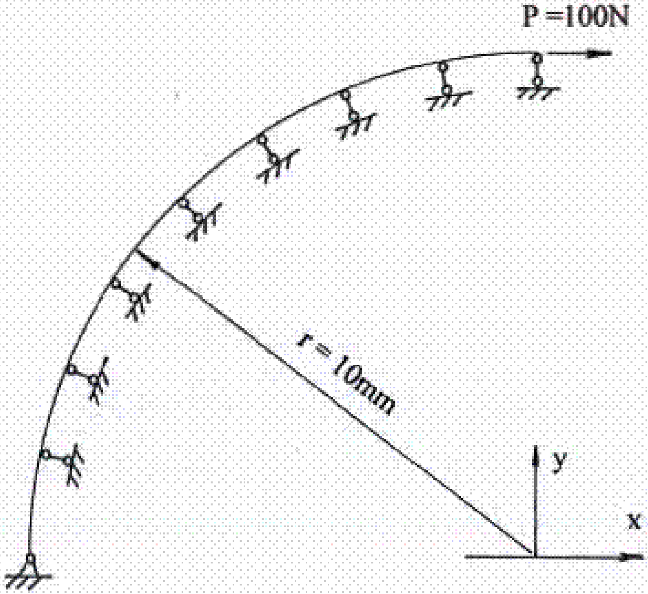

Figure 2.18 First example for bar element

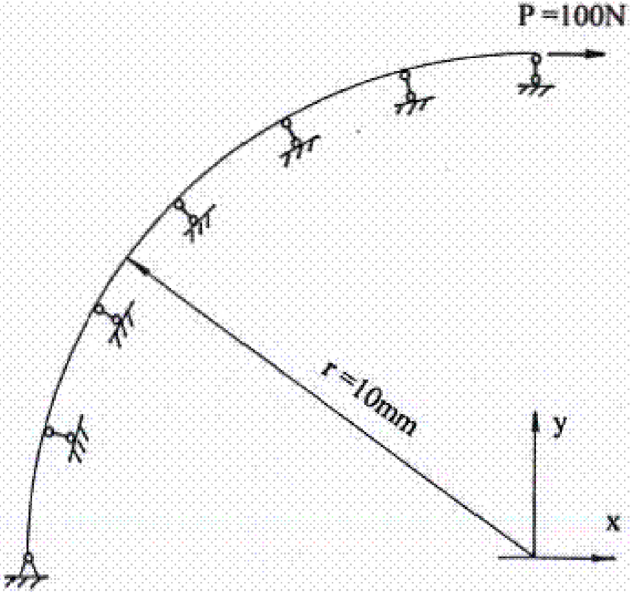

Figure 2.19 Second example for bar element

CHAPTER 3 PRELIMINARY TWO-DIMENSIONAL STUDY

3.1 INTRODUCTION

This chapter describes a two-dimensional analysis of pipe joint behaviour. More detailed three-dimensional analyses are described in later chapters. For the two-dimensional analysis described in this chapter, the finite element program OXFEM (Burd 1996) was used. The program contains simple elastic-plastic material models and various types of elements including interface elements used to simulate the interaction between the concrete pipe and the packing material. The mesh generation program OXMESH (Houlsby 1988) available in the Civil Engineering Research Group at the Department of Engineering Science was used to generate the finite element meshes.

The main purpose of this preliminary study is to provide experience with the use of interface elements for interaction between the pipe and the packing material, numerical material models and non-linear analysis procedure. In this chapter, a simplified two-dimensional numerical model is described in Section 3.2. The effect of the properties of the packing material and the effect of the misalignment of the pipeline are discussed in Sections 3.3 and 3.4 respectively. Finally, Section 3.5 gives the conclusion.

3.2 TWO-DIMENSIONAL MODEL

In the two-dimensional analysis, the pipe wall instead of the complete pipe was examined. Although the concrete pipe, loading condition and boundary conditions in pipe jacking are three-dimensional in nature, a small region of the concrete pipe walls around the joint including the packing material was simplified as a plane strain model in order to carry out some simple, preliminary, calculations. The simplified numerical model and its finite element mesh are shown in Figure 3.1(a) and 3.1(b) respectively. The dimensions of the model are also given in the figure. In the analysis, the nodes at the bottom of the lower pipe (it is actually a small region of the pipe wall but is referred to as 'pipe' in this chapter for simplicity) were pinned, which leads to a pipe boundary condition that is effectively fixed. The strength of the jacking pipe is approximately 65MPa as discussed in Chapter One. The maximum pressure on the pipe end in practice should be less than 30MPa for safety reasons. In this simple model, a uniform pressure q = 30MPa was applied vertically to the top of the upper pipe to simulate the thrust force during pipe jacking and the upper pipe was rotated through a small angle β to simulate the misalignment of the pipeline. In the analysis, this misalignment angle β was simulated by an equivalent given displacement δ in the x direction at the top of the upper pipe. Equivalence here means that if the displacement in the x direction at the bottom of the upper pipe is zero, the displacement δ at the top would produce the same rotation angle β (that is, $\tan\beta = \delta / L$, L = 150mm is the length of the 'pipe'). The load and the misalignment rotation were applied simultaneously in the numerical analysis. To examine the influence of the misalignment angle, two different misalignment angles $\beta = 0.1^0$ and 0.3^0 were studied in the analysis (the equivalent displacements at the top of the upper pipe in x direction for $\beta = 0.1^0$ and 0.3^0 are 0.26mm and 0.79mm respectively).

In the numerical analysis, the concrete pipe and the packing material were assumed to be linearly elastic. The material constants of the concrete pipe were chosen with a typical shear modulus $G_c = 40000$MPa and a Poisson's ratio $\mu_c = 0.20$. The main type of element used in the mesh was 6-node triangle. A layer of 6-node line interface elements was used on each interface between the pipe and the packing material to simulate the interaction between them. The stiffness of the interface should be high in theory. However, high interface stiffness could cause calculation difficulties in analysis. According to the research carried out by Burd (1986), Beer (1985), Burd and Brocklehurst (1992), and Adhikary and Dysin (1998), the stiffness of the interface was chosen in such a way that the deformation of the interface is about 5 percent of that of the packing material. With reference to the properties and dimensions of the packing material, the properties of the interface model were chosen with the normal stiffness Kn = 800MPa /mm, the shear stiffness Ks = 400MPa /mm, the frictional angle $\phi = 20^0$ and the dilation angle $\psi = 20^0$. To assess the sensitivity of the stiffness of the interface in this model, analyses were also carried out with high interface stiffness Kn = 8000MPa /mm and Ks = 4000MPa /mm. The modified Euler iteration procedure (Burd 1986) was used for this preliminary analysis and the total number of calculation steps was 400.

3.3 EFFECT OF PACKING MATERIAL PROPERTIES

The experimental research by Milligan and Ripley (1989), Ripley (1989), Husein (1989), and Boot and Husein (1991) has shown that packing materials play an important role in pipe jacking by reducing the stress concentration at the pipe joint which in turn reduces the risk of pipe damage. In order to understand the interaction between the packing material and the pipe, a parametric study has been carried out to examine the influence of the properties of the packing materials using the two-dimensional model. The research carried out by Milligan and Ripley (1989) and Husein (1989) showed that the stiffness of the packing material could vary from about

260MPa for plywood and chipboard to 2600MPa for nylon, and that the Poisson's ratio would change from almost zero for plywood and chipboard to almost 0.5 for LDPE and Elastomer. In the analyses, three typical Poisson's ratios of the packing material, μ_p = 0.1, 0.4 and -0.3 representing low, high and negative Poisson's ratios with a typical shear modulus G_p = 300MPa were studied for the influence of the Poisson's ratio; and three typical shear moduli G_p = 300MPa, 600MPa and 900MPa with $\mu_p = 0.1$ were included to examine the influence of the stiffness of the packing material (the stiffness of the packing material is $E_p = 2\ G_p(\ 1 + 2\mu_p\ )$, and shear modulus and Poisson's ratio are the input data of the material constants in program OXFEM).

The normal stresses on the lower interface with $\beta = 0.1^0$ are shown in Figure 3.2. The figure shows that the normal stresses are approximately linearly distributed with x on the interface with their maximum magnitudes in the right end region (x=150mm) except in the case of $\mu_p = 0.4$ where the magnitude of normal stress is higher in the middle area on the interface and highly non-linear at the two end regions. In general, packing material with higher shear modulus induces higher maximum normal stress with the same Poisson's ratio. The influence of the Poisson's ratio of the packing material is complex, packing material with both high and negative Poisson's ratio induce higher non-linearity at the two end regions. However, the normal stress in the case of $\mu_p = -0.3$ is close to that in the case of $\mu_p = 0.1$, while the magnitude of the normal stress in the case of $\mu_p = 0.4$ is higher in the middle area on the interface.

The shear stresses on the lower interface with $\beta = 0.1^0$ are shown in Figure 3.3. The figure shows that in the case of $\mu_p = 0.1$ the distribution patterns are similar for different packing materials with different shear modulus, that is, the shear stresses are almost constant and small on the interface except in the two end regions, and that packing material with higher shear modulus induces slightly higher shear stress on the interface. In the cases of $\mu_p = 0.4$ and $\mu_p = -0.3$, the shear stresses are also small in the middle area, however, the magnitude of the shear stresses are high in the two end regions. The direction of the shear stresses at the two end regions is towards the centre in the case of $\mu_p = -0.3$ and in the opposite direction in the other case. (The stresses on the interface are calculated at Gauss points and the shear stresses at each end ($x = 0$mm and 150mm) of the interface are zero because there is no shear stress on the plane $x = 0$ and $x = 150$mm .)

The most tensile principal stresses around the joint with $\beta = 0.1^0$ are shown in Figure 3.4(a), 3.4(b), 3.4(c) and 3.4(d) for the case of $\mu_p = 0.1$, $\mu_p = 0.4$ and $\mu_p = -0.3$ with $G_p = 300$MPa, and $\mu_p = 0.1$ with $G_p = 900$MPa respectively. From the figure, it is clear that the tensile stresses are mainly located in the region of the pipe joint while the tensile stresses are very small in other regions. Moreover, the results indicate that with the same shear modulus $G_p = 300$MPa, packing materials with a high Poisson's ratio ($\mu_p = 0.4$) generate much larger tensile stresses in the concrete than those with a lower Poisson's ratio ($\mu_p = 0.1$) due to the high shear stresses on the interface in the case of $\mu_p = 0.4$ as shown in Figure 3.3, and that if a negative Poisson's ratio is used for the packing material then tensile stresses in the concrete are almost zero (high tensile stresses appear in the packing material). With the same Poisson's ratio ($\mu_p = 0.1$), packing material with higher shear modulus $G_p = 900$MPa also produce higher tensile stresses in the concrete, although the influence is not significant compared with that of the Poisson's ratio.

In order to assess the sensitivity of the stiffness of the interface, analyses were also carried out with high interface stiffness Kn = 8000MPa /mm and Ks = 4000MPa /mm while other conditions were unchanged. Figure 3.5 shows the most tensile principal stresses around the joint with $\beta = 0.1^0$ and the high interface stiffness. Comparing with the stresses in Figure 3.4, it is clear that both the stress distribution patterns and the maximum stresses are similar. This means that the influence of the interface stiffness on the computed stresses is small in this model. This is why the same material constants of the interface were used in this chapter for all the analyses with different packing materials.

3.4 EFFECT OF THE PIPELINE MISALIGNMENT

This section describes the parametric study with a high misalignment angles $\beta = 0.3^0$ to examine the influence of the amount of the pipeline misalignment. The analyses were carried out with the properties of the packing material and other conditions unchanged as in Section 3.3. The normal stresses on the lower interface with $\beta = 0.3^0$ are shown in Figure 3.6. Again, the normal stresses are approximately linearly distributed with x on the interface with their maximum magnitude at the right end region (x = 150mm). In general, the normal stresses are more localized than those with $\beta = 0.1^0$. Again, with the same Poisson's ratio, packing material with higher shear modulus induces higher maximum normal stress on the interface. With the same shear modulus (G_p = 300MPa), the normal stresses in the case of $\mu_p = 0.1$ and -0.3 are somewhat similar, while the normal stresses in the case of $\mu_p = 0.4$ are more localized. This means that the influence of the packing material on the normal stresses on the interface is not only due to the change of the stiffness of the packing material $E_p = 2\,G_p(\,1 + 2\,\mu_p)$ but also due to the change of the Poisson's ratio of the packing material.

The shear stresses on the lower interface with $\beta = 0.3^0$ are shown in Figure 3.7. The distribution patterns of the shear stress on the interface are similar to those with $\beta = 0.1^0$ in Section 3.3 but the magnitudes of the shear stresses are higher. The influence of the properties of the packing material are also similar to that in the case with $\beta = 0.1^0$ (refer to Section 3.3, see Figure 3.3).

The most tensile principal stresses around the joint with $\beta = 0.3^0$ are shown in Figure 3.8(a), 3.8(b), 3.8(c) and 3.8(d) for the case of $\mu_p = 0.1$, $\mu_p = 0.4$ and $\mu_p = -0.3$ with $G_p = 300$MPa, and $\mu_p = 0.1$ with $G_p = 900$MPa respectively. Again, the tensile stresses are mainly located in the region of the pipe joint. The stress distribution patterns and the influence of the properties of the packing material are similar to those with $\beta = 0.1^0$ as shown in Figure 3.4, however, the maximum tensile stress is much higher. (The scale in Figure 3.4 is different from that in Figure 3.8.)

3.5 CONCLUSION

The results in this chapter show that the pipeline misalignment causes high shear stresses and localization of the normal stresses on the interface which in turn may generate high tensile stresses and concentrations of compressive stress in the concrete. Moreover, the effect of the misalignment is coupled with the effect of the Poisson's ratio and the shear modulus of the packing material. That is, the higher the value of β, the higher the peak value of the stresses with the same μ_p and G_p, and the higher the value of μ_p and/or G_p, the higher the peak value of stresses with the same β.

From the numerical results of the simplified two-dimensional model in this chapter, a few conclusions may be drawn:

(1) The packing material with high Poisson's ratio ($\mu_p = 0.4$) induces higher tensile stresses at the pipe joint than that with low Poisson's ratio ($\mu_p = 0.1$). The packing material with negative Poisson's ratio produces even better results although the result difference is not significant between the low Poisson's ratio and the negative Poisson's ratio.

(2) Material with high shear stiffness increases the stresses on the interface and in the pipe, although the influence of the shear stiffness on the stresses is not significant compared with that of the Poisson's ratio.

(3) Misalignment of the pipeline is the main factor for inducing both high tensile stresses and high compressive stresses at the pipe joint. The higher the misalignment angle, the higher the tensile stresses in the concrete pipe.

(4) Interface elements are useful for the study of contact problems because they can simulate the interaction between different structures and be used to extract details about the stress distribution on the interface. The influence of the stiffness of the interface on the computed stresses is small in this model.

(5) The main purpose of the two-dimensional model is to gain experience. The results need to be verified with three-dimensional models due to the three-dimensional nature of the problem.

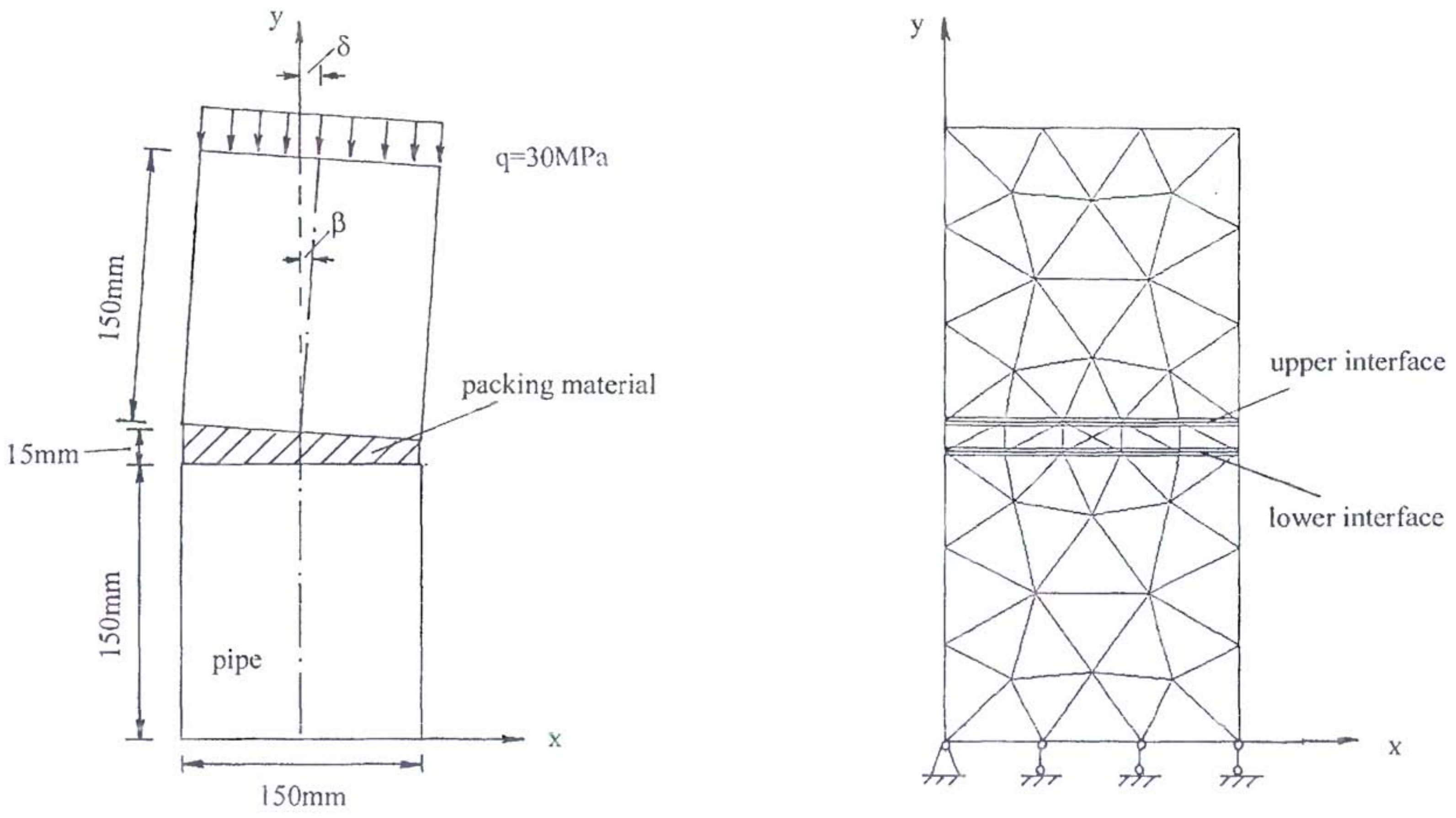

(a) Two-dimensional model

(b) Finite element mesh

Figure 3.1 Simplified model and its finite element mesh

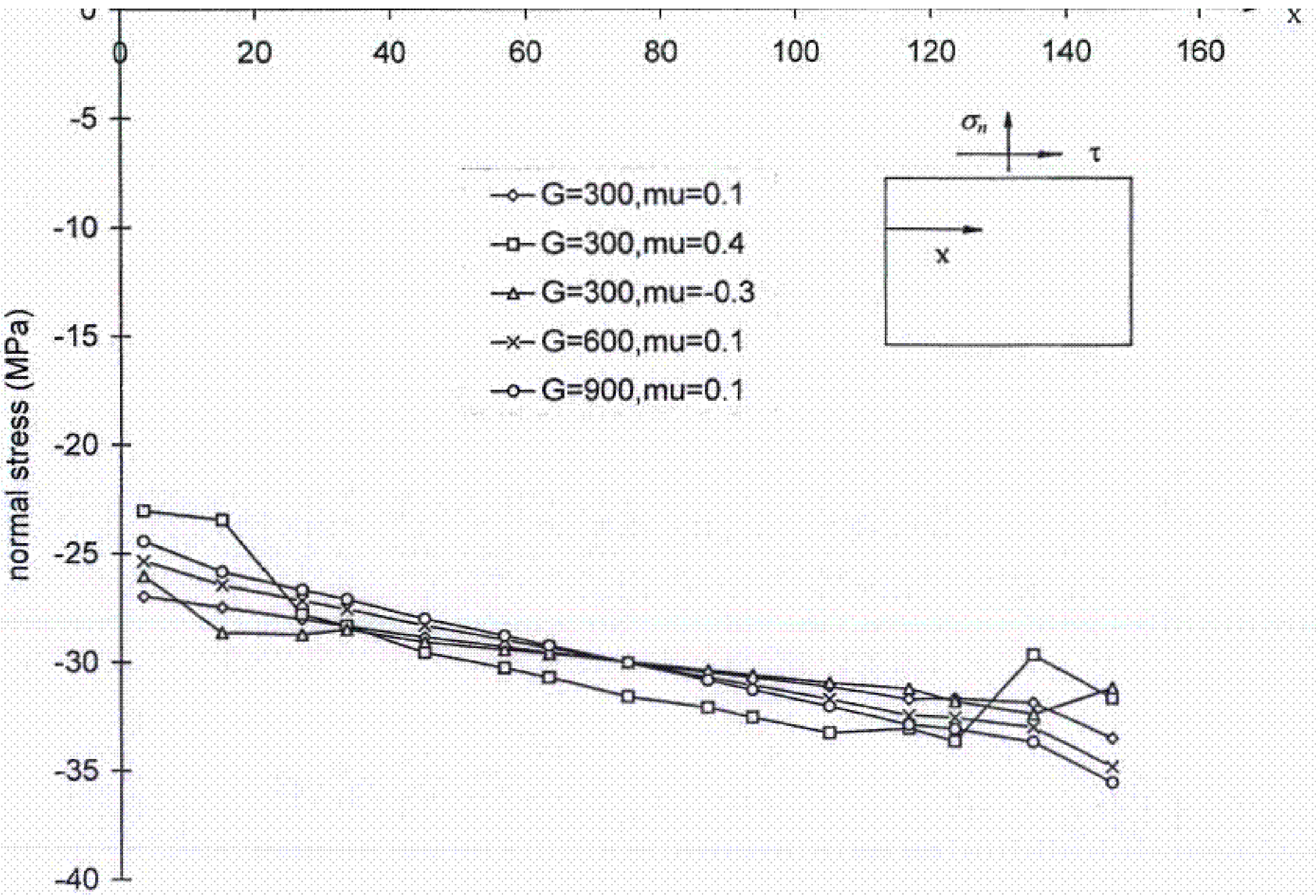

Figure 3.2 Normal stresses on the lower interface with $\beta=0.1^0$

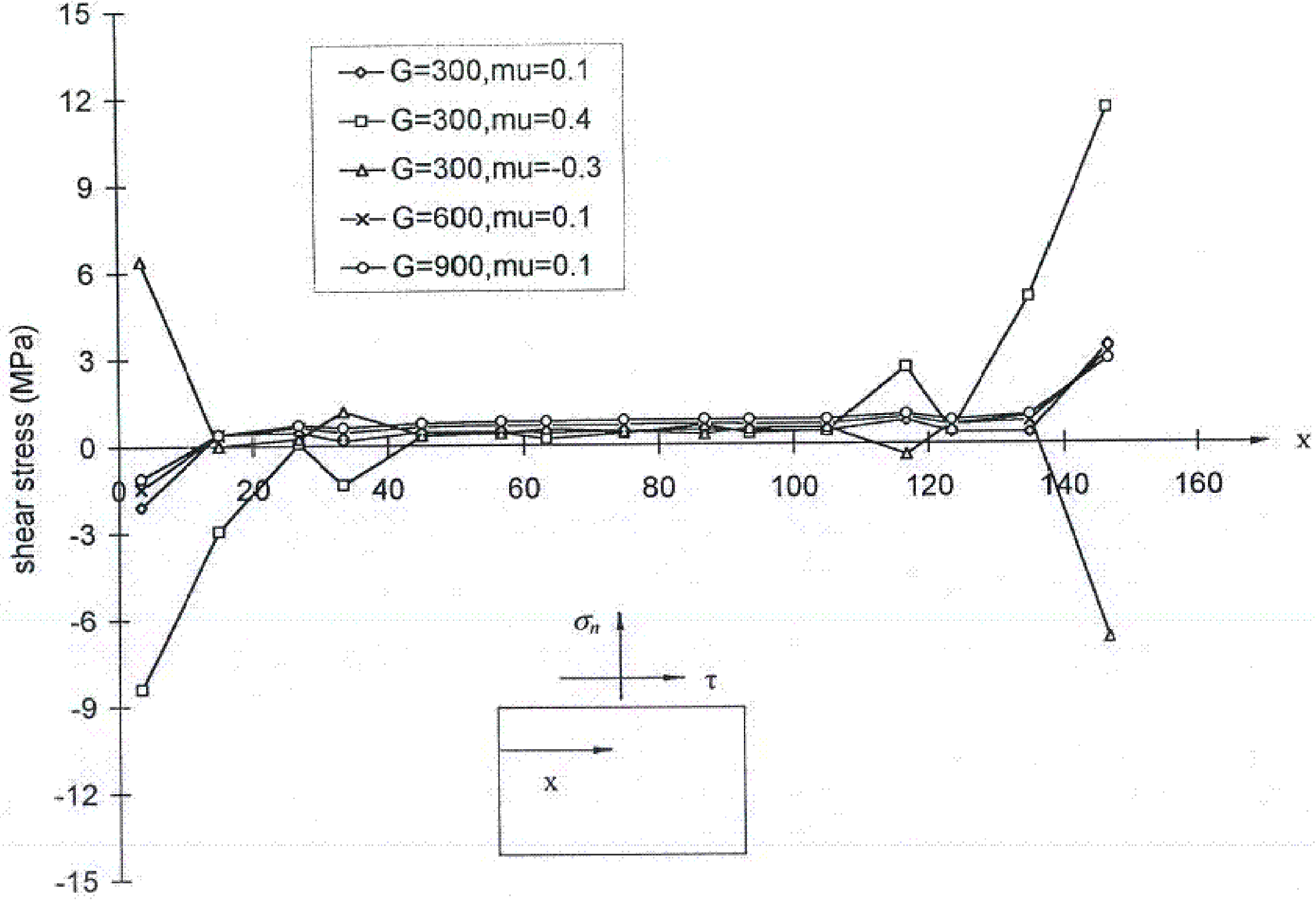

Figure 3.3 Shear stresses on the lower interface with $\beta=0.1^0$

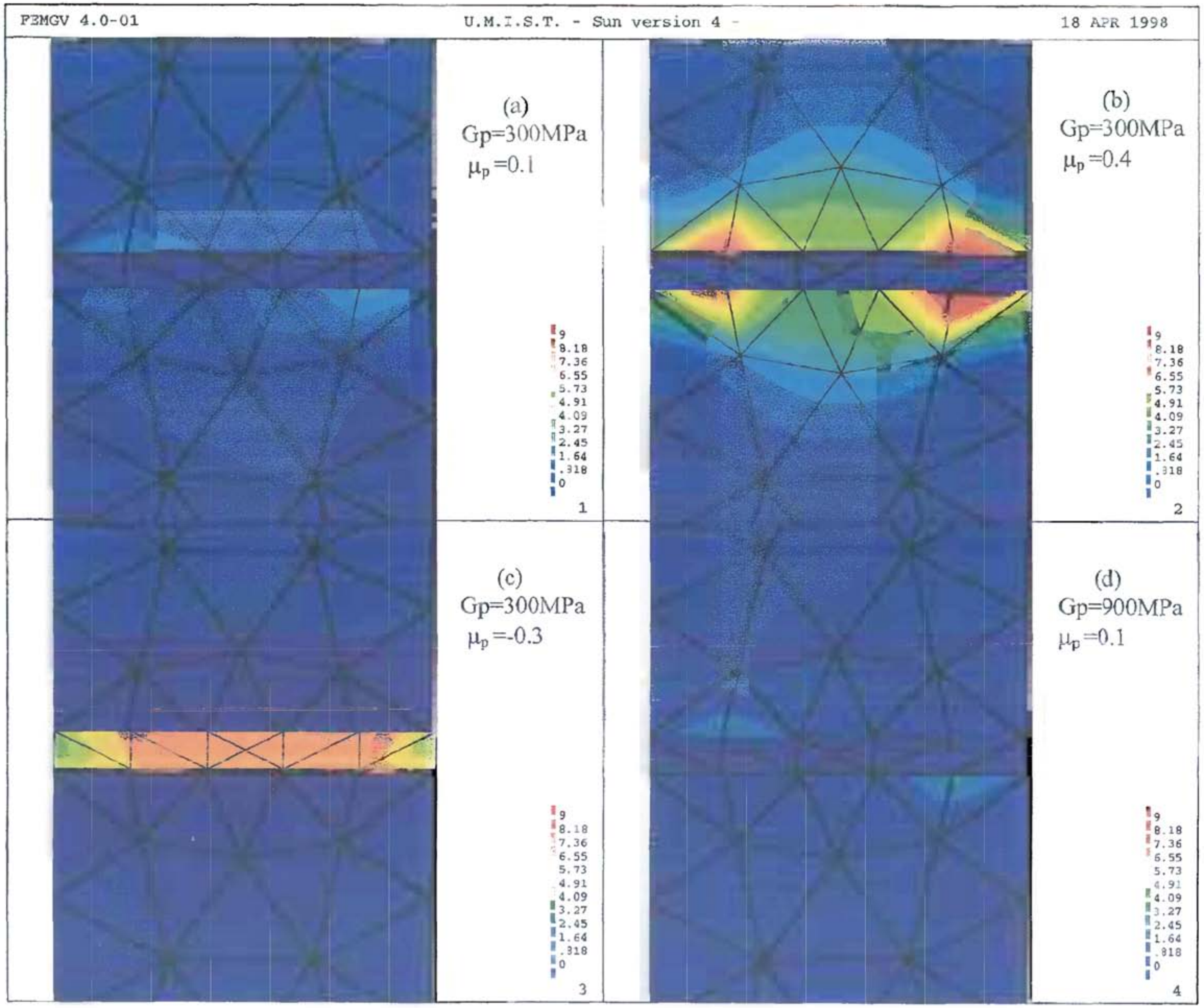

Figure 3.4 Most tensile principal stresses at the joint with $\beta=0.1^0$ (MPa)

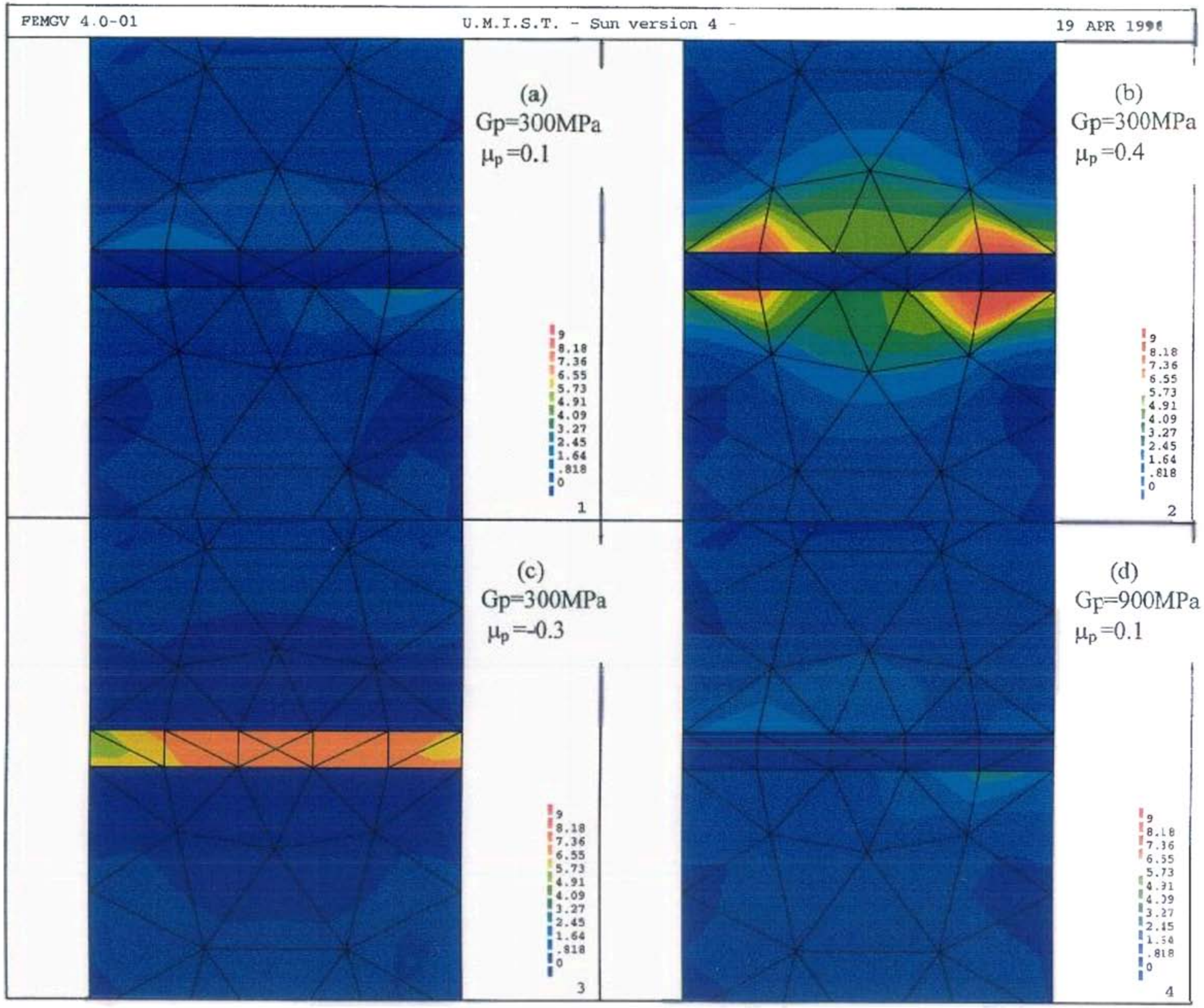

Figure 3.5 Most tensile principal stresses at the joint with $\beta=0.1^0$ and high interface stiffness (MPa)

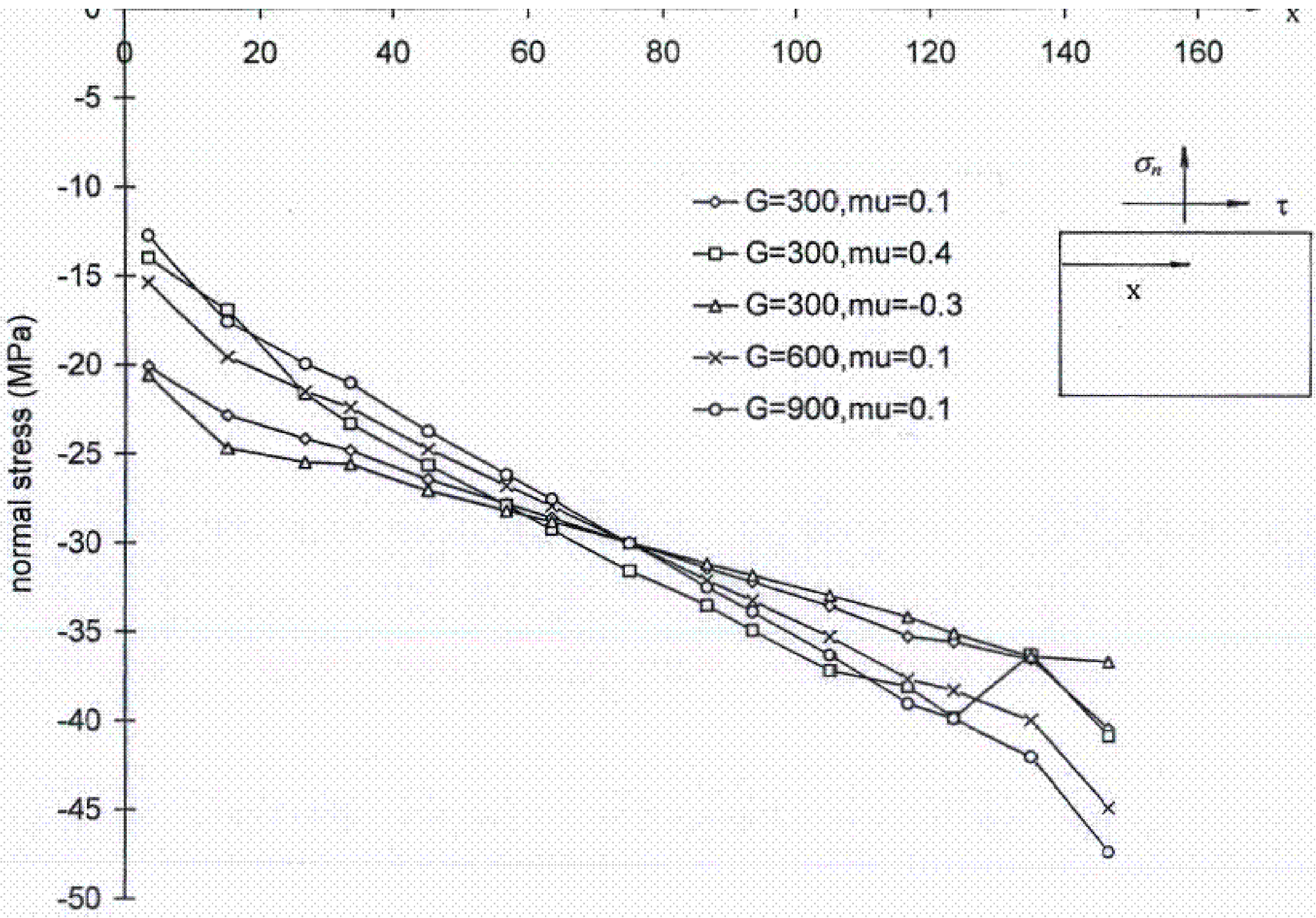

Figure 3.6 Normal stresses on the lower interface with $\beta=0.3^0$

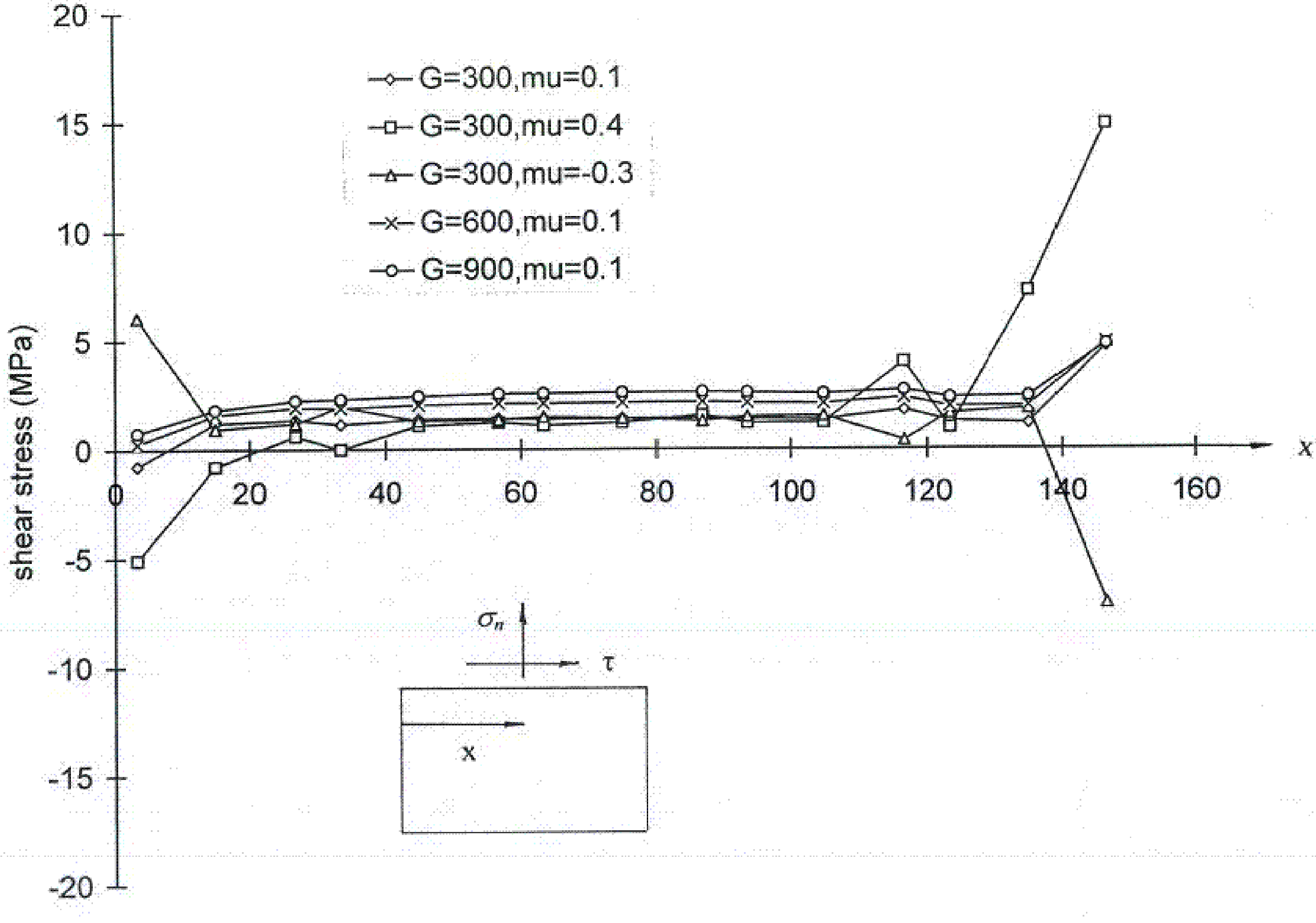

Figure 3.7 Shear stresses on the lower interface with $\beta=0.3^0$

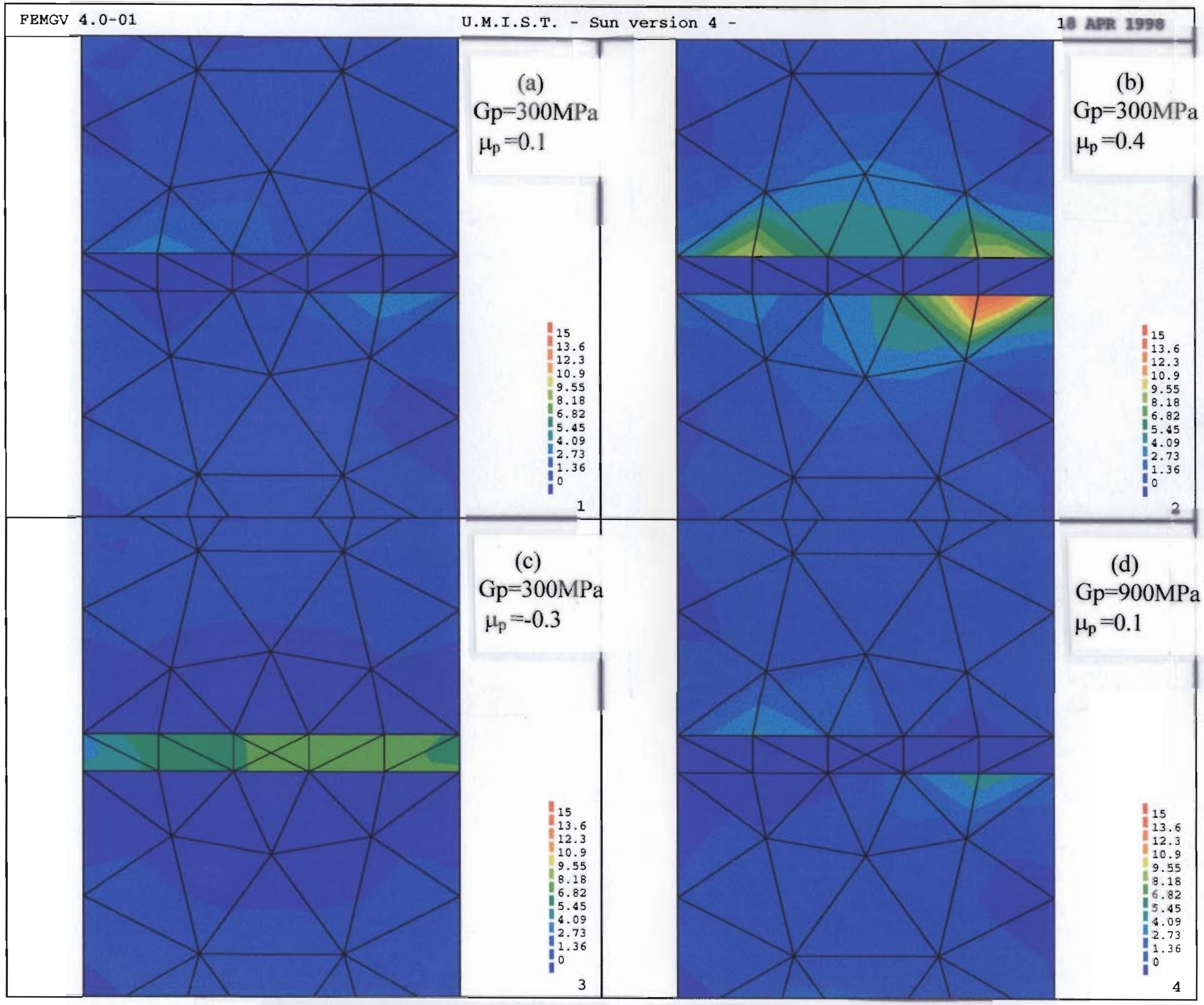

Figure 3.8 Most tensile principal stresses at the joint with $\beta=0.3^0$ (MPa)

CHAPTER 4 THREE-DIMENSIONAL ANALYSIS -- NUMERICAL MODEL A

4.1 INTRODUCTION

This chapter describes the three-dimensional analysis of a single pipe. This single pipe model is used to obtain information about the overall behaviour of the concrete pipe under different loading conditions and to carry out back analysis of Ripley's (1989) experimental data from small-scale model pipes. The more detailed models, involving a pipe with its surrounding soil and a symmetric three-pipe system, are discussed in Chapters 5 and 6 respectively. The pipe was treated as a three-dimensional structure because the applied load was non-uniformly distributed at the pipe end due to the misalignment of the pipeline in practice. Moreover, since the pipe is a regular structure in a cylindrical co-ordinate system, the advantage of this system has been taken to simplify the input data and to make the output results more readable.

In this chapter, the single pipe model is described in Section 4.2. The effect of load distribution and the effect of the pipe wall thickness are discussed in Sections 4.3 and 4.4 respectively. The conclusion from this model is given in Section 4.5. Finally, a numerical back analysis of Ripley's (1989) experimental data is discussed in Section 4.6.

4.2 NUMERICAL MODEL A

The numerical model A, a single concrete pipe, and its finite element mesh are shown in Figure 4.1 (since the geometry of the pipe and the applied loads are symmetrical about the plane of $y = 0$, just half of the pipe was used in the analysis as shown in the figure). The pipe is shown in Figure 4.1(a); a surface of r = constant unfolded on a plane is shown in Figure 4.1(b); the top end of the pipe in Figure 4.1(c) and the section $\theta = 0^0$ in Figure 4.1(d). The element type used in the analysis was 8-node hexahedron. The pipe was treated as linearly elastic and the material constants obtained by Ripley (1989), the Young's modulus E_c = 31700MPa and the Poisson's ratio μ_c = 0.2, were used in the analysis for the convenience of comparison between the numerical results and Ripley's experimental data. The dimensions of the pipe are the same as those of the test pipes used by Ripley in his experiment and are shown in Figure 4.1(d). To investigate the effect of the thickness of the pipe wall, both the thick wall (wall thickness t = 25mm) and the thin wall (t = 14.3mm) pipe were included in the analysis.

4.3 EFFECT OF LOAD DISTRIBUTION

In this section, the effect of the load distribution is examined using the thick wall pipe. The analysis was carried out with two different types of applied loads, the 'edge' loading and the 'diagonal' loading. These two types of loading are the extreme loading condition of pipes in practice due to the misalignment of the pipe line.

4.3.1 EDGE LOADING WITH THICK WALL PIPE

The first analysis is with the 'edge' loading which is transferred along one edge of the pipe. The total load applied in the analysis was P = 5kN. To study the effect of different load distributions, the analysis included three types of 'edge' loading: the bi-linearly distributed concentrated load (case E1), the uniform load on the outer half thickness of the pipe end over 22 degrees in the circumferential direction (case E2) and the uniform load across the pipe thickness over 11 degrees in the circumferential direction (case E3). All three load distributions on the upper pipe end are shown in Figure 4.2 and the load distributions on the bottom pipe end are the same as those on the upper end except in the opposite direction. All the loading conditions are simplified approximations to extreme conditions in practice. In the numerical analysis, in addition to the symmetrical condition on the plane of $y = 0$ (that is, all the nodes on that plane were fixed in the y direction), three nodes on the external surface at each end of the pipe at the loaded edge were fixed in the x direction and the node at the bottom loaded corner was fixed in the z direction as well as shown in Figure 4.3(a) and 4.3(c).

If the load (P = 5kN) is uniformly distributed over the pipe end (half of the pipe in the analysis), the average pressure over the pipe end is q = 0.73MPa. For convenience of result comparison, all the computed stresses in the thick wall pipe in this chapter are normalised by this pressure when presented in the stress contours.

The results of the normalized most tensile principal stresses in the thick pipe under the 'edge' load are shown in Figure 4.4. The result for the case E1 is in Figure 4.4(a), the case E2 in Figure 4.4(b) and the case E3 in Figure 4.4(c). From the figure, it is clear that in all three cases the stresses are concentrated in two small regions which are adjacent to the loaded areas on the two pipe ends, while the stresses in other regions are very small except that some tensile stresses exist at the middle length of the pipe in the region of $\theta = 180^0$ on the internal surface. The highest stress is in the case E1 and the maximum value of stress in the load case E3 is the smallest of the three. The stresses are symmetrical about the middle section of the pipe in the z direction (that is, the section of z = 116mm) since the loads are symmetric about this plane. The direction of the most tensile principal stress within the pipe is complex and difficult to be expressed in a three-dimensional contour. However, in the two high tensile stress regions on the internal surface, the tensile stresses are mainly in hoop direction in all three loading cases as shown in Figure 4.4(d).

The normalized most compressive principal stresses in the thick pipe under the 'edge' load are shown in Figure 4.5. The results of the case E1, E2 and E3 are shown in Figure 4.5(a), 4.5(b) and 4.5(c) respectively. The figure clearly shows that the stresses are concentrated at the two loaded corners, while the stresses in other regions are very small; and that on the pipe ends the distribution patterns of the stresses are similar to those of the loads. Again, the highest magnitude of the stress is in the case E1, and the peak magnitudes of stress in case E2 and E3 are similar.

4.3.2 DIAGONAL LOADING WITH THICK WALL PIPE

The 'diagonal' loading is another type of extreme loading condition in practice. Under the 'diagonal' loading condition, the load is transferred diagonally between the opposite corners of the concrete pipe. Again three types of 'diagonal' loading were included in the analysis: the bi-linearly distributed concentrated load (case D1), the uniform load on the outer half thickness of the pipe end over 22 degrees in the circumferential direction (case D2) and the uniform load across the pipe thickness over 11 degrees in the circumferential direction (case D3). The total applied load was also P = 5kN as under the 'edge' loading condition. On the upper end of the pipe, the load distribution for each load was the same as that of the corresponding 'edge' load as shown in Figure 4.2. However, on the bottom end of the pipe, the load distribution of each load was obtained by rotating the corresponding 'edge' load through 180 degrees in the θ direction (that is, the load was in the region of $\theta = 0^0$ at the bottom end of the pipe). For the boundary condition, three nodes between $\theta = 169^0$ and $\theta = 180^0$ on the external surface at the upper end of the pipe were fixed in the x direction, as were the three nodes between $\theta = 0^0$ and $\theta = 11^0$ on the external surface at the bottom end of the pipe as shown in Figure 4.3(b) and 4.3(d). The symmetrical condition on the plane $y = 0$ was also applied.

From Figure 4.3(b), it is clear that under 'diagonal' loading condition, the constraints have to produce reaction forces to prevent rotation of the pipe, and these reaction forces are dependent on the type and the location of the constraints. This means that the computed stresses may be affected by the local effect of the constraints. The boundary conditions used in this chapter may represent a boundary condition in which the pipe is surrounded by hard rocks or a constraint condition used in laboratory tests, which might deviate from the boundary condition in practice. However, this effect of local constraints will be overcome by including the surrounding soil in the analysis in Chapter 5.

The normalized most tensile principal stresses in the thick wall pipe under the 'diagonal' loading are shown in Figure 4.6, with the result of the load case D1, D2 and D3 in Figure 4.6(a), 4.6(b) and 4.6(c) respectively. From the figure, it is clear that the in all cases high stresses appear in the two regions near the two loaded diagonal corners on the internal surface of the pipe, and that the stresses are almost zero in the region of $\theta = 90^0$ and are small at the other two diagonal corners. The peak values of the stress are higher than those under 'edge' loading condition, but the differences between the three cases are less than for the 'edge' loading. The highest tensile stress is in the case D1. Again, the distribution of the directions of the principal stresses are complex. However, on the internal surface of the pipe the directions of the principal stresses in the small regions with high tensile stresses are somewhat similar in all three cases and are approximately shown in Figure 4.6(d). In general, the principal tensile stresses in the region of $\theta = 180^0$ and 0^0 are mainly in the hoop direction, and when away towards to the central region of $\theta = 90^0$ the direction of the principal tensile stress changes from the hoop direction towards to the direction normal to the line connecting the two loaded corners.

To view the stresses on the external surface of the pipe, the pipe has been rotated through 180 degrees in the θ direction and the same most tensile principal stresses are now shown in Figure 4.7. Clearly, the stress distributions on the external surface are different from those on the internal surface of the pipe. On the external surface of the pipe, the high stresses are located in the region of $\theta = 90^0$, however, the peak values are much lower than those on the internal surface. The stresses in other regions are very small (the high stress points near the loaded diagonal corner are possibly caused by the effect of local constraint as discussed above in this section and is examined in Chapter 5). The directions of the principal stresses in the region $\theta = 90^0$ are similar in all three cases and shown in Figure 4.7(d). The figure shows that the tensile direction changes from the hoop direction at two pipe ends to the direction normal to the line connecting the two loaded corners at the central area on the surface.

The normalized most compressive principal stresses in the thick wall pipe under 'diagonal' loading D1, D2 and D3 are shown in Figure 4.8(a), 4.8(b) and 4.8(c) respectively. Again the figure clearly shows that the stresses are highly concentrated in the two diagonal loaded corners. The low stresses are located in the band connecting the two loaded corners. And the stress patterns and the peak magnitudes of the stress are similar in all three cases.

4.4 EFFECT OF THE THICKNESS OF THE PIPE WALL

The analysis of the effect of the pipe wall thickness was carried out using the thin wall pipe under similar loading conditions as described in Section 4.3. The results are compared with those in the thick wall pipe in Section 4.3.

4.4.1 EDGE LOADING WITH THIN WALL PIPE

The finite element mesh and the boundary conditions were the same as those described in the last section as shown in Figure 4.1 and 4.3, except that the thickness of the pipe wall was 14.3mm instead of 25.0mm. The total applied load was also P = 5kN. The three 'edge' loads (EN1, EN2 and EN3) have the same distribution patterns on the pipe ends as those in case E1, E2 and E3 in Section 4.3 as shown in Figure 4.2 except that the load intensity is higher than in Section 4.3 due to the reduced pipe wall thickness. Now the average pressure is q = 1.20MPa when the applied load is uniformly distributed over the end of the thin wall pipe. The computed stresses in the thin wall pipe have been normalised with respect to this pressure in all the stress contours in this chapter.

The normalized most tensile principal stresses in the thin wall pipe under 'edge' loading are shown in Figure 4.9(a), 4.9(b) and 4.9(c) for the loading case EN1, EN2 and EN3 respectively. As expected, the figure shows that the stress distribution patterns are similar to those in the thick wall pipe for all three loading cases except that the peak values of the normalised stress are slightly higher. Again the highest stress is in the case EN1. The most tensile principal stresses in the high stress regions are mainly in the hoop direction in all three cases as in the thick wall pipe (refer to section 4.3.1 and see Figure 4.4(d)). As for the normalized most compressive principal stresses in the thin wall pipe, the stress patterns and the peak magnitudes of the normalized stress in all three cases are similar to those in the thick wall pipe and are not discussed in detail here (refer to the Section 4.3.1 and see Figure 4.5).

4.4.2 DIAGONAL LOADING WITH THIN WALL PIPE

Similarly, under the 'diagonal' loading condition, the finite element mesh, the boundary conditions and the total applied load were the same as those in the analysis with the thick wall pipe. The only parameter changed was the thickness of the pipe wall. The three 'diagonal' loads called DN1, DN2 and DN3 have the same distributions on the two pipe ends as those of D1, D2 and D3 in section 4.3.2 as shown in Figure 4.2 except with higher load intensity due to the reduction of the wall thickness of the pipe as discussed under the 'edge' loading condition.

The results of the normalized most tensile principal stresses in the thin wall pipe under the three 'diagonal' loads are shown in Figure 4.10(a), 4.10(b) and 4.10(c) respectively. The figure shows that in all three cases the stress distribution patterns are similar to those in the thick wall pipe, however the peak values of the normalised stress are higher than those in the thick wall pipe. The regions of the high stresses now extend further towards the non-loaded corners of the concrete pipe along the *z* direction. The distribution patterns of the principal direction in the high stress regions on the internal pipe surface are similar in all three cases as shown in Figure 4.10(d). On the external surface of the pipe, the high stresses are located in the region of $\theta = 90^0$ as in the thick wall pipe except that the stresses are higher than those in the thick pipe, and the distribution of the principal directions is also similar to that in the thick wall pipe (refer to Section 4.3.2 and see Figure 4.7).

As for the normalized most compressive principal stresses in the thin wall pipe under edge loading, the distribution patterns in all three cases are very similar to those in the thick wall pipe, and the peak magnitudes are slightly higher than those in the thick wall pipe (refer to Section 4.3.2 and see Figure 4.8).

4.5 CONCLUSION

So far, analyses of six types of loads (three 'edge' loads and three 'diagonal' loads) and two pipe sizes (the thick wall and the thin wall pipe) have been described in this chapter. The localization of the applied load induces not only high concentrated compressive stresses but also high tensile stresses in the concrete pipe. The stresses in all load cases are neither uniformly distributed across the thickness of the pipe nor linearly distributed in the circumferential direction, but are more complex three-dimensional patterns. High stresses appear in two regions at the pipe joints near the two loaded corners. In general, the more localised the applied load, the higher the maximum tensile stress. Moreover, under a similar load intensity, the load distribution in the cases E2 and D2 produces higher tensile stresses at the pipe joints than in the case E3 and D3.

From the numerical results of the numerical model A in this chapter, some conclusions are drawn as following:

(1) The greatest potential damage is at the pipe joint, that is, cracking due to the high tensile stresses or crushing due to the very high compressive stresses. Due to the very low tensile strength in the concrete pipe, another possible type of damage is cracking at the middle length of the pipe on the internal surface under the 'edge' loading condition and in the region of $\theta = 90^0$ on the external surface under the 'diagonal' loading condition. For the cases studied, the joint behaviour is most severe. However, the loading conditions in this chapter are extremely severe ones due to high pipeline misalignment and uneven pipe end; presumably, loading on a larger end area would result in reduction in stresses at the pipe joint.

(2) Stresses in the thin wall pipe exceed those in the thick wall pipe by more than the thickness ratio. This means that the pipe capacity is not proportional to the pipe thickness. Presumably this is a result of local bending effects in the pipe wall (under the same bending moment in the pipe wall, the maximum stress in the pipe is proportional to $\frac{1}{(pipe\ thickness)^2}$).

(3) Diagonal loading is more severe. However, this may be because of the effect of local constraints which might deviate from the boundary conditions in practice as discussed in Section 4.3.2.

(4) Local joint stresses are greatly influenced by the distribution of the joint loads and the stresses change dramatically across the pipe thickness at the joint. This suggests that careful joint design is needed.

(5) To obtain better understanding about the pipe behaviour, a few more aspects should be examined, for example the interaction between the pipe and its surrounding soil and the interaction between the adjacent pipes.

4.6 BACK ANALYSIS OF RIPLEY'S EXPERIMENT

To model the effect of the misalignment of the pipe line in practice, Ripley(1989) carried out some laboratory tests. Two sizes of pipe, the thick wall and the thin wall pipe, were used in his tests and the dimensions of the test pipes are the same as those shown in Figure 4.1. A misalignment apparatus shown in Figure 4.11 was designed by Ripley in his tests to model the extreme loading condition with a limited area of contact. The yokes in the apparatus could be arranged to provide support to the pipe and could be adjusted at different angles to simulate different misalignment conditions, that is, the 'edge' and the 'diagonal' loading condition as shown in Figure 4.12(a) and 4.12(b). During the tests, the strains at the middle length section (z = 116mm) of the concrete pipe were measured with strain gauges; the load distributions on the pipe ends were not measured.

The purpose of the back analysis is to compare the numerical results with the measured strains and to check the effectiveness of numerical model A. The pipe is assumed to be linearly elastic with the Young's modulus E_c = 31700MPa and the Poisson's ratio $\mu_c = 0.2$ as found by Ripley in his laboratory tests. In the numerical back analysis, the finite element mesh is the same as that used in Section 4.3 shown in Figure 4.1 since the loads are again symmetrical about the plane of $y = 0$. Due to the deformation of the yokes, the loading areas are not extremely small, but could be up to one third of the cross section of the pipe as found by Ripley (1989) and the contact areas between the pipe and yokes are also fairly large. Since there is no measured information about the load distribution on the pipe ends, a linear distribution of the applied load is assumed over one third of the cross section of the pipe as shown in Figure 4.13(a) and 4.13(b) for the 'edge' and the 'diagonal' test. The total applied load in the analysis is P = 5kN (on half of the pipe) to simulate an early stage in the test since an elastic pipe model is used in the analysis. There is also no measured information on the contact area between the concrete pipe and the yokes, and the contact area is assumed over about 70 degrees along circumferential direction (35 degrees for half of the pipe in the analysis) and the nodes within this area are fixed in the x direction to model the support of the yokes as shown in Figure 4.13(c) and 4.14(d). The boundary conditions also include the symmetrical condition on the plane $y = 0$.

The strains measured during the test were all on the external and the internal surface of the pipe in a two-dimensional state, this is, ε_{θ}, ε_z and $\gamma_{\theta z}$. In the numerical analysis, the strains are calculated at Gauss points, that is, the numerical strains on a surface of r = constant very near the external or the internal surface are used in the comparison. The numerical strains chosen for comparison are in the same two-dimensional state as the measured ones. For the convenience of comparison, several tests from Ripley's experimental data (1989) are chosen to represent different situations. Under 'diagonal' loading, test 8 is chosen for thick wall pipe and test 16 for thin wall pipe; and under 'edge' loading, test 19 is chosen for thick wall pipe and test 23 for thin wall pipe. The tests chosen in comparison are typical from the point of view of average measured strains.

The most tensile (1st) principal microstrain and the most compressive (2nd) principal microstrain under the 'diagonal' loading condition in the thick wall pipe and in the thin wall pipe are shown in Figure 4.14(a) and 4.14(b) respectively. In the figure, the squares and the crosses denote the most tensile principal microstrains on the external surface of the pipe from numerical analysis and from experiment, and the triangles and the circles denote the most compressive principal microstrains on the external surface of the pipe from numerical analysis and from experiment respectively. From the figure, it is very clear that the numerical results and the experimental data agree well.

The most compressive principal microstrains under the 'edge' loading condition in the thick wall pipe and in the thin wall pipe are shown in Figure 4.15(a) and 4.15(b) respectively.

In the figure, the squares and the crosses denote the principal microstrains on the external surface of the pipe from numerical analysis and from experiment, and the triangles and the circles denote the principal microstrains on the internal surface of the pipe from numerical analysis and from experiment respectively. Again, the numerical results and the experimental data agree well except for the strain at point G ($r = 100$mm and $\theta = 180^0$). In theory, the compressive strain at the point G on the external surface should be higher than that at the point H on the internal surface under the 'edge' loading condition as indicated by the numerical results. The experimental data show that the compressive strain at point G is just over half of that at point H. This experimental result is very difficult to explain in theory and further investigation may be needed.

The results above suggest that numerical mode A is reliable to model the tests in the early stage in which the pipe is behaving in a linearly elastic manner. To obtain more detailed information about the behaviour of the concrete pipe at late test stage with cracks, a complex concrete material model is needed in future.

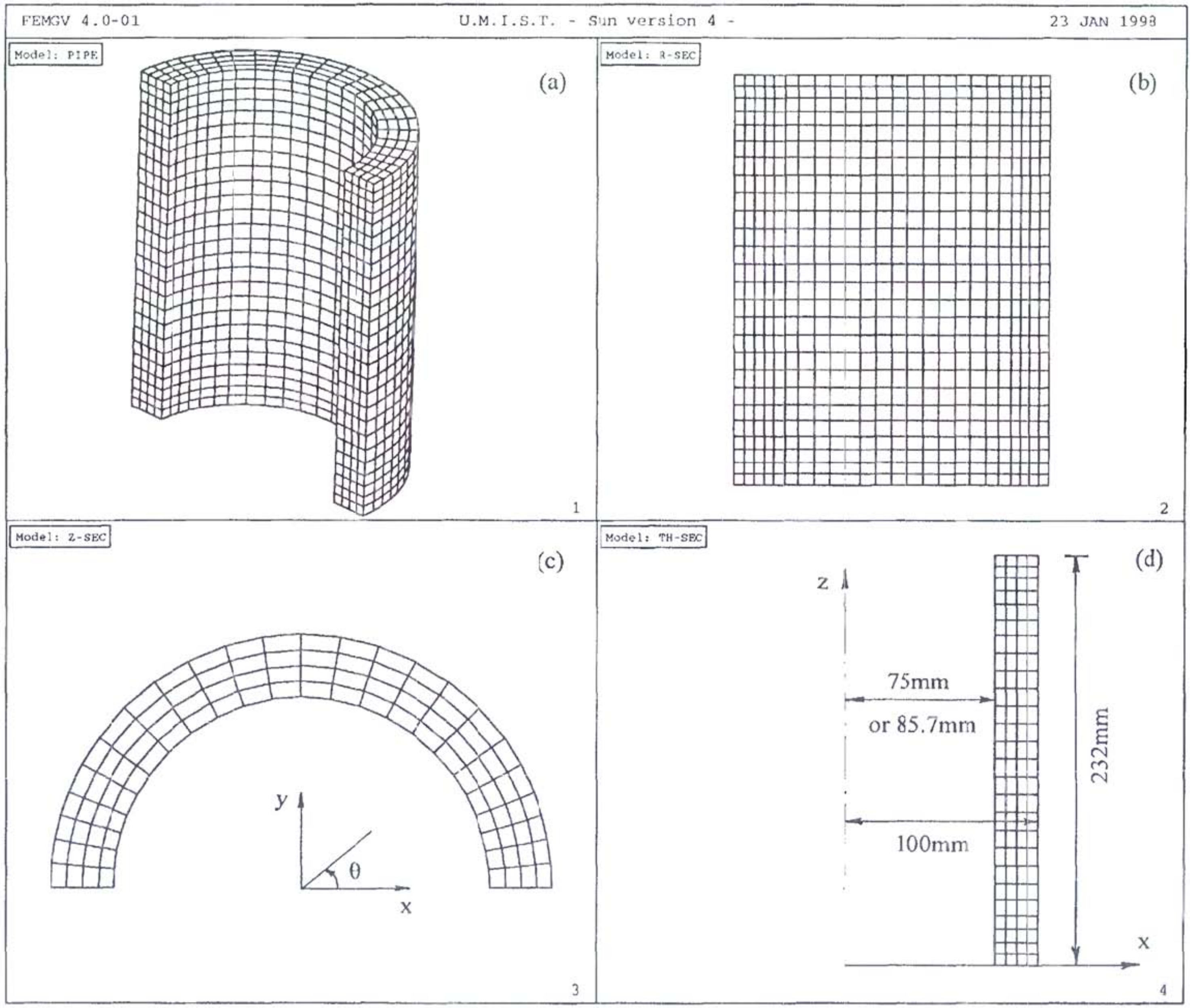

Figure 4.1 Numerical model A and its FE mesh

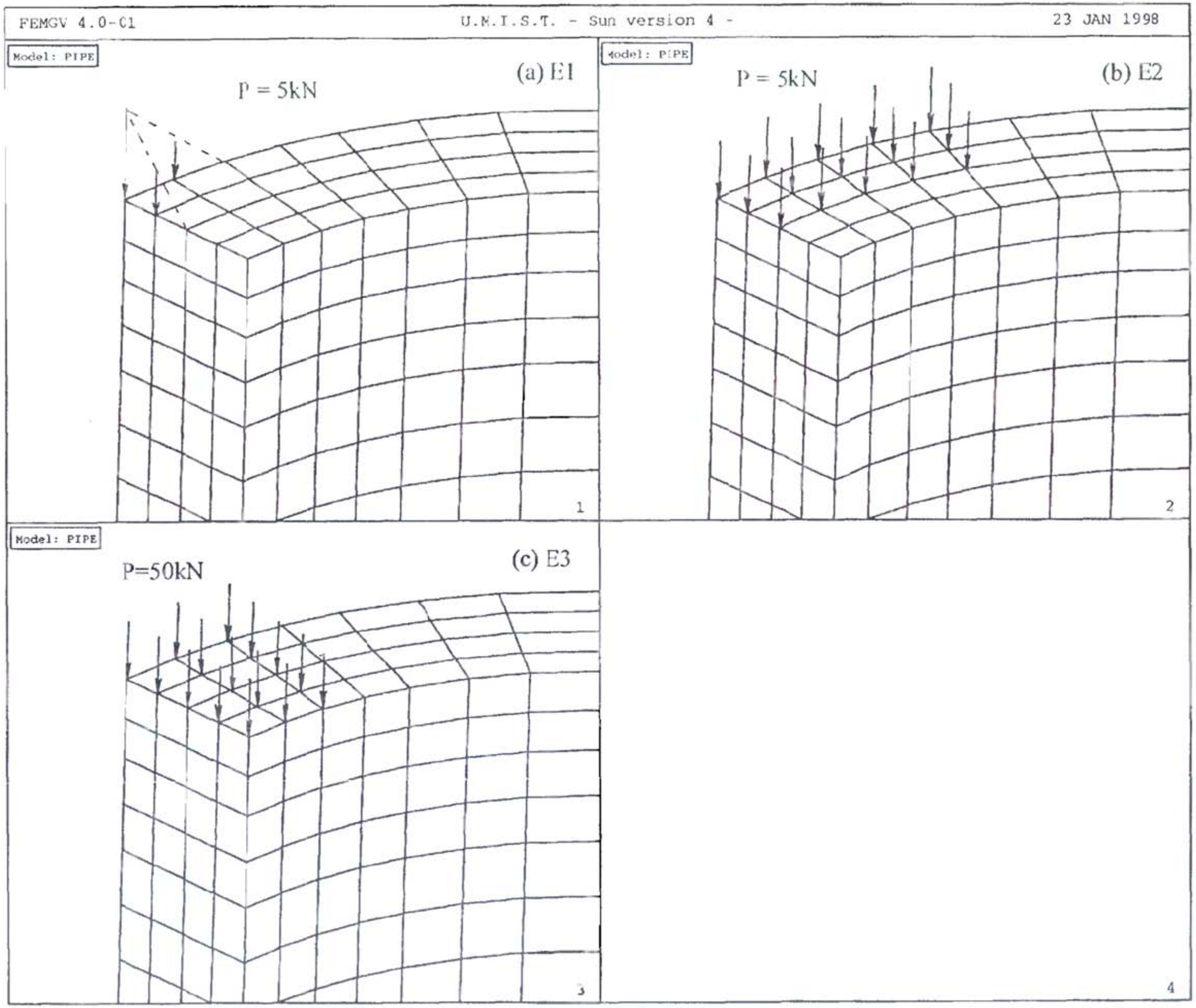

Figure 4.2 Three load distributions on the upper pipe end

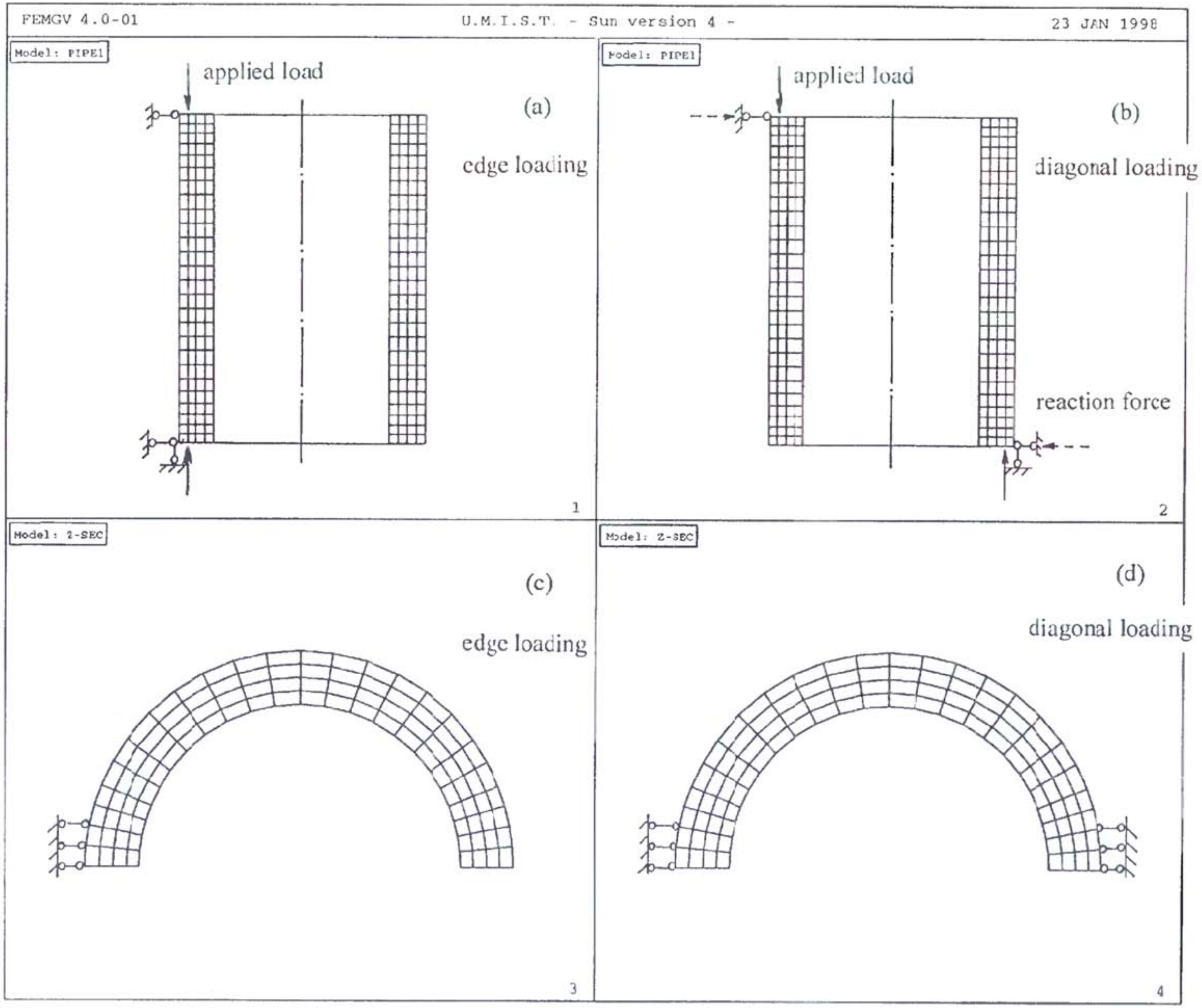

Figure 4.3 Boundary condition under 'edge' and 'diagonal' loading

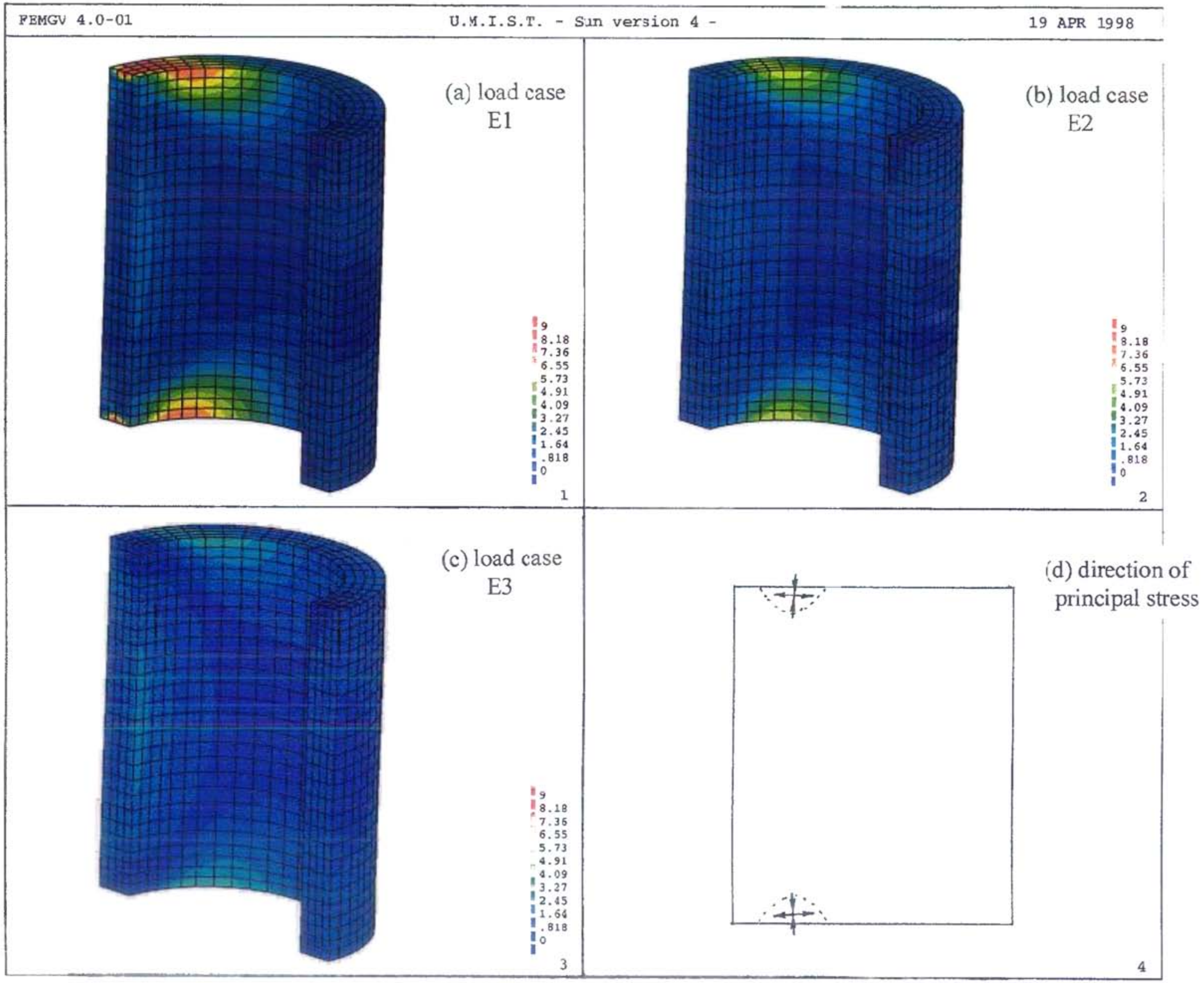

Figure 4.4 Normalized most tensile principal stresses in the thick wall pipe under 'edge' loading

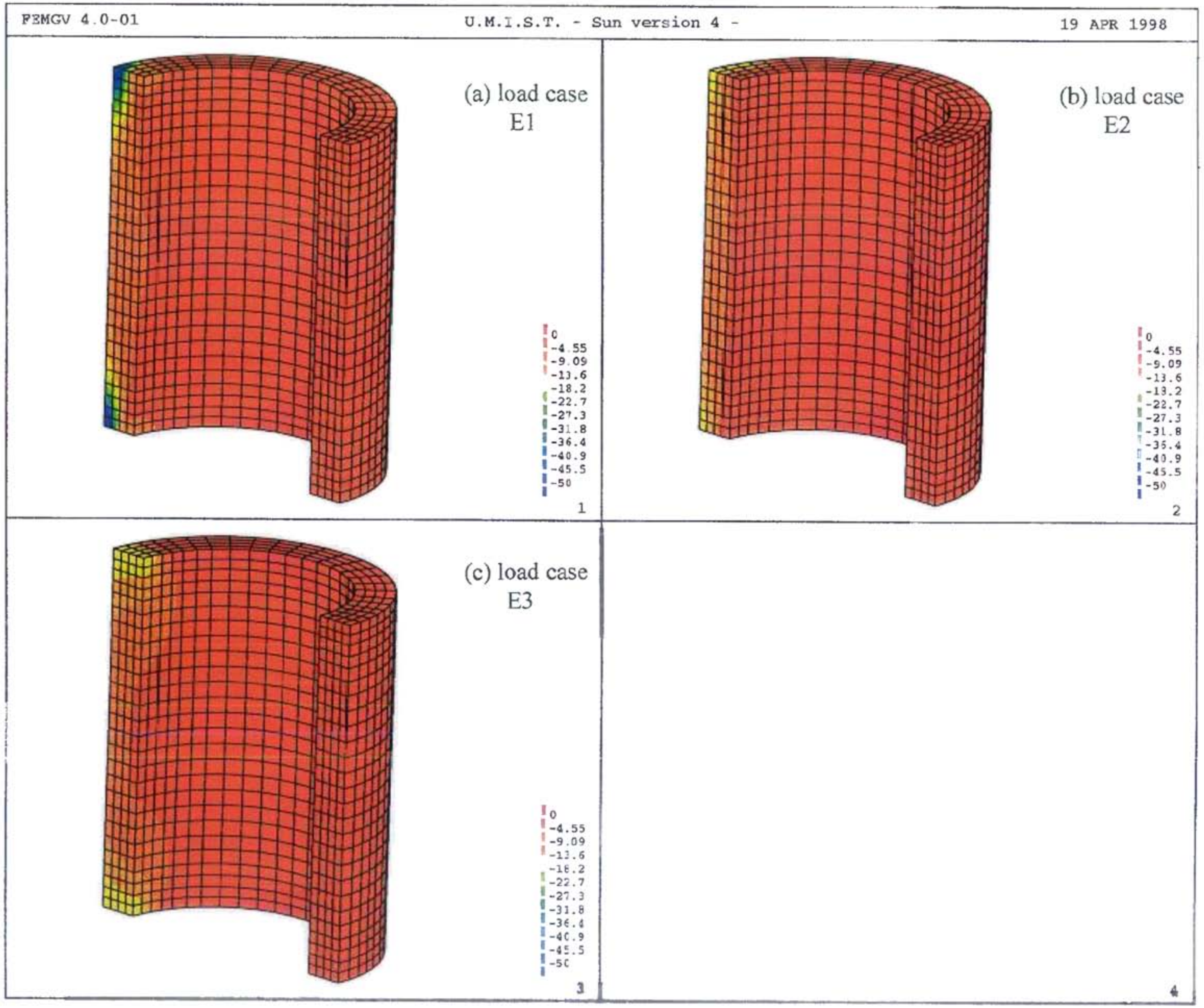

Figure 4.5 Normalized most compressive principal stresses in the thick wall pipe under 'edge' loading

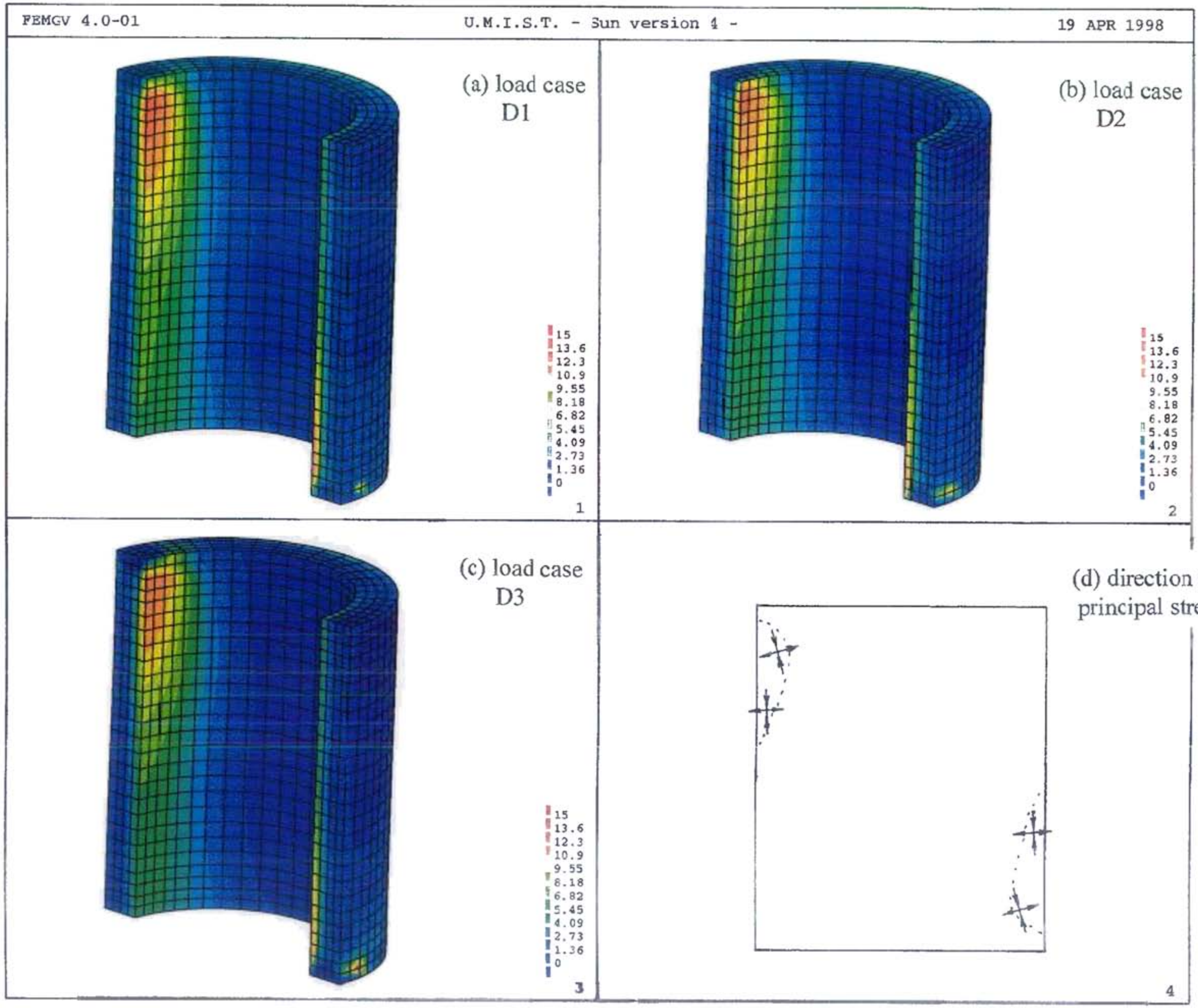

Figure 4.6 Normalized most tensile principal stresses in the thick wall pipe under 'diagonal' loading

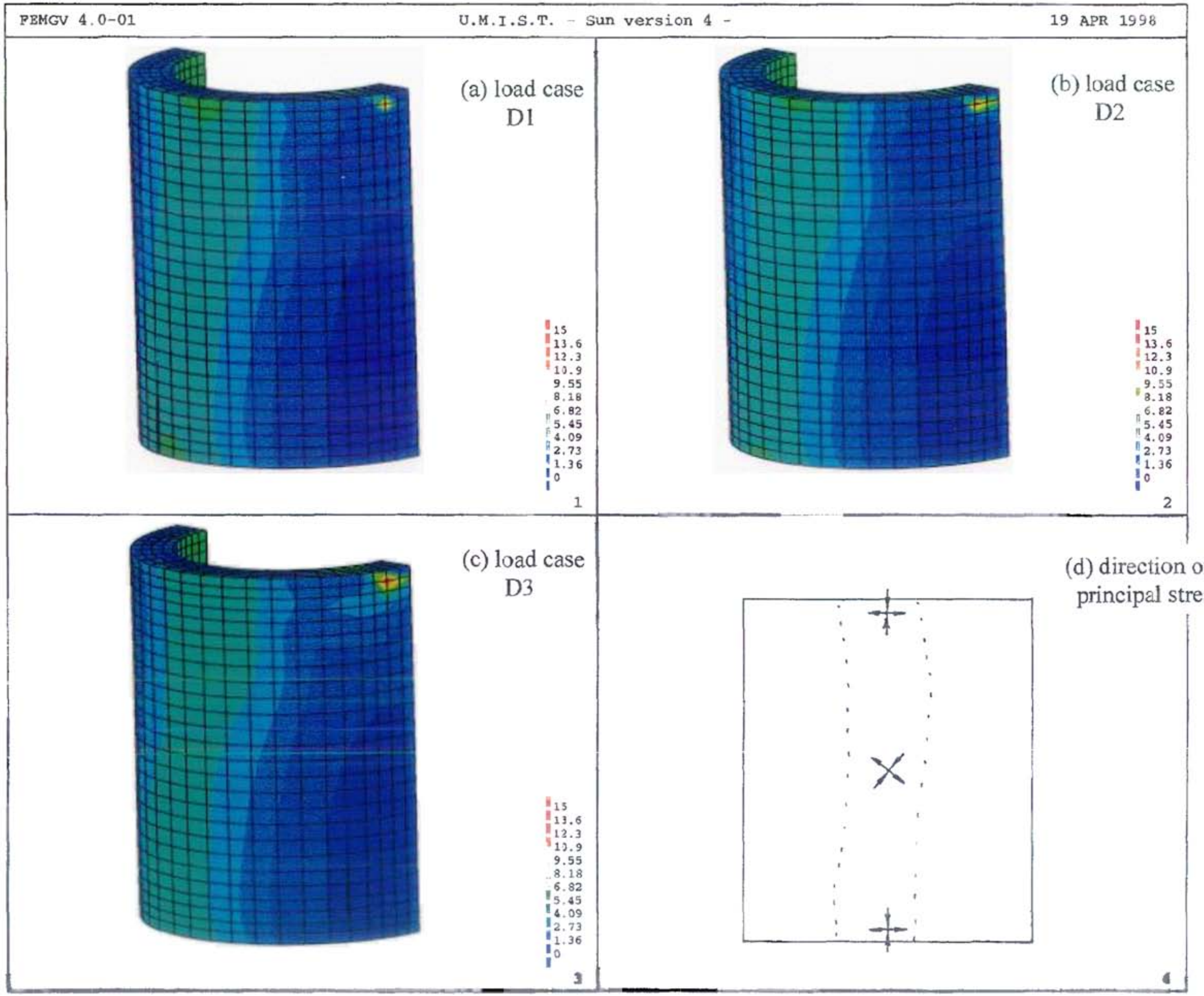

Figure 4.7 Normalized most tensile principal stresses in the thick wall pipe viewed from opposite direction under 'diagonal' loading

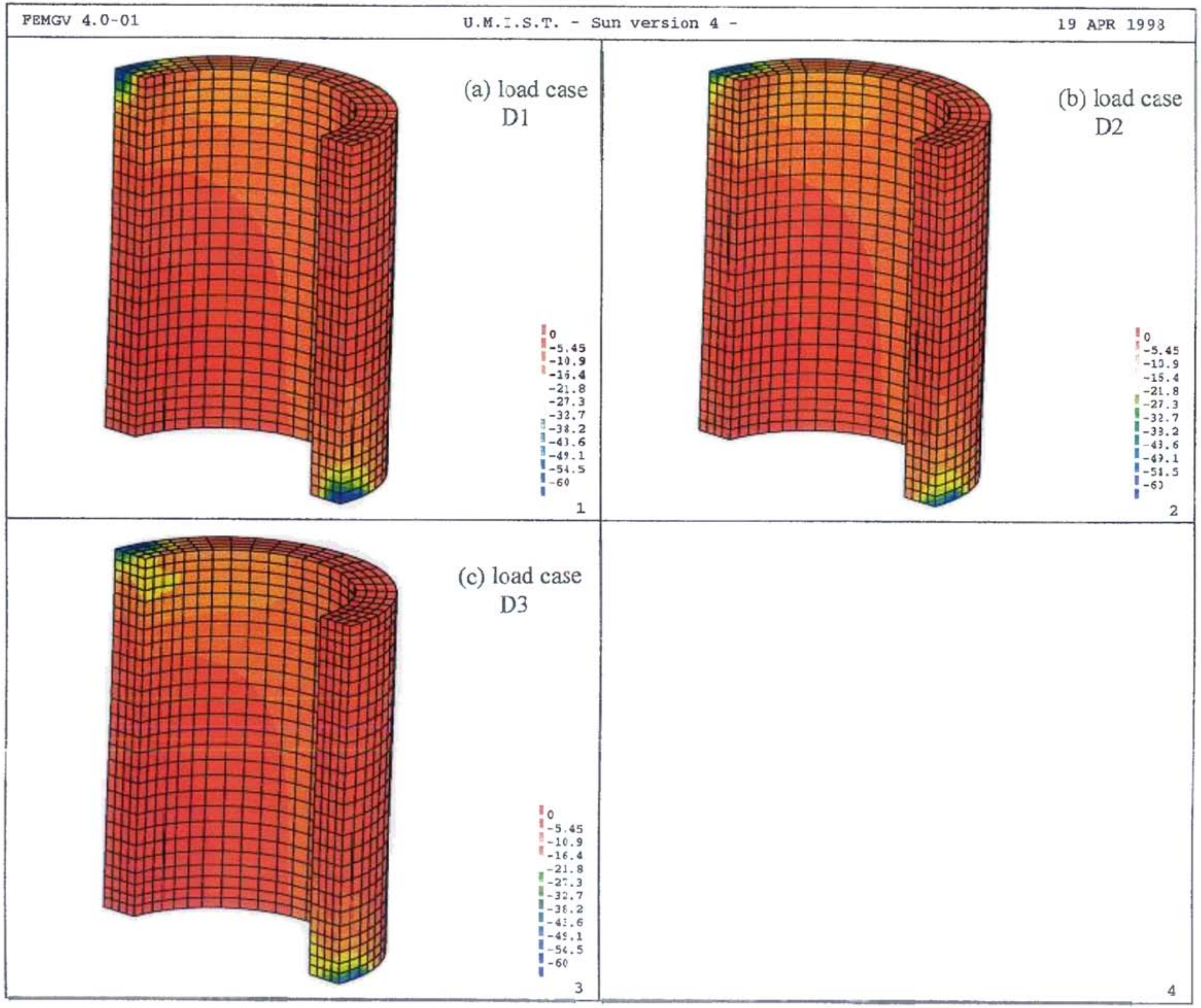

Figure 4.8 Normalized most compressive principal stresses in the thick wall pipe under 'diagonal' loading

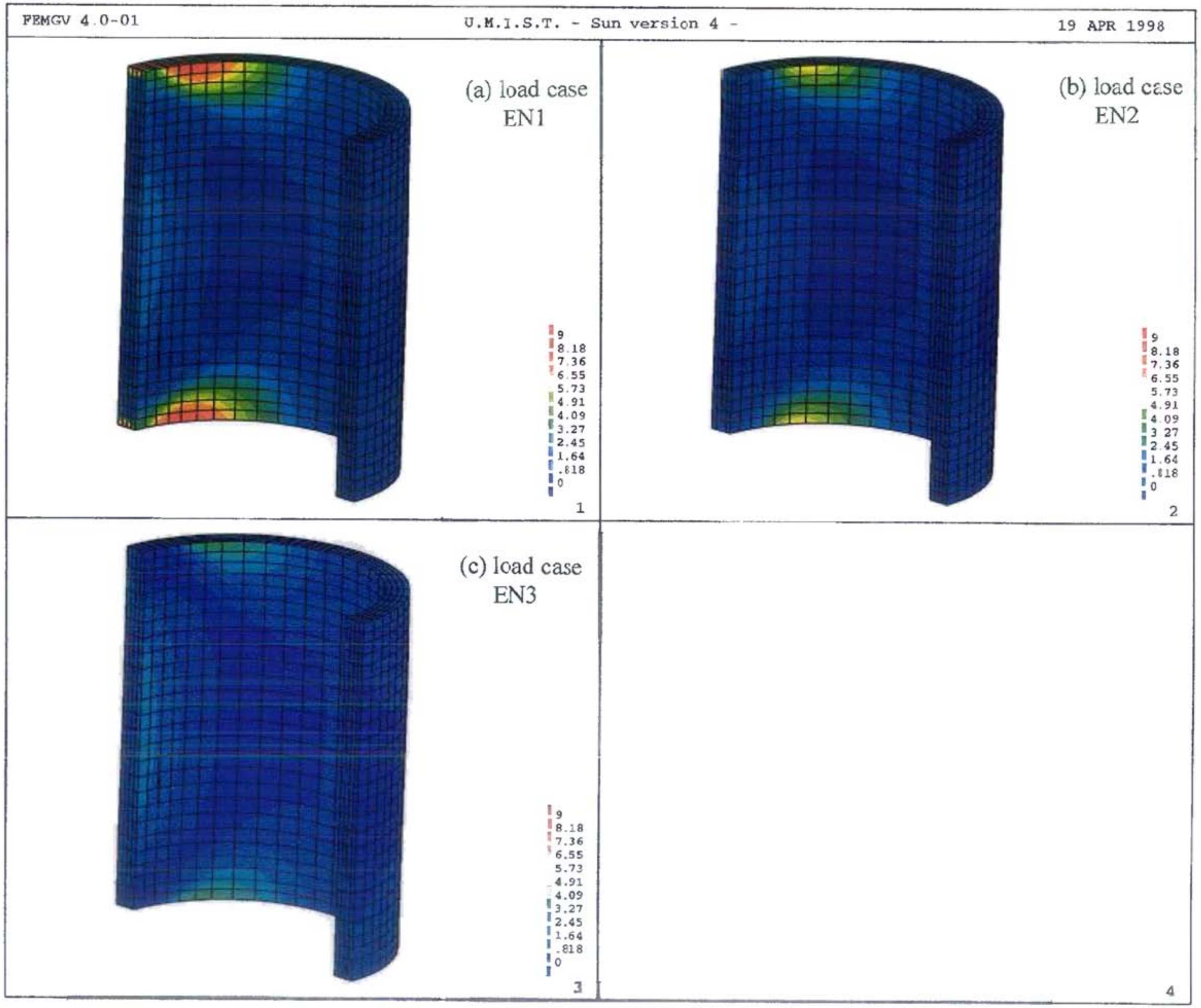

Figure 4.9 Normalized most tensile principal stresses in the thin wall pipe under 'edge' loading

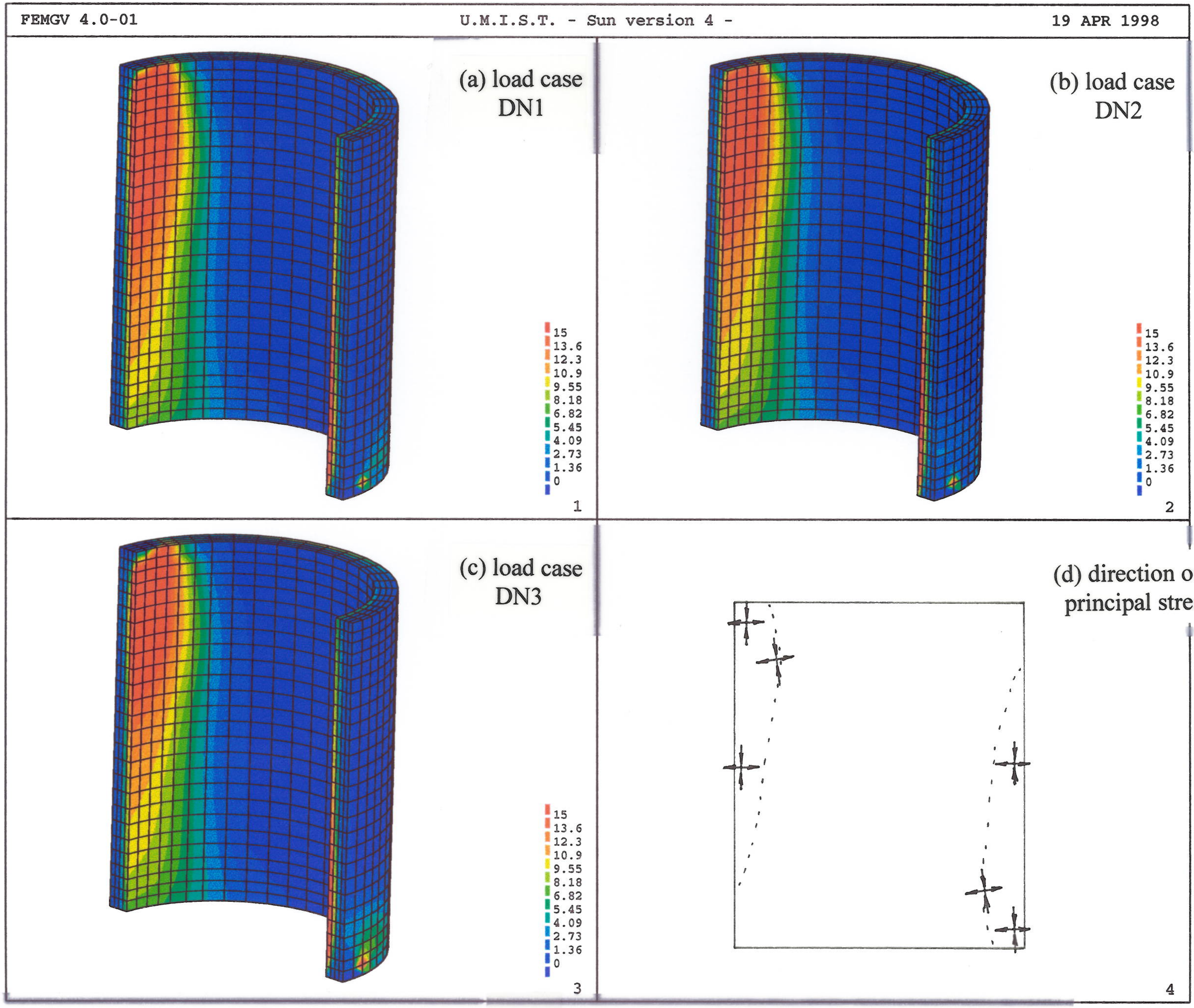

Figure 4.10 Normalized most tensile principal stresses in the thin wall pipe under ‘diagonal’ loading

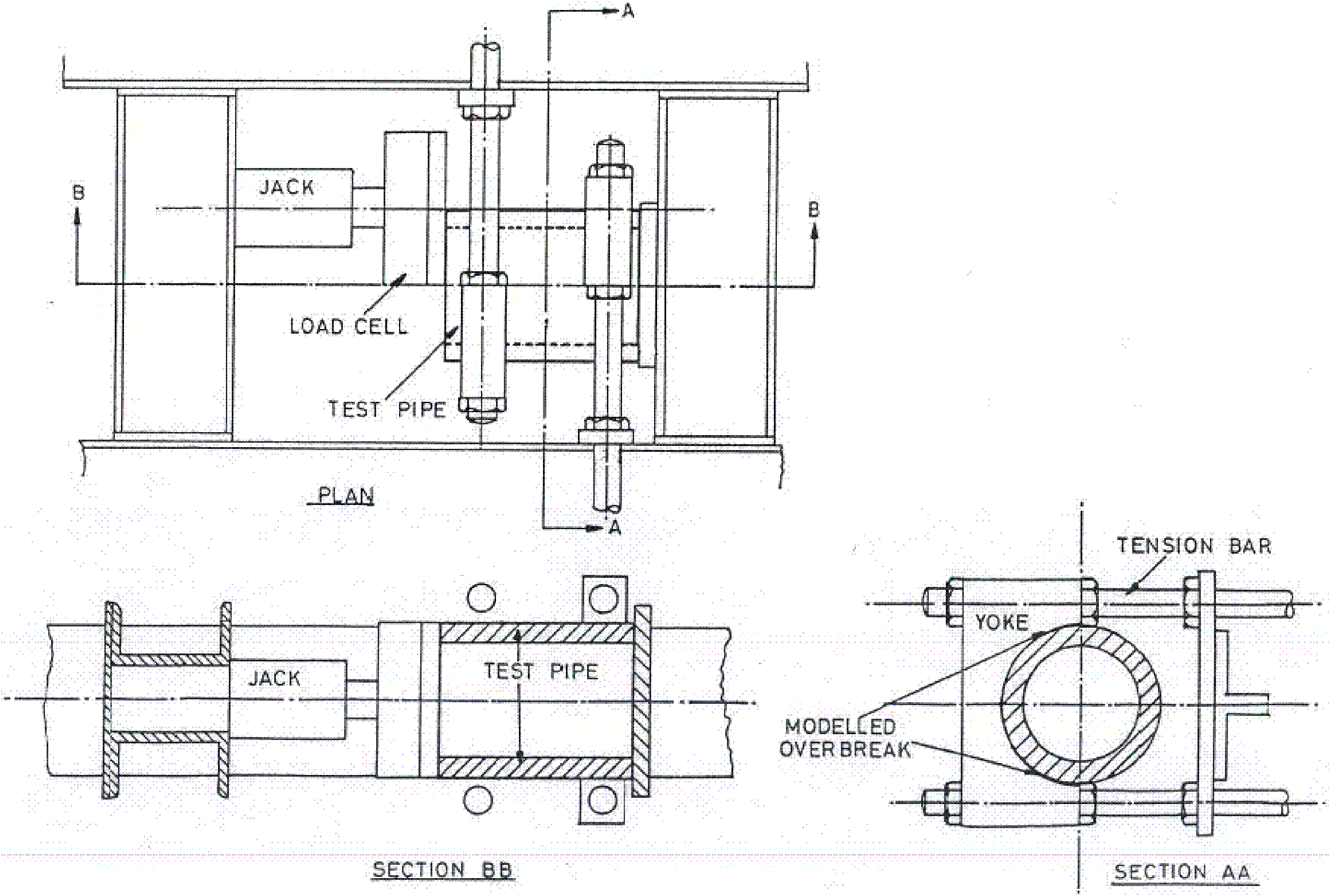

Figure 4.11 Misalignment apparatus general arrangement (from Ripley 1989)

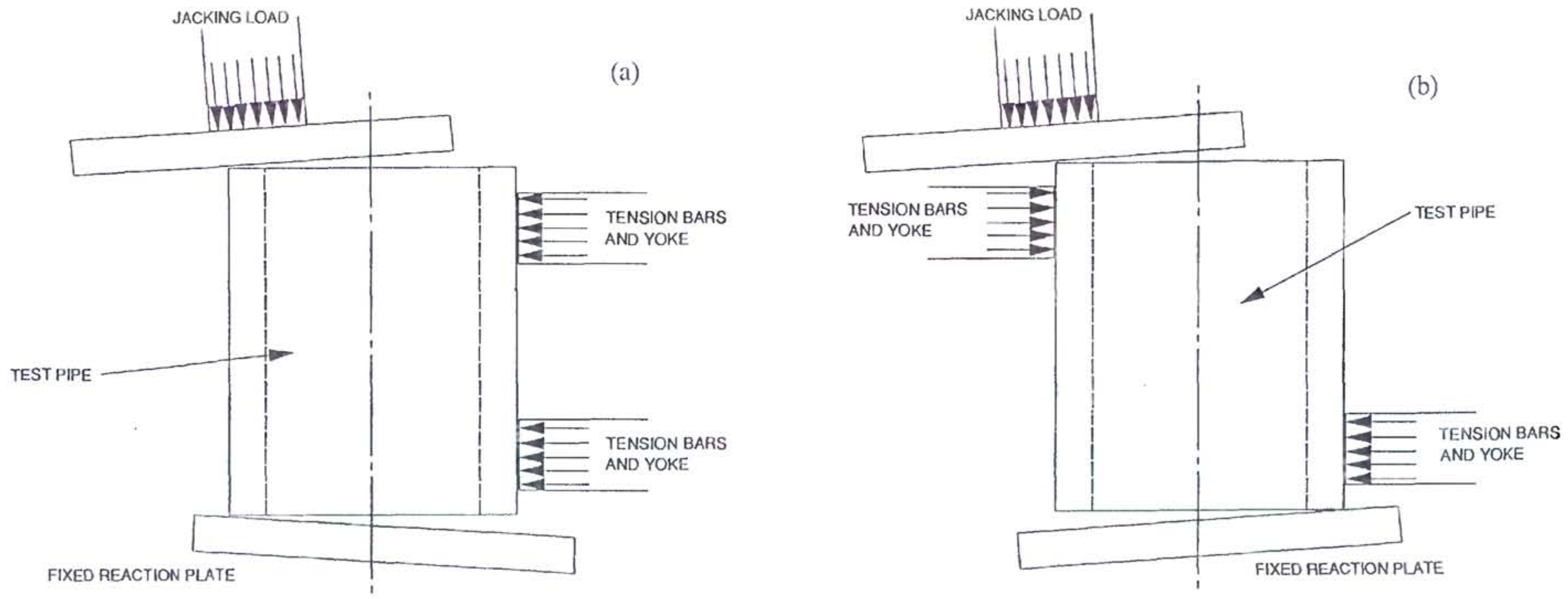

Figure 4.12 Loading arrangement for both edge and diagonal test (from Ripley 1989)

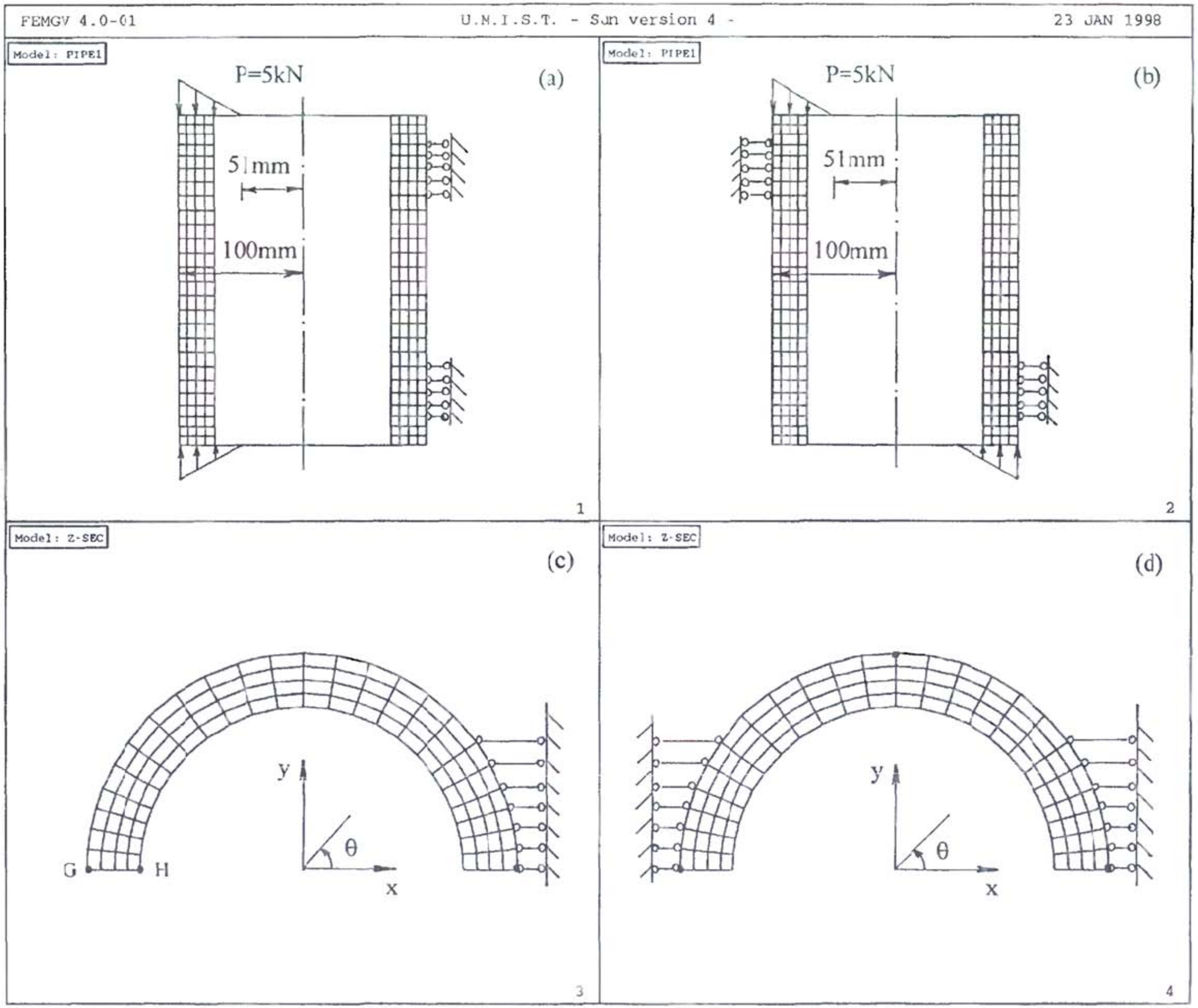

Figure 4.13 Loading and boundary condition of Numerical model A for back analysis

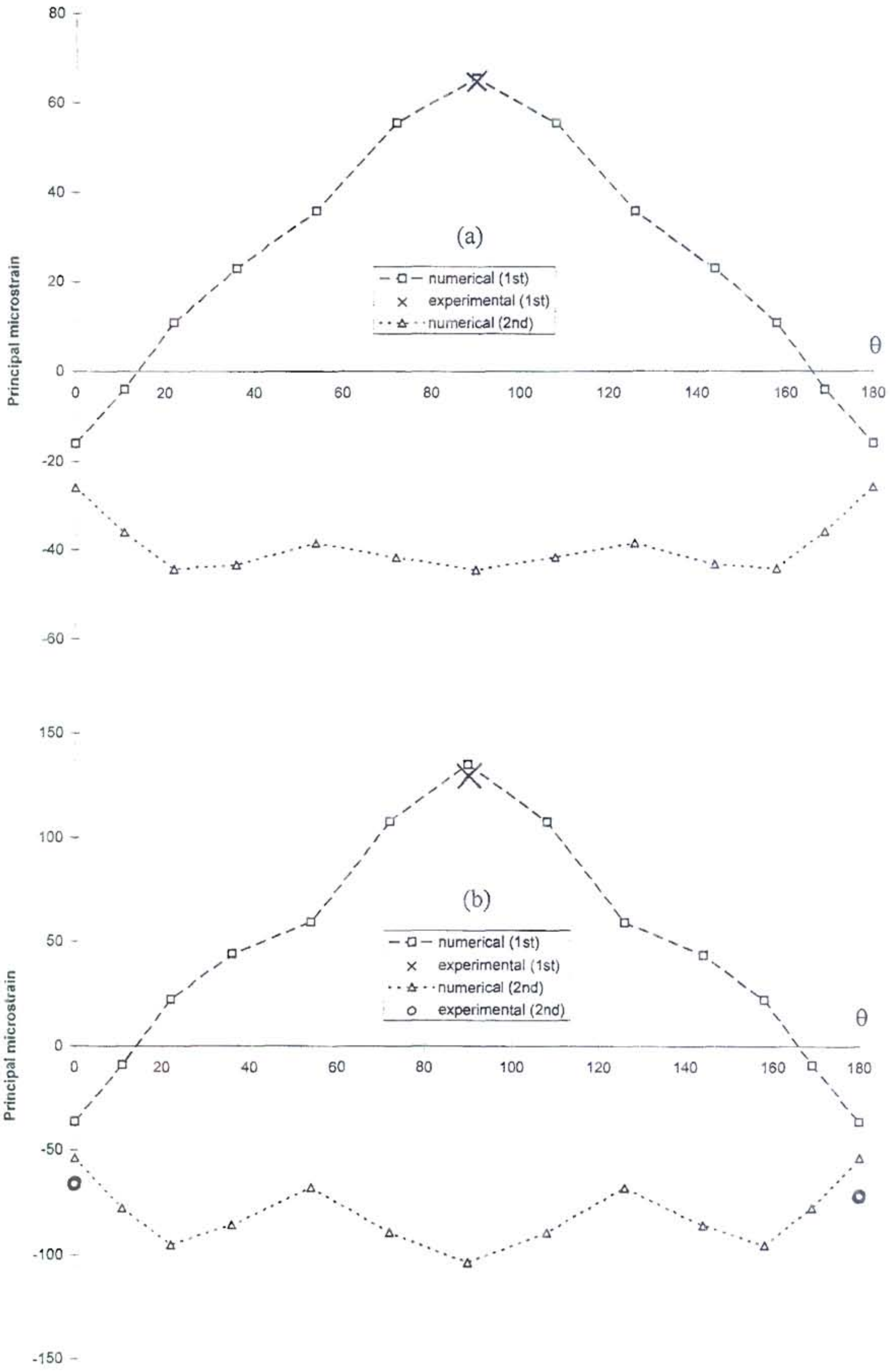

Figure 4.14 Comparison between numerical results and experimental data under ‘diagonal’ loading

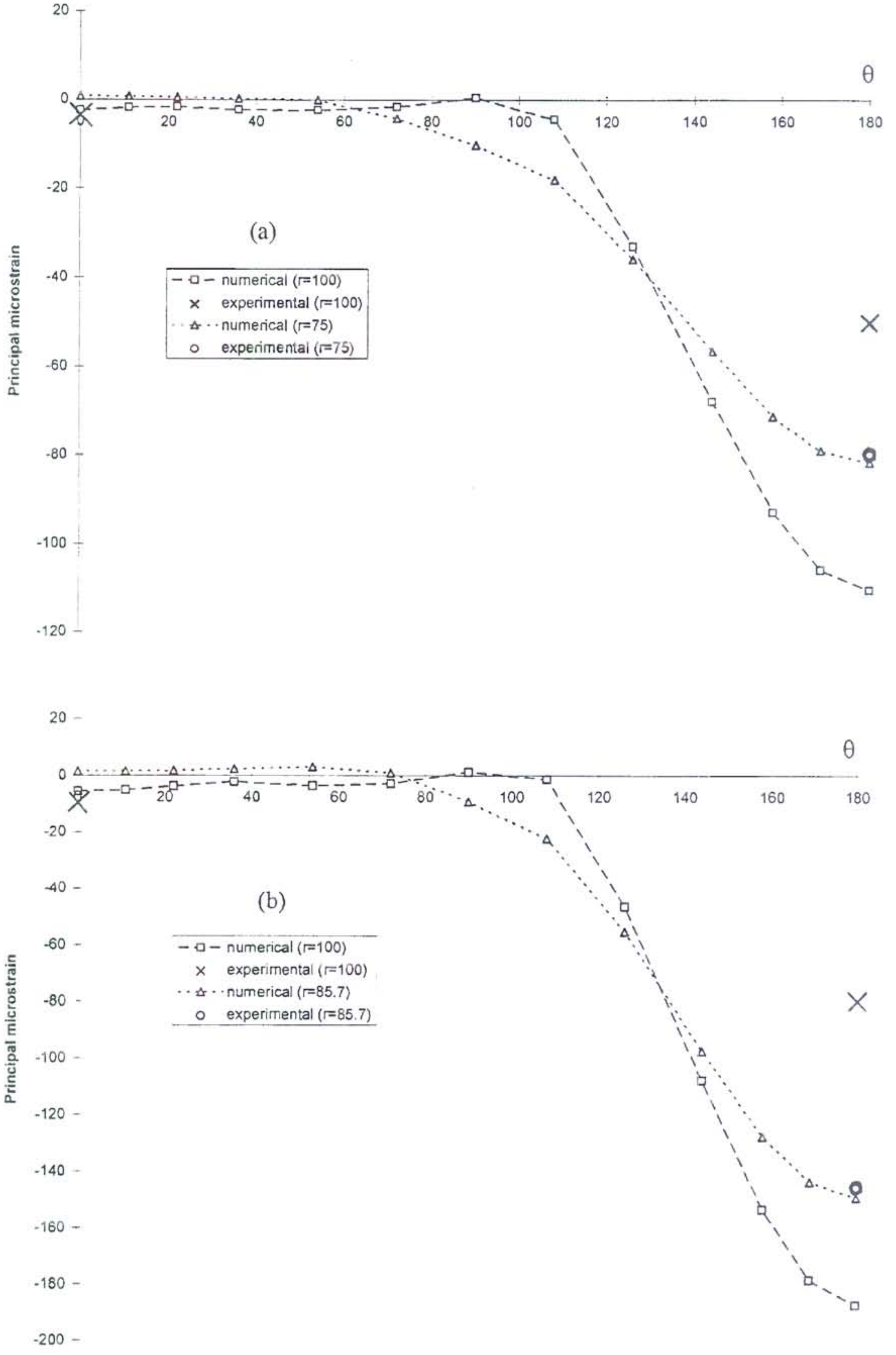

Figure 4.15 Comparison between numerical results and experimental data under 'edge' loading

CHAPTER 5 THREE-DIMENSIONAL ANALYSIS -- NUMERICAL MODEL B

5.1 INTRODUCTION

This chapter describes a three-dimensional analysis of a single full scale concrete pipe with surrounding soil. Emphasis of the analysis was placed on the interaction between the pipe and the surrounding soil. The results from numerical model A in Chapter 4 show that the computed stresses near the joint under the 'diagonal' load may be affected by the local constraints. This local effect was also examined in the analysis. In this chapter, a three-dimensional model, numerical model B, is described in Section 5.2. The analysis with elastic surrounding soil, the interaction between the pipe and the surrounding soil, and the analysis with plastic surrounding soil are discussed in Sections 5.3, 5.4 and 5.5 respectively. Section 5.6 gives the conclusion from the analysis with this model. Finally, a numerical back analysis of site measured data (Norris 1992) is described in Section 5.7.

5.2 NUMERICAL MODEL B

The numerical model B, a concrete pipe with surrounding soil, and its finite element mesh are shown in Figure 5.1 (again, since the geometry of the domain of the model B and the loads are symmetrical about the plane of $y = 0$, only half of the domain was used in analysis and shown in the figure). For simplicity, it was assumed in the analysis that there was no initial gap between the pipe and the surrounding soil and that there was no initial pressure on the pipe from the surrounding soil. The three-dimensional mesh is shown in Figure 5.1(a); the surface of r = constant unfolded on a plane is shown in Figure 5.1(b); the section of z = constant in Figure 5.1(c) and the section of $\theta = 0^0$ in Figure 5.1(d). The dimensions of the model are also shown in Figure 5.1(d). In the numerical analysis, the nodes on the outer surface of the soil mesh were all fixed in both x and y directions and on the symmetrical plane

$y = 0$ the nodes were all fixed in the y direction. The element type of 8-node hexahedron was used. The pipe was treated as linear elastic in the analysis and the material constants used by Norris (1992), the Young's modulus $E_c = 40000$MPa and the Poisson's ratio $\mu_c = 0.2$, were adopted for convenience in order to compare the numerical results with his experimental data. The surrounding soil was taken as linear elastic except in the analysis described in Section 5.5 where the soil was modelled by an elastic-plastic Matsuoka model. (To examine the mesh sensitivity, the analyses were carried out with two, four and six layers of soil elements at first. The difference between the results with four layers of soil elements and those with six layers of soil element was small. So the analyses were carried out with four layers of soil elements for the parametric study described in this chapter.)

5.3 ANALYSIS WITH ELASTIC SOIL

In this section, the effect of the soil Young's modulus is investigated with the results from an elastic analysis. In the analysis, the surrounding soil was treated as linearly elastic with a Poisson's ratio $\mu_s = 0.2$ and three different Young's moduli $E_s =$ 144MPa, 14.4MPa and 1440MPa in three different analysis cases (SE1, SE2 and SE3). The Poisson's ratio and the first Young's modulus ($E_s =$ 144MPa) were adopted from thesis of Norris (1992) to represent a typical soil (Das 1983, Bolton 1979), while the second and third Young's moduli were obtained from the first one by reducing and enlarging 10 times to model the arbitrary soft and stiff soil. Two different types of load, the 'edge' load and the 'diagonal' load , were also included in the analysis to examine the effect of the soil stiffness under different loading conditions. The two loads were used to simulate the two extreme loading conditions occurring in practice (Norris 1992) due to the misalignment of the pipe line during pipe jacking. The total load applied at each end of the pipe was the same P = 1000kN (on half of the pipe). The load distributions are shown in Figure 5.2(a) and 5.2(b) for the 'edge' and the 'diagonal' loading respectively (for clarity, the mesh of the surrounding soil is not included). The 'edge' load is distributed linearly in the x direction on both ends of the pipe as shown in

Figure 5.2(a). The distribution of the 'diagonal' load was the same as that of the 'edge' load on the upper pipe end, and the distribution on the bottom pipe end was obtained by rotating that of the 'edge' load by 180^0 in the θ direction.

If the applied load is uniformly distributed over the pipe end, the average pressure is q = 4.21MPa. The stresses shown in the contours in this chapter are all normalized with respect to this pressure for convenience of comparison. Furthermore, for a better view, the soil is excluded in all stress contours in this chapter since the study is on the behaviour of the concrete pipe.

5.3.1 EDGE LOADING

This section describes the effect of the soil stiffness under the 'edge' loading condition. The results of the normalized most tensile principal stresses in the pipe are shown in Figure 5.3. The results with the soil Young's modulus E_s = 144MPa (case SE1) is in Figure 5.3(a), the results with E_s = 14.4MPa (case SE2) in Figure 5.3(b) and the results with E_s = 1440MPa (case SE3) in Figure 5.3(c). From the figure, it is clear that in all three cases the stresses in the pipe are highly concentrated in two small domains adjacent to the loaded border at the pipe ends on the internal surface of the pipe; while the stresses in other regions are very small except that there are some tensile stresses at the middle length position of the pipe on the internal surface in the region of $\theta = 180^0$. The highest stress is in case SE2, while the peak value of the stresses in case SE3 is much lower than those in case SE1 and SE2. The results are symmetric to the plane of the middle length of pipe (z = 1250mm) since the load is also symmetric about this plane. The distribution of the principal direction is complex and difficult to be expressed in a three-dimensional contour. However, in all three cases the tensile stresses in the high stress domains are mainly in the hoop direction as shown in Figure 5.3(d).

The results of the normalized most compressive principal stresses in the pipe are shown in Figure 5.4. The results with E_s = 144MPa , 14.4MPa and 1440MPa are shown in Figures 5.4(a), 5.4(b) and 5.4(c) respectively. Again, the stress patterns in all three cases are similar except that in the case ES3 the magnitudes of the stresses at the middle length of the pipe in the region of $\theta > 110^0$ are much lower than those in the other two cases. The magnitudes of the stresses are very high in the region of $\theta = 180^0$ especially at the two loaded corners, and the stresses in the region of $\theta < 80^0$ are very small. In general, the magnitude of the stress on a plane z = constant reduces when θ decreases, and on a section of θ = constant, the magnitude of stress is high at the two ends of the pipe and reduces towards the middle of the pipe (z = 1250mm) in the region of $\theta > 80^0$ due to the friction between the pipe and the soil, especially in the case of stiff soil. (The friction between the pipe and surrounding soil is discussed in Section 5.4 with the interface elements. It should be pointed out that if a lubricant is used in pipe jacking, the friction between the pipe and the soil will reduce significantly under both the 'edge' and the 'diagonal' loading.) The change of magnitude across the pipe thickness is not significant. The maximum values of the stress magnitude are similar in all three cases.

5.3.2 DIAGONAL LOADING

Under the 'diagonal' loading condition, the load is transferred diagonally between opposite corners of the pipe as shown in Figure 5.2(b). Again, three cases (SD1, SD2 and SD3) with the same three different Young's moduli of the surrounding soil E_s = 144MPa, 14.4MPa and 1440MPa were adopted in the analysis.

The normalized most tensile principal stresses in the pipe under the 'diagonal' loading are shown in Figure 5.5(a), 5.5(b) and 5.5(c) for the case SD1, SD2 and SD3 respectively. From the figure, it is clear that in case SD1 and SD2 the stress patterns are similar. High tensile stresses are located near the loaded borders on the internal surface and at the two non-loaded diagonal corners, and there is a low stress band in the region of $\theta = 90^0$ connecting the high stress domains near the loaded borders. In case SD3, the high stresses are mainly at the central area on the internal surface of the pipe in addition to the edge of the loaded area and the two non-loaded corners. It should be pointed out that the high tensile stresses on the external surface of the pipe at the two non-loaded corners are possibly due to the unrealistic high stresses acting on the external surface of the pipe at these areas from the surrounding elastic soil as shown in Figure 5.5(d). However, in practice, a gap would form between the pipe and the soil at these two corners under the 'diagonal' loading condition which is examined in section 5.4. The highest peak value is in case SD2 and the peak value in case SD3 is much lower than those in the cases SD1 and SD2. The principal direction in the high stress region of $\theta = 90^0$ on the internal surface is similar in all three cases and is shown in Figure 5.5(d). The figure shows that the tensile stresses are mainly in the hoop direction at the pipe ends and the tensile direction changes to the normal direction of the line connecting the two loaded corners when towards to the middle length of the pipe.

Figure 5.6 shows the same normalized principal stresses in the concrete pipe with the pipe rotated 180 degrees in the θ direction. From the figure, it is clearly seen that the stress distribution patterns on the external surface of the pipe are quite different from those on the internal surface. Now the stress patterns are similar in all three cases, and the high stresses are located at the central area on the external surface and the two non-loaded corners (the reason for high stress at the non-loaded corners was discussed above for Figure 5.5) . Again, the highest stress is in the case SD2 and the peak value in case SD3 is much lower than those in the other two cases. Figure 5.6(d) shows the principal direction in the high stress regions (similar in all three cases). Again, the tensile stresses are in the hoop direction at the two non-loaded corners and in the normal direction of the line connecting the two loaded corners at the central area on the external surface.

The normalized most compressive principal stresses are shown in Figure 5.7. The figure shows that the high magnitudes of the stresses are located at the two diagonal loaded corners and there is a small band connecting these two corners with lower magnitudes of stress; and that the stress magnitudes reduce when away from the band towards the other two non-loaded corners. The change of the stress magnitude is small across the pipe thickness. The peak magnitudes are very similar to those under the corresponding 'edge' loading conditions.

5.4 INTERACTION BETWEEN THE PIPE AND THE SURROUNDING SOIL

To remove effect of unrealistic stresses acting on the external surface of the pipe from the surrounding soil as discussed in Section 5.3 and to study the interaction between the pipe and its surrounding soil, a layer of interface elements was used between the pipe and the soil in the analysis described in this section. For simplicity, the soil was also treated as linearly elastic with the same Poisson's ratio $\mu_s = 0.2$ and the same three different Young's moduli E_s = 144MPa, 14.4MPa and 1440MPa.

The interaction between the pipe and its surrounding soil was modelled by using the elastic perfectly-frictional Mohr-Coulomb model described in Chapter 2. In the second stage of research at Oxford about pipe jacking (Milligan and Norris 1993a, Norris 1992), it was found that the frictional angle between the pipe and its surrounding soil varied from 12^0 to 37^0 under different ground conditions and the cohesion parameter c was small. However, the analysis is not aimed at representing any particular ground condition in practice but to study the general effect of the interaction between the pipe and the surrounding soil. In the analysis, an arbitrary frictional angle $\phi = 15^0$ and an associated dilation angle $\psi = 15^0$ were used. A small cohesion parameter c = 0.05MPa was taken for the purpose of numerical stability in the analysis because there was no initial contact stresses between the pipe and the surrounding soil. The shear stiffness K_s and the normal stiffness K_n of the interface were chosen according to the stiffness and dimensions of the soil in the model, that is, 50MPa /mm and 100MPa /mm for E_s =144 MPa, 5MPa /mm and 10MPa /mm for E_s =14.4MPa, and 500MPa /mm and 1000MPa /mm for E_s =1440MPa.

The finite element mesh and the dimensions of the domain are shown in Figure 5.8(a) to 5.8(d), which are almost the same as those used in Section 5.3 except that there is a layer of interface elements between the pipe and its surrounding soil. The boundary conditions and the loading conditions are the same as those without the interface in Section 5.3. The solution method for the analysis described in this section is the initial stiffness method due to the difficulties with the modified Euler method. (When the modified Euler iteration procedure was used in the analysis with this model, the convergence was very slow and the unbalanced force was large, especially under the diagonal loading condition.) The total numbers of calculation steps were 400 for the 'edge' loading case and 500 for the 'diagonal' loading case. Within each calculating step, there were several iterations depending on the convergent condition while the maximum number of iterations was 10.

5.4.1 EDGE LOADING WITH INTERFACE ELEMENTS

This section describes the analysis with the 'edge' load and with three cases FE1, FE2 and FE3 for the same three different soil stiffness. The normalized normal stresses on the unfolded interface in case FE1, FE2 and FE3 are shown in Figure 5.9(a), 5.9(b) and 5.9(c) respectively. From the figure, it is clear that the stress patterns in all three cases are similar and that the high magnitudes of the normal stresses are at the two corners in the region of θ = 180^0. However, the peak magnitudes are small in case FE1 and FE2. In case FE3, the peak magnitude of the normalized normal stresses is about 0.45.

The normalized shear stresses on the unfolded interface in case FE1, FE2 and FE3 are shown in Figure 5.10(a), 5.10(b) and 5.10(c) respectively. Clearly, the shear stress patterns on the interface in all three cases are similar to those of the normal stresses. The normalized stresses are concentrated at the two corners in the region of $\theta = 180^0$ and the peak values are small except in case FE3. (It should be pointed out that the stresses in the soil might be beyond the soil strength under both 'edge' and 'diagonal' loading, especially in the case of soft soil. The soil plasticity is discussed in Section 5.5 with the modified Matsuoka model. If a lubricant is used in pipe jacking, the friction between the pipe and the soil will reduce significantly.)

From the discussion above, it is clear that the pipe is separated or almost separated from the surrounding soil over most of the external surface. However, the effect of the distribution of the stresses from the surrounding soil on the stresses in the pipe are believed to be small since the magnitudes of the stresses on the interface are small except in the case FE3.

The normalized most tensile principal stresses in the pipe are shown in Figure 5.11(a), 5.11(b) and 5.11(c) for case FE1, FE2 and FE3 respectively. The figure shows that the stress distributions and the peak values of the tensile stresses are similar to those in the case without interface elements in Section 5.3.1. The difference between the stresses with stiff soil in Figure 5.11(c) and those in Figure 5.11(a) and 5.11(b) is due to the reaction stresses from the soil on the interface as discussed above. The principal direction in the regions with high tensile stresses is also similar to that in Section 5.3.1 (refer to Figure 5.3(d)). Similar comments are applied to the normalized most compressive principal stresses in the concrete pipe which are not discussed in detail here (refer to Section 5.3.1, and see Figure 5.4).

5.4.2 DIAGONAL LOADING WITH INTERFACE ELEMENTS

Under the 'diagonal' loading condition, again, three calculation cases, FD1, FD2 and FD3, for the same three different soil stiffnesses have been studied. The normalized normal stresses on the unfolded interface under the 'diagonal' load are given in Figure 5.12(a), 5.12(b) and 5.12(c) for case FD1, FD2 and FD3 respectively. From the figure, it is clearly seen that in all three cases the distribution patterns of the normal stresses on the unfolded interface are similar and the stresses are concentrated at the two diagonal loaded corners, and that the stresses on the other two corners and central area are almost zero. The highest stress magnitude is in case FD3 while the peak magnitudes in case FD1 and FD2 are slightly lower.

The normalized shear stresses on the unfolded interface under the 'diagonal' load are given in Figure 5.13(a), 5.13(b) and 5.13(c) for case FD1, FD2 and FD3. Again, the shear stresses are concentrated in the two diagonal loading corners. The stresses at the two non-loaded diagonal corners are zero and the stresses at the central area are very small. The highest stress is also in case FD3 with the highest soil Young's modulus.

The results of the normal and shear stresses on the interface clearly suggest that the pipe is separated from its surrounding soil at the two non-loaded diagonal corners and is almost separated at the central area of the external surface while the pipe is supported by the surrounding soil at the two diagonal loaded corners.

The normalized most tensile principal stresses in the pipe under the 'diagonal' load are shown in Figure 5.14, with the stresses in case FD1 in Figure 5.14(a), the stresses in case FD2 in Figure 5.14(b) and the stresses in case FD3 in Figure 5.14(c). The figure shows that in case FD1 and FD2 the stress patterns are similar, but they are quite different from those without interface elements in Section 5.3, and that the tensile stresses on the external surface of the pipe at the two non-loaded corners in Figure 5.5 vanished due to the gap between the pipe and the soil as discussed above. The stresses are concentrated on the internal surface of the pipe near the non-loaded corners and the stresses at the two diagonal loaded corners are almost zero. In the case FD3, the high stresses are in the central area on the internal surface while its peak stress is much lower than those in the other two cases due to the higher reaction stresses from the soil as discussed above. The highest stress is in case FD2 with the soft soil. The principal direction in the high stress regions is somewhat similar for all three cases and is shown in Figure 5.14(d). In general, the tensile stresses are in the hoop direction in the region of $\theta = 180^0$ and 0^0, and change towards to the normal direction of the line connecting the two loaded corners when moving towards to the central region of $\theta = 90^0$.

Figure 5.15 shows the normalized most tensile principal stresses in the pipe under the 'diagonal' load viewed from the opposite direction. The stresses on the external surface of the pipe are very high at the central area and the stresses at the two loaded corners are almost zero as on the internal surface. The peak values are higher than those on the internal surface with the highest stress still in case FD2. The tension direction at the central area of the external pipe surface is mainly in the normal direction of the line connecting the two loaded corners in all three cases as shown in Figure 5.15(d).

The normalized most compressive principal stresses in the pipe under the 'diagonal' loading condition are shown in Figure 5.16. From the figure, it is clear that the stress patterns are similar to those without the interface elements in Section 5.3.2 except that the peak magnitudes are slightly higher (see Figure 5.7).

5.5 ANALYSIS WITH PLASTIC SOIL

In this section, a further analysis with plastic surrounding soil without the interface is described. In general, the yielding behaviour of the soil is dependent on the type of soil (Das 1983, Bolton 1979). For example, von-Mises' model is appropriate to describe the behaviour of clays under undrained conditions, and the Matsuoka model and Mohr-Coulomb model with a high frictional angle are suitable for sands. In the analysis described in this section, the soil was modelled by the elastic perfectly-plastic Matsuoka model described in Chapter 2. One thing that should be stressed here is that the plastic model is not intended to describe any particular soil in practice. Rather, the analyses were carried out to study the effect of the surrounding soil in which frictional behaviour was important, as pointed out in Section 5.4. To enable the soil model to describe the friction between the pipe and the surrounding soil and to perform some functions of an interface, the material parameters of the soil were chosen to be the same as those used for the interface model in Section 5.4, that is, the triaxial frictional angle $\phi = 15^0$, the triaxial dilation angle $\psi = 15^0$, the soil cohesion c = 0.05MPa, the Poisson's ratio $\mu_s = 0.2$ and the three different Young's moduli. (It should be pointed out that the dilation angle of the soil is defined as $\tan\psi = \frac{d\varepsilon_v}{d\gamma}$, where $d\varepsilon_v$ and $d\gamma$ are the volumetric strain and shear strain in the soil shear test (Atkinson 1993). However, in the current research, only the friction of the soil was considered and an associated flow rule was used. In the modified Matsuoka model, the plastic potential was assumed to be the same as the yield function, that is, $\psi = \phi$ (see Section 2.4.2).) In the analysis described in this section, the solution method was also the initial stiffness method described in Chapter 2. The total numbers of calculation steps were 400 for the 'edge' loading case and 500 for the 'diagonal' loading case. Again, within each calculating step, there were several iterations depending on the convergent condition.

5.5.1 EDGE LOADING WITH PLASTIC SOIL

The finite element mesh, boundary condition and the loads were the same as those shown in Figure 5.1 and 5.2 in Section 5.3.1. Again, three cases (PE1, PE2 and PE3) with the same three different Young's moduli of the surrounding soil E_s = 144MPa, 14.4MPa and 1440MPa were included in the analysis.

The normalized most tensile principal stresses in the pipe under 'edge' loading with the plastic surrounding soil are shown in Figure 5.17. The figure shows that in all three cases the tensile stress distributions are almost same as those with the elastic surrounding soil in Sections 5.3 and 5.4. The peak value in case PE3 is higher than that in case E3 and FE3 although it is still much lower than those in case PE1 and PE2. The principal direction in the high stress regions is mainly in the hoop direction in all three cases as discussed in Section 5.3 (see Figure 5.3(d)). As for the most compressive stresses in the pipe, the distribution patterns and the peak magnitudes are also the same as those with the corresponding elastic surrounding soil, and are not discussed here in detail (refer to the discussion in Section 5.3.1 and see Figure 5.4).

5.5.2 DIAGONAL LOADING WITH PLASTIC SOIL

Under the 'diagonal' loading case and with the plastic surrounding soil, the three calculation cases are called PD1, PD2 and PD3 with the same three different Young's moduli of the surrounding soil E_s = 144MPa, 14.4MPa and 1440MPa. All other conditions were unchanged from those in the cases with the elastic surrounding soil in Section 5.3.2.

Figure 5.18 shows the normalized most tensile principal stresses in the pipe under the 'diagonal' loading with the plastic surrounding soil. The stress distributions in all three cases are similar to those in case FD1 and FD2 in Section 5.4.2 except that the centres of the high stresses are slightly further away from the two non-loaded corners and the high stress domains extend further towards the pipe centre in the θ direction. The peak value of the stress in case PD3 is much higher than that in case FD3 in Section 5.4.2 and SD3 in Section 5.3.2 although it is still lower than those in case FD1 and FD2 . The principal direction in the high stress regions is also similar in all three cases and shown in Figure 5.18(d). Again, the tension is mainly in the hoop direction in the region of $\theta = 180^0$ and 0^0, and changes towards the normal direction of the line connecting the two loaded corners when moving towards the central region of $\theta = 90^0$.

Figure 5.19 shows the most tensile principal stresses in the pipe under the 'diagonal' load with the plastic surrounding soil with the pipe rotated 180 degrees in the θ direction. The figure shows that the stress patterns are similar in all three cases and that the stresses are highly concentrated at the central areas on the external surface of the pipe as in the case with interface except that the peak stresses are higher than the corresponding ones in Section 5.4.2, especially in the case PD3. Similar to the case with interface in Section 5.4, in all three cases the tension at the central area of the external pipe surface is mainly in the normal direction of the line connecting the two loaded corners as shown in Figure 5.19(d).

As for the normalized most compressive principal stresses in the pipe under the 'diagonal' load with the plastic surrounding soil, both the distribution patterns and the peak magnitudes of the stress are very similar to those shown in Figure 5.16 in Section 5.4.2 and it is not discussed any further about them here (refer to Section 5.4.2 and see Figure 5.16).

5.6 CONCLUSION

This chapter describes the analyses of the numerical model B with elastic surrounding soil, interface elements between the pipe and its elastic surrounding soil and plastic surrounding soil under both the 'edge' load and the 'diagonal' load. In all cases, the stress distributions are complex three-dimensional patterns as found in Chapter 4. In general, under the 'edge' load, high tensile stresses are located near the loading border at the pipe joint and the compressive stresses are concentrated at the loaded corners; under the 'diagonal' load, the high tensile stresses are in two domains near the diagonal loaded corners on the internal surface and at the central area on the external surface, and the compressive stresses are also concentrated at the loaded corners.

After analyzing the results from the numerical model B in this chapter, some conclusions about the behaviour of the pipe with its surrounding soil are reached as follows:

(1) Under the 'edge' load, the effect of the interaction between the pipe and soil, and the plasticity of the surrounding soil is very small; while under the 'diagonal' load, the effect of the interaction and the plasticity of the surrounding soil is significant.

(2) Under the same loading condition, the surrounding soil tends to reduce the tensile stresses in the pipe under both the 'edge' and the 'diagonal' loading condition, especially with a very stiff surrounding soil.

(3) Pipe testing under 'diagonal' loading without soil surrounding the pipe may give incorrect results due to the interaction between the pipe and the soil.

(4) The tensile stresses in the concrete pipe could be more important than the compressive stresses during pipe jacking due to the misalignment of the pipeline and the low tensile strength of the concrete which is usually one tenth of its compressive strength (Jiang and Feng 1991, Neville 1981).

(5) The 'diagonal' loading condition seems to be more severe than the 'edge' loading condition since the tensile stresses in the pipe are higher and over a wider region under the 'diagonal' loading condition.

(6) The results suggest that the surrounding soil has removed the local constraint effect under the 'diagonal' loading condition found in Chapter 4, and that both the interface and the plastic surrounding soil have eased the unrealistic tensile stresses acting on the external surface of the pipe from the surrounding soil.

5.7 BACK ANALYSIS OF NORRIS' EXPERIMENTAL DATA

In the second stage of the Oxford research on pipe jacking, Norris (1992) carried out monitoring of field behaviour of pipes at full scale on five active construction sites. In his research, the loading distribution at the pipe joint was measured using pressure cells glued to the pipe ends. The measured load distributions of case BA1 and BA2 and the location of the pressure cells on site 5 are shown in Figure 5.20(a) and 5.20(b) respectively. Furthermore, average strains on the internal surface of the pipe were measured by using tube extensometers which were of 1600mm gauge length and located at the middle part of the pipe. An analysis was carried out by Norris (1992) taking the pipe as a stocky column subject to axial load and biaxial bending as shown in Figure 5.21(a) and 5.21(b) for case BA1 and BA2 respectively.

Since in both cases the change of the bending moment along the pipe length is very small (less than one percent), Norris calculated the analytical strains at the section of z = 1250mm instead of the average ones. In the numerical analysis, since the strains were calculated at Gauss points, the numerical strains were calculated on a surface r = constant very near the internal surface of the pipe instead of on the internal surface.

In the back analysis. a full scale concrete pipe and the surrounding soil were used as shown in Figure 5.22. The three-dimensional mesh is shown in Figure 5.22(a); the surface of r = constant unfolded on a plane is shown in Figure 5.22(b); the section of z = constant in Figure 5.22(c) and the section of $\theta = 0^0$ in Figure 5.22(d). The dimensions of the pipe are the same as those of the full scale pipe used by Norris in his experiment. The dimensions of the pipe and of the domain are also shown in Figure 5.22(d). For the boundary condition, the nodes on the external surface of the domain were all fixed in both *x* and *y* directions. The applied load was assumed to be constant across the thickness of the pipe since the pressure cells on the pipe end spanned across the full pipe thickness and to have the same distribution patterns in θ direction as the measured data shown in Figure 5.20. The total applied load on the pipe end was P = 4525kN and P = 3640kN for case BA1 and BA2 respectively. The assumed distributed loads on the external surface of the pipe were ignored in the analysis since the surrounding soil was included to deal with the interaction between the pipe and the surrounding soil. The distributions of applied load showed that it was an 'edge' load, and that the load was over half the cross section of the pipe. So both the concrete pipe and the surrounding soil were treated as linear elastic in the analysis (refer to the conclusion in Section 5.6). The material constants were the same as those used by Norris (1992) in his research, that is, the Young's modulus $E_c = 40000$MPa and the Poisson's ratio $\mu_c = 0.2$ for the concrete pipe, and the Young's modulus $E_s = 144$MPa and the Poisson's ratio $\mu_s = 0.2$ for the surrounding soil.

The average microstrains in the *z* direction over 1600mm in the middle part of the pipe on the internal surface (r = 600mm) are given in Figure 5.23(a) and 5.23(b) for cases BA1 and BA2 respectively. In the figure, the *y* axis is the microstrain and the *x* axis is θ in degrees. From the figure, it is clear that in case BA1 the numerical results, the measured values and the analytical results agree well with each other except that the analytical results deviate slightly when the strains are small and tensile in the region of $\theta = 180^0$. In case BA2, the agreement between the numerical results, the measured values and the analytical results are also good except that there is some deviation with the measured value in the region of $\theta = 150^0$, and with the analytical results in the regions of $\theta = 210^0$ and $\theta = 330^0$.

The results above suggest that both the numerical model B and the stocky column model are capable of obtaining reliable results for the average compressive strains in the middle part of the pipe under the 'edge' loading condition. However, one thing should be stressed here is that the stocky column model cannot gain accurate predictions at the pipe joint due to strain concentrations at the joint and lack of changes of the bending moment in the stocky column model; and that there is no similar simple analytical model for 'diagonal' loading.

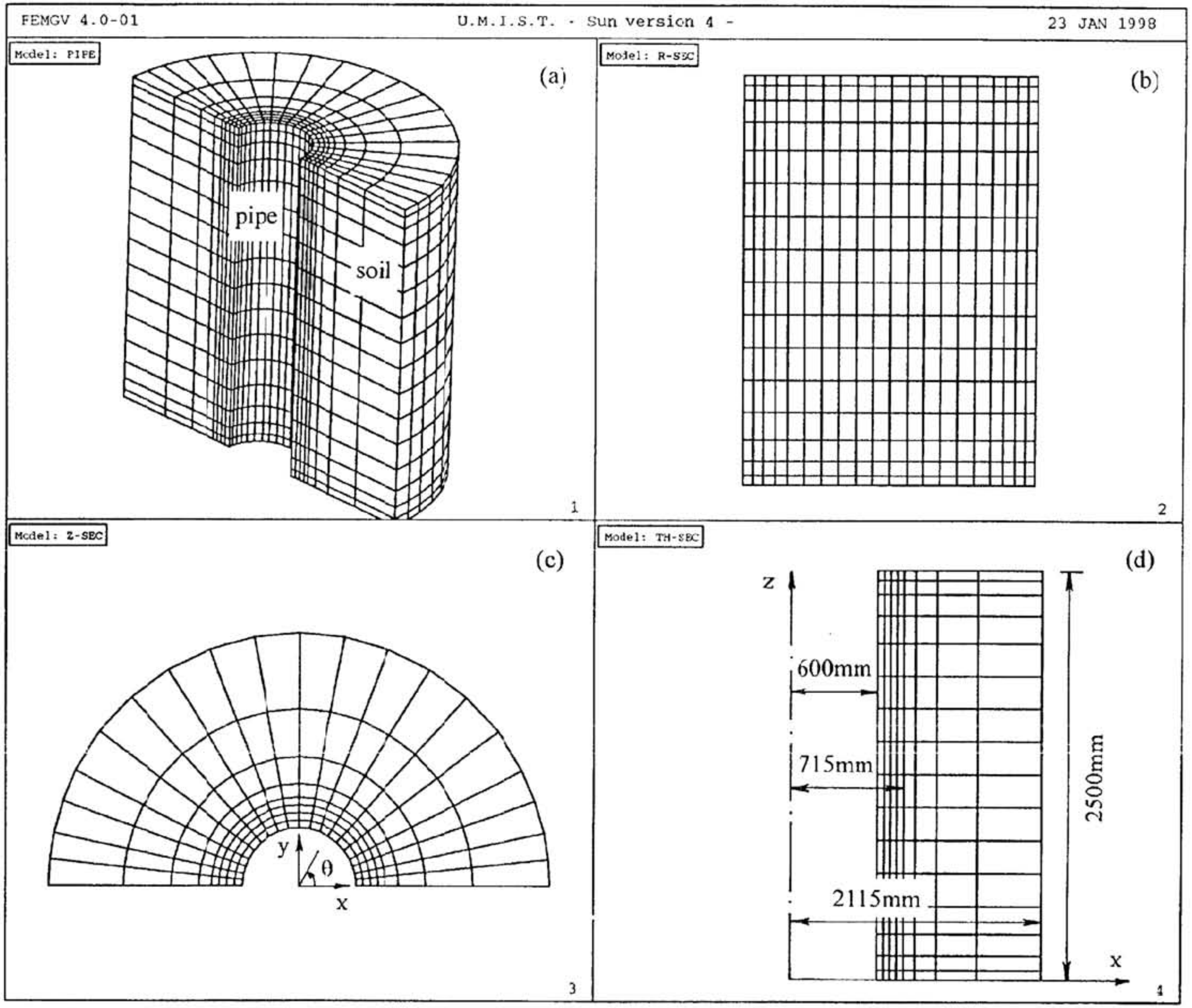

Figure 5.1 Numerical model B and its FE mesh

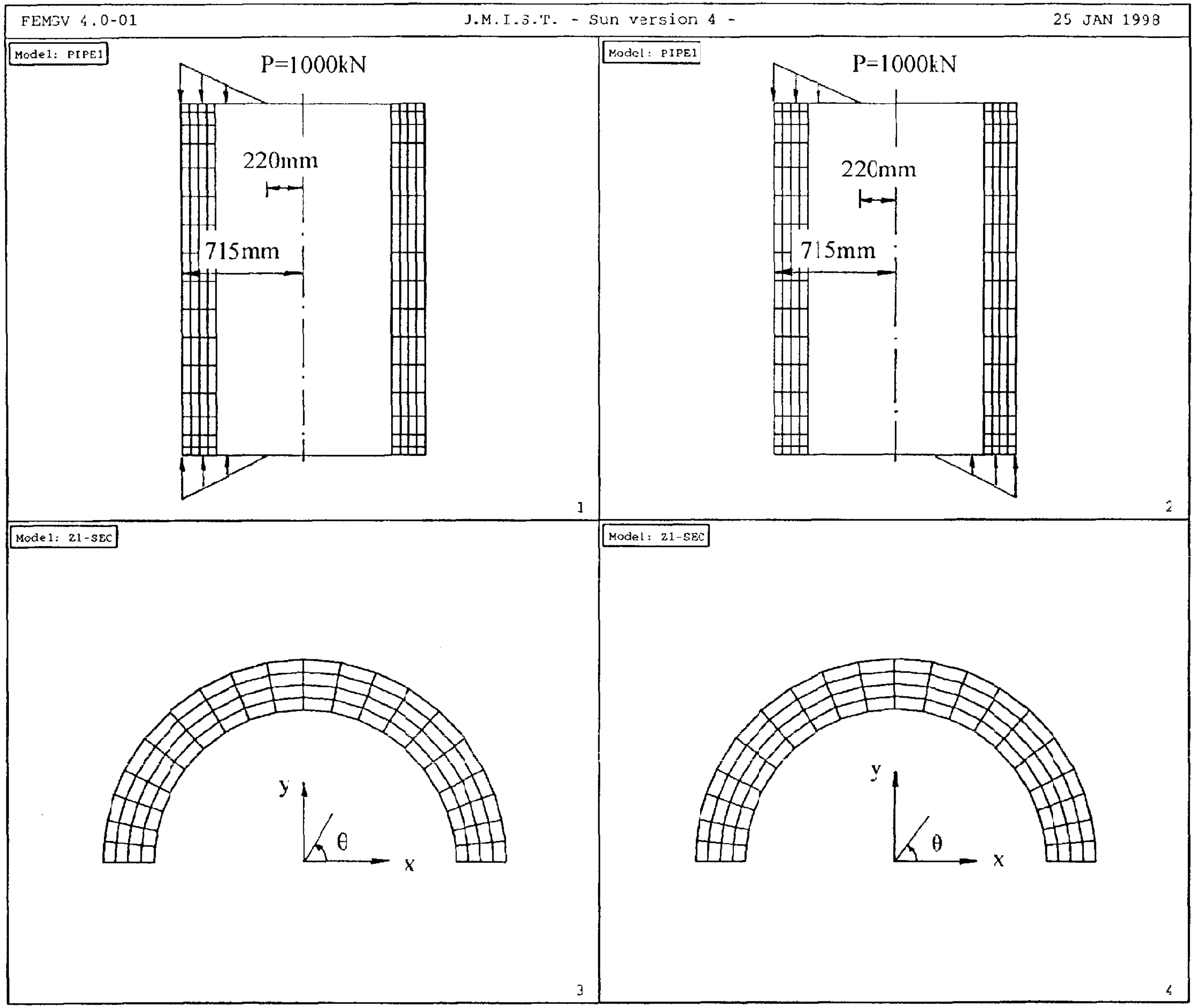

Figure 5.2 'Edge' load and 'diagonal' load

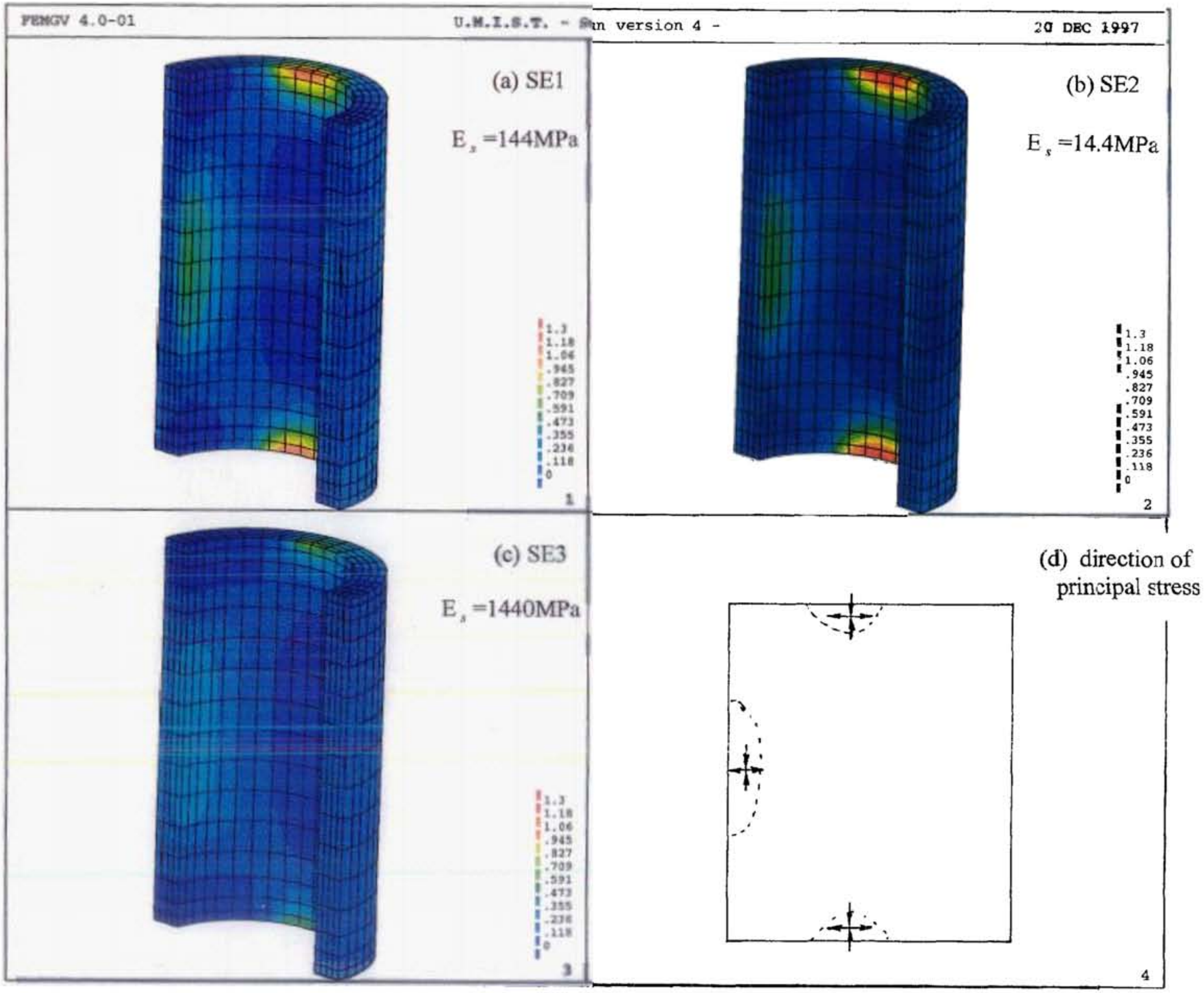

Figure 5.3 Normalized most tensile principal stresses in the pipe under 'edge' loading with elastic soil

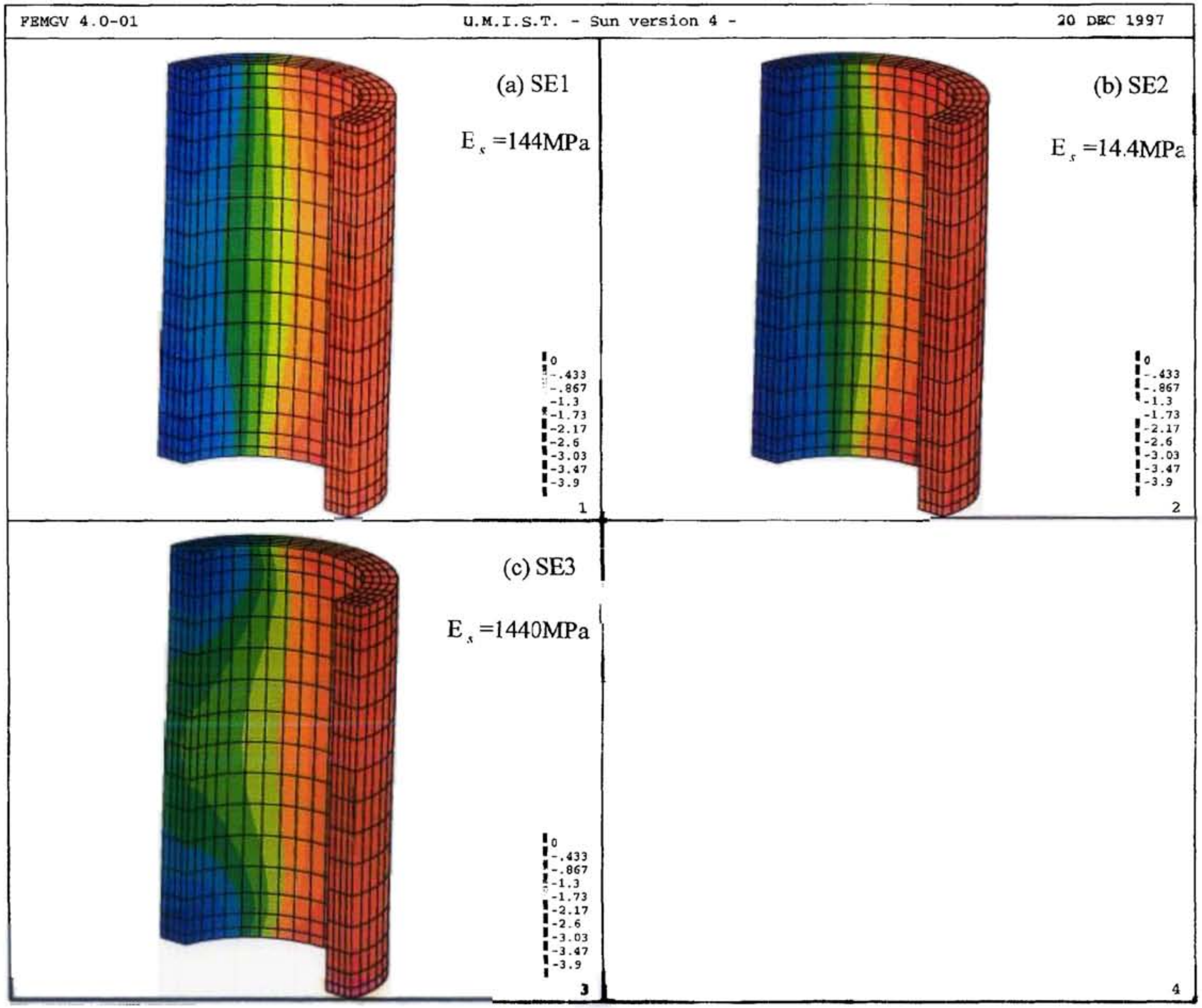

Figure 5.4 Normalized most compressive principal stresses in the pipe under ‘edge’ loading with elastic soil

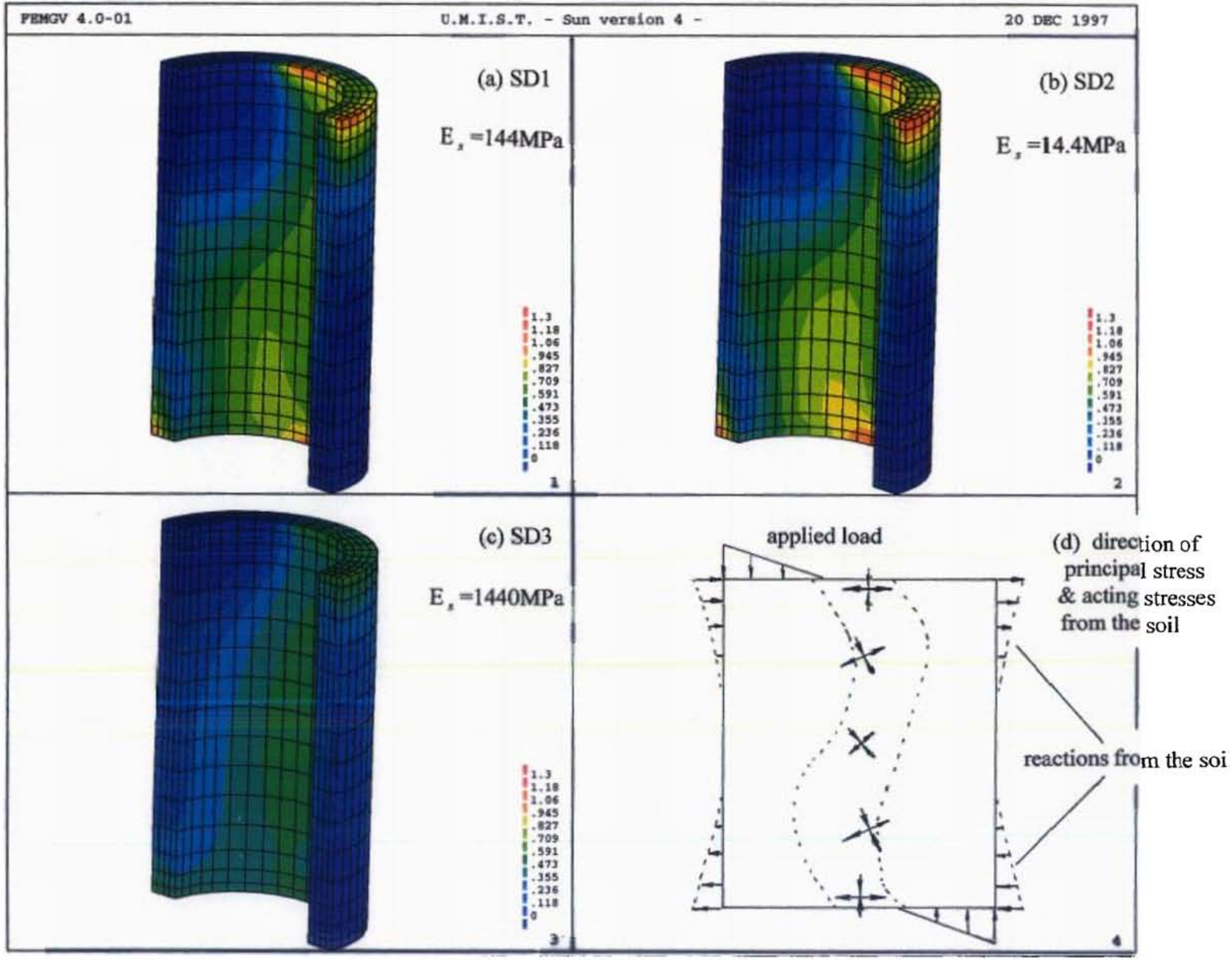

Figure 5.5 Normalized most tensile principal stresses in the pipe under 'diagonal' loading with elastic soil

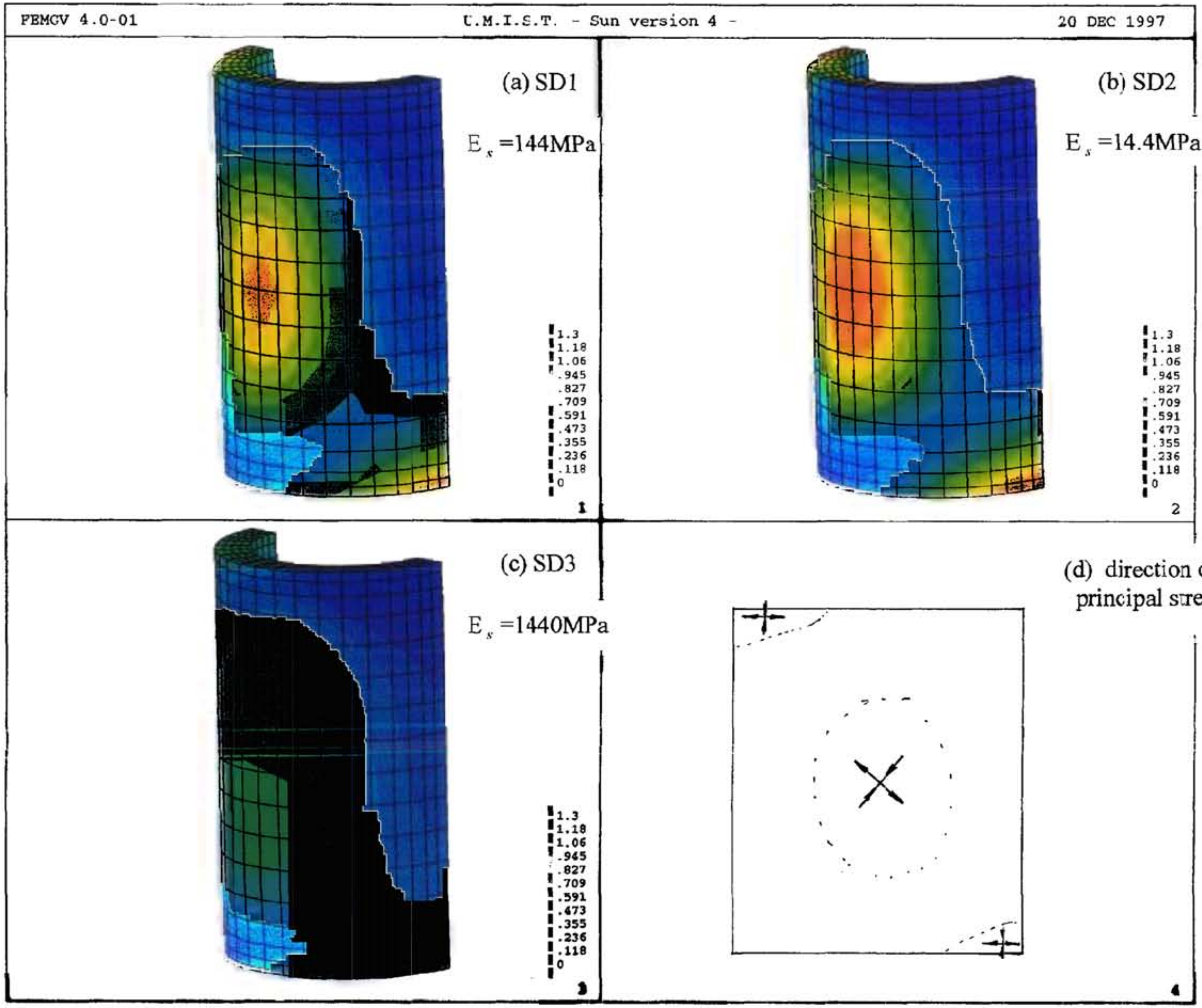

Figure 5.6 Normalized most tensile principal stresses in the pipe under 'diagonal' loading with elastic soil by looking from opposite direction

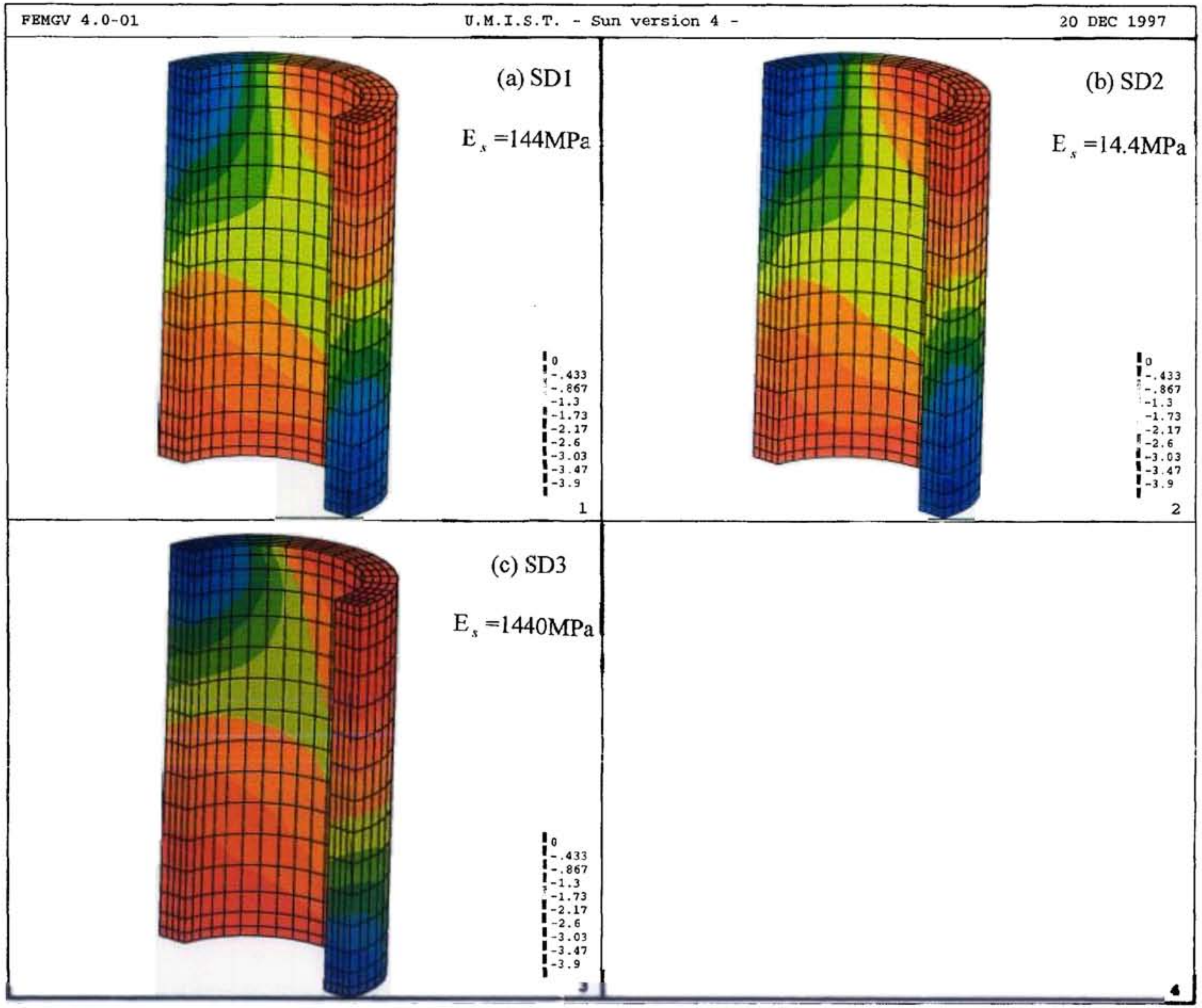

Figure 5.7 Normalized most compressive principal stresses in the pipe under 'diagonal' loading with elastic soil

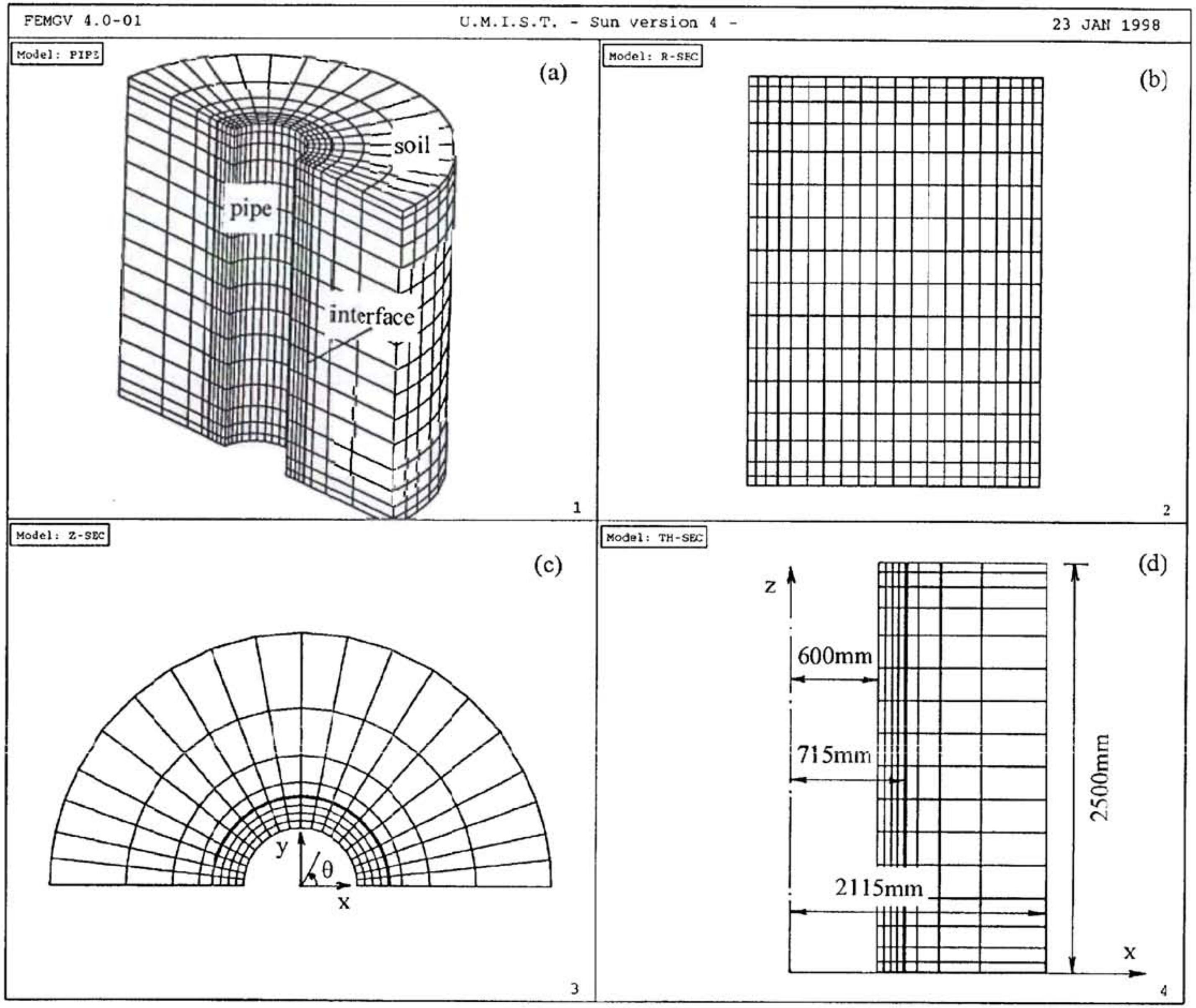

Figure 5.8 FE mesh of numerical model B with interface elements

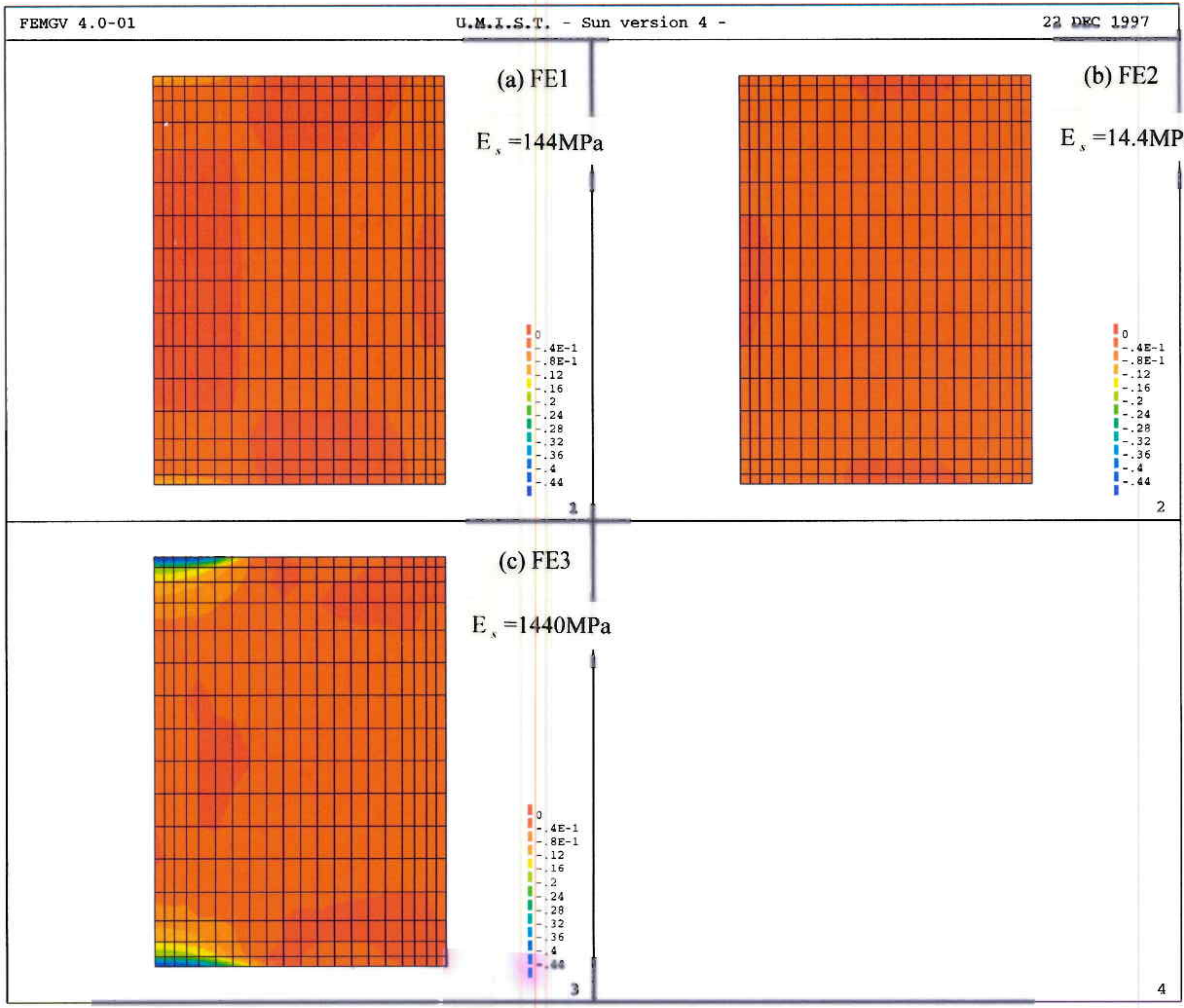

Figure 5.9 Normalized normal stresses on the unfolded interface under ‘edge’ loading

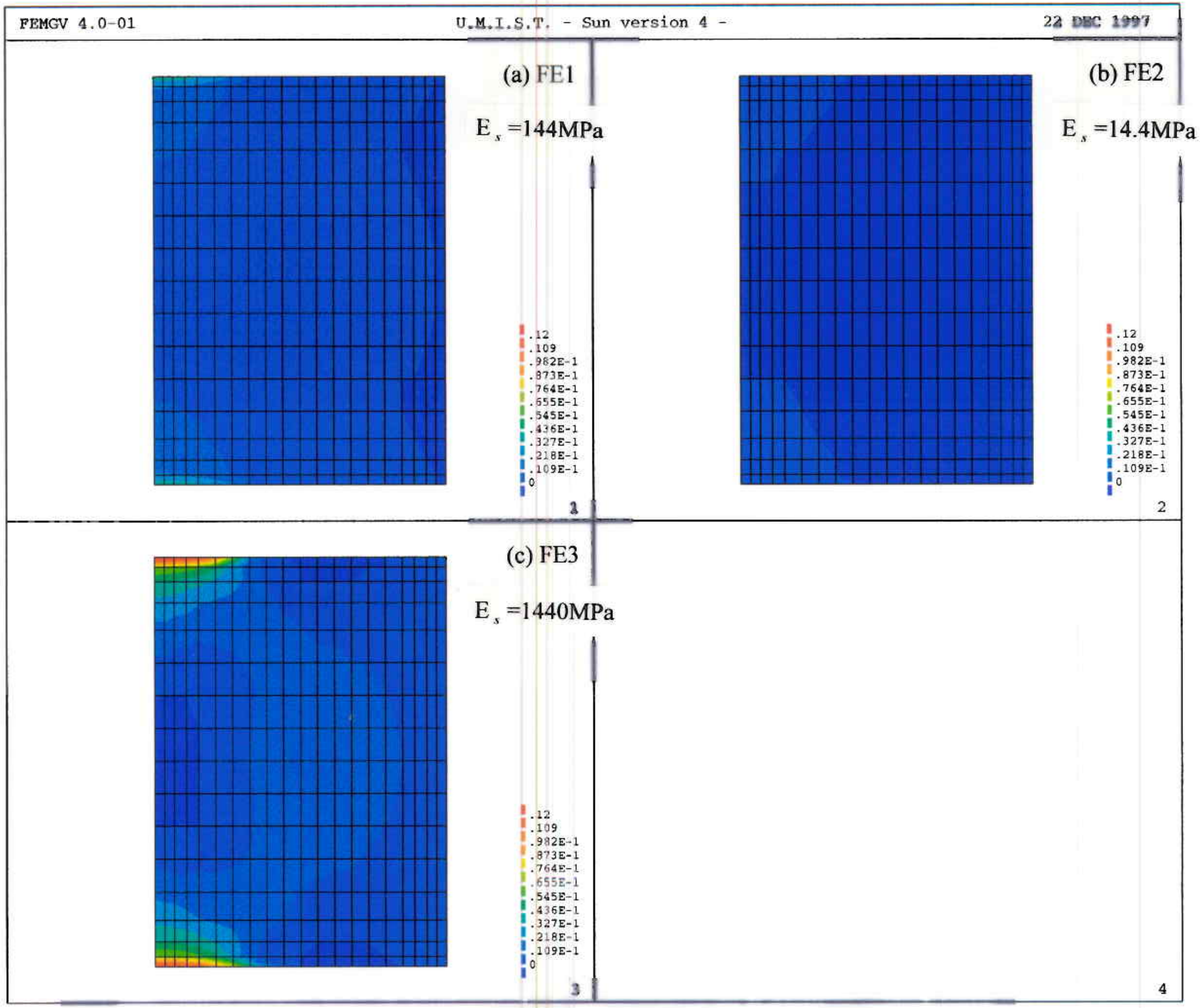

Figure 5.10 Normalized shear stresses on the unfolded interface under 'edge' loading

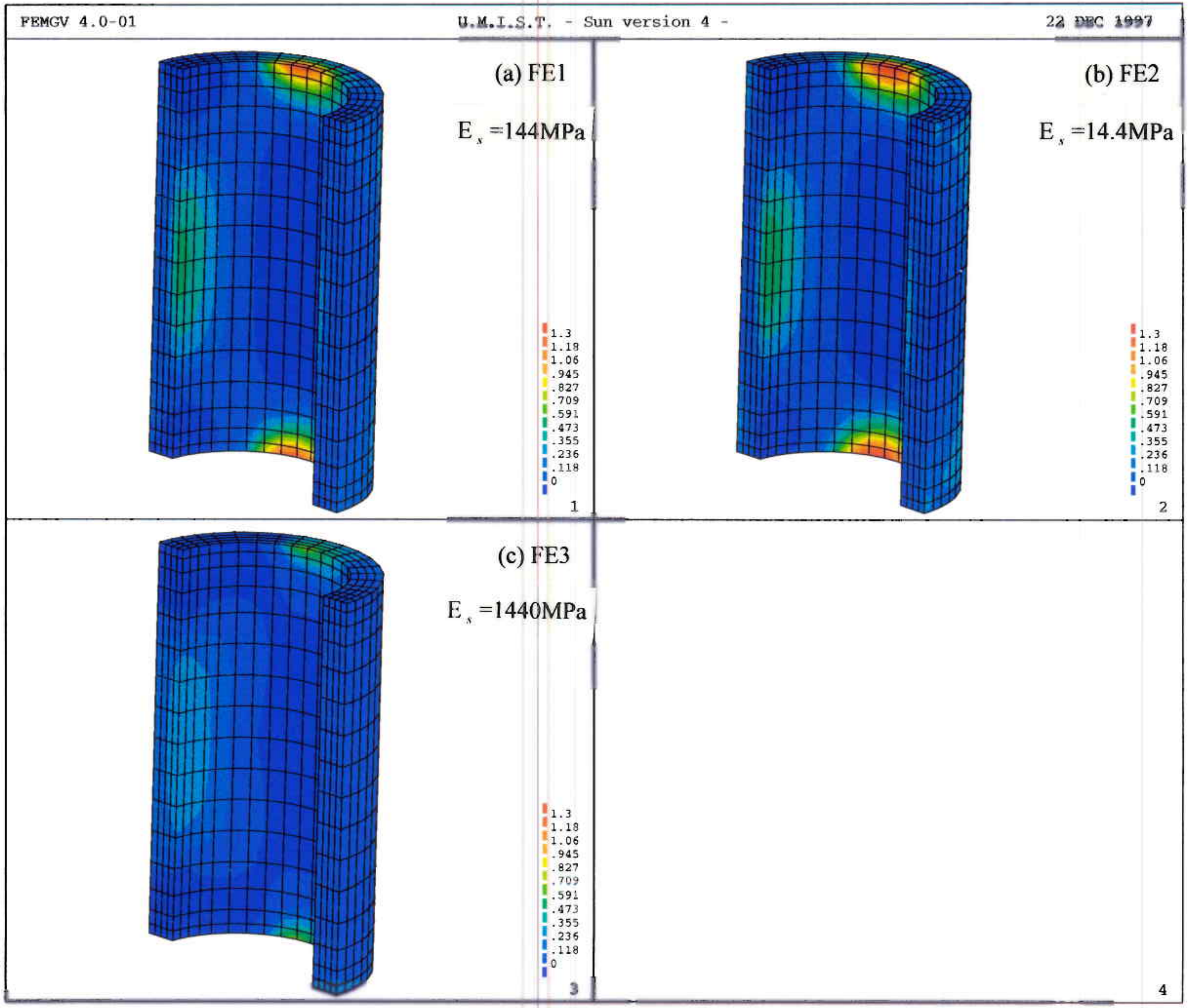

Figure 5.11 Normalized most tensile principal stresses in the pipe under ‘edge’ loading with interface

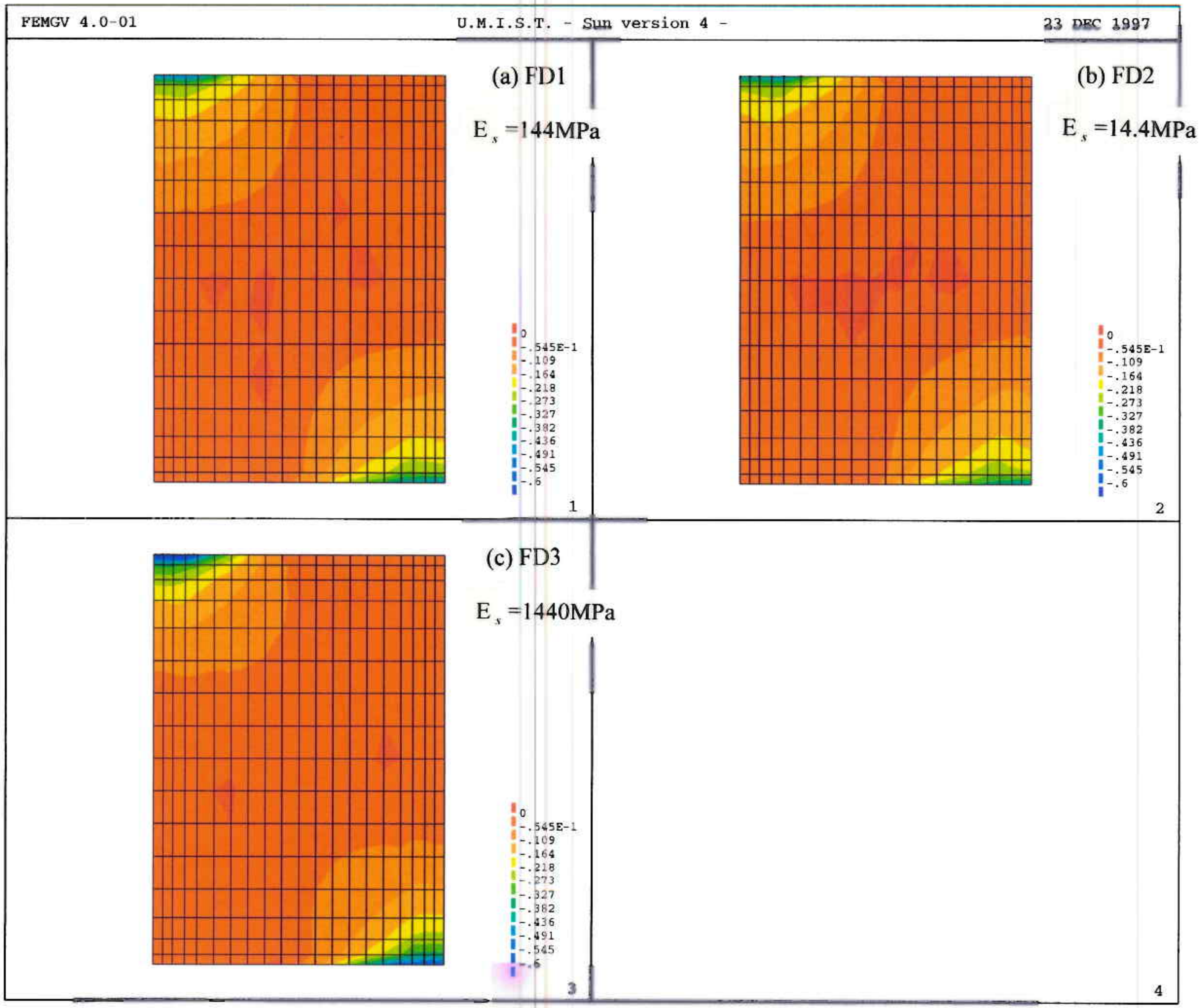

Figure 5.12 Normalized normal stresses on the unfolded interface under ‘diagonal’ loading

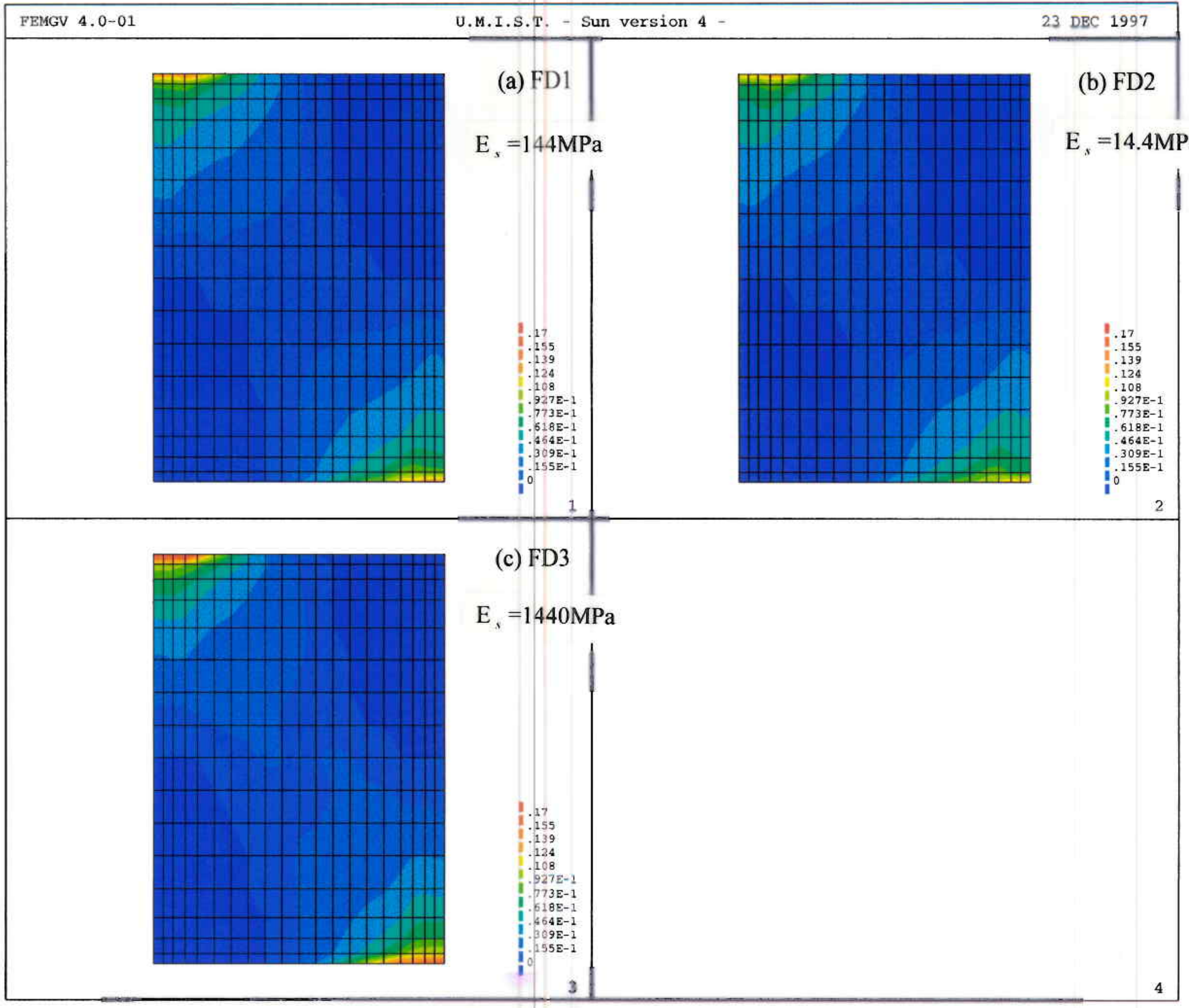

Figure 5.13 Normalized shear stresses on the unfolded interface under 'diagonal' loading

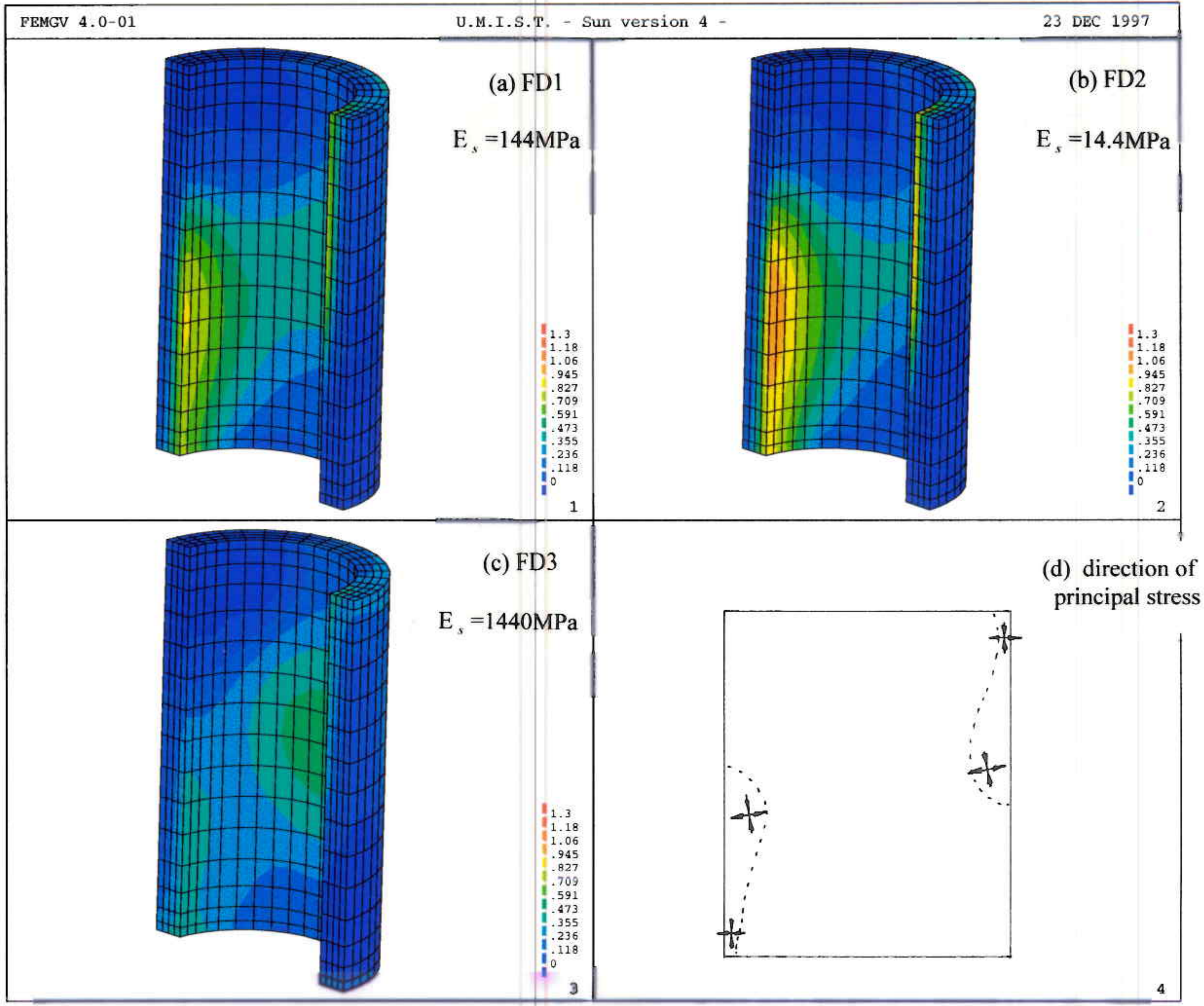

Figure 5.14 Normalized most tensile principal stresses in the pipe under 'diagonal' loading with interface

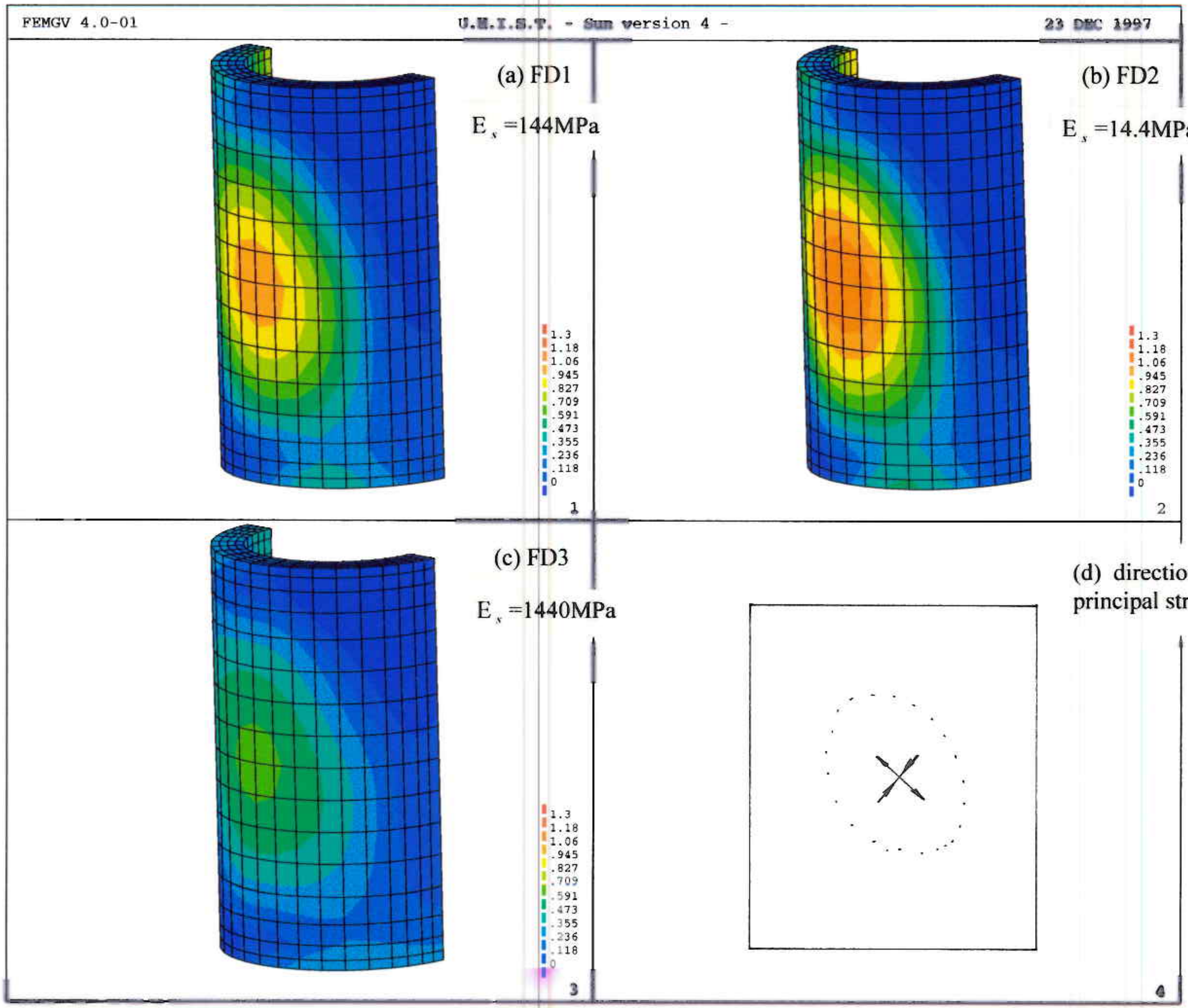

Figure 5.15 Normalized most tensile principal stresses in the pipe under 'diagonal' loading with interface by looking from opposite direction

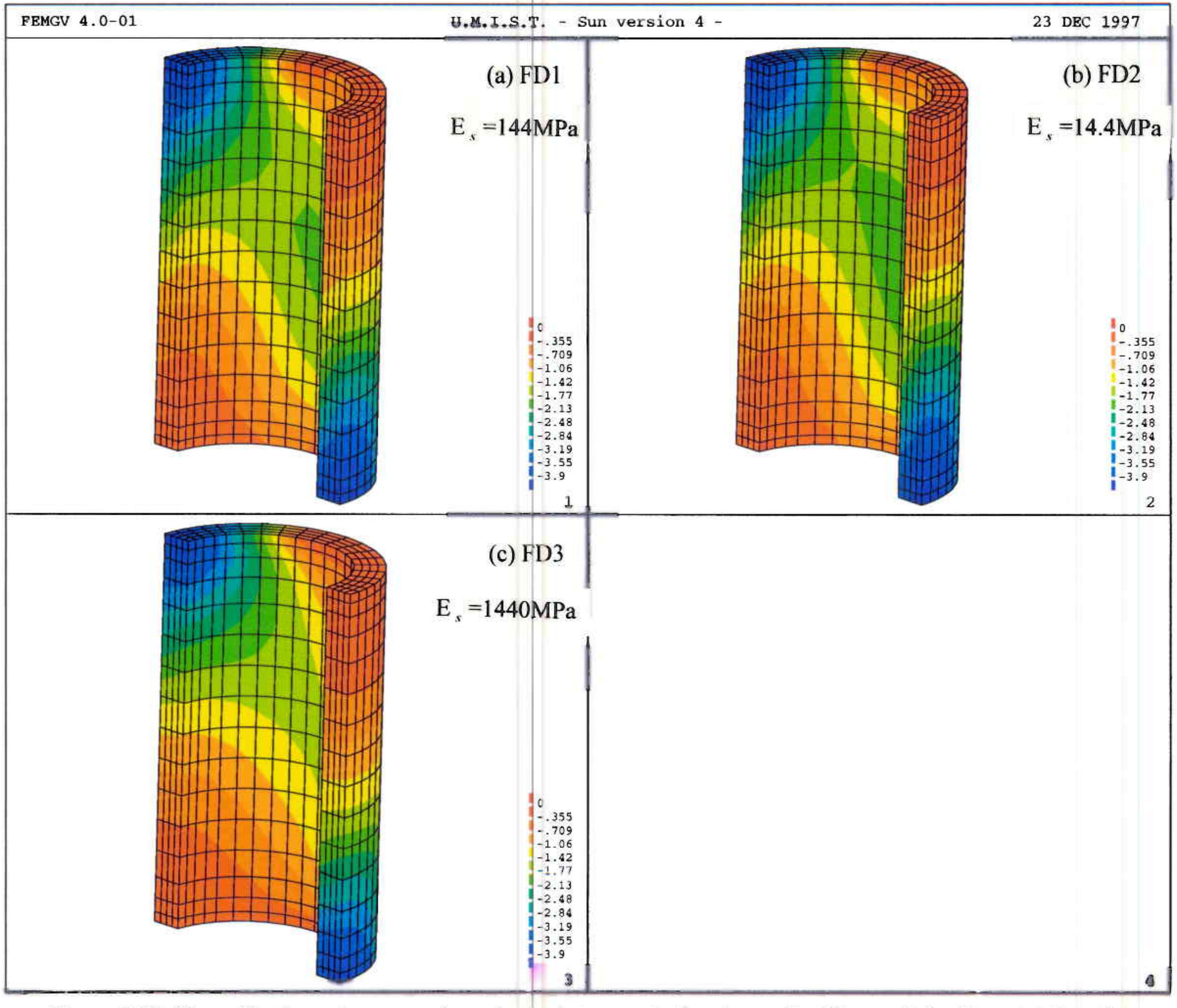

Figure 5.16 Normalized most compressive principal stresses in the pipe under 'diagonal' loading with interface

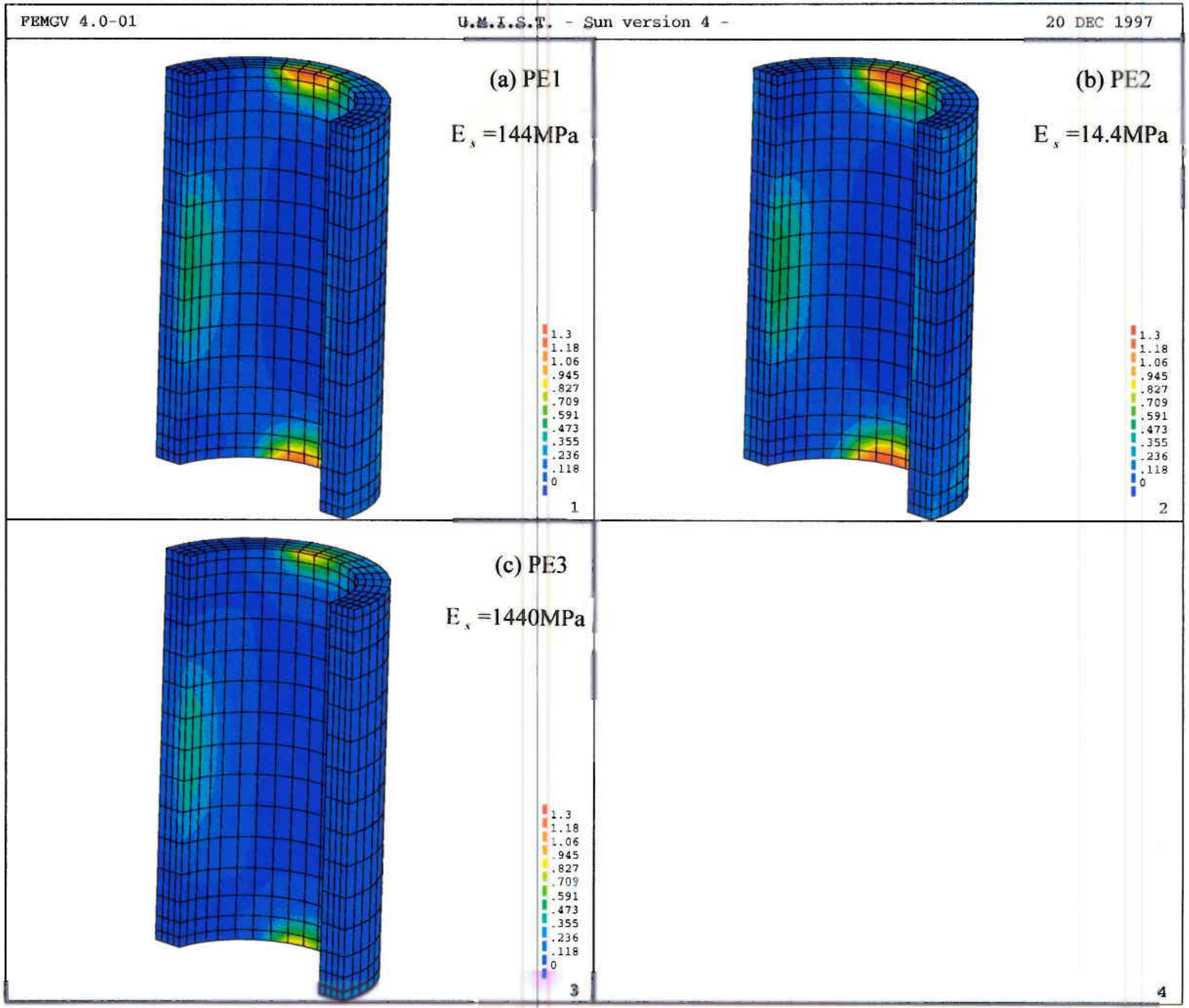

Figure 5.17 Normalized most tensile principal stresses in the pipe under ‘edge’ loading with plastic soil

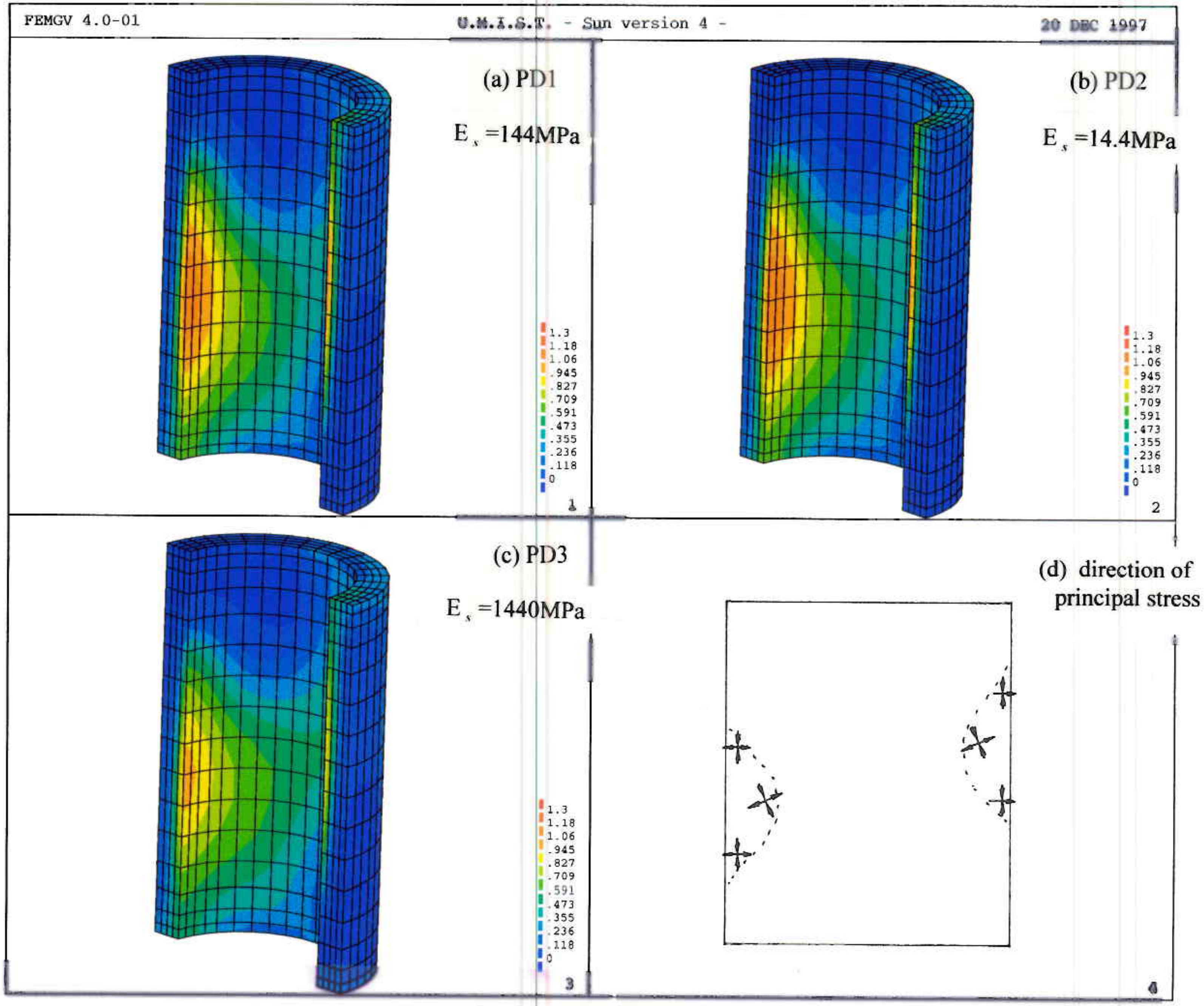

Figure 5.18 Normalized most tensile principal stresses in the pipe under 'diagonal' loading with plastic soil

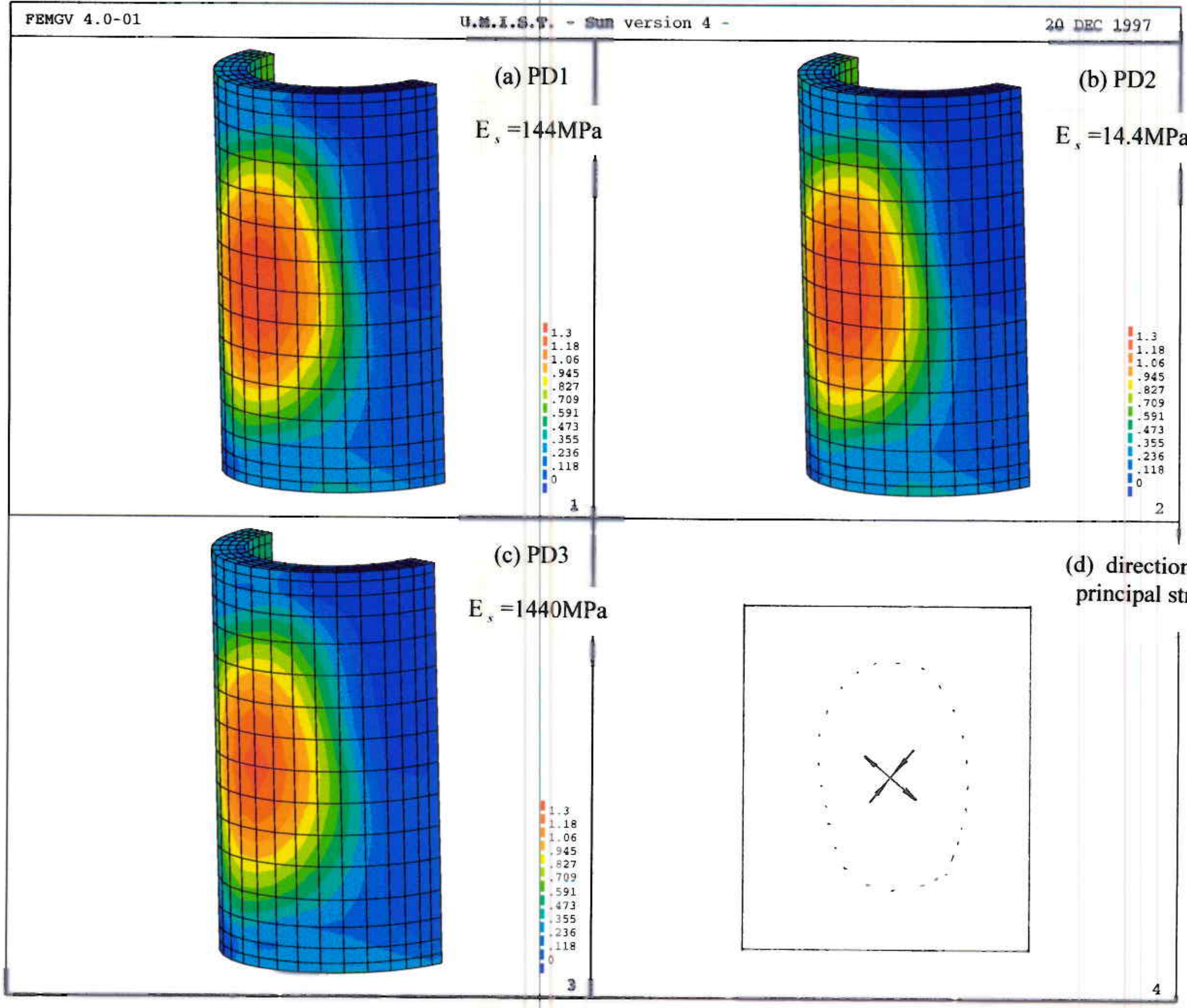

Figure 5.19 Normalized most tensile principal stresses in the pipe under 'diagonal' loading with plastic soil by looking from opposite direction

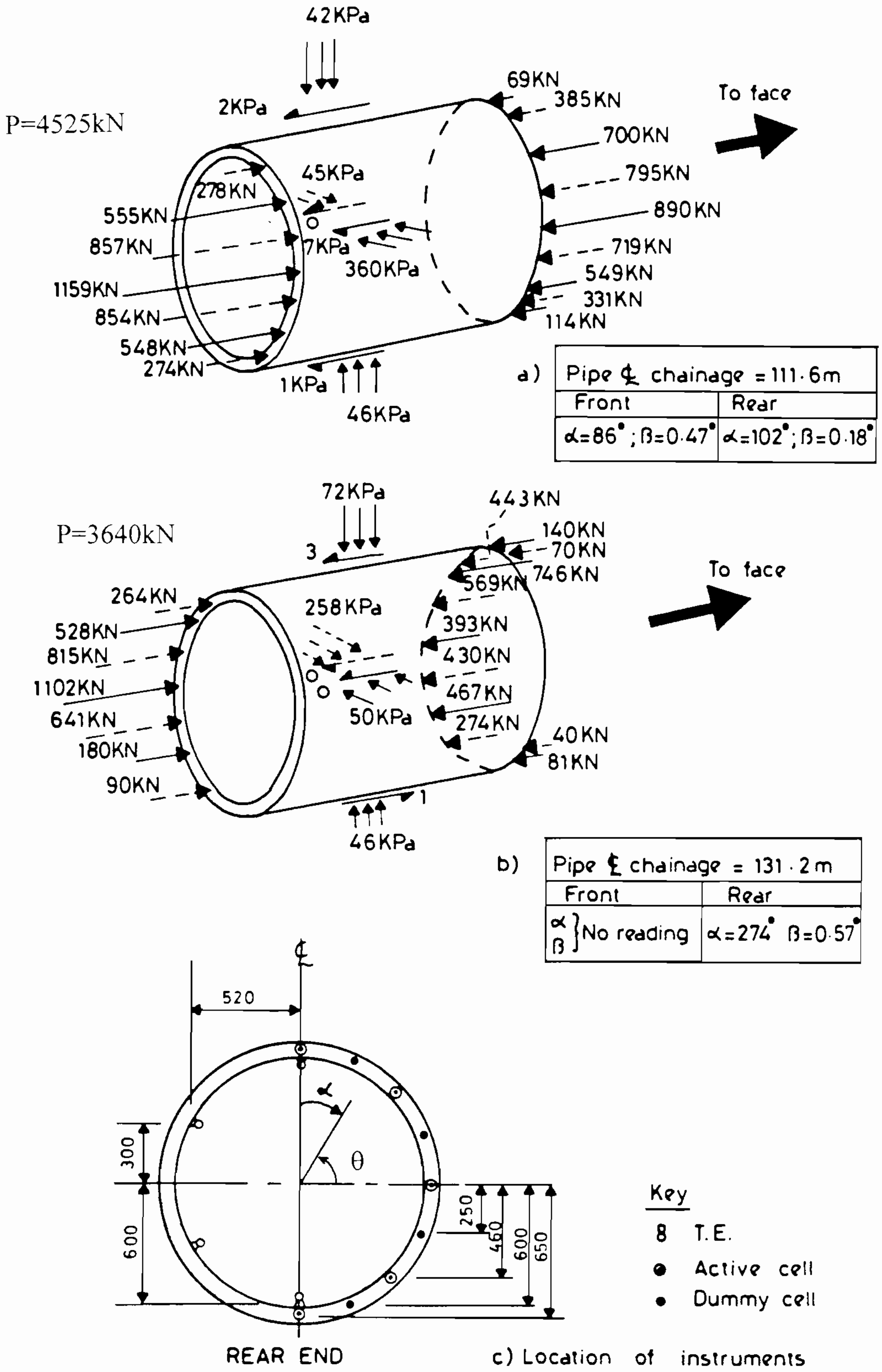

Figure 5.20 Measured load distribution at pipe joint (from Norris 1992)

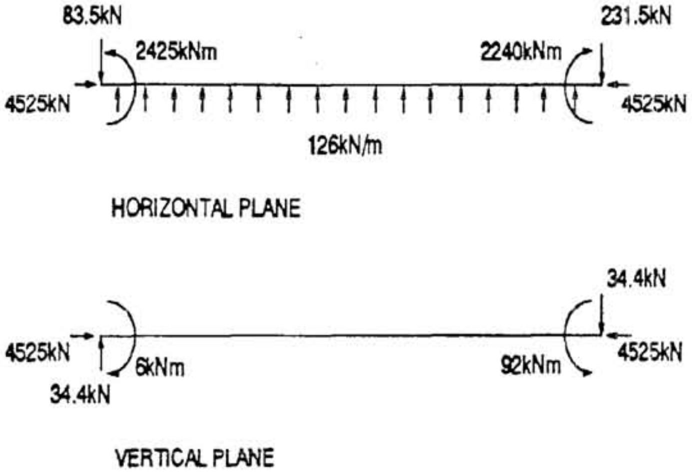

(a) BA1

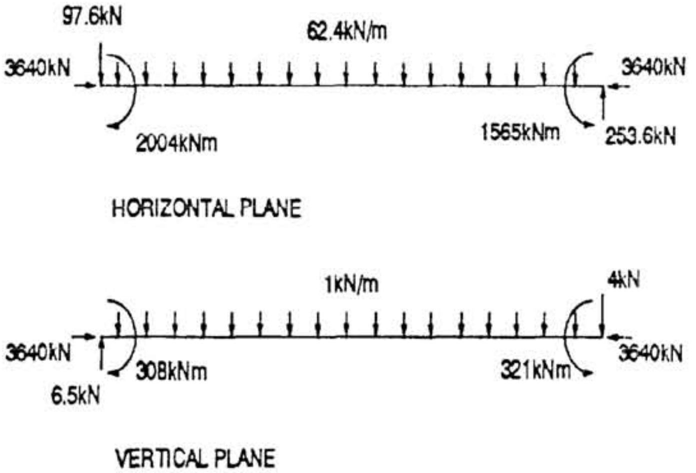

(b) BA2

Figure 5.21 Stocky column model (from Norris 1992)

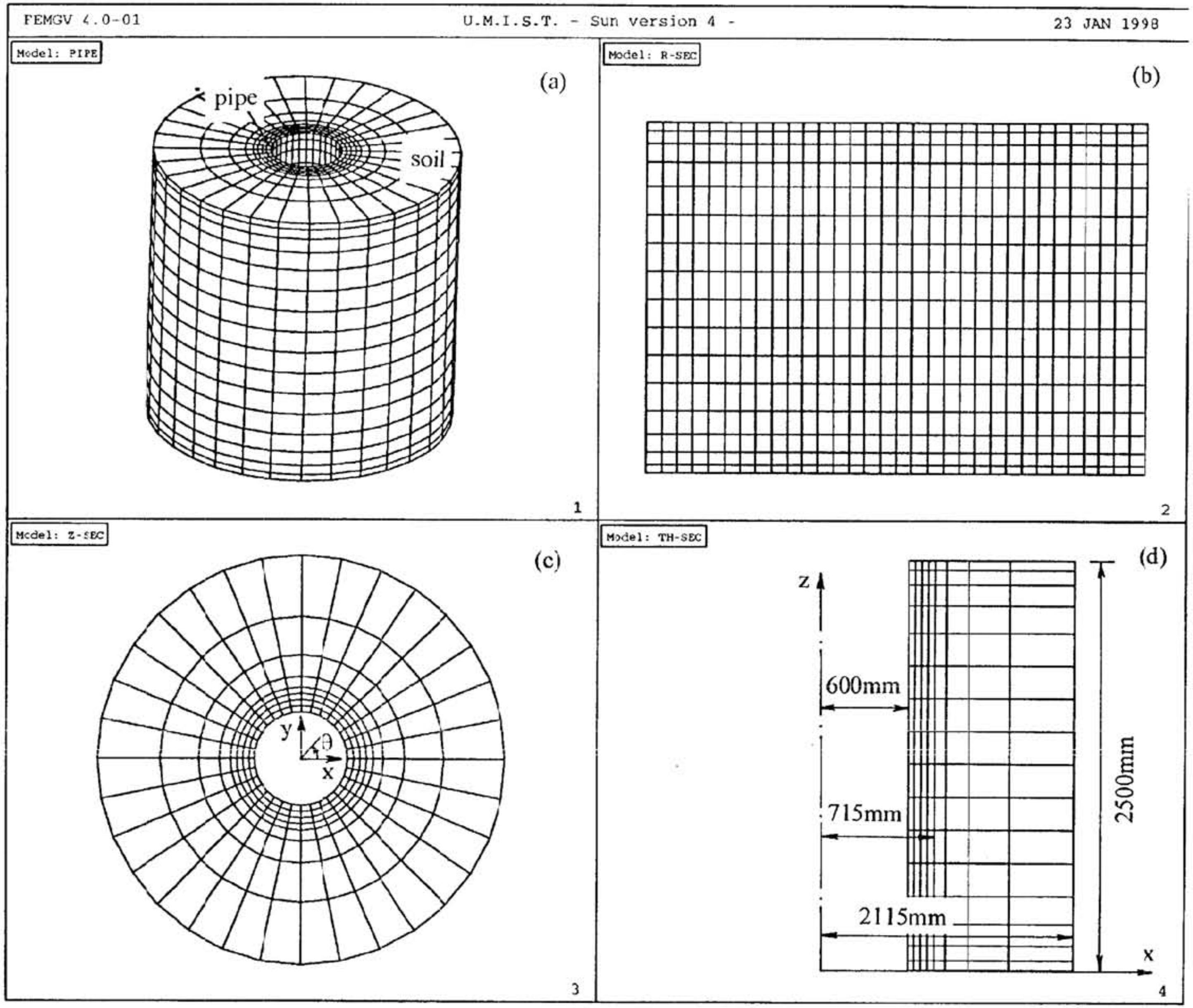

Figure 5.22 FE mesh of numerical model B for back analysis

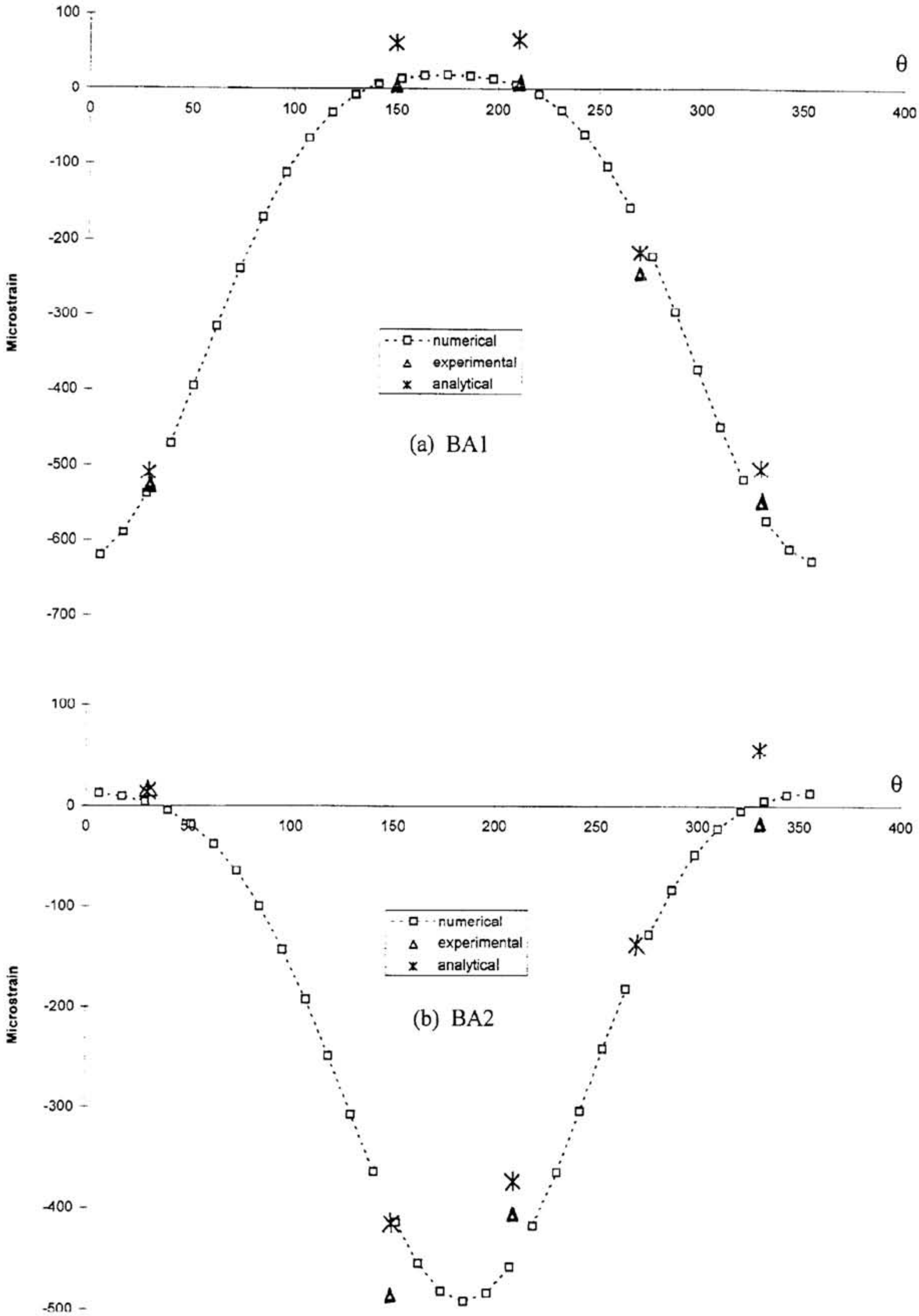

Figure 5.23 Comparison between numerical results, experimental data and analytical results

CHAPTER 6 THREE-DIMENSIONAL ANALYSIS -- NUMERICAL MODEL C

6.1 INTRODUCTION

This chapter describes the analysis using numerical model C, a symmetric three-pipe system (defined in Section 6.2). From the study of the results from numerical models A and B in Chapters 4 and 5, it is known that the non-uniform distribution of the load at the pipe joint induces not only concentrated compressive stresses, but also high tensile stresses in the concrete pipe. In fact, once the load distribution on the pipe ends is known, it is easy to obtain the stresses within the concrete pipe by using the numerical model B described in Chapter 5 and the results can then be used to estimate the safety of the jacking pipe in practice. To obtain load distributions at the pipe joint with a misalignment of the pipeline during pipe jacking, the analyses were carried out with numerical model C and the results from this model are examined in this chapter. To extend the two-dimensional work and to verify the conclusions from the two-dimensional model, similar aspects were investigated using the numerical model C under full three-dimensional conditions.

Again, the concrete pipe, the surrounding soil and the packing material are all treated as linearly elastic throughout this chapter. The material constants for the concrete pipe and the soil are the same as those used in Chapter 5, that is, a Young's modulus E_c = 40000MPa and a Poisson's ratio μ_c = 0.2 for the concrete pipe, and a Young's modulus E_s = 144MPa and a Poisson's ratio μ_s = 0.2 for the soil. Similar material constants of packing material used in Chapter 3 are adopted here to study the influence of the properties of the packing material.

In this chapter, the numerical model C is described in Section 6.2. The effect of the properties of the packing material and the effect of the pipeline misalignment are discussed in Sections 6.3 and 6.4 respectively. Finally, the conclusion is given in Section 6.5.

6.2 NUMERICAL MODEL C

One common misalignment of the pipeline is caused by gradual changes in direction of the pipeline as shown in Figure 6.1. For simplicity, it is assumed that the jacking force on the left end and the reaction force on the right end are symmetrical about the plane $z = 0$ and that the misalignment angles β_1 and β_2 have the same value. So it is simplified as a symmetrical problem about the plane $z = 0$ (it should be pointed out here that similar symmetries have been applied in the numerical model A and B for the 'edge' loading condition in Chapters 4 and 5). To model this simplified problem, numerical model C is established as shown in Figure 6.2. The model consists of a half pipe with its surrounding soil at the bottom, a complete pipe on the top and a packing material between the two pipes. The soil is included to avoid any local effect of constraints as discussed in Chapter 4. The dimensions of the model are also shown in the figure. For numerical convenience, there was just one interface used between the packing material and the bottom pipe in analysis. Furthermore, the geometry of the domain and the loads are also symmetric about the plane $y = 0$, so just a quarter of the problem was used in the analysis.

The three-dimensional finite element mesh of the numerical model C used in the analysis is shown in Figure 6.3(a); the unfolded surface of $r = 600$mm is in Figure 6.3(b); the section of $z = 0$mm is in Figure 6.3(c) and the section of $\theta = 0^{\circ}$ is in Figure 6.3(d). For the boundary conditions in the numerical analysis, the nodes on the outer surface of the soil mesh were all fixed in both x and y directions, while the nodes on the plane $z = 0$ were fixed in the z direction and the nodes on the plane $y = 0$ were fixed in the y direction due to the symmetrical condition. The main element type used in the analysis was the 8-node hexahedron, while quadrilateral interface elements were used between the packing material and the bottom pipe. In the analysis, the misalignment angle β of the pipe line was simulated by giving an equivalent displacement δ in x direction at the upper end of the top pipe as shown in Figure 6.2. Equivalence means that if the displacement at the centre of the bottom end of the top pipe is zero, the displacement δ in the x direction at the upper end will produce the same rotation angle β (that is, $\tan\beta = \delta / L$, where L is the pipe length). The applied jacking force was assumed uniformly distributed over the upper pipe end with a load intensity q = 10MPa as shown in Figure 6.2. For numerical convenience, the analysis was carried out in two stages. At first, 20% of the total load was applied without rotation of the top pipe, then the other 80% of the total load and the rotation of the top pipe were applied simultaneously. The stresses in the contours of this chapter are all normalized with respect to q = 10MPa.

Similar to the analysis described in Chapter 3, the interaction between the bottom pipe and the packing material was modelled by an elastic perfectly-frictional Mohr-Coulomb model described in Chapter 2 with the normal stiffness K_n = 800MPa /mm, the shear stiffness K_s = 400MPa/mm, the frictional angle $\phi = 20^0$, the dilation angle $\psi = 20^0$ and the cohesion parameter c = 0.05MPa.

6.3 EFFECT OF THE PROPERTIES OF THE PACKING MATERIAL

In this section, the effect of the properties of the packing material, the shear modulus and the Poisson's ratio of the packing material, is investigated. In the analysis, the packing material was linearly elastic with two different shear moduli G_p = 300MPa and 900MPa simulating soft and stiff packing materials, and with different Poisson's ratios μ_p = 0.1, 0.4 and -0.3 representing low, high and negative Poisson's ratio respectively as in Chapter 3. The applied displacement in the x direction at the upper end of the top pipe was δ = 3.93mm which is equivalent to a rotation angle $\beta = 0.09^0$ of the top pipe.

The solution procedure used in the analysis was the initial stiffness method described in Chapter 2. There was just one step in the first calculation stage with 20% applied load since the interface was elastic. In the second calculation stage there are 250 and 300 steps in the case G_p = 300MPa and 900MPa respectively and there were several iterations within each step depending on solution convergence.

6.3.1 EFFECT OF THE POISSON'S RATIO

The analysis of the effect of the Poisson's ratio of the packing material was carried out with the shear modulus G_p = 300MPa corresponding to a soft packing material and three different Poisson's ratios μ_p = 0.1, 0.4 and -0.3.

The normalized normal stresses on the interface are shown in Figures 6.4(a), 6.4(b) and 6.4(c) for the case of μ_p = 0.1, 0.4 and -0.3 respectively. From the figure, it is clear that in the case of μ_p = 0.1 and μ_p = -0.3 the stress distribution patterns are very similar showing an almost linear distribution with x. In the case of μ_p = 0.4, the normal stresses have a similar linear distribution when $\theta > 120^0$, while in the region $\theta < 120^0$ the stresses have lower magnitudes at the two sides r=600mm and r=715mm and a higher magnitude at the middle on the line x = constant. In general, the stresses are zero (or almost zero) in the region of x = -715mm, and the stress magnitudes increase with x and reach their peak values at x = 715mm. (Note: The higher stress magnitude in the case of μ_p = 0.4 is possibly due to the higher stiffness of the packing material since $E_p = 2\ G_p\ (\ 1 + \mu_p\ )$, however, the different distribution pattern in the case of μ_p = 0.4 is mainly due to the high Poisson's ratio because the distribution patterns are similar in the case of μ_p = 0.1 and μ_p = -0.3 without the influence of the stiffness of the packing material.)

The normalized shear stresses on the interface are shown in Figure 6.5(a), 6.5(b) and 6.5(c) for the cases μ_p = 0.1, 0.4 and -0.3 respectively. The figure shows that the distribution patterns of the shear stresses are more complicated than those of the normal stresses. In the case of μ_p = 0.1, the stresses increase when θ decreases in the region of

$\theta > 110^0$; and in the region of $\theta < 70^0$, the stresses increase with θ on the line r = constant and increase with r on the line θ = constant. The high stresses are located in the region of $\theta = 90^0$. In the case with negative Poisson's ratio ($\mu_p = -0.3$), the stresses have a similar distribution pattern as that in the case of $\mu_p = 0.1$ except in the region of $\theta < 70^0$ where the stresses reduce when r increases on the line θ = constant. In the case of $\mu_p = 0.4$, the stresses almost increase linearly with x in the region of $\theta > 110^0$; and in the region of $\theta < 110^0$, the stresses are higher on the two sides especially on the outer side (r = 715mm). The peak stresses are similar in the case of $\mu_p = 0.1$ and -0.3, and much higher in the case of $\mu_p = 0.4$. (Note: With $E_p = 2\ G_p(\ 1 + \mu_p\ )$, the difference of the stiffness between the case of $\mu_p = -0.3$ and $\mu_p = 0.1$ is larger than that between the case of $\mu_p = 0.4$ and $\mu_p = 0.1$. However, the shear stresses in the case of $\mu_p = -0.3$ and $\mu_p = 0.1$ are similar and quite different from those in the case of $\mu_p = 0.4$. This means that the difference is due to the influence of the high Poisson's ratio of the packing material.)

After the discussion about the stresses on the interface, the stresses within the concrete pipes are examined. In order to avoid the average effect of the stresses from packing materials and the interface and to obtain a better view of the stress contours, the packing material and the interface are removed in the stress contours of the concrete pipes throughout this chapter.

The normalized most tensile principal stresses in the concrete pipes are shown in Figure 6.6(a), 6.6(b) and 6.6(c) for the cases of $\mu_p = 0.1$, 0.4 and -0.3 respectively. The figure shows that in all three cases the stress distribution patterns are similar to some extent. The high tensile stresses are mainly within the top pipe at the top right and bottom left corners and in the region of $\theta = 90^0$ on the upper end except in the case $\mu_p = 0.4$ where the high tensile stresses also exist at the joints of both pipes in the region $\theta = 0^0$. The peak values are similar in all three cases with the highest stress in the case of $\mu_p = 0.4$. The tensile stresses in these high stress regions are mainly in the hoop direction in all three cases as shown in

Figure 6.6(d). (The tensile stresses on the upper end of the top pipe are due to the given displacements on that end, which are used to produce the misalignment needed to examine the behaviour of the pipe joint and the bottom pipe and might deviate from the loading and constraint conditions on this pipe end in practice. However, the effort in this Chapter is placed on the pipe joint and the bottom pipe.)

The normalized most compressive stresses in the pipes are shown in Figure 6.7. It is clear from the figure that the stress distributions are similar in all three cases. In the bottom pipe, the stresses are almost zero in the region of $\theta = 180^0$ and the stress magnitudes increase when θ decreases with its peak magnitude at $\theta = 0^0$. In the top pipe, the stresses are almost constant at the upper end with the magnitude of the applied load, while in the region of the pipe joint the stresses have similar patterns as those in the bottom pipe.

6.3.2 EFFECT OF THE SHEAR MODULUS

In this section, the effect of another property of the packing material, the shear modulus, is examined. Since a low shear modulus was used in the analysis of the effect of the Poisson's ratio of the packing material, a high shear modulus (G_p = 900MPa) was used in the analysis described in this section with the same three different Poisson's ratios μ_p = 0.1, 0.4 and -0.3. The results are compared with those in Section 6.3.1.

Again, the normalized stresses on the interface are discussed first. The normalized normal stresses in case μ_p = 0.1, 0.4 and -0.3 are now shown in Figure 6.8(a), 6.8(b) and 6.8(c) respectively. The figure shows that the stress patterns are very similar to those with the low shear modulus G_p = 300MPa except that the areas with zero stresses in the region $\theta = 180^0$ are larger than those with G_p = 300MPa and that the peak values are higher than those with G_p = 300MPa. The peak magnitudes of stress in all three cases are similar with the highest magnitude still in the case of $\mu_p = 0.4$.

The normalized shear stresses on the interface are given in Figure 6.9(a), 6.9(b) and 6.9(c) for the case μ_p = 0.1, 0.4 and -0.3. Again, the stresses in all three cases show similar distribution patterns to those with G_p = 300MPa except that the peak stresses increase in the case of μ_p = 0.1 and -0.3 and reduce in the case of μ_p = 0.4. However, the highest shear stress is still in the case of μ_p = 0.4. (Following the same argument in Section 6.3.1 for Figure 6.5, it is known that difference of the shear stresses on the interface is mainly due to the influence of the Poisson's ratio. The comparison of the results in Figures 6.5 and 6.9 suggests that the influence of the Poisson's ratio reduces when the shear modulus increases.)

Figure 6.10 shows the normalized most tensile principal stresses in the concrete pipes. Clearly, the stress distribution patterns are very similar to those with the low shear modulus as shown in Figure 6.6. The direction of the tensile stresses in all three cases is also mainly in the hoop direction as with G_p = 300MPa (refer to Section 6.3.1 and see Figure 6.6(d)). For the most compressive stresses in the pipes, the distribution patterns are very similar to those with G_p = 300MPa except that the peak magnitudes are just slightly higher (the stress contours are not included here to avoid repetition, refer to Section 6.3.1 and see Figure 6.7).

6.4 EFFECT OF THE PIPELINE MISALIGNMENT

In Section 6.3, the effect of the properties of the packing material have been studied. The effect of the misalignment of the pipe line is examined in this section. Again, in the analysis the soil and the packing material were treated as linearly elastic with the same material constants as in the Section 6.3. The applied misalignment angle of the pipe line was $\beta = 0.27^0$ which was simulated in the analysis by the equivalent given displacement of

δ = 11.78mm in the x direction at the upper end of the top pipe. The load, boundary conditions and the properties of the interface were unchanged.

The solution procedure used in this section is also the initial stiffness method described in Chapter 2. There was again one step in the first stage with 20% applied load. In the second calculating stage, the other 80% load and the rotation of $\beta = 0.27^0$ of the top pipe were applied and there were 400 and 500 steps in the case G_p = 300MPa and 900MPa respectively with several iterations within each step depending on convergence and controlled by the program.

6.4.1 ANALYSIS WITH SOFT PACKING MATERIAL

At first, the analysis was carried out with a soft packing material (G_p = 300MPa) and with the same three Poisson's ratios μ_p = 0.1, 0.4 and -0.3. The normalized normal stresses on the interface are given in Figure 6.11(a), 6.11(b) and 6.11(c). From the figure, it is clearly seen that the stress patterns are similar in all three cases. The stresses are zero in the region of $\theta > 100^0$ (the exact regions are slightly different in different cases as shown in the figure) and in general the stresses increase when θ reduces in the region of $\theta < 100^0$. The changes of the stresses across the thickness of the pipe are significant especially in the case of $\mu_p = 0.4$. The maximum values of the stress magnitudes are similar in all three cases but are much higher than those in Section 6.3.1 with $\beta = 0.09^0$ and the highest magnitude is in the case of $\mu_p = 0.4$.

Figure 6.12 shows the normalized shear stresses on the interface. Again, in all three cases there is a large area with zero stress in the region about $\theta > 100^0$ on the interface. This means that there is a big gap between the packing material and the bottom pipe in all three cases with this misalignment angle $\beta = 0.27^0$. High stresses in all three cases are located on the outer side of the cross section (r=715mm) with its centre in the region of $\theta=54^0$, 48^0 and 58^0 in the case of $\mu_p = 0.1$, 0.4 and -0.3 respectively. In general, the stresses reduce when away from the high stress centre except in the case of $\mu_p = 0.4$ where the high stresses also exist at the outer side of the cross section over all of the region of $\theta < 65^0$. The peak values of the stress are much higher than those with $\beta = 0.09^0$ in Section 6.3.1 and the highest stress is also in the case of $\mu_p = 0.4$.

The normalized most tensile stresses within the concrete pipes are shown in Figure 6.13(a), 6.13(b) and 6.13(c) for the three cases $\mu_p = 0.1$, 0.4 and -0.3. The stress patterns are similar in all three cases but quite different from those in Section 6.3.1 with $\beta = 0.09^0$ due to the big gap on the interface. The high stresses are now at the pipe joint of the bottom pipe with its centre in the region of $\theta = 90^0$ (in fact, the stress patterns in the bottom pipe are similar to those in Figure 5.3 in Chapter 5 since the bottom pipe is also under 'edge' loading condition). The stresses in other domains are small. The peak values of the stress are similar in all three cases but much higher than those with $\beta = 0.09^0$ in Section 6.3.1. The highest stress is still in the case of $\mu_p = 0.4$. The tensile stresses in the high stress region are mainly in the hoop direction in all three cases as shown in Figure 6.13(d).

Figure 6.14 gives the distributions of the normalized most compressive principal stresses within the concrete pipes. The stress patterns are similar in all three cases to some extent. In the bottom pipe, the stresses are almost zero in the region of $\theta > 90^0$ and the magnitude of the stress increases when θ reduces in the region of $\theta < 90^0$ with the peak magnitudes in the region of $\theta < 10^0$. In the top pipe, the stresses are almost constant at the upper end of the pipe with the magnitude of the applied load. In general, the stress magnitudes increase when θ reduces on a section z = constant. The peak stress magnitudes are similar in all three cases and are much higher that those with $\beta = 0.09^0$ as shown in Figure 6.7.

6.4.2 ANALYSIS WITH STIFF PACKING MATERIAL

This section describes the analysis with a stiff packing material ($G_p = 900MPa$) and with all other conditions unchanged as in Section 6.4.1. The normalized normal stresses on the interface are now shown in Figure 6.15. When comparing with Figure 6.11 in Section 6.4.1, it can be seen that the stress distributions on the interface are very similar apart from three small differences. The first difference is that the areas with zero stresses are slightly larger than with the soft packing material. The second difference is that the changes of the stresses across the pipe thickness are more significant than with the soft packing material. Finally, the peak stress values are higher and the difference of the peak stresses between different cases with different Poisson's ratio reduces.

Figure 6.16 shows the normalized shear stresses on the interface. To some extent, the stress patterns are similar to those with soft packing as shown in Figure 6.12. The areas with zero stresses are larger than with soft packing as discussed for the normal stresses. This means that the gaps between the packing material and the bottom pipe are wider. Now the high stresses in all three cases are located in the same region of $\theta = 46^0$ and the peak values are higher than with soft packing, especially in the case $\mu_p = 0.1$ and -0.3.

The normalized most tensile principal stresses within the concrete pipes are shown in Figure 6.17. From the figure, it is clear that the stress distribution patterns are similar to those with soft packing material as shown in Figure 6.13 except that the maximum values are higher than those with the soft packing material, especially in the case of $\mu_p = 0.1$ and -0.3. The tensile stresses in the high stress regions are also in the hoop direction as with the soft packer (see Figure 6.13(d)). As for the most compressive principal stresses in the concrete pipes, the stress patterns and the peak stress magnitudes in all three cases are almost same as those with the soft packing material and are not discussed here in detail (refer to Section 6.4.1 and see Figure 6.14).

6.5 CONCLUSION

The numerical results from the analysis with numerical model C show that the misalignment of the pipeline induces not only high normal stresses but also high shear stresses at the pipe joint which in turn produce high concentrated compressive stresses and high tensile stresses in the jacking concrete pipes. The results from the analysis have given a good understanding about the effect of the misalignment of the pipeline and of the properties of the packing material. The two-dimensional analysis described in Chapter 3 has also shown a similar effect of the properties of the packing material and the effect of the misalignment. However, the three-dimensional results in this chapter give a clearer picture and better understanding about these aspects and also provide some new aspects which the two-dimensional model cannot take into account, for example, the distribution of the shear stresses at the pipe joint.

In general, the normal stresses on the interface increase with x since the misalignment rotation is about the y axis. However, the shear stress patterns on the interface are very complicated and the high stress centre is usually located on the outer side of the pipe thickness at the mid-way between the edge of the open gap and the right end ($\theta = 0^0$). The results also show that the high stresses are mainly at the pipe joint of the bottom pipe with the high applied misalignment angle. The stress distribution patterns in the bottom pipe are very similar to those in Chapter 5 under the 'edge' loading condition since the bottom pipe is assumed to be under a symmetrical loading condition, and this confirms that once the stresses at the pipe joint are known the numerical model B in Chapter 5 can be used to calculate the stresses in the concrete pipe.

From the results of numerical model C in this chapter, a few conclusions are drawn out as following:

(1) The dominating factor inducing high concentrated stresses in the concrete pipes is the misalignment angle of the pipeline, especially with the high rotation angle where the stress concentrations are enhanced due to the separation between the packing material and the concrete pipe. So the good control of this misalignment angle is critical in the practice of pipe jacking.

(2) Under the same condition, the packing material with high Poisson's ratio induces higher shear stresses on the interface and higher tensile stresses in the concrete pipe than that with low Poisson's ratio, while the material with a negative Poisson's ratio produces even better results although the difference between the low Poisson's ratio and the negative one is not significant. A negative Poisson's ratio is difficult to achieve, thus a good packing material should possess a very low Poisson's ratio. In practice, currently used packing materials, eg. chipboard and fibreboard have a Poisson's ratio close to zero.

(3) The high shear modulus also increases the stresses on the interface and in the pipe although not by a significant amount. This means that a good packing material should have a low shear modulus.

(4) In numerical model C, it means no packing material if the material constants of the packing material are same as those of the concrete pipe. Combining conclusion 2 and 3 above, it is clear that a good packing material will reduce the stresses in the concrete pipes.

(5) In the numerical model C, the bottom pipe is assumed under a symmetrical loading condition (or under an 'edge' loading condition). For more general loading conditions, a more complicated three-pipe model is needed in future research.

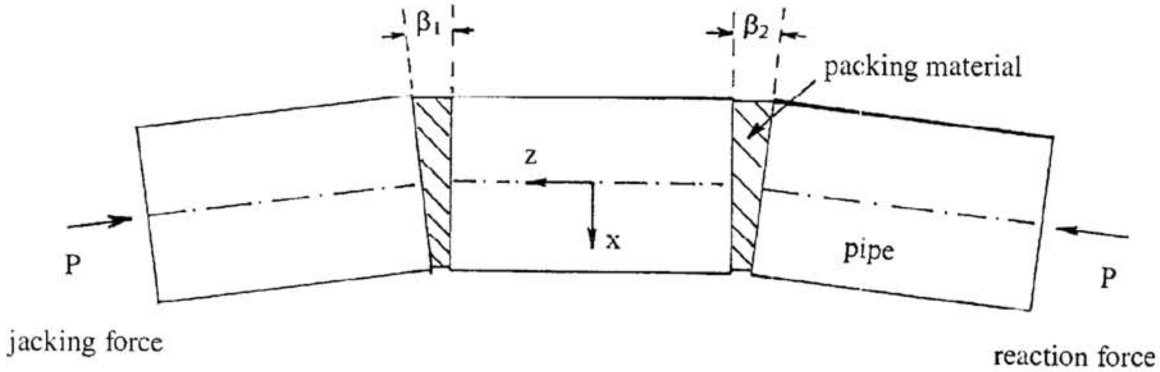

Figure 6.1 A common pipe line misalignment

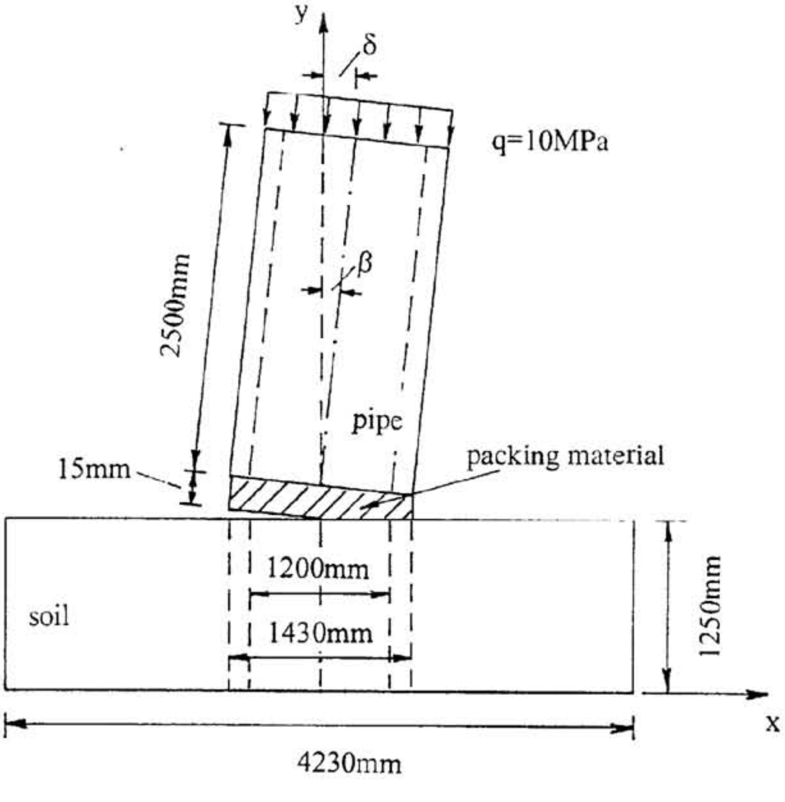

Figure 6.2 Numerical model C

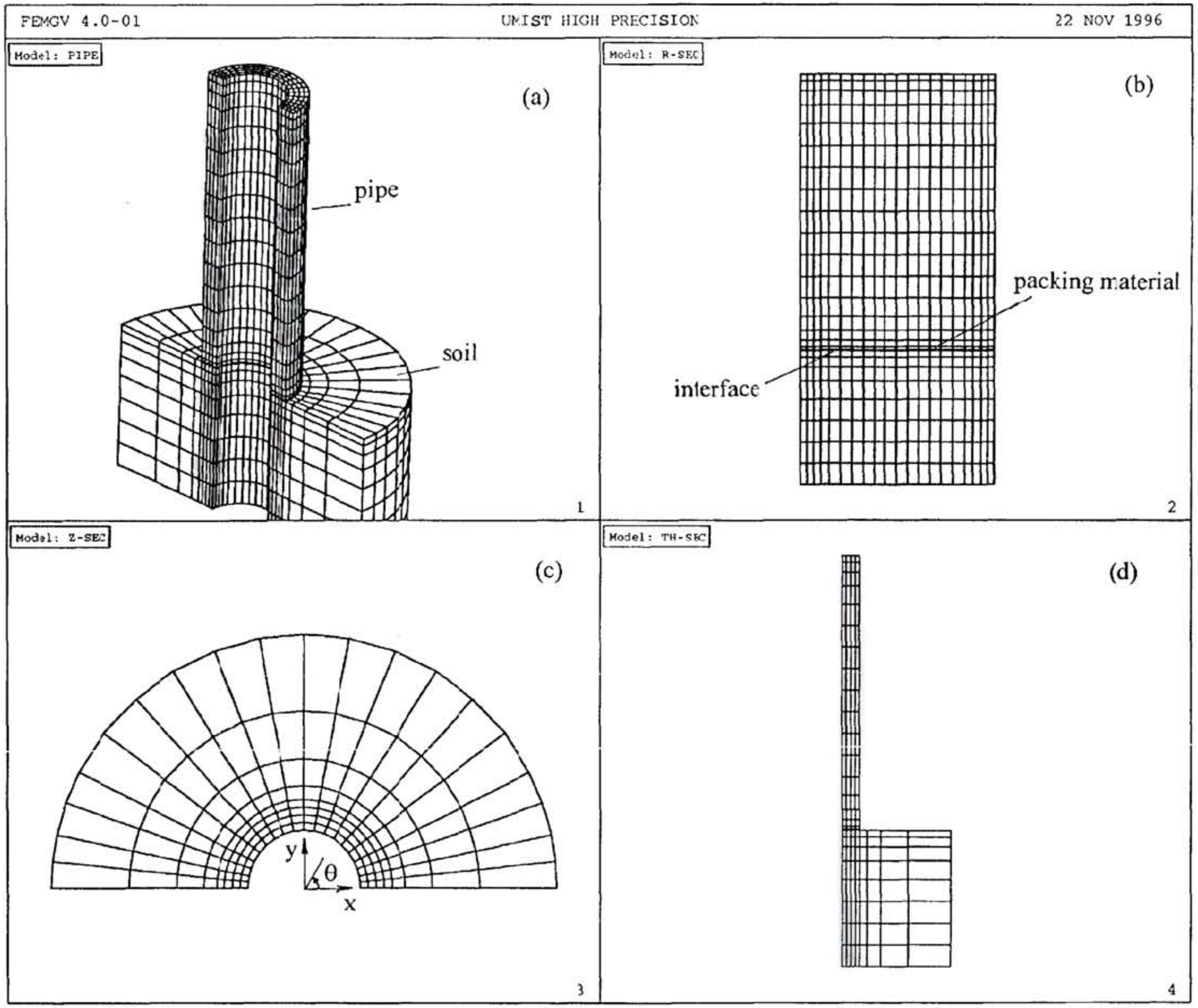

Figure 6.3 FE mesh of numerical model C

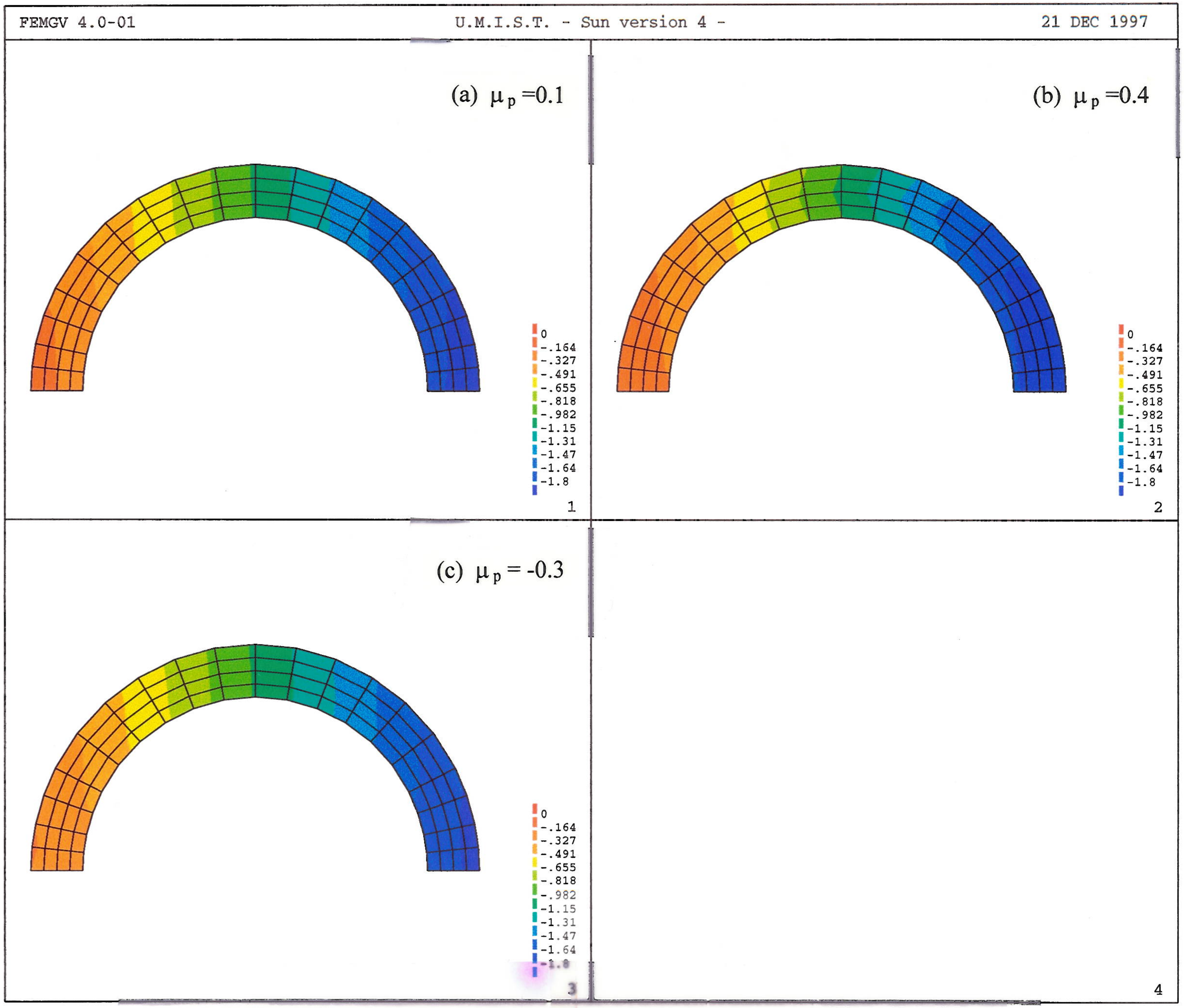

Figure 6.4 Normalized normal stresses on the interface with soft packing and $\beta=0.09^0$

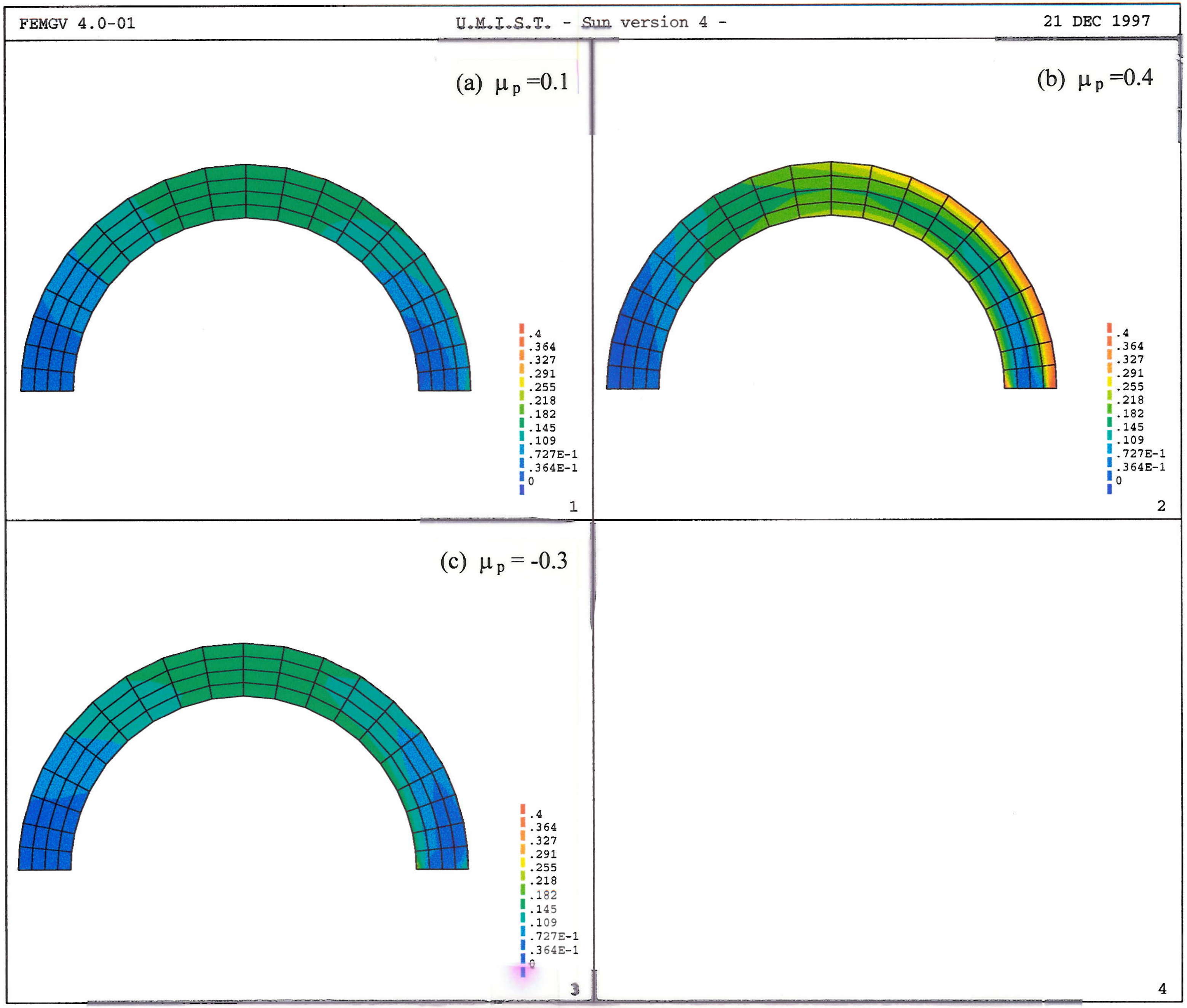

Figure 6.5 Normalized shear stresses on the interface with soft packing and β=0.09 ^{0}

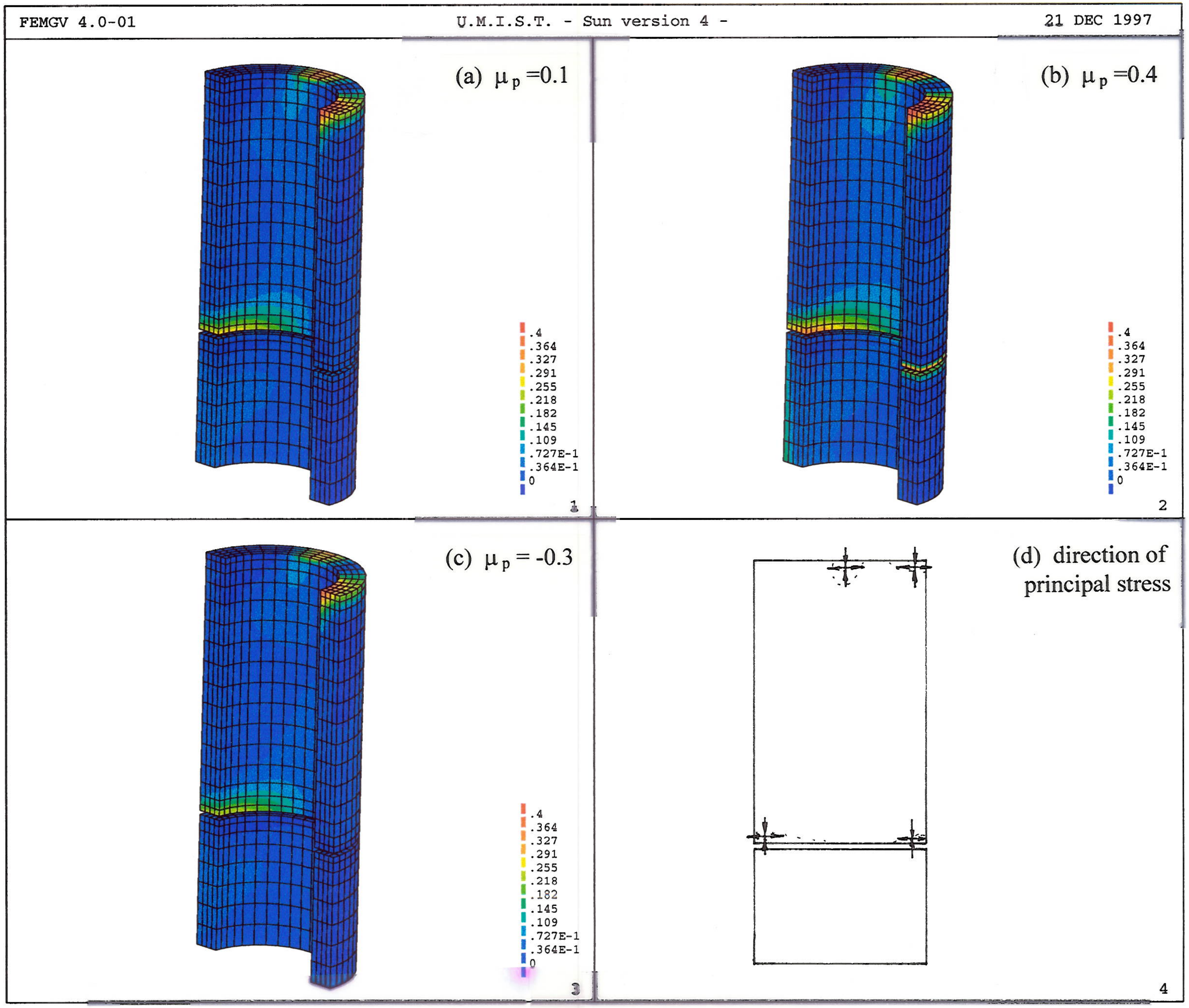

Figure 6.6 Normalized most tensile principal stresses in the pipes with soft packing and $\beta=0.09^0$

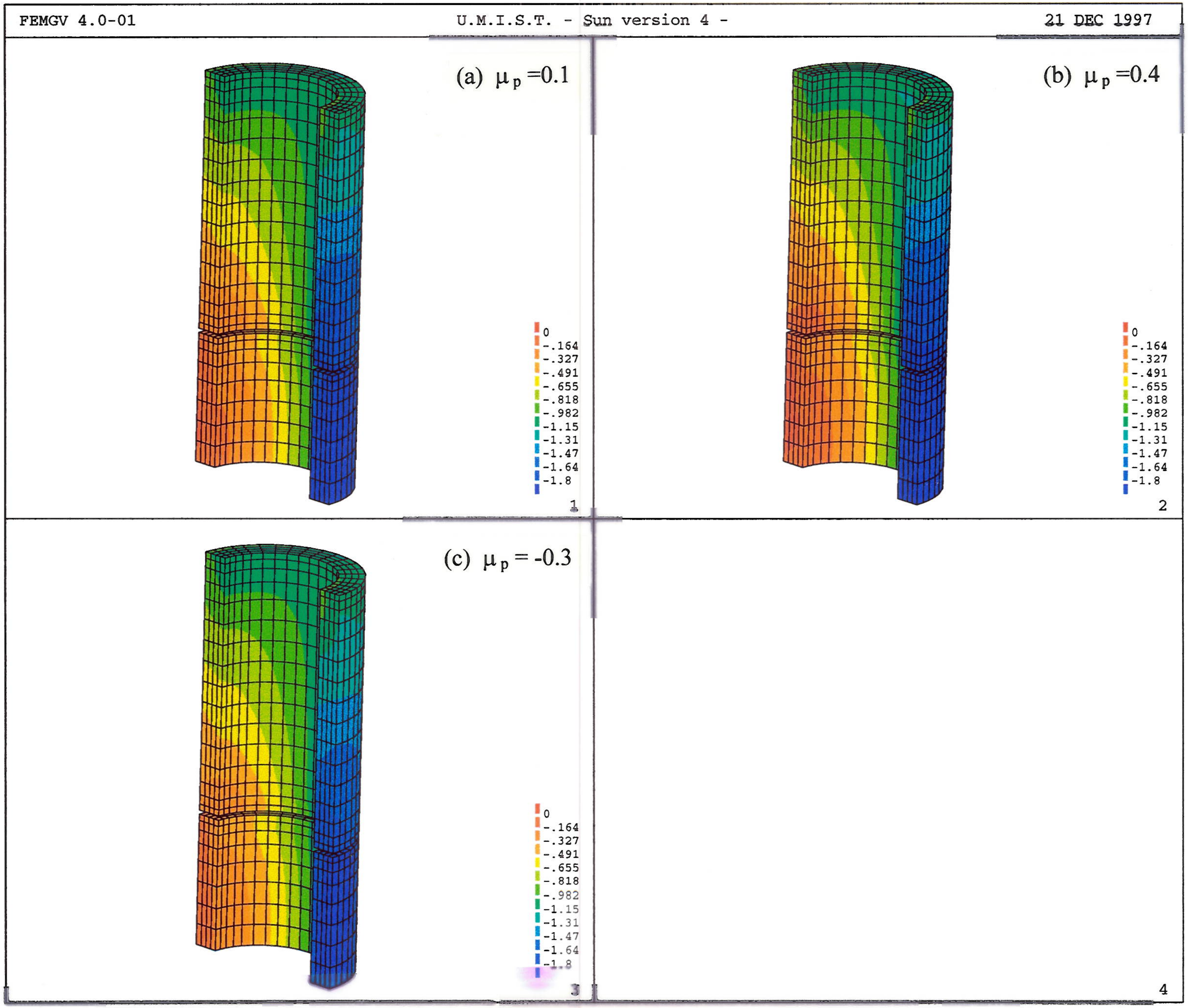

Figure 6.7 Normalized most compressive principal stresses in the pipes with soft packing and β=0.09^0

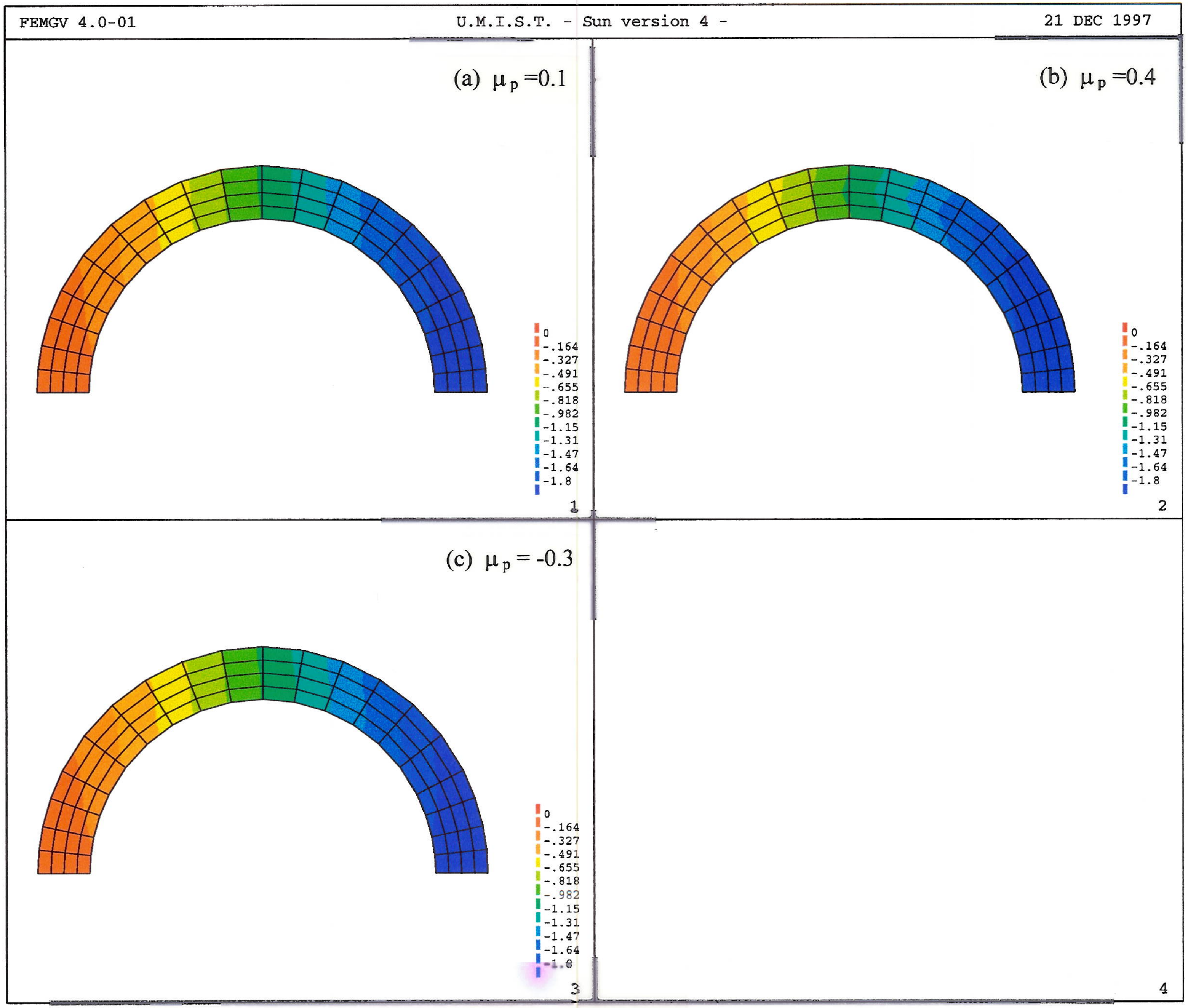

Figure 6.8 Normalized normal stresses on the interface with stiff packing and $\beta=0.09^0$

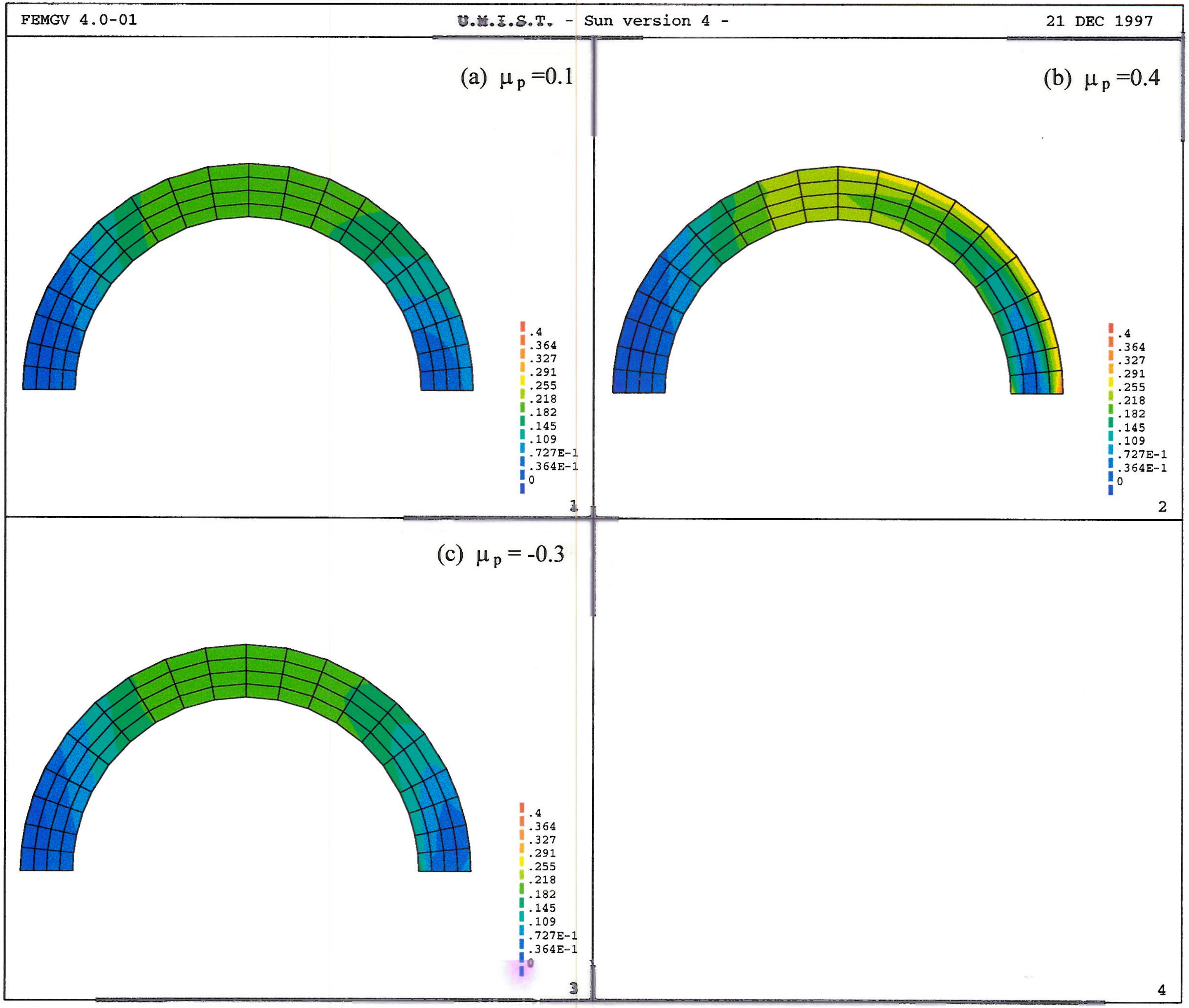

Figure 6.9 Normalized shear stresses on the interface with stiff packing and β=0.09 ^{0}

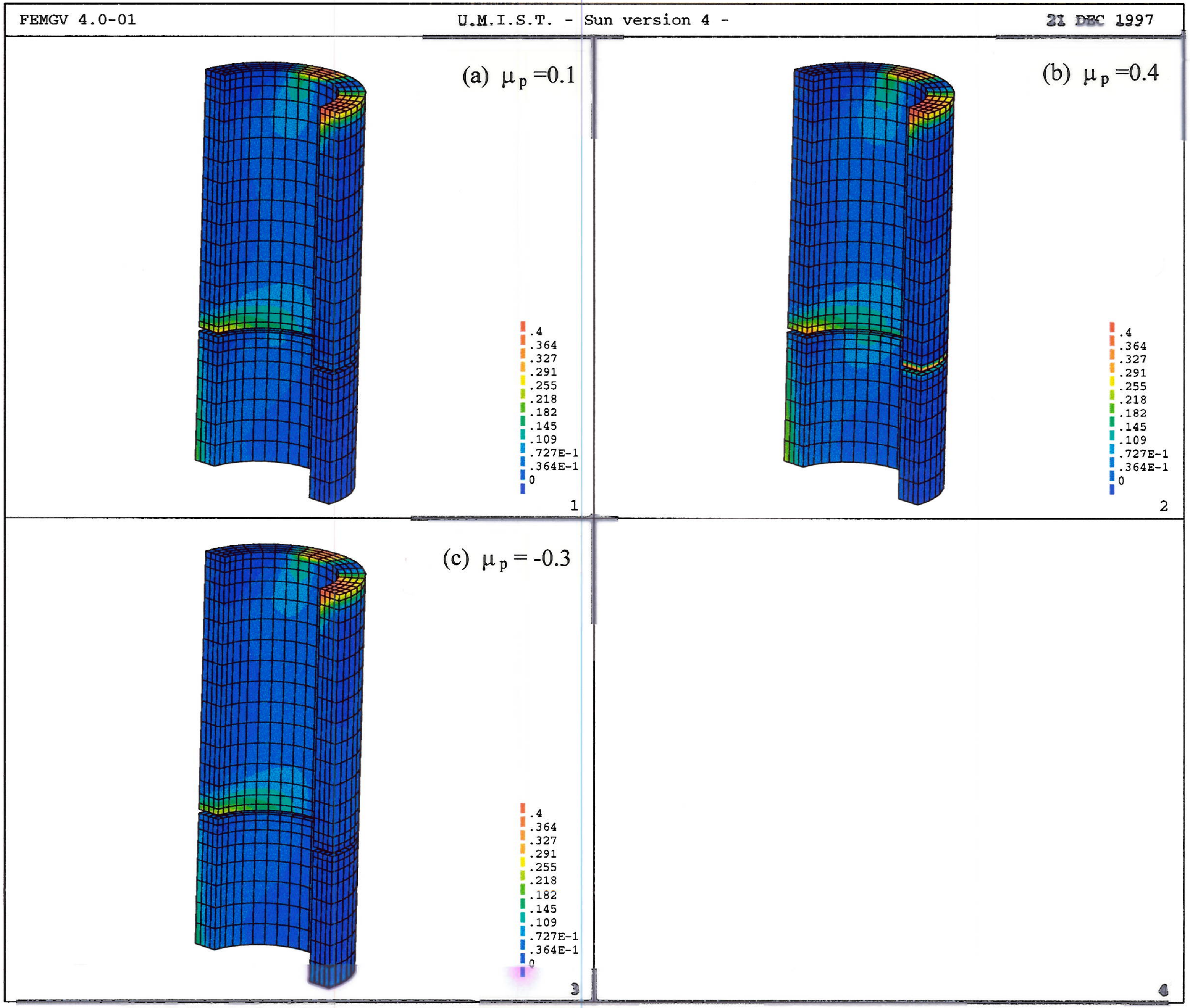

Figure 6.10 Normalized most tensile principal stresses in the pipes with stiff packing and $\beta=0.09^0$

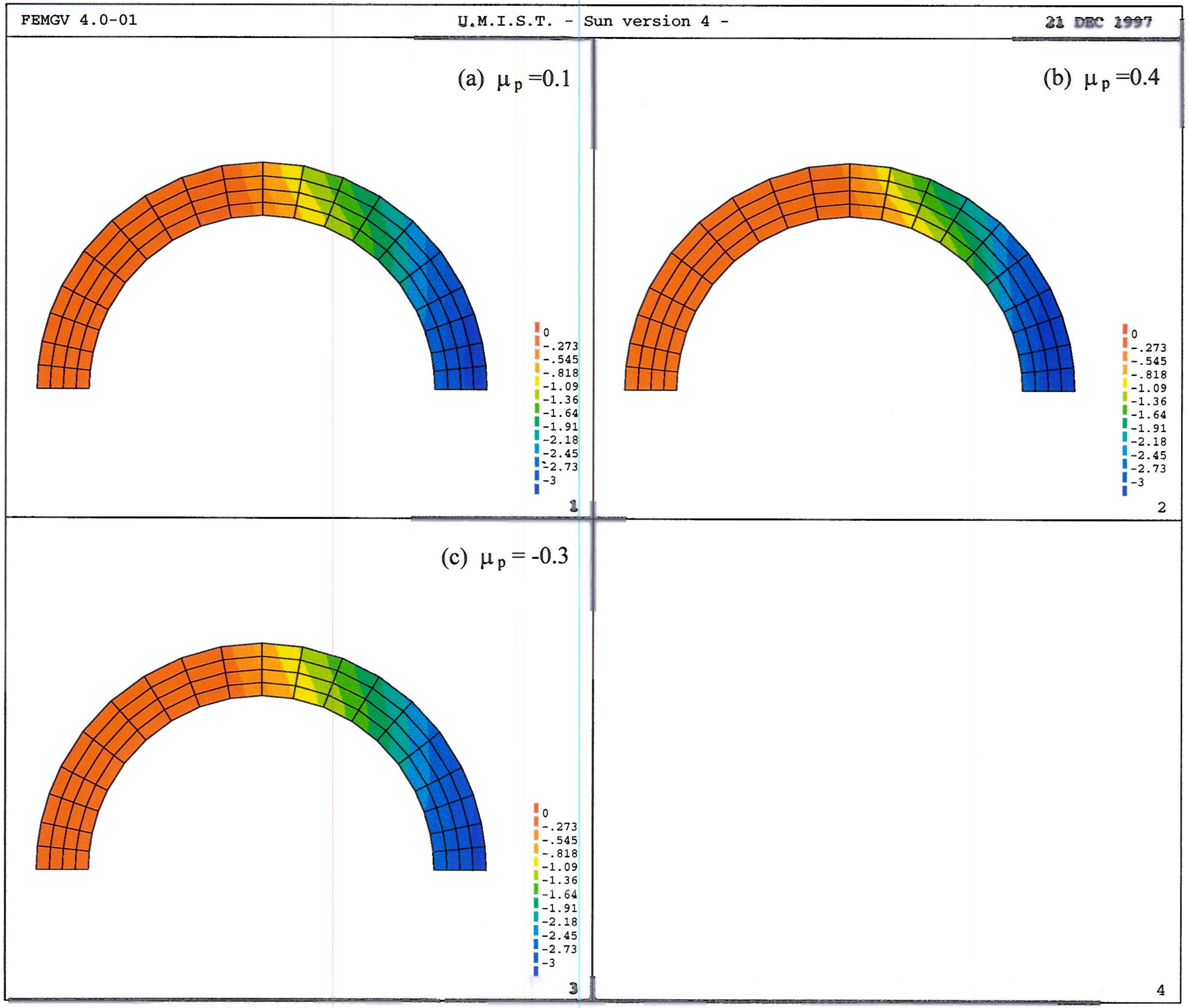

Figure 6.11 Normalized normal stresses on the interface with soft packing and β=0.27^0

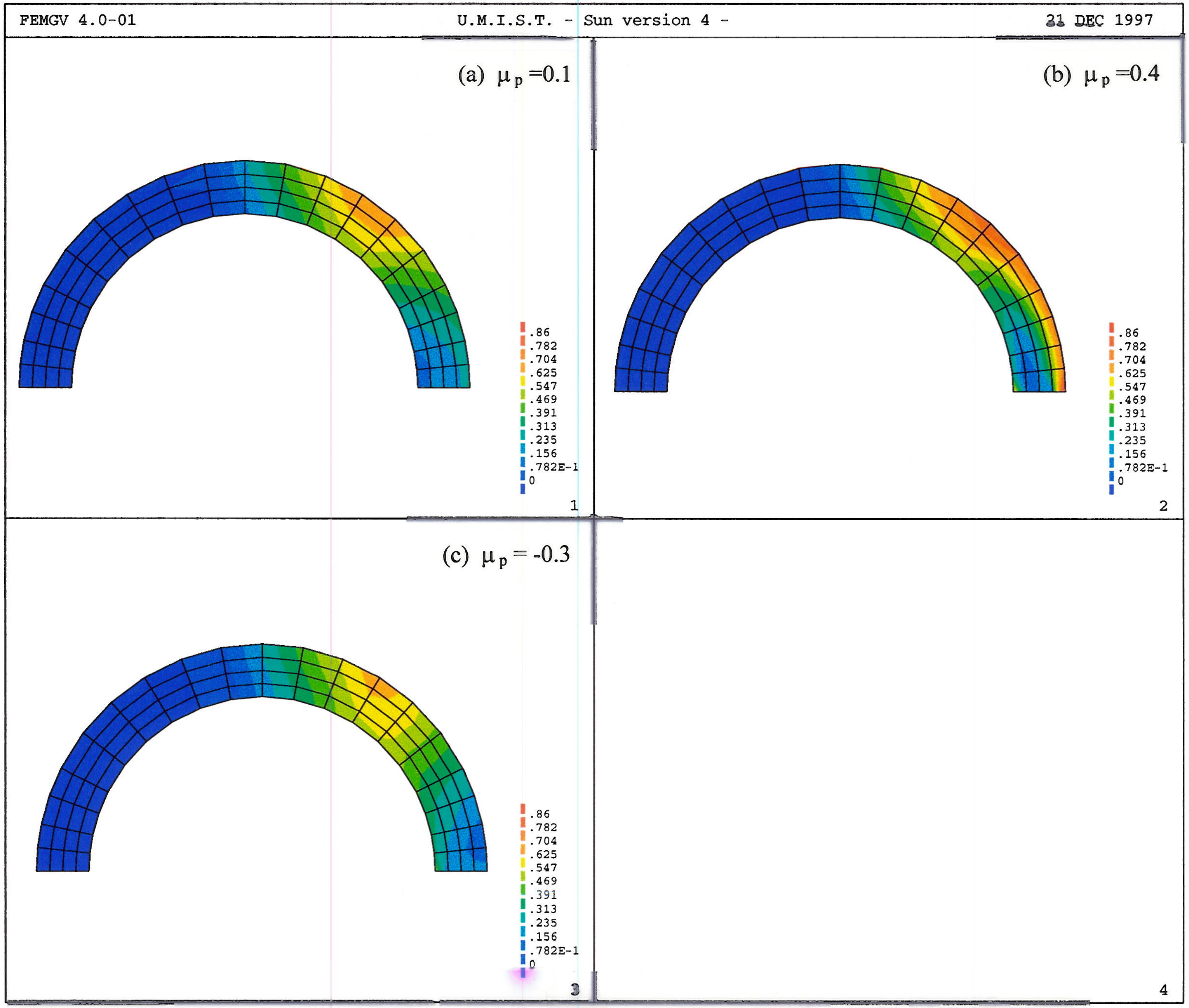

Figure 6.12 Normalized shear stresses on the interface with soft packing and $\beta=0.27^0$

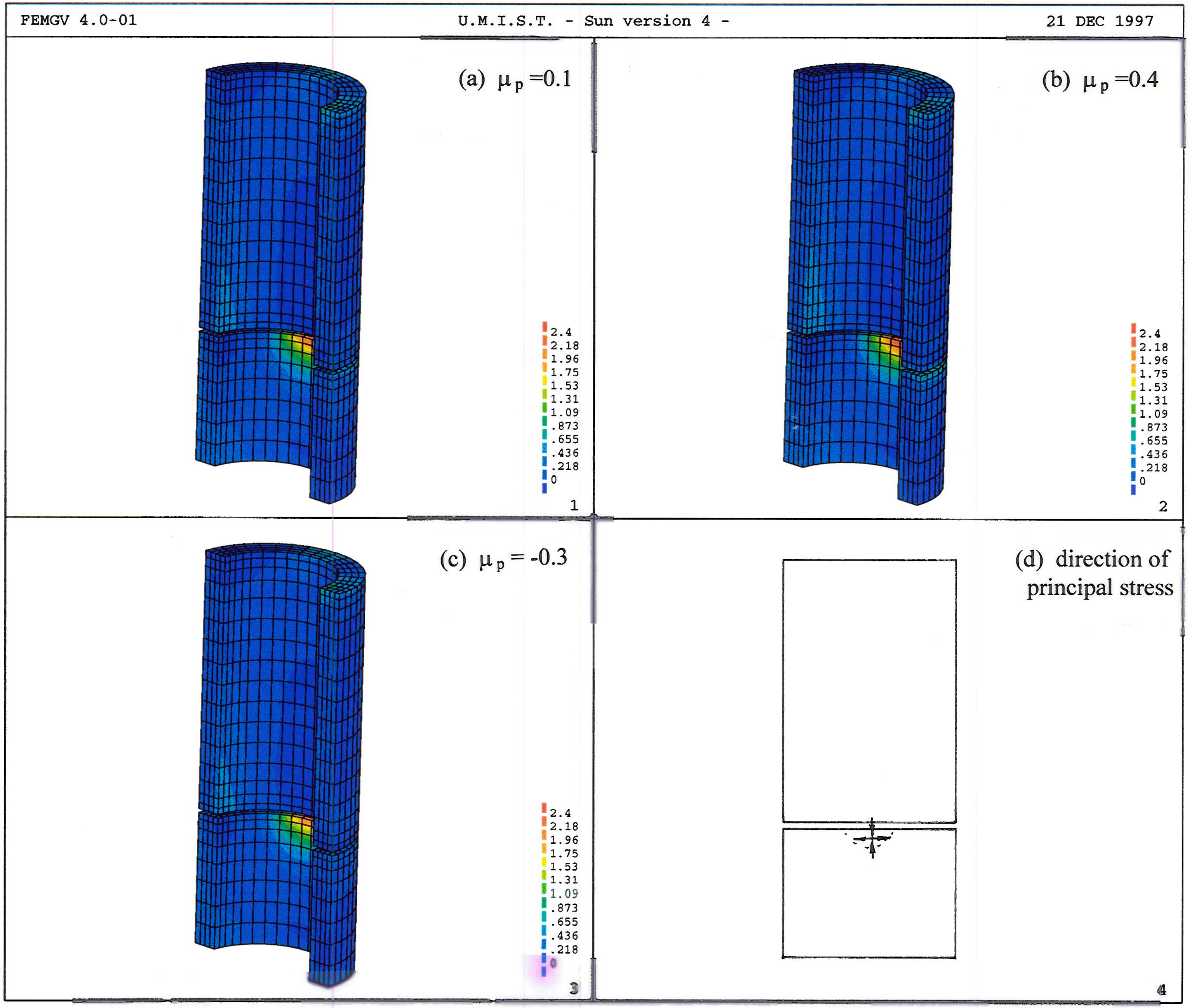

Figure 6.13 Normalized most tensile principal stresses in the pipes with soft packing and $\beta=0.27^0$

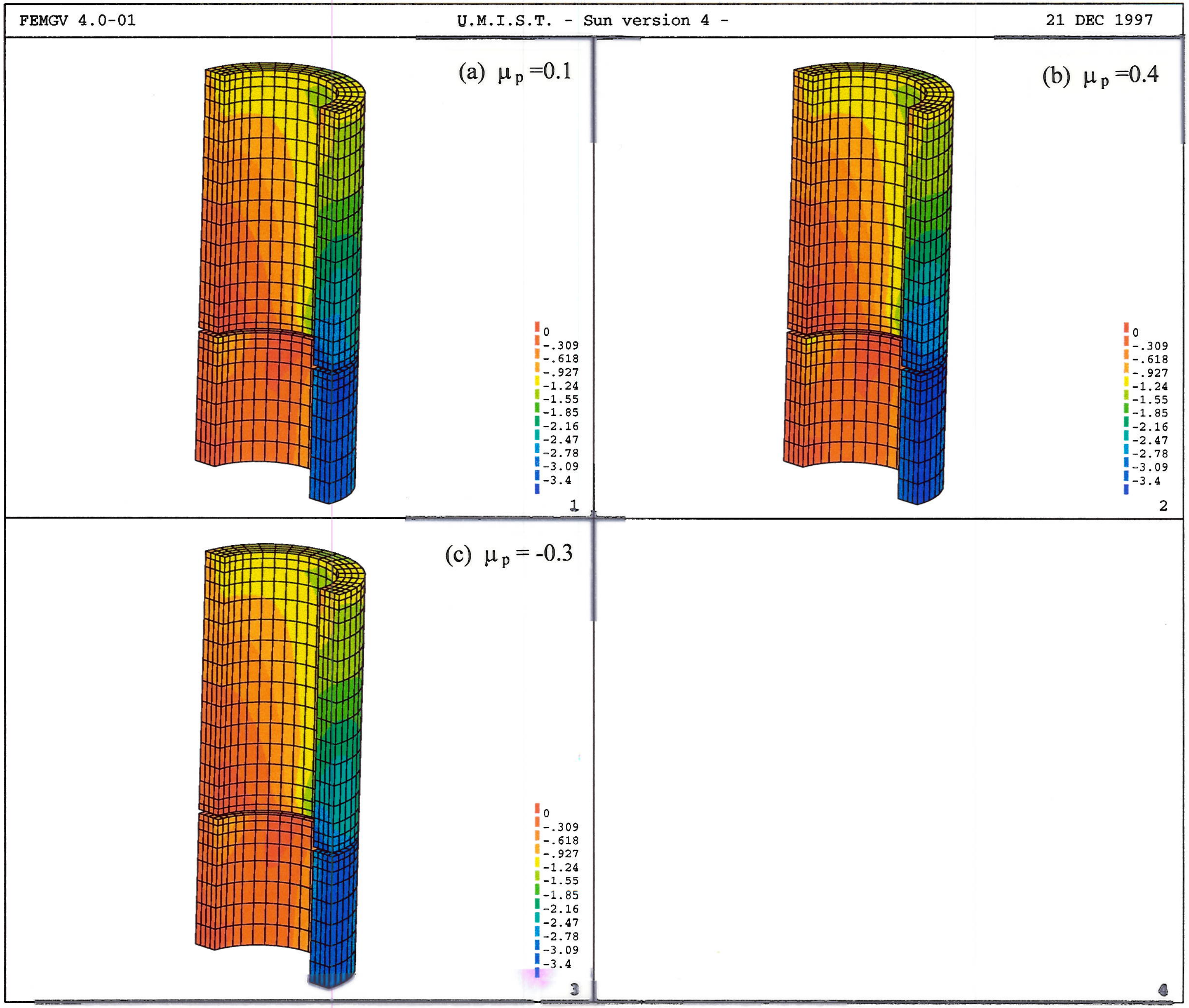

Figure 6.14 Normalized most compressive principal stresses in the pipes with soft packing and $\beta=0.27^0$

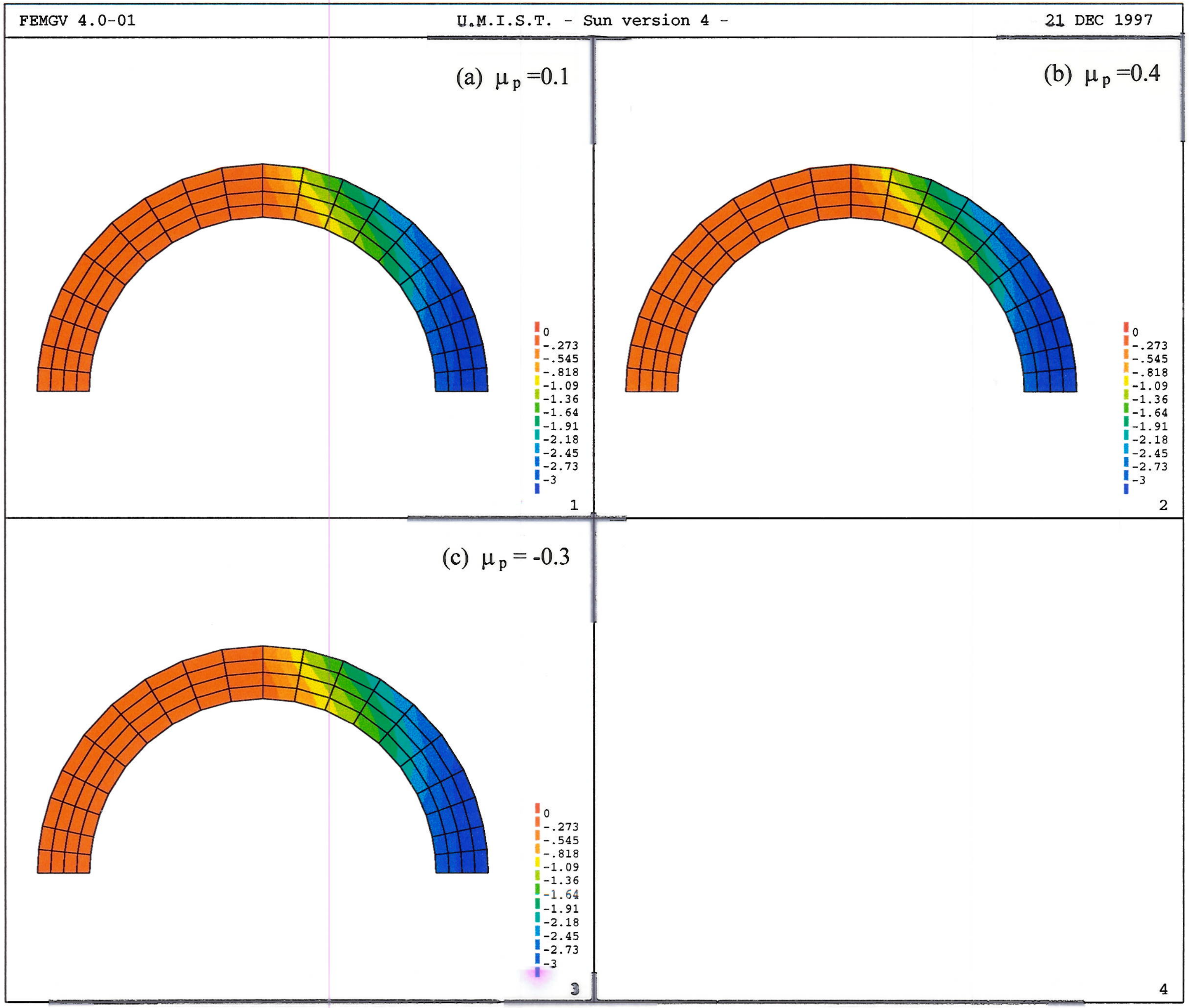

Figure 6.15 Normalized normal stresses on the interface with stiff packing and $\beta=0.27^0$

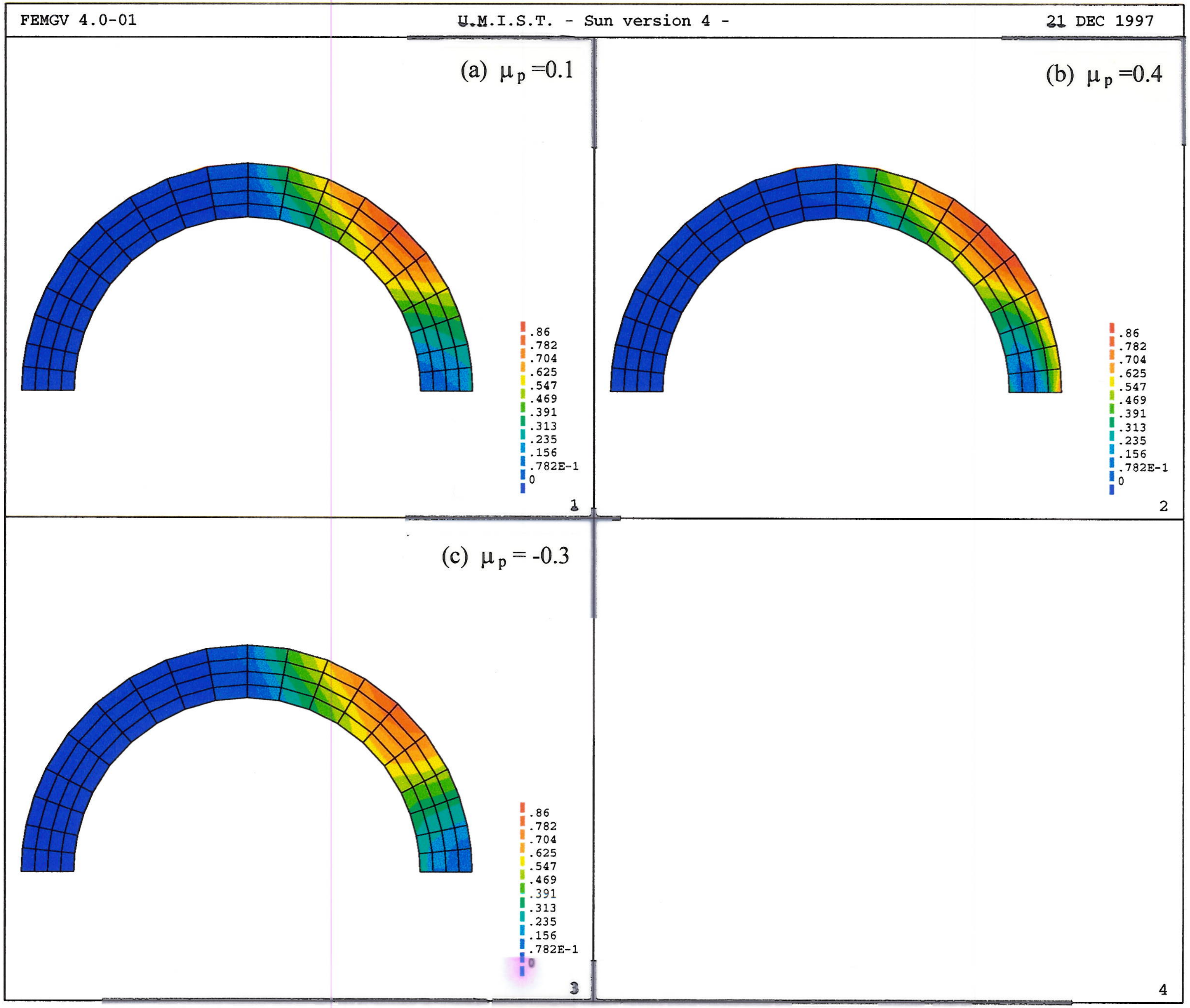

Figure 6.16 Normalized shear stresses on the interface with stiff packing and $\beta=0.27^0$

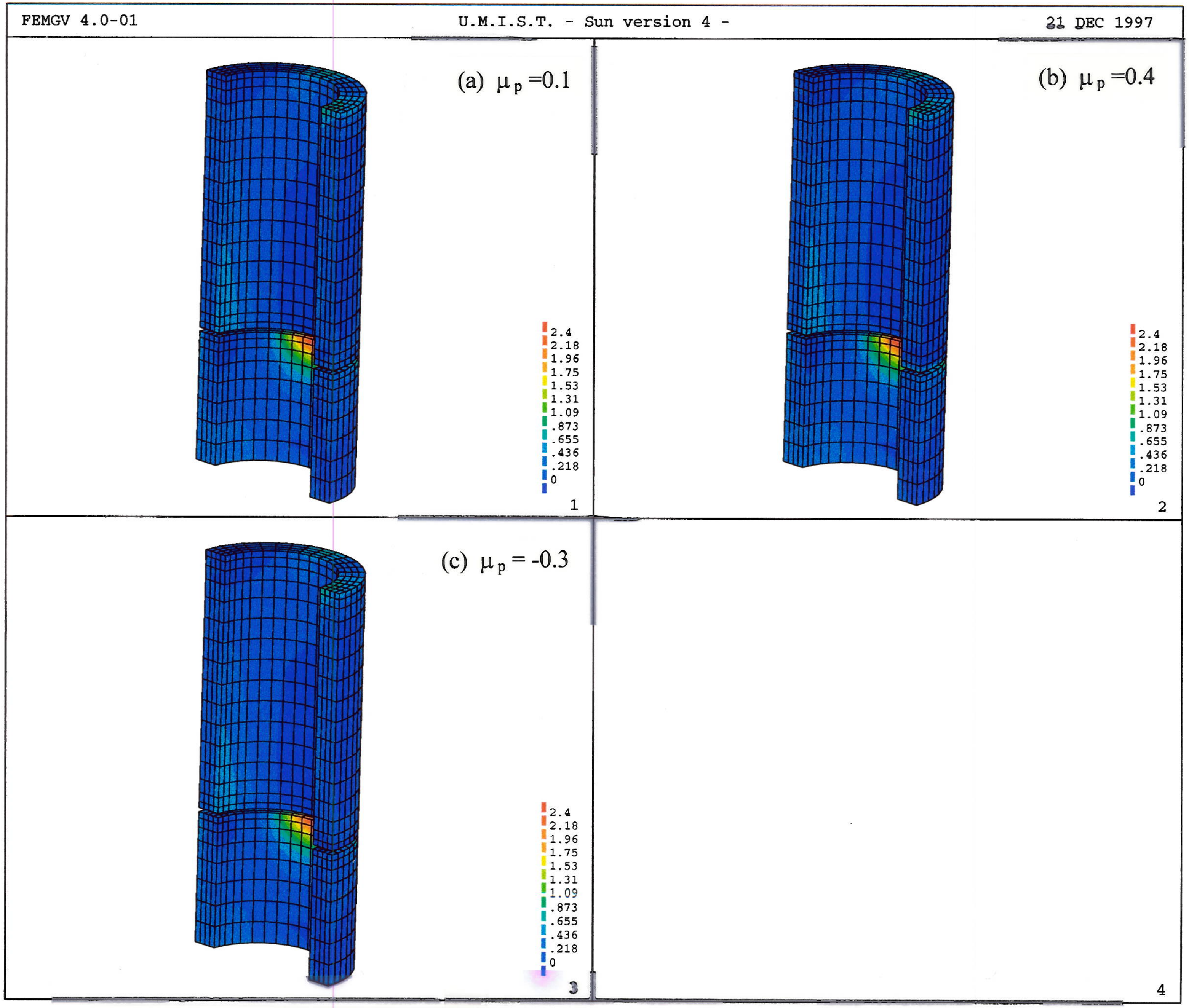

Figure 6.17 Normalized most tensile principal stresses in the pipes with stiff packing and $\beta=0.27^0$

CHAPTER 7 JOINT DEFORMATION AND COMPARISON WITH ANALYTICAL RESULTS

7.1 INTRODUCTION

To study the stress distribution and the deformation at the pipe joint, various attempts have been made (the Concrete pipe Association of Australia 1983, Milligan and Ripley 1989, Norris 1992, and Haslem 1996). For its simplicity, the Australian model is now widely used in practice. In this chapter, two analytical models, the Australian model and the flexible pipe model (Haslem 1996), are briefly reviewed in Section 7.2. The displacements at the joint from numerical model B in Chapter 5 are discussed in Section 7.3. The results from the numerical model C in Chapter 6 are described and compared with those from the Australian model and the flexible pipe model in Section 7.4. The conclusion is given in Section 7.5.

7.2 ANALYTICAL MODELS

Two analytical models, the Australian model and the flexible pipe model (Haslem 1996), are discussed in this section. In both models, the pipes adjacent to the joint are assumed to be under the edge loading condition, and shear stresses at the joint are ignored.

7.2.1 THE AUSTRALIAN MODEL

The Concrete Pipe Association of Australia (1983) published a theory of joint behaviour. In the Australian model, it is assumed that there exists a partial gap between the pipe and the packing material and the diametrical contact width is Z as shown in Figure 7.1. Moreover, it is assumed that the normal stress varies linearly from zero at the front of the gap to the maximum stress σ_{max} at the pipe edge on the interface (see Figure 7.1) and that the stresses in the pipe and in the packing material have the same distribution pattern as that on the interface. The axial strain in the pipe and the packing material are linearly related to the normal stress at the joint. The analysis presented by the Concrete Pipe Association of Australia is summarised below.

The total load transferred at the pipe joint is obtained by integrating the normal stresses distributed over the joint (on the interface). As discussed above, the stresses are distributed over a contact width Z and the maximum stress $\sigma_{\max}$ is at the pipe edge ($x = R$). Figure 7.2 shows a diagram of the stress integration and the integration procedure is described as following. The cross length of the element at x in the figure is L_x:

$$L_x = 2\sqrt{R^2 - x^2} - 2\sqrt{r^2 - x^2} \qquad \text{when } |x| < |r|$$

$$L_x = 2\sqrt{R^2 - x^2} \qquad \text{when } |x| > |r| \qquad (7.2.1)$$

where R and r are the external radius and internal radius of the pipe. The stress intensity on this element is:

$$\sigma = \sigma_{min} + \sigma_m\ (x - H_1)\ /\ (R - H_1) \qquad (7.2.2)$$

where

$$\sigma_{min} = \max\left(0,\ \frac{(Z-2R)\sigma_{\max}}{Z}\right), \qquad \sigma_m = \sigma_{max} - \sigma_{min}$$

$$H = R - Z, \quad H_1 = \max(H,\ -R) \qquad (7.2.3)$$

The total force transferred at the joint (P) is derived as follows:

$$P = \int_{H_1}^{R} \sigma L_x\, dx = P_0 + P_1 - P_2 \qquad (7.2.4)$$

where

$$P_0 = \pi\,(R^2 - r^2)\sigma_{\min} \qquad (7.2.5)$$

$$P_1 = \int_{H_1}^{R} 2\sigma_m \left(\frac{x - H_1}{R - H_1}\right)\sqrt{R^2 - x^2}\,dx$$

$$= \frac{1}{R - H_1}\left[\frac{2}{3}(R^2 - H_1^2)^{\frac{3}{2}} + H_1^2\sqrt{R^2 - H_1^2} - H_1 R^2 \cos^{-1}\left(\frac{H_1}{R}\right)\right]\sigma_m \qquad (7.2.6)$$

$$P_2 = \int_{H_2}^{r} 2\sigma_m (\frac{x-H_1}{R-H_1})\sqrt{r^2 - x^2}dx$$

$$= \frac{1}{R-H_1}[\frac{2}{3}(r^2 - H_2^2)^{\frac{3}{2}} + H_1 H_2 \sqrt{r^2 - H_2^2} - H_1 r^2 \cos^{-1}(\frac{H_2}{r})]\sigma_m \qquad (7.2.7)$$

where

$$H_2 = \mathrm{sgn}(H)\min(|H|, r) \qquad (7.2.8)$$

Clearly, the maximum stress on the joint σ_{max} can be obtained by combining equation (7.2.1) to (7.2.8) when the contact width Z and the total transferred load P are known.

The total maximum compression deformation at the pipe edge (where σ_{max} is located) is derived as following:

$$\Delta a = \Delta a_p + \Delta L \qquad (7.2.9)$$

Where Δa is the total compression deformation, Δa_p is the deformation of the packing material and ΔL is the deformation of the two halves of the pipes adjacent to the joint. Assuming a linear relationship between the stress and strain, equation (7.2.9) becomes:

$$\Delta a = \frac{\sigma_{max}\, a}{E_p} + \frac{\sigma_{max}\, L}{E_c} \qquad (7.2.10)$$

where a is the thickness of the packer, L is the length of the pipe, E_p and E_c are the Young's modulus of the packing material and the concrete pipe. (In the original description of the Australian model, the possibility of different values of pipe thickness and wall thickness at joint was included. In the discussion in this project, the wall thickness at pipe joint is the same as the pipe thickness.)

From the Figure 7.1, the misalignment angle β can obtained from the total maximum compression deformation of the joint using the equation:

$$\tan\beta = \frac{\Delta a}{Z} \qquad (7.2.11)$$

Where Z is the diametrical contact width at the pipe joint.

7.2.2 HASLEM'S FLEXIBLE PIPE MODEL

To extend the Australian model to include tensile stresses, Haslem (1996) proposed a flexible pipe model. In this model, the stress distribution pattern at the pipe joint and the deformation pattern of the packing material are assumed to be the same as those in the Australian model. However, the concrete pipes are assumed to be under uniform pressure and bending moment due to the eccentric jacking load at the joint. The misalignment angle of the pipeline at the joint consists of the angular deflection angle of the compressed packing material and the sum of the angular deflections (due to the bending moment) of the two halves of the pipes adjacent to the joint. Furthermore, it is assumed that the ends of the pipes remain plane during bending and that the bending moment is constant along the length of the two pipe halves.

The additional analysis of bending of the concrete pipes in this model is summarised as below. With the stress distribution as shown in Figure 7.1, the bending moment about the axis y can be calculated using the diagram in Figure 7.2 as following:

$$M = \int_{H_1}^{R} \sigma L_x \, x \, dx = \sigma_m F_e \qquad (7.2.12)$$

where:

$$\begin{aligned} F_e = & \int_{H_1}^{R} 2x\left(\frac{x-H_1}{R-H_1}\right)\sqrt{R^2-x^2}\,dx - \int_{H_2}^{r} 2x\left(\frac{x-H_1}{R-H_1}\right)\sqrt{r^2-x^2}\,dx \\ & - \frac{1}{R-H_1}\left[\frac{R^4}{4}\cos^{-1}\left(\frac{H_1}{R}\right) - \frac{H_1}{4}(2H_1^2-R^2)\sqrt{R^2-H_1^2} - \frac{2}{3}H_1(R^2-H_1^2)^{\frac{3}{2}}\right] \\ & - \frac{1}{R-H_1}\left[\frac{r^4}{4}\cos^{-1}\left(\frac{H_2}{r}\right) - \frac{H_2}{4}(2H_2^2-r^2)\sqrt{r^2-H_2^2} - \frac{2}{3}H_1(r^2-H_2^2)^{\frac{3}{2}}\right] \end{aligned} \qquad (7.2.13)$$

The misalignment angle β is obtained from the angular deflection of the compressed packing material (β_p) and the sum of the angular deflections of the two halves of the pipes adjacent to the joint (β_c) is as follows:

$$\beta = \beta_p + 2\,\beta_c \tag{7.2.14}$$

where:

$$\beta_p = \frac{\Delta a_p}{Z} = \frac{\sigma_{\max}\, a}{Z E_p} \tag{7.2.15}$$

$$\beta_c = \frac{M L}{2 E_c I_c} \tag{7.2.16}$$

Where L is the length of the pipe, $I_c = \frac{\pi}{4}(R^4 - r^4)$ is the second moment of area of the cross-section of the concrete pipe. Similar to the Australian model, there is a relationship between the misalignment angle β, the maximum joint stress σ_{max}, the total transferred load P and the contact width Z. For example, with a constant load P, β and σ_{max} are both functions of Z as shown by equation (7.2.4) to (7.2.16).

7.3 JOINT DEFORMATION OF NUMERICAL MODEL B

In Chapter 5, several analyses using numerical model B are described. The load distribution pattern at the pipe end under 'edge' loading in Chapter 5 (refer to Figure 5.2) is the same as that assumed in the analytical model shown in Figure 7.1. This section describes the compression deformations at the pipe end (the axial displacements at the pipe end along the line of r = 715mm) in numerical model B with interface elements between the pipe and the surrounding soil (refer to Figure 5.8 and Section 5.4 in Chapter 5). The results under the 'edge' loading are compared with those from the Australian model and Haslem's flexible pipe model.

The computed displacements in the z direction at the top pipe end (axial displacements w at the bottom end are in the opposite direction) under 'edge' loading in numerical model B and the analytical results, from the Australian model and Haslem's flexible pipe model, are shown in Figure 7.3. The numerical results show that the distributions of the displacements are non-linear over the pipe end, and that the distribution patterns of the displacement are similar in the cases of typical soil and soft soil while with some deviations in the case of stiff soil. The maximum magnitudes of the displacements are located at the pipe edge as expected. In the region close to the pipe edge (x < -400mm), the displacements vary almost linearly; On the right side (x > 0mm), the displacements are small and positive with the typical and soft soil; while in the region of the edge of the applied load (x = - 220mm), the tangent angles of the displacement curves change rapidly possibly due to the local bending effects. The results from the Australian model shows a linear displacement distribution in the loaded region (x = -220mm), and there is no displacement in the non-loaded region since the stresses in the concrete pipe are zero in this region. The displacements from the flexible pipe model is linearly distributed over the pipe end.

From the figure, it is clear that the numerical results with typical soil and soft soil are close to the analytical data from the Australian model to some extent except in the region of the edge of the applied load (x = -220mm). The results from Haslem's flexible pipe model deviate from the numerical ones. A possible reason is that the concrete pipes in the flexible pipe model are assumed to sustain tensile stresses in the axial direction due to the bending moment. From the numerical analysis in this research, the tensile stresses under edge loading are localised in the region of the pipe joint and are mainly located in the hoop direction. From Figure 7.1 and 7.3, the Australian model shows that the distribution of the misalignment angle at the pipe joint due to the deformation of the concrete pipe is dependent on the part with higher compression displacements in the loaded region. The deflection angles at the pipe end from the numerical and the analytical models are given in Table 7.1.

Table 7.1 Deflection angle at pipe end under edge load (degree)

typical soil	soft soil	stiff soil	Australian model	Haslem (1996)
0.0502	0.0544	0.0370	0.0675	0.0198

From the table, it is clear that the deflection angle from the Australian model is slightly higher than that from the numerical model with typical and soft soil, and the deflection angle from the flexible pipe model is much smaller due to the assumption of tensile stresses in the concrete pipe as discussed above.

Figure 7.4 shows the displacements (w) in z direction at the top pipe end under 'diagonal' loading in numerical model B. From the figure, it is clear that with the typical and soft soil the deformations at the pipe end are much larger than those under 'edge' loading and are mainly due to the rigid body rotation of the pipe in the soil. The influence of the stiffness of the surrounding soil is significant. The total deflection angles and the rigid rotation angles with different soils derived from the displacements are given in Table 7.2. It should be pointed out that these deformations tend to reduce the original misalignment angle at the pipe joint (Norris 1992, Ripley 1989). This means that the load distribution at the pipe end would change significantly under the diagonal load due to the deformation of the concrete pipe with typical and soft soil (Ripley 1989). In practice, misalignment angles under 'diagonal' loading condition are usually found to be much smaller than those under 'edge' loading condition due to the large pipe deformation. Unfortunately, there is no analytical model for this aspect of pipe behaviour.

Table 7.2 Deflection angle at pipe end under diagonal load (degree)

	typical soil	soft soil	stiff soil
Total deflection angle	0.2521	2.116	0.0587
Rigid rotation angle	0.2080	2.071	0.0238

7.4 RESULTS OF NUMERICAL MODEL C

In this section, the results from numerical model C are discussed. The deformation of the bottom pipe (in fact, it is half a pipe as shown in Figure 6.2 in Chapter 6) is described in Section 7.4.1. Section 7.4.2 discusses the misalignment angles at the pipe joint. The maximum stress and the diametrical contact width at the joint from the numerical model C are compared with the results from the Australian model and the flexible pipe model (Haslem 1996) in Section 7.4.3.

7.4.1 DEFORMATION OF THE BOTTOM PIPE

The deformation of the bottom pipe (again along the line of r = 715mm), which is under the 'edge' loading condition (see Figure 6.2 in Chapter 6), is discussed first. The displacements in the axial direction at the top end of the bottom pipe (*w*) with low applied misalignment angle $\beta=0.09^{0}$ and different packing materials are shown in Figure 7.5. The figure shows that the displacements change linearly (or almost linearly) over the pipe end and have their maximum magnitudes at the pipe edge and that the packing material with higher shear modulus and higher Poisson's ratio has higher rate of change of displacement at the pipe end. However, the influence of the properties of the packing material is small. (It is also seen that the influence is not only due to the stiffness of the packing material $E_p = 2G_p(1+\mu_p)$ because the maximum compression displacement in the case of G_p = 300MPa, $\mu_p = 0.4$ (E_p = 840MPa) is higher than that in the case of E_p = 900MPa, $\mu_p = -0.3$ (E_p = 1260MPa).)

Figure 7.6 shows the displacements in the axial direction at the top end of the bottom pipe with high applied misalignment angle $\beta=0.27^{0}$. From the figure, it is clear that the displacements vary non-linearly over the pipe end and have a similar distribution pattern to that in numerical model B except that the loaded region is now on the right side ($x > 100$mm). The displacements are high and almost linearly distributed in the region of $x > 200$mm, and are small and positive in the region of the left end ($x < -150$mm). The tangent angles of the displacement curves change rapidly in the region of the gap front (refer to Section 6.4, and see Figure 6.11 and 6.15 in Chapter 6). The influence of the properties of the packing material is small and similar to that under small applied misalignment angle.

7.4.2 MISALIGNMENT ANGLES AT PIPE JOINT

The total deformation at the pipe joint consists of the deformation of the packing material and the deformations of the two halves of the pipes adjacent to the joint (that is, the axial displacement w at the middle length cross section A-A of the top pipe in Figure 7.7 less the deformation of the interface). The total deformations at the pipe joint under low applied angle $\beta=0.09^0$ are shown in Figure 7.7. From the figure, it is clear that similar to the deformations of the bottom pipe the total deformations at the joint are almost linearly distributed over the pipe joint in all cases. The total deformation is smaller with the packing material having higher shear modulus and higher Poisson's ratio. However, the influence of the properties of the packing material is small.

Figure 7.8 shows the total deformations at the pipe joint under the high applied misalignment angle $\beta=0.27^0$. From the figure, it is clear that the total deformations are non-linear over the joint, and to some extent have similar distributions pattern as those of the deformation of the bottom pipe. Again, the influence of the properties of the packing material is small.

As discussed in Section 7.3, the actual misalignment angle at the joint can be obtained from the total deformation in the high compression region (loaded region). In the numerical model C, the diametrical contact width Z varies with y across the pipe thickness (refer to

Section 6.3 in Chapter 6, and see Figure 6.11, 6.12, 6.15 and 6.16). For simplicity, the misalignment angles under different conditions are calculated from the total deformation in the region $x > 250$mm. (In the case of low applied misalignment angle, the computed actual misalignment angles are independent of the calculation region.) The computed misalignment angles ($\overline{\beta}$) are given in Table 7.3.

The applied misalignment angle used in the numerical analysis is calculated from the given displacement δ in the x direction at the upper end of the top pipe as discussed in Chapter 6:

$$\tan \beta = \delta / L \tag{7.4.1}$$

where L is the length of the pipe. However, the displacement in the x direction at the centre of the bottom end of the top pipe (δ_b) is not zero. So the actual applied misalignment angle is as follows:

$$\tan \beta^* = (\delta - \delta_b) / L \tag{7.4.2}$$

The actual applied misalignment angles derived from this equation are also given in Table 7.3 for comparison with the computed misalignment angles.

Table 7.3 Actual applied and computed misalignment angle (degree)

$\beta = 0.09^0$		$\beta = 0.27^0$		packer's properties	
β^*	$\overline{\beta}$	β^*	$\overline{\beta}$	μ_p	G_p (MPa)
0.0671	0.0662	0.2100	0.2061	0.1	300
0.0643	0.0646	0.2056	0.1971	0.4	300
0.0685	0.0687	0.2124	0.2123	-0.3	300
0.065	0.0643	0.2076	0.1982	0.1	900
0.0641	0.0637	0.2063	0.1951	0.4	900
0.0656	0.0649	0.2083	0.1998	-0.3	900

From the table, it is clear that the computed misalignment angles agree well with the actual applied ones and that the influence of the properties of the packing material is small.

7.4.3 MAXIMUM STRESS AND DIAMETRICAL CONTACT WIDTH AT PIPE JOINT

In this section, the maximum stress σ_{max} and the diametrical contact width Z at the pipe joint from numerical model C are compared with the results from the analytical models under the computed misalignment angle $\overline{\beta}$. From the numerical results in Chapter 6 (refer to Figures 6.4, 6.5, 6.8, 6.9, 6.11, 6.12, 6.15 and 6.16), it is known that the stresses are non-linearly distributed over the joint, and that the diametrical contact width Z varies with y across the pipe thickness. In comparison, the average value of Z is used, or the contact width Z is calculated by interpolating linearly the stresses to a zero point if there is no gap between the pipe and the packing material; and the maximum stress σ_{max} at the pipe edge (x = 715mm) is calculated from the average stresses at the centre of elements in the region of the pipe edge ($\theta < 6^0$) with a linear interpolation.

In the analytical models, the stresses are assumed linearly distributed at the joint as shown in Figure 7.1 and for a particular joint the diametrical contact width Z and the maximum joint stress σ_{max} can be obtained as a function of the misalignment angle β under a constant applied load P as discussed in Section 7.2. The comparison between the numerical results and the analytical data is given in Table 7.4 for various packing materials. The results are obtained under uniform pressure q = 10MPa at the upper end of the top pipe as shown in Figure 6.2 in Chapter 6.

From the table, it is clearly seen that under small misalignment angles ($\overline{\beta} < 0.07^0$), the numerical results and the results from both analytical models agree well in all cases. With high misalignment angles ($\overline{\beta} > 0.195^0$), the numerical results and the results from the Australian model agree well, while the flexible pipe model gives much smaller contact width Z and much higher maximum stress σ_{max} due to the assumption of tensile stresses in the pipe, as discussed in Section 7.3. This means that the Australian model provides a good approximation for the diametrical contact width Z and the maximum normal stress σ_{max} on average when the misalignment angle of the pipe line is known. Bearing in mind that the normal stresses in the region of the pipe edge ($\theta < 6^0$) change a little in the case of $\mu_p = 0.4$ as shown in Chapter 6 (refer to Figures 6.4, 6.8, 6.11 and 6.15), the Australian model likely underestimates the normal stresses in this region at the pipe joint.

Table 7.4 Comparison between the numerical and analytical results

	Australian model		Haslem (1996)		Numerical model C			
$\overline{\beta}$	Z	σ_{max}	Z	σ_{max}	Z	σ_{max}	packer's properties	
(degree)	(mm)	(MPa)	(mm)	(MPa)	(mm)	(MPa)	μ_p	G_p (MPa)
0.0662	1435.0	19.48	1435.0	19.48	1438	19.48	0.1	300
0.0646	1428.5	20.02	1428.5	20.02	1417	20.25	0.4	300
0.0687	1453.8	17.74	1453.8	17.74	1476	18.99	-0.3	300
0.0643	1335.7	21.39	1327.3	21.51	1390	20.98	0.1	900
0.0637	1326.2	21.57	1315.5	21.71	1338	21.20	0.4	900
0.0649	1370.3	20.87	1368.4	21.01	1415	21.00	-0.3	900
0.2061	768.0	32.4	505.0	43.69	804	33.50	0.1	300
0.1971	761.6	32.59	464.8	46.45	739	34.48	0.4	300
0.2123	820.1	30.95	621.8	37.62	848	30.40	-0.3	300
0.1982	700.4	34.6	296.7	66.40	698	36.90	0.1	900
0.1951	696.8	34.71	267.4	72.75	659	36.34	0.4	900
0.1998	722.3	33.83	371.0	55.20	704	36.50	-0.3	900

Note: $\overline{\beta}$ is computed misalignment angle (Section 7.4.3)

7.5 CONCLUSION

After the discussion and result comparison above, a few conclusions are drawn as following:

(1) With a linear stress distribution at two pipe ends under the 'edge' loading condition, the deformation of the pipe is non-linear over the pipe end, that is, the deformation is neither bilinear as the Australian model predicts nor linear as the flexible pipe model predicts. However, the Australian model, in general, gives a somewhat close prediction to the numerical results.

(2) Under small misalignment angle ('edge' loading) especially when the normal stress covers the whole (or almost whole) pipe joint, the pipe deformation and the normal stress at the pipe joint are almost linearly distributed, and the two analytical models give very close predictions to the numerical results.

(3) With a high misalignment angle ('edge' loading), there is a big gap between the pipe and the packing material, and both the deformation and the normal stress are non-linear over the pipe joint. From the point of view of average values, the Australian model gives good approximations about the diametrical contact width Z and the maximum normal stress σ_{max} at the joint; while the prediction from the flexible pipe model is poor, especially with the stiff packing material. due to the assumption of tensile stresses in the axial direction within the pipe.

(4) Under the 'diagonal' loading condition, the displacements at the pipe ends are mainly due to the rigid body rotation of the pipe within the soil, and with typical and soft soil, the deflection angle is higher than that under 'edge' loading. Because the deflection angle in this case reduces the original misalignment angle at the joint, in practice the misalignment angle is usually found to be small under 'diagonal' loading.

(5) Neither analytical model considers shear stress at the joint, which plays an important role in the pipe's performance.

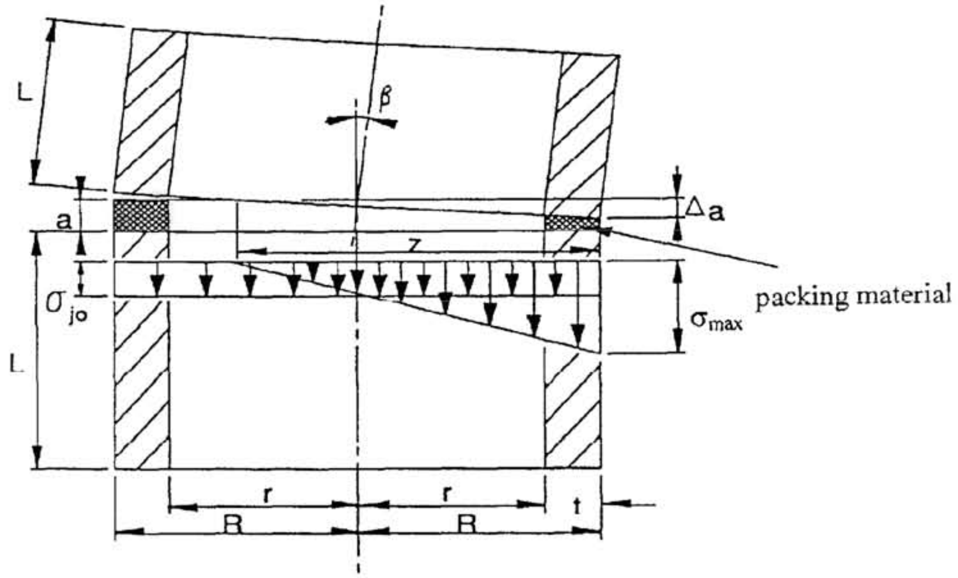

Figure 7.1 Australian joint stress distribution

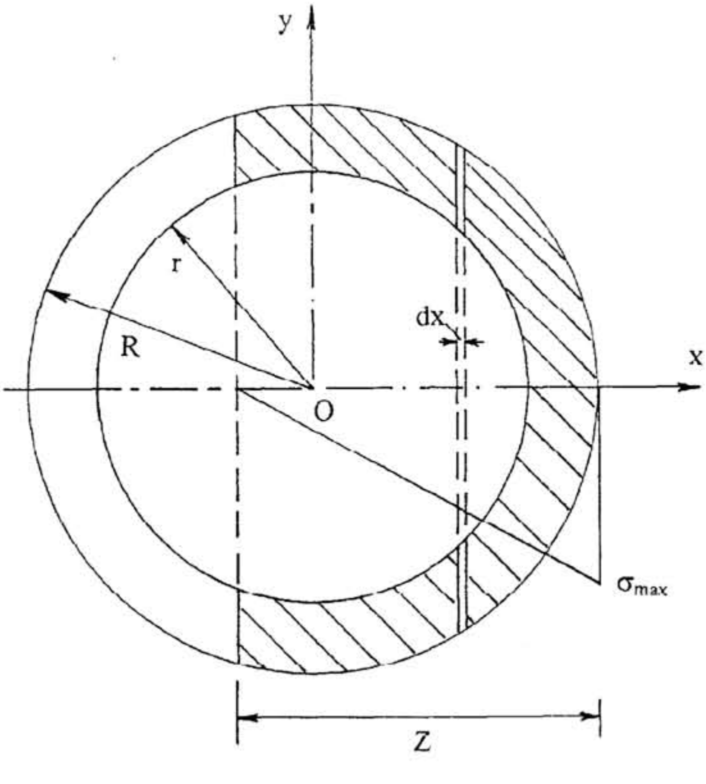

Figure 7.2 Integration diagram for joint stresses

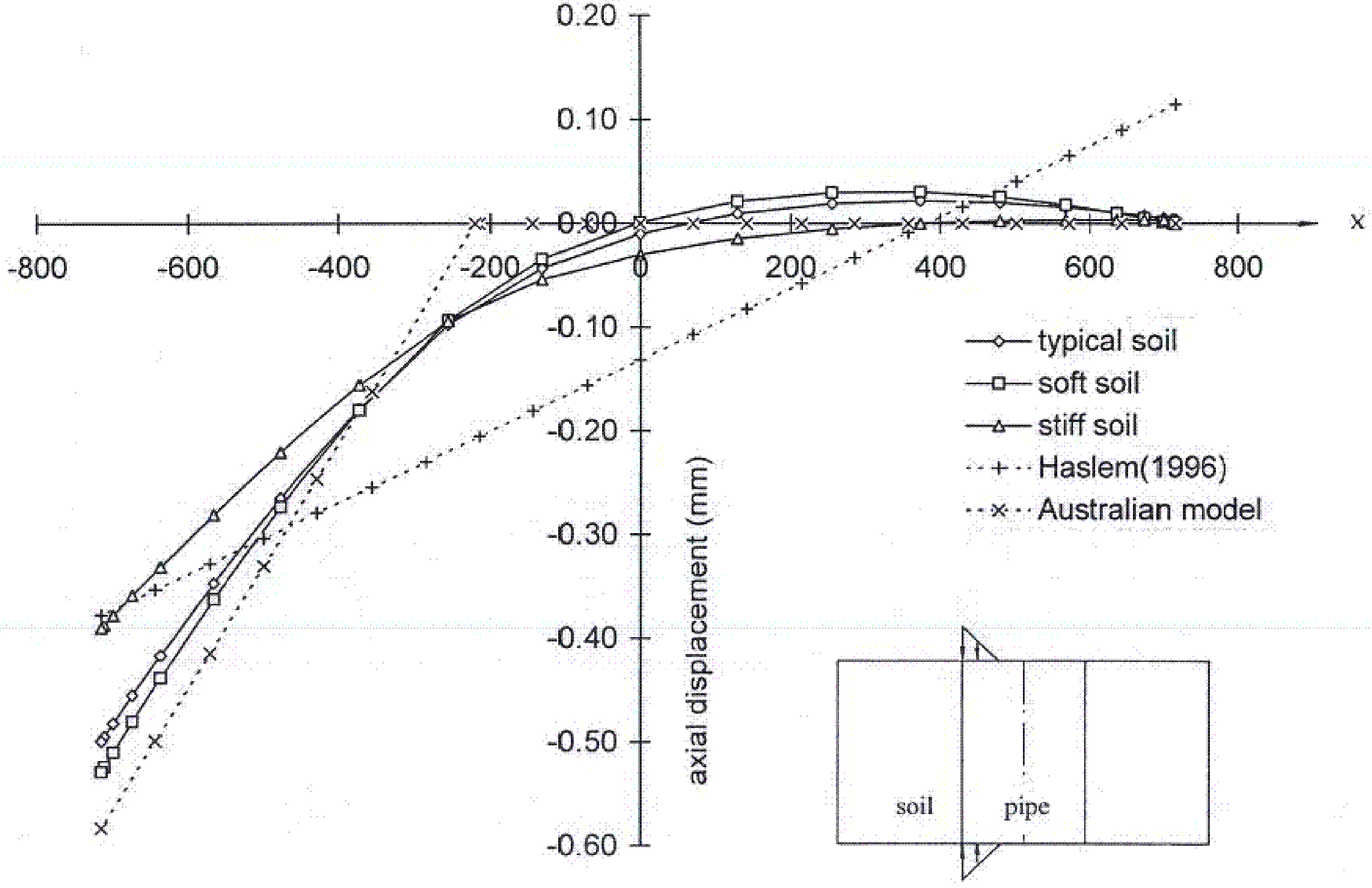

Figure 7.3 Compression displacement at the pipe end in numerical model B under edge loading

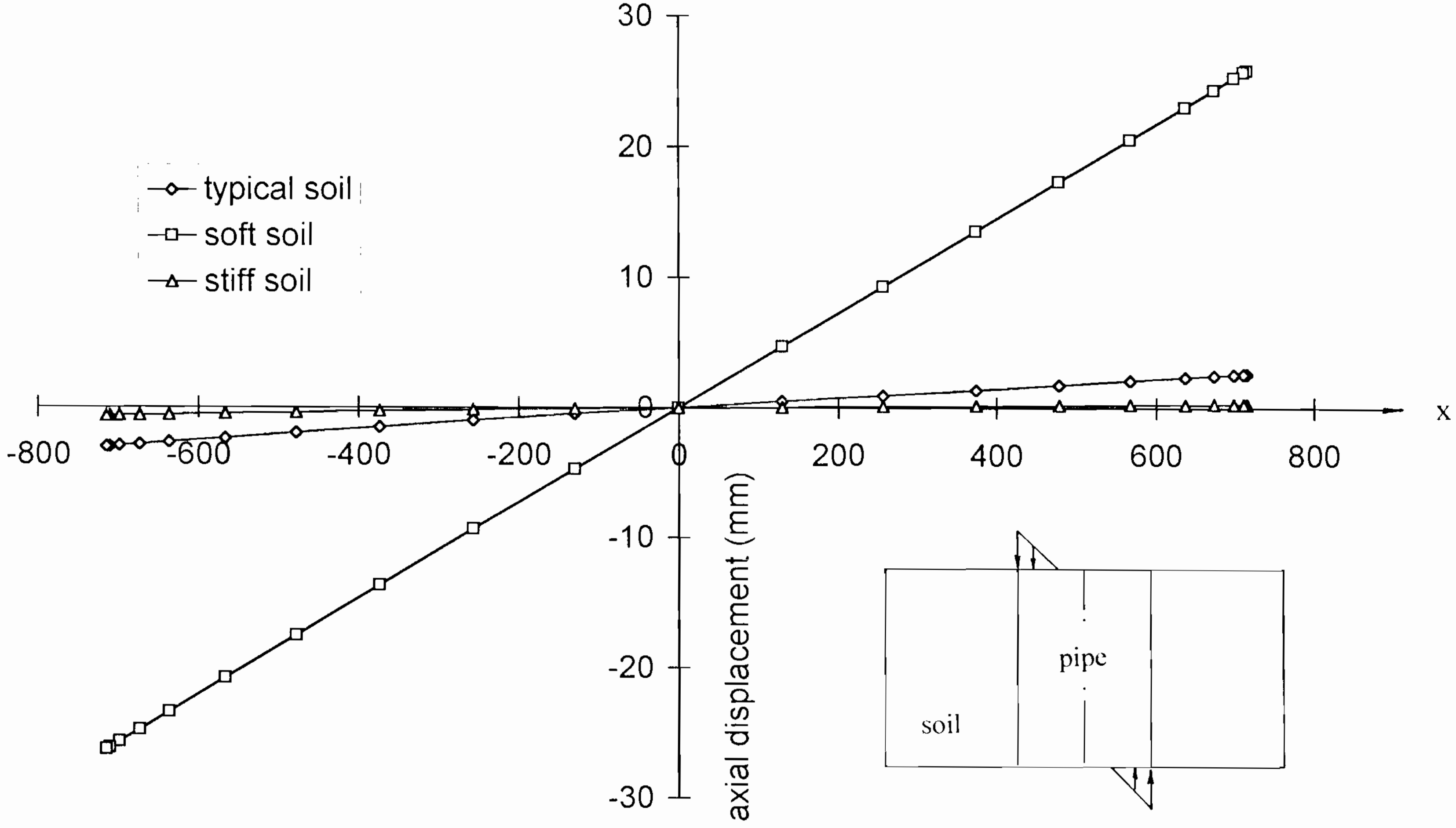

Figure 7.4 Compression displacement at the pipe end in numerical model B under diagonal loading

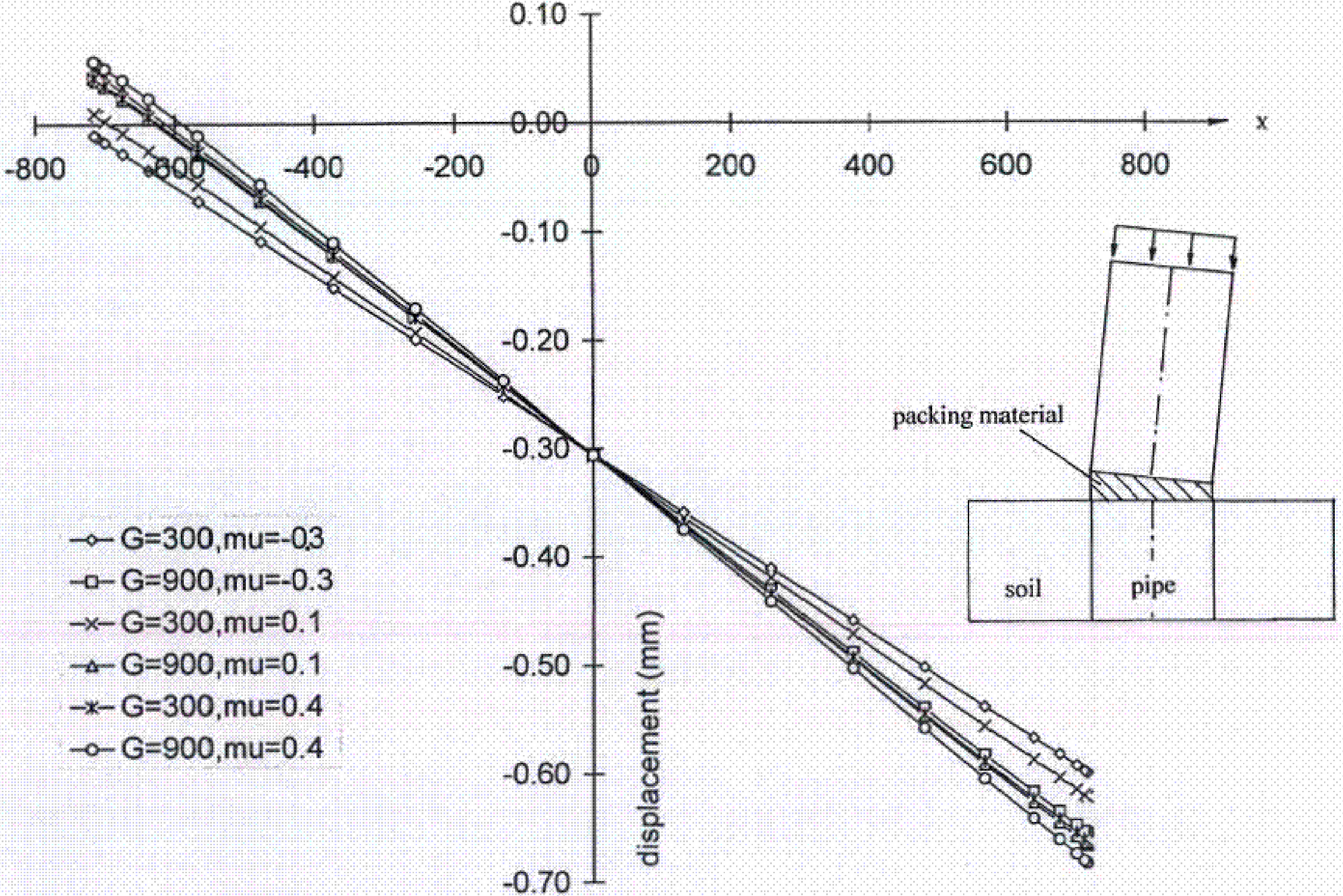

Figure 7.5 Compression displacement of the bottom pipe in numerical model C with $\beta=0.09^0$

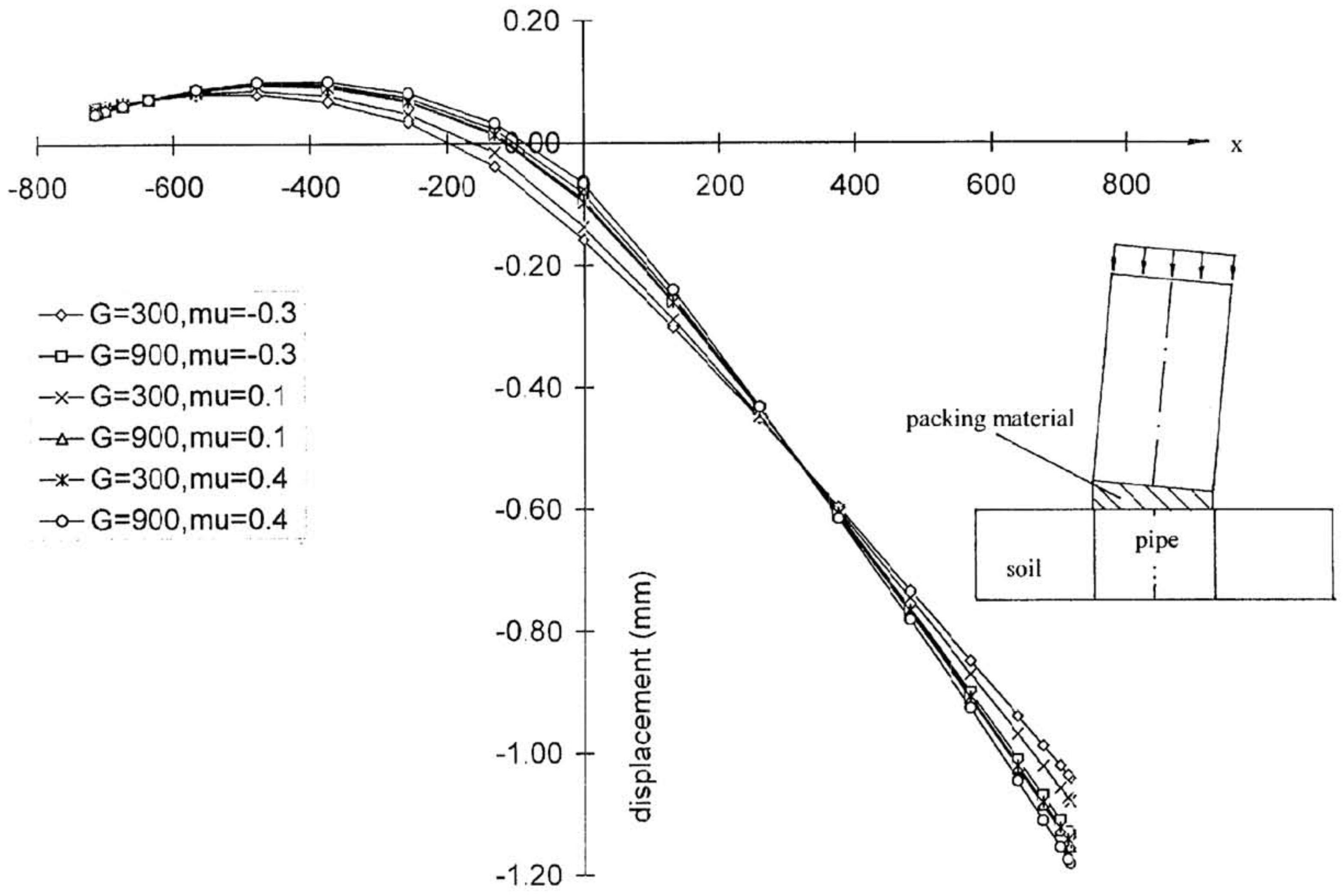

Figure 7.6 Compression displacement of the bottom pipe in numerical model C with $\beta=0.27^0$

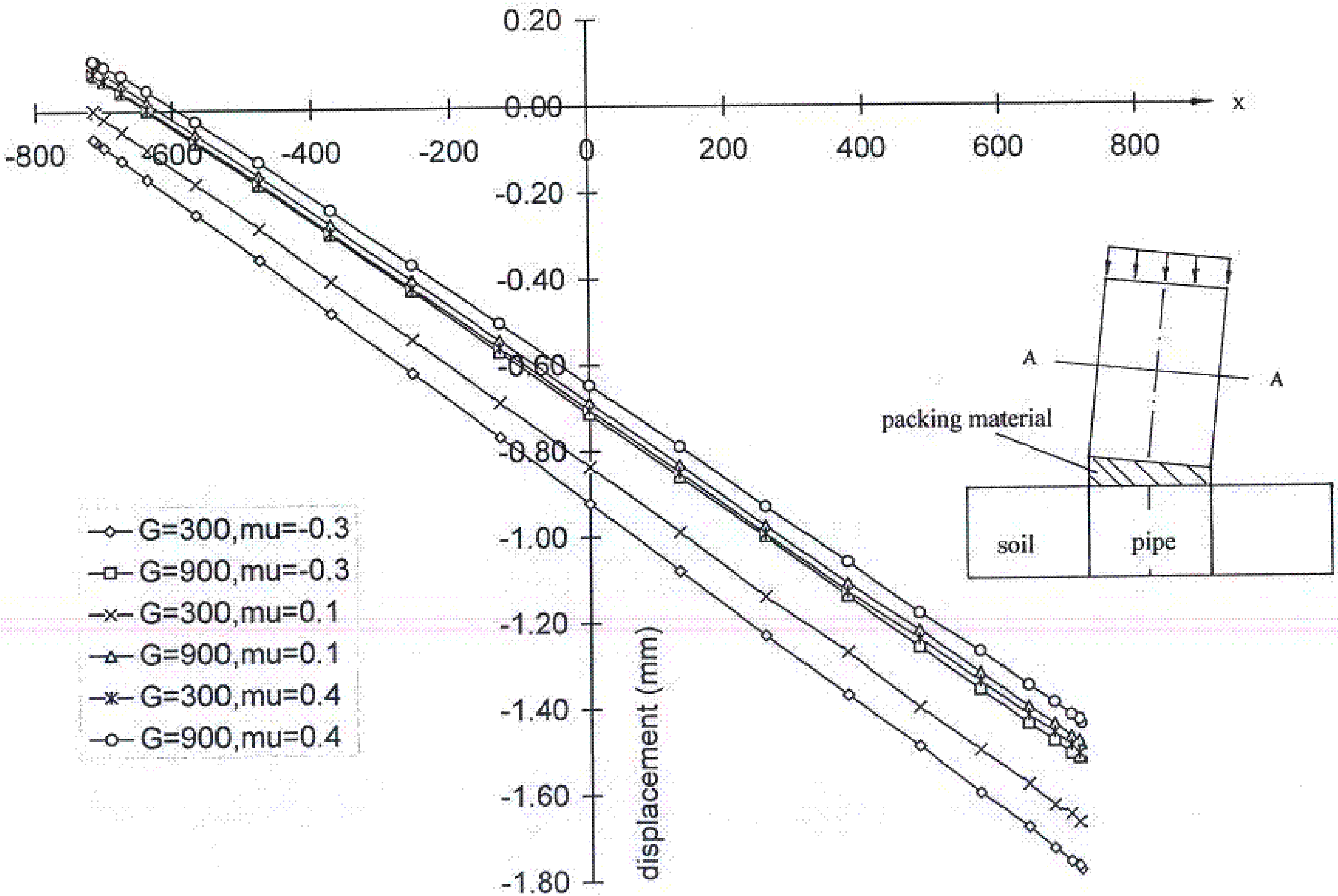

Figure 7.7 Total deformation at the joint in numerical model C with $\beta=0.09^0$

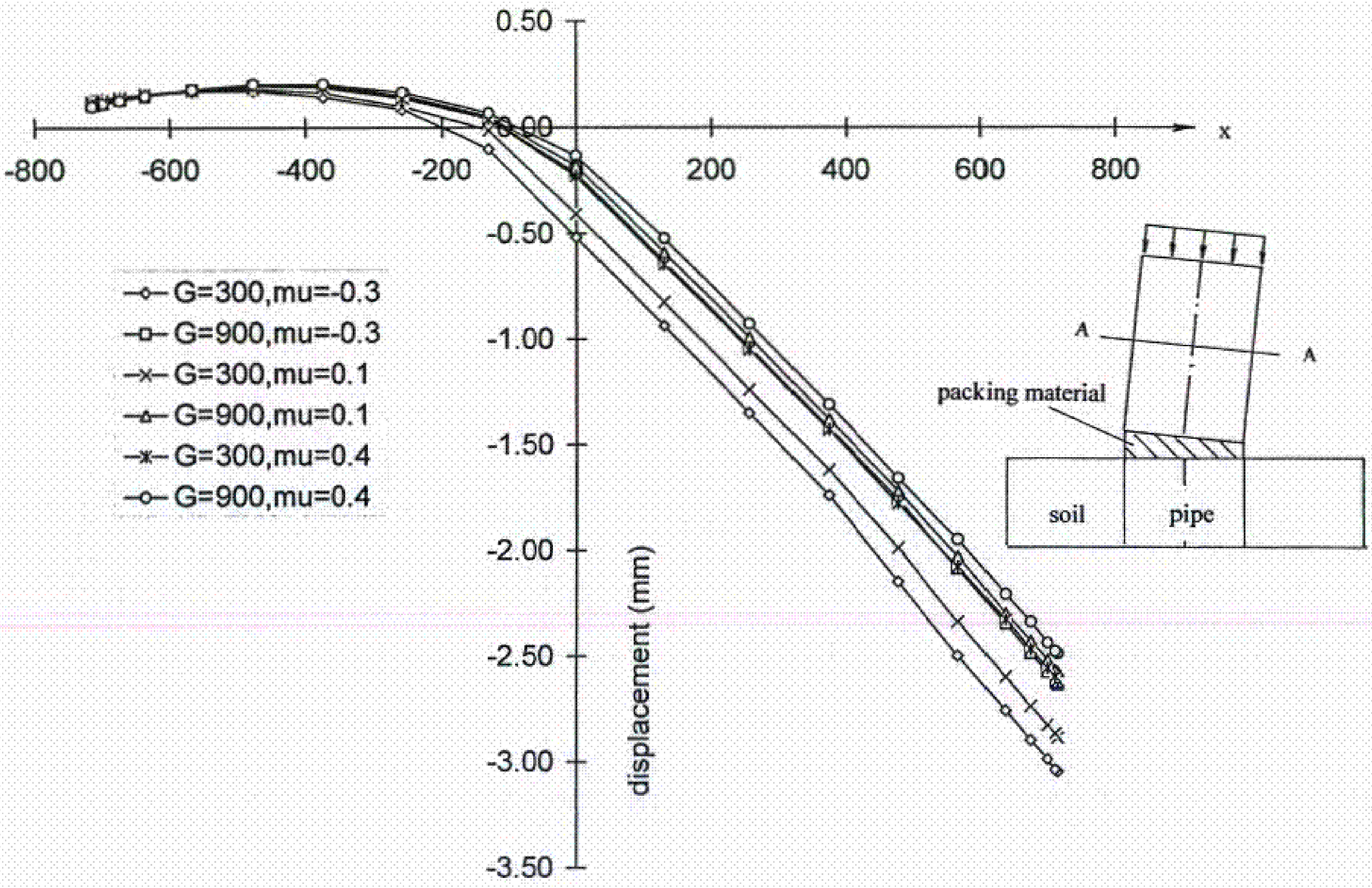

Figure 7.8 Total deformation at the joint in numerical model C with $\beta=0.27^0$

CHAPTER 8 LABORATORY TEST OF PIPE JOINTS

8.1 INTRODUCTION

Previous research (Craig 1983, Norris 1989, Milligan and Norris 1993) and the numerical results in Chapters 3 and 6 of the current research reveal that the misalignment of the pipeline causes stress concentrations in the region of the pipe joint under 'edge' loading condition. These stress concentrations will damage the pipe in severe cases. Since in practice all pipelines will contain some misalignments, improvement of the jacking pipes and the pipe joints will obviously reduce the chance of failures during pipe jacking. In general, there are two ways to achieve this. The first one is to reduce the stress concentrations at the pipe joint and the other is to raise the pipe's strength.

Use of packing material between pipes is proven to be a good way to reduce the stress concentrations (Milligan and Ripley 1989, Ripley 1989, Boot and Husein 1991, Husein 1989) and changing pipe end geometry is another possible way to lessen the stress concentrations. Two possible ways to raise the pipe strength are prestressing and reinforcement in the region of the pipe joint. All these four methods have been tested in the laboratory with model pipes. They are discussed in detail in Section 8.4 to Section 8.8 of this chapter after the discussion of the pipe casting and the test apparatus in Sections 8.2 and 8.3

8.2 PIPE CASTING AND CHARACTERISTIC TESTS

The model pipes were cast with sand as delivered to simulate the prototype pipes. To achieve a common cube strength of about 65MPa, the proportions of the different ingredients, cement, water, fine sand and coarse sand as shown in Table 8.1, were used after taking reference of the results from Ripley's research (1989). The cement was rapid hardening to reduce the curing period and hence shorten the overall time taken for the tests. This type of cement should produce the 28 day strength for ordinary Portland cement when samples are 7 days old. The results of the characteristic tests for the concrete cubes also show that the cube strength changed only a little after 7 to 9 days in summer.

Table 8.1 Ingredients of the concrete

cement	water	fine sand	coarse sand
23.68 %	7.58 %	28.84 %	39.87 %

One pipe and six associated 100mm cubes were cast each time using a vibration technique. The model pipes represented typical 1200mm internal diameter prototype pipes at a scale of about 1:6, and were produced using the mould designed by Ripley (1989), shown in Figure 8.1 and Plate 8.1. The dimensions of the model pipe are also shown in the figure. The modified end plate for an alternative pipe end geometry is discussed in section 8.5.

After casting, the associated cubes were then tested for crushing strength. The 9 day strength in summer and the 14 day strength in winter were used to normalize the pipe strength to allow for some factors such as water temperature, moisture content of the sand and curing. The strengths of the corresponding cubes are given in Table 8.2 and Table 8.3.

The results from the characteristic tests show that:

(1) The cube strengths are very close within one group (associated with the same pipe) although there are some strength differences between different groups.

(2) In general, the difference in strength between cubes of different groups reduces with time. The difference on the 9th day in summer or on the 14th day in winter is the smallest of the current test.

(3) On average, the compressive strength rises very little after 7-9 days in summer or after 12-14 days in winter.

(4) Combining the facts above, the strength on the 9th day in summer or on 14th day in winter is considered as a good reference strength for normalizing the pipe strength.

Table 8.2 Cube strength in summer (MPa)

pipe number	2 days	5 days	other time (No. of days)	9 days
1	38.25		51.8 (6)	55.7
1	36.23		63.6 (6)	54.9
2	30.59	46.8		51.7
2	29.96	42.9		52.9
3	42.77		57.9 (8)	58.1
3	43.04		60.7 (8)	60.4
4	41.17		55.5 (6)	59.0
4	41.65		57.5 (6)	58.8
5	49.98	62.1		66.3
5	49.4	63.5		65.9
6	50.4	62.4		65.8
6	50.3	66.4		69.1
7	47.04	64.2		66.0
7	45.91	63.2		66.2
8	45.84	57.2		64.5
8	46.31	57.8		63.5
9	46.03	58.5		64.3
9	45.86	58.3		63.6
10	42.54		59.9 (6)	64.0
10	42.41		57.1 (6)	63.3
11	46.71	59.6		63.6
11	45.77	59.6		64.4
12	47.27	61.1		67.3
12	47.23	60.9		66.4
14	50.40		60.7 (5.5)	64.7
14	50.50		60.9 (5.5)	64.6
19	50.10		64.0 (8)	63.7
19	50.50		63.7 (8)	65.2

Table 8.3 Cube strength in winter (MPa)

pipe number	2 days	9 days	other time (No. of days)	14 days
20	31.47		44.2 (5)	61.3
20	32.79		53.5 (7)	60.2
21	31.57		51.8 (5)	62.0
21	32.26		44.4 (3)	62.4
22	32.40		57.6 (11)	59.7
22	30.92	56.7		59.4
23	28.43		50.3 (7)	54.4
23	28.02	55.2		54.4
24	24.44		48.6 (10)	53.9
24	23.51		50.1 (12)	56.4
25	24.53		50.7 (8)	55.6
25	23.52		53.5 (10)	54.2

8.3 TEST APPARATUS

Since the damage of the jacking pipes is mainly due to the pipeline misalignment, it is essential to include the localization effect of the load distribution to assess the strength of the jacking pipes. To do this, two load plates have been designed as shown in Figure 8.2 and plate 8.2. Plate A with a square end is used to apply uniform pressure, while the plate B with an angled end ($\beta = 1.0^0$, this angle is similar to the actual applied misalignment angle in the numerical analysis; refer to Chapter 7) is used for non-uniform pressure to simulate the load localization caused by the pipeline misalignment. The upper steel ring and the stiffeners are designed to prevent bending deformation of the plate, so that the plate will move as a rigid block when loaded. In the tests, the load was applied to the centre solid steel block which also enhanced the stiffness of the load plate.

The test apparatus is shown in Figure 8.3 and Plate 8.3. The pipe was bedded on to the bottom steel block with plaster and the packing ring was stuck on the top of the concrete pipe when packing material is used. One of the load plates was then placed on the top of the pipe to provide uniform or non-uniform pressure depending on the type of test. A load cell was placed between the load plate and the hydraulic jack to record the applied load. Since the load plate is assumed to be rigid as discussed above, the pressure with plate B would be linearly distributed on each half of the pipe end if the packing material and the concrete pipe are linearly elastic. The maximum load of the test machine was 2000kN and the minimum load increment was 100N.

8.4 EFFECT OF PACKING MATERIAL

The use of packing material to reduce the stress concentrations is clearly seen to be effective, but its working mechanism is still not well understood. The ideal material is considered to be one that compresses greatly when loaded and recovers its thickness when unloaded, and has a low Poisson's ratio so that it does not induce extra tensile stresses in the concrete pipe. Ripley (1989) has done comprehensive laboratory tests for various packing materials, such as dense fibreboard, chipboard, plywood, softboard, German chipboard, plane timber and blockboard, to seek the material closest to the ideal. The tests were carried out to investigate the responses of the packing materials between two concrete blocks under compression. The tests included the effects of cyclic loading, material thickness and material saturation condition. The conclusion is that fibreboard, chipboard and to a lesser extent plywood are good packing materials (Milligan and Ripley 1989, Ripley 1989). The research from Boot and Husein (1991) and Husein (1989) gives a similar conclusion about the importance of the packing material in pipe jacking with clay pipes, as discussed in Chapter 1.

In the present test, however, the aim is to investigate the effect of the packing material on the pipe strength instead of the response of the packing material, that is, the test is used to investigate the effect of material properties on the stress distribution in the concrete pipes.

Similar work has also been done by numerical analysis in the current research and the numerical results of the current research (refer to Chapter 3 and Chapter 6) confirm that materials which have a low Poisson's ratio and are very compressible are good packing materials.

Plywood and rubber were chosen for this test because they have quite different Poisson's ratio, which showed a significant influence on the stress distributions at the pipe joint according to the numerical results in the current research. The size of the packing ring is shown in Figure 8.4. Plate 8.4 shows a typical plywood packing ring. The scales of the pipe and packing ring were the same, about one sixth of those used in practice. The tests were carried out in three pipe groups, one without packing material, one with plywood packing and one with rubber packing. The pipe strength without packing material is used as reference strength. Within each group, one pipe was tested under uniform pressure with load plate A, while the rest were tested under non-uniform pressure with load plate B to include the effect of load distribution.

The purpose of the tests was to investigate the overall improvement in pipe performance rather than to study localised deformations. Therefore the pipe themselves were not instrumented , but the load was accurately monitored with a load cell and careful observations were made of spalling, crack generation and failure mode. The failures were all global ones for pipes under uniform pressure, while failures under non-uniform pressure showed more or less localization. For the first pipe group (without packing), there was some spalling in the region of the pipe joint, then some cracks appeared at the early load stage (35 to 50 percent of final load) near the pipe joint especially under non-uniform pressure. For the pipes with rubber packing, the phenomena were similar, except that the spalling was more severe, and cracks appeared much earlier (at 20 to 30 percent of final load) and developed into big cracks very quickly. As for the group with plywood packing material, only at a late load stage was there some spalling and cracking, and the failure modes were less localized than those in the other two groups. The results of the final pipe strengths are given in Table 8.4, where normalized strength is defined as $\frac{ultimate\ load}{pipe\ cross\ section\ area \times cube\ strength}$.

Table 8.4 Final pipe strength with different packing materials

pipe	load type	packing	normalized strength (%)
1	uniform (A)	no	84.87
3	non-uniform (B)	no	42.98
4	A	plywood	82.76
5	B	plywood	53.49
6	B	plywood	54.04
7	A	rubber	55.20
8	B	rubber	cracked very early
9	B	rubber	45.51
10	B	rubber	41.95

The results from the tests are summarised as following:

(1) For the uniform pressure, plywood packing material has almost no effect on the final pipe strength while rubber lowers the pipe strength. This has also been noticed in the numerical analysis, although some people consider that as a packing material rubber has no effect on the pipe strength.

(2) Under non- uniform pressure, the plywood packing material improves the pipe strength by over ten percent, while the rubber has almost no effect on the final pipe strength. However, the rubber packing makes the pipe crack at a very low load stage (about 20-30 percent of final load), which would make the pipe lose its function due to leaking. This result was somewhat unexpected.

(3) Under non-uniform pressure, the spalling mainly appeared at the positions under the maximum pressure (in the region of $\theta=0^0$ and 180^0), while the cracks appeared at first in the region of $\theta=90^0$ and 270^0 near the pipe joint. Moreover, after failure it was found that there were more cracks on the internal surface in some pipes than on the external surface observed during the tests.

(4) From the results of both laboratory tests and numerical analyses in Chapters 3 and 6, it is easy to see that any material with a high Poisson's ratio should be avoided for use as packing material in pipe jacking.

(5) Further tests should be carried out to investigate other properties of packing material, such as stiffness and thickness, although some numerical analyses have been carried out about the stiffness of the packing material.

8.5 EFFECT OF PIPE END GEOMETRY

Another possible way to reduce stress concentrations is to use a pipe with different end geometry which can increase the contact area in the case of misalignment of the pipeline. To achieve this, an end plate was designed as shown in Figure 8.5. Three pipes were cast with this new end plate.

The tests included all three pipes with plywood packing material. One pipe was tested under uniform pressure and the other two under non-uniform pressure. The final results are given in Table 8.5.

Table 8.5 Final pipe strength with new end geometry

pipe	load type	packing	new pipe end	normalized strength (%)
11	A	Plywood	yes	73.89
12	B	Plywood	yes	54.42
13	B	Plywood	yes	57.29

In comparison with the conventional pipe end group with the same packing material in Section 8.4, failure under non-uniform pressure appeared more global. There was no spalling and fewer cracks even at a late load stage. Again, the cracks were first spotted in the region of $\theta = 90^0$ and 270^0 (under the minimum pressure positions) near the pipe joint. The test results are summarised as follows:

(1) The pipe strength falls a little under uniform load due to the contact area reduction at the pipe joint as expected.

(2) For non-uniform load, the pipe strength with new pipe end is only a little higher than that with the conventional pipe end. However, the new geometry effectively prevents the problem of spalling at the pipe joint and cracking at low load level. Hence it will allow the pipe to perform more effectively during its working life.

(3) In the current tests, the bevel angle (1^0) of the pipe end is the same as that of the load plate, further experiments are needed with different angles of the pipe end to form a better understanding of the effect of alternative geometry of the pipe end.

(4) A more detailed study could also be carried out by numerical analysis, for instance to investigate the effects of varying different parameters of the pipe end, such as the magnitude of the bevel angle and the extent of the bevel.

8.6 EFFECT OF LOCAL PRESTRESSING

In order to prevent pipe failure, the pipe strength can be improved rather than reducing the stress concentrations. The numerical analysis in the current research shows that non-uniform axial (longitudinal) pressure will induce some tensile stresses (mainly in the circumferential direction) in the region of the pipe joint; and it is also known that concrete usually fails due to tensile stresses and has quite high strength under compression (Jian and Feng 1991, Neville 1981). According to the theory of elasticity (Timoshenko and Goodier 1970), local prestressing (pressure in the radial direction on the external surface of the pipe) will produce compression stresses in the circumferential direction in the region of the pipe joint, in turn such pressures will reduce any tensile stresses in the region without inducing new stress concentrations and hence in theory improve the pipe strength. In order to apply local prestressing to the concrete pipes in the region of the pipe joint, a steel band was designed as shown in Figure 8.6 and Plate 8.5. The internal diameter of the steel band was slightly smaller than the external diameter of the concrete pipe, so prestresses could be applied by tightening the steel band.

The tests again included three pipes all with plywood packing material, and with local prestressing provided by the steel band shown in Figure 8.6. Again one pipe was tested under uniform pressure and other two under non-uniform pressure. The phenomena were similar to those in the group with the new pipe end geometry in Section 8.5. More precisely, there was again no spalling problem and cracks appeared only at a very late load stage. The pipes suffered global failures in general. The final pipe strengths are shown in Table 8.6 and are higher than those without prestressing.

Table 8.6 Final pipe strength with local prestressing

pipe	load type	packing	prestressing	normalized strength (%)
14	A	plywood	yes	76.53
15	B	plywood	yes	61.03
16	B	plywood	yes	56.71

The results in this section are summarised as following:

(1) The pipe strength falls a little under uniform pressure due to the local effect of the prestressing.

(2) For non uniform pressure, the final pipe strength is improved by about ten percent. The prestressing also prevents the spalling and cracking problems.

(3) Cracks on the external pipe surface appeared at the late load stage and were located below the steel band.

(4) Some more research should be done about the effect of the magnitude and the location of the prestressing.

8.7 EFFECT OF LOCAL REINFORCEMENT

Local reinforcement is another possible way to improve the pipe strength. Unlike local prestressing, its working mechanism is to let the steel reinforcement take the tensile stresses at the pipe joint. From the numerical analysis in the current research, it is known that the stress concentrations appear in the region of the pipe joint and tensile stresses exist mainly in the circumferential direction. To make use of the reinforcement efficiently, a steel cage was designed for local reinforcement in only the circumferential direction in the region of the pipe joint. The cage is shown in Figure 8.7 and Plate 8.6, where the few small longitudinal wires only were required to form the cage.

The tests in this group again included three pipes with plywood packing material, one under uniform pressure and the other two under non-uniform pressure. Similarly, the pipes suffered global failures. There was again no spalling before failure of the pipe and some small cracks appeared just before failure. However, the final pipe strengths under non-uniform pressure were much higher than those without reinforcement as discussed in Section 8.4. The results are shown in Table 8.7.

Table 8.7 Final pipe strength with local reinforcement

pipe	load type	packing	reinforcement	normalized strength (%)
17	A	plywood	yes	78.55
18	B	plywood	yes	67.11
19	B	plywood	yes	62.25

The test results are summarised as follows:

(1) The pipe strength falls very little under uniform pressure due to the local effect of the reinforcement.

(2) For non-uniform pressure, the final pipe strength has improved by about twenty percent. Reinforcement has also prevented the spalling and cracking problems.

(3) Cracks appeared at first below the reinforcement in the region of $\theta=0^0$ and 180^0 (under the two maximum pressure positions).

(4) The location of the local reinforcements, the difference between circumferential and longitudinal reinforcement, and the difference between local and overall reinforcement should be studied in the future.

8.8 FURTHER INVESTIGATIONS OF COMBINING FACTORS

So far, several factors such as packing material, pipe end geometry, local prestressing and local reinforcement, have been discussed. All the tests were with packing material except those for reference strength. To check how the improved pipe would perform without packing material, a few more pipes were tested. In the current group, one pipe was tested under uniform pressure with the modified end geometry and local reinforcement. The other four were tested under non-uniform pressure with local reinforcement, and with the end geometry and packing condition shown in Table 8.8.

During the tests, there was no spalling problem except for the pipe with the square end. However, cracks appeared at about 55-65 percent of the final load, excepting the pipe with plywood packing material where cracks occurred just before failure of the pipe. The final strengths of the pipes are given in Table 8.8.

Table 8.8 Final pipe strength of different factors

pipe	load type	packing	new end	reinforcement	normalized strength (%)
21	A	No	Yes	Yes	52.41
22	B	No	Yes	Yes	34.50
23	B	No	Yes	Yes	44.00
24	B	plywood	Yes	Yes	63.30
25	B	No	No	Yes	39.76

The summarisation of the test results in this section is as follows:

(1) The modified end geometry and local reinforcement cannot achieve their goal of improving the pipe strength without good packing material.

(2) The modified end geometry has a small effect on the final pipe strength, but prevents the spalling problem very efficiently even without packing material.

(3) The results show once more that local reinforcement can increase the pipe strength by about twenty percent when with a good packing material.

8.9 A FEW COMMENTS

So far, four different methods for possible improvement of pipe strength have been tested with model pipes and discussed in detail in Sections 8.4 to 8.8. A few failed pipes are shown in Plate 8.7. From a general point of view, a few more comments are given as following:

(1) Packing material is the key factor for strength improvement of the jacking pipe under non-uniform pressure because other methods increase the pipe's strength only with the help of good packing material. However, packing material can improve the pipe strength or make things worse depending on the type of packing material. Material with high Poisson's ratio, like rubber, should be avoided for use as packing material.

(2) All these methods prevented spalling and early cracking to some extent. With plywood packing, the local prestressing and local reinforcement improve the pipe strength by about ten and twenty percent respectively.

(3) Numerical analyses, especially parametric studies, can be carried out to examine some effects in detail, such as the location of the reinforcements and the magnitude of the prestressing.

(4) In the current tests, the pattern of the non-uniform pressure is not exactly that in pipe jacking and the tests were carried out with model pipes. In future, tests more accurately simulating prototype conditions should be carried out.

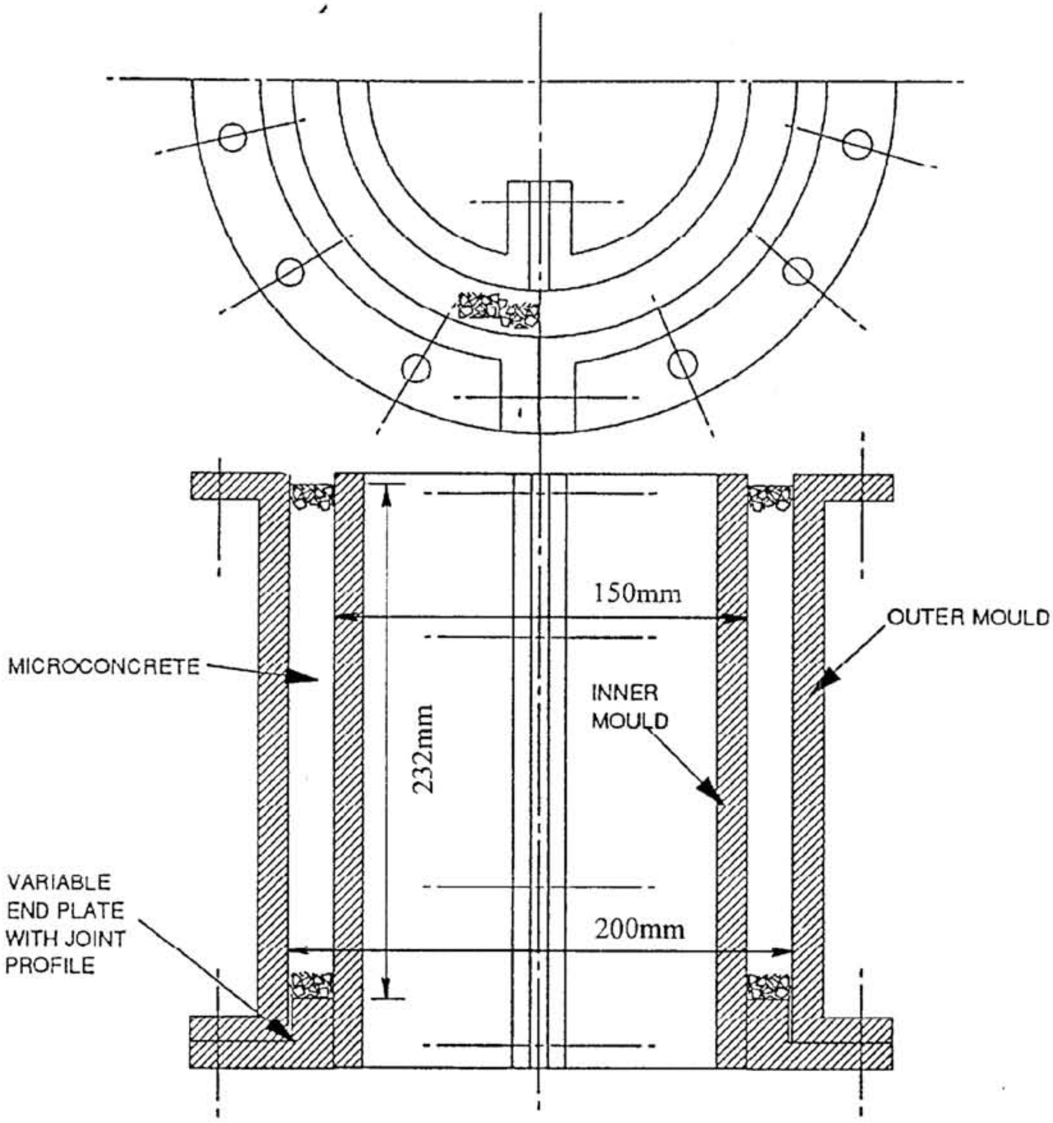

Figure 8.1 Model pipe mould (from Ripley 1989)

Plate 8.1 Mould used for construction of model pipes (from Ripley 1989)

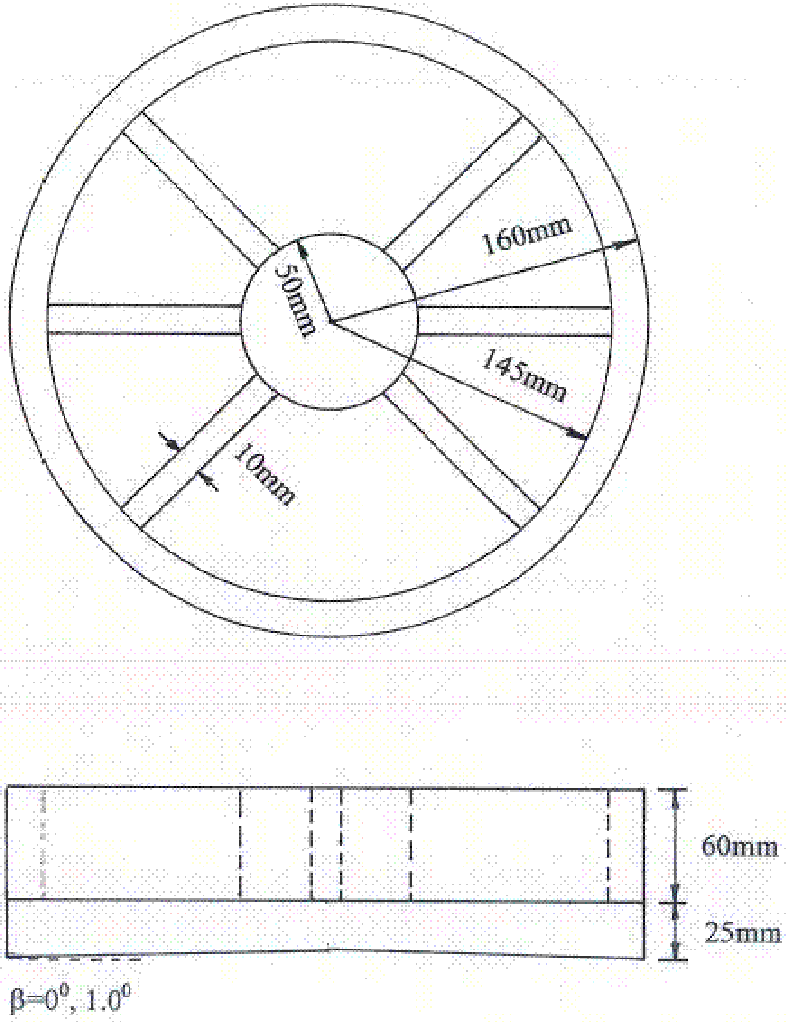

Figure 8.2 Design of load plates

Plate 8.2 A steel load plate

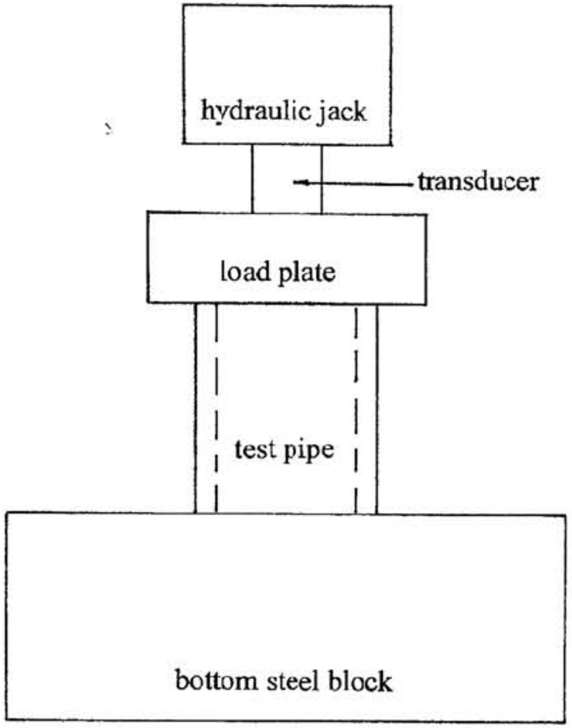

Figure 8.3 Arrangement of the test apparatus

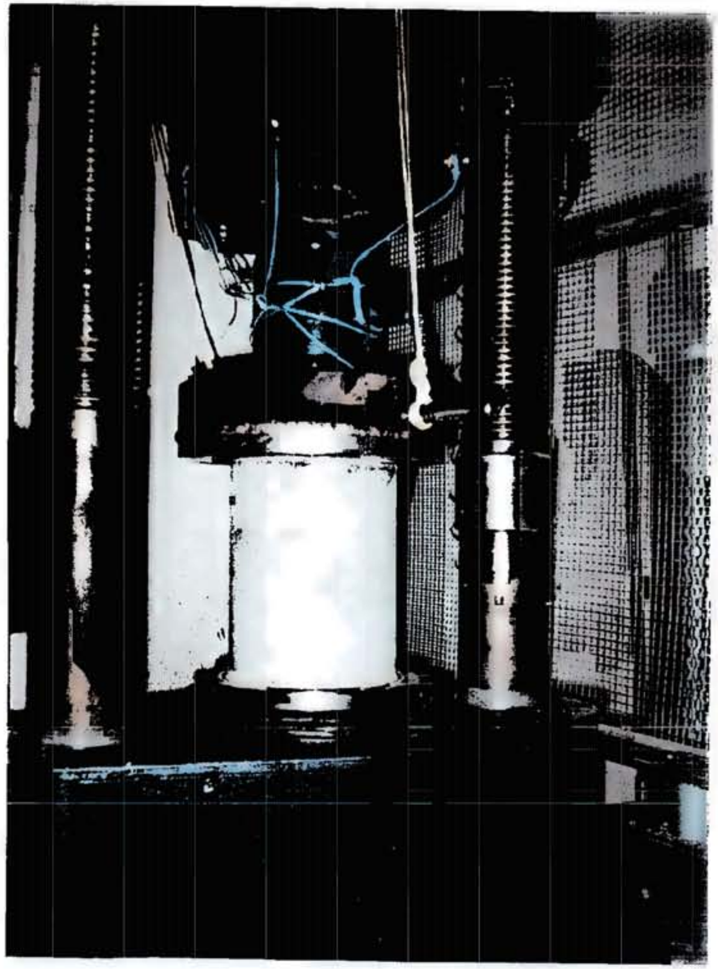

Plate 8.3 A general view of the test apparatus

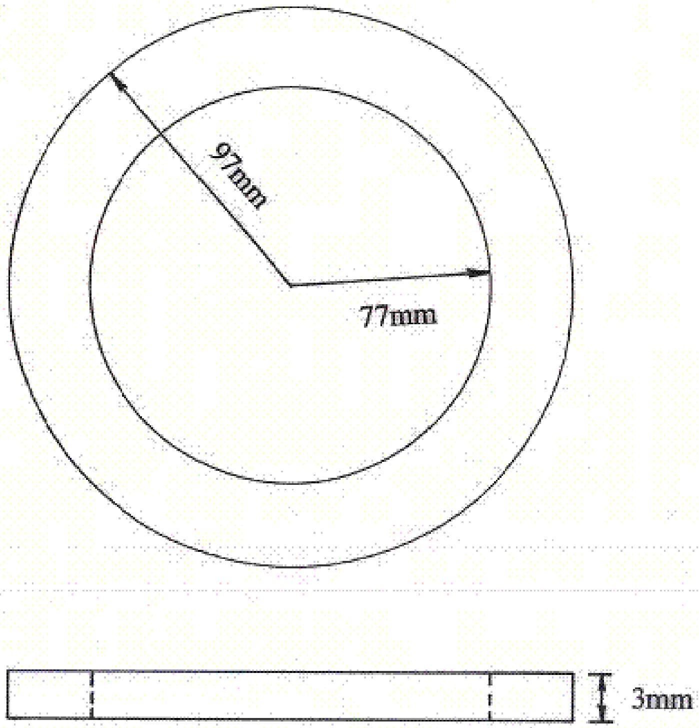

Figure 8.4 Design of the packing ring

Plate 8.4 A plywood packing ring

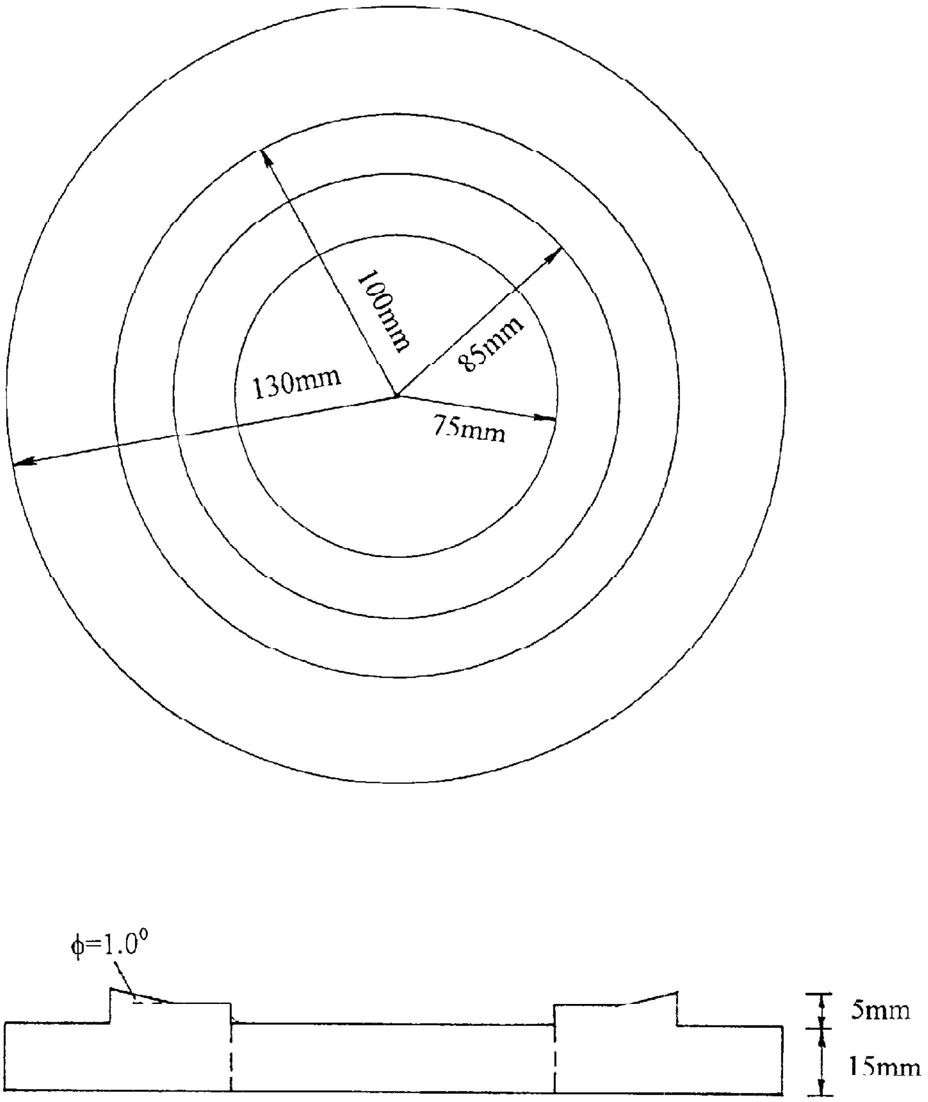

Figure 8.5 Plate for alternative pipe end geometry

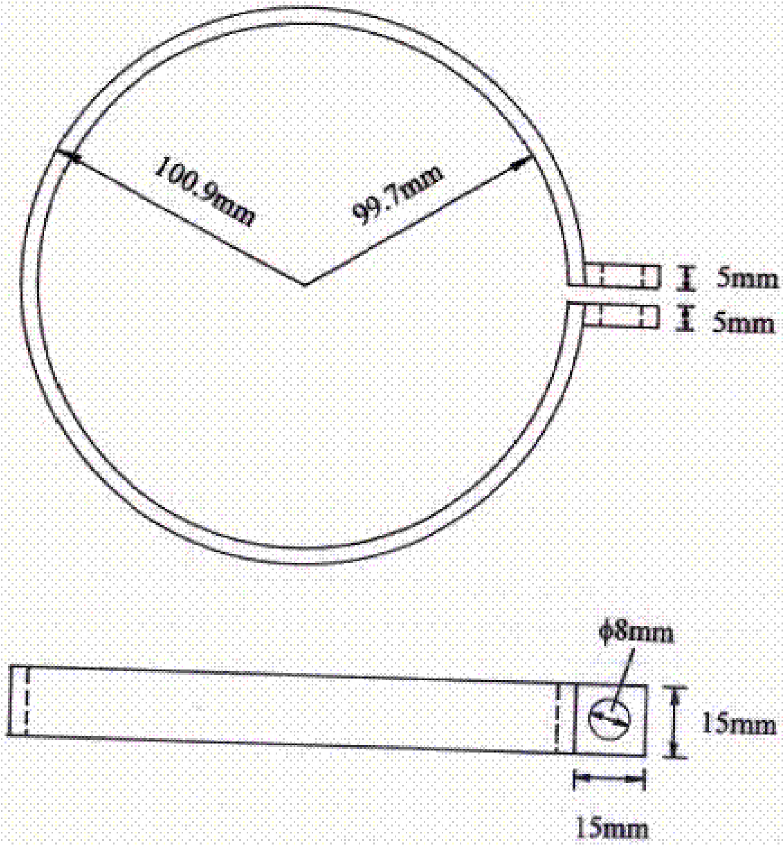

Figure 8.6 Steel band for prestressing

Plate 8.5 A prestressing steel band

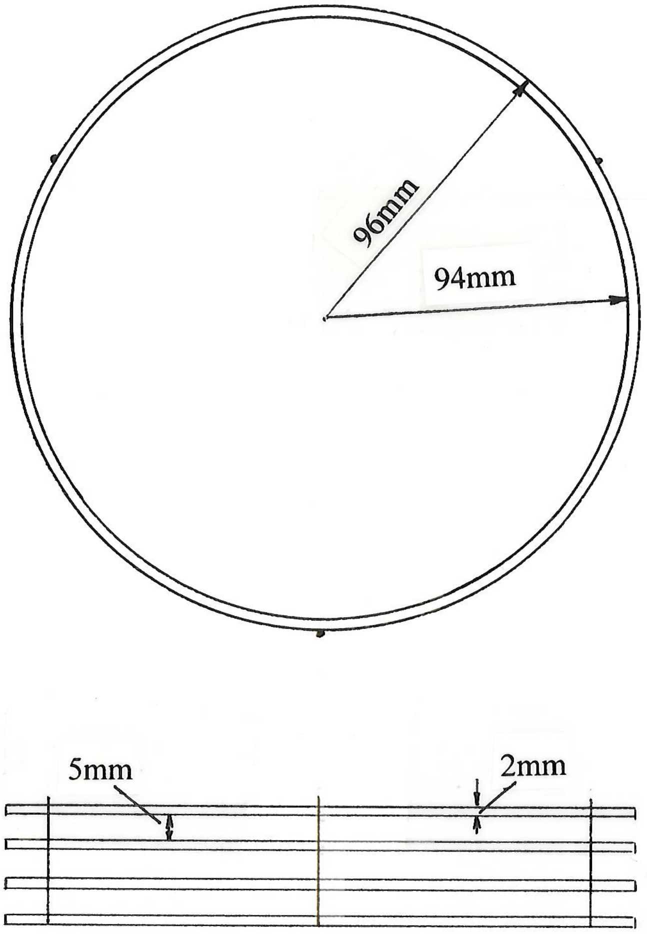

Figure 8.7 Steel cage for local reinforcement

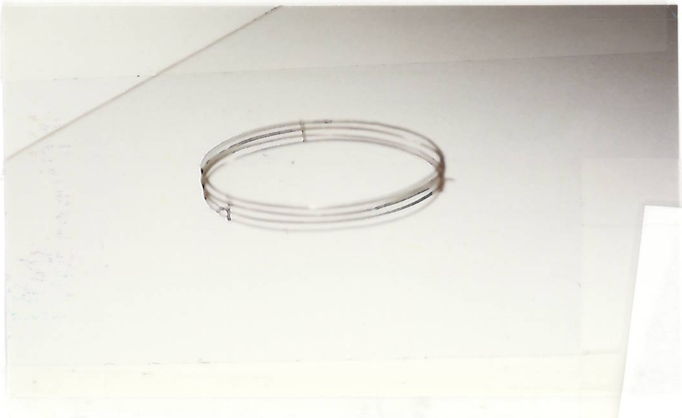

Plate 8.6 A typical reinforcement cage

Plate 8.7 Three Typical failed pipes

CHAPTER 9 BACK ANALYSIS OF TEST DATA

The experimental results show clearly the advantages of local reinforcement, local prestressing and good packing material. The influence of the packing material has been studied in Chapters 3 and 6. In this chapter, a numerical model of back analysis is described in Section 9.1. Numerical back analysis of the local reinforcement and of the local prestressing are discussed in Sections 9.2 and 9.3 respectively. The numerical back analysis was extended to include the effect of the location of the reinforcement and the effect of the magnitude of the prestress.

9.1 NUMERICAL MODEL OF BACK ANALYSIS

The arrangement of the test apparatus was described in Figure 8.3 in Chapter 8. There were two load plates used in the tests, plate A to apply uniform pressure and plate B for non-uniform pressure. Because the plain concrete pipe performs very well under uniform pressure, the back analysis was only carried out for the tests with the angled load plate B to assess the effect of the reinforcement and of the prestressing at the pipe joint. Although the total applied load was recorded by a load transducer, there was no measurement of the load distribution at the top of the pipe. In the back analysis, a linear load distribution was assumed at each side on the top of the pipe as shown in Figure 9.1 according to the observation from the carbon film paper which was put between the pipe and the load plate during the test. The total applied load on the pipe end was P = 200kN. Due to the symmetry of the pipe, the boundary condition and the applied loads, only a quarter of the pipe was used in the analysis as shown in Figure 9.2. The boundary conditions in the analysis included the nodes fixed at the pipe bottom, and the symmetrical conditions on the plane $x = 0$ and $y = 0$.

In the back analysis, the concrete pipe was assumed to have the same elastic material constants as the model pipes used by Ripley (1989), the Young's modulus E_c = 31700MPa and the Poisson's ratio μ_c = 0.22, since they were constructed with the ingredients in the same ratio (refer to Table 8.1 in Chapter 8). To model the stress redistribution in the pipe without using complex concrete models, a modified Matsuoka model described in Chapter 2 was used for the concrete pipe in the back analysis. From the characteristic tests described in Chapter 8, it is known that the cube strength and the compression strength of the concrete pipe in the experiment were about 60MPa and 50MPa respectively. When a typical ratio of $\frac{1}{10}$ (Jiang and Feng 1991, Neville 1981) between the tensile and compression concrete strength was used with an associated flow rule, the material parameters with this model in the analysis were a triaxial frictional angle $\phi = 54.9^0$, a triaxial dilation angle $\psi = 54.9^0$ and a tensile strength f_t = 5MPa.

As discussed in Chapter 2, the modified Matsuoka model does not consider the cracking behaviour of the concrete which is beyond the scope of the current project, instead the maximum tensile stress in the concrete pipe was restricted to be below or equal to the tensile strength of the concrete in this model. This means that the back analysis described in this Chapter didn't examine the cracking behaviour of the concrete pipe and the failure load. Rather, the aim was to understand the working mechanism of the local reinforcement and the local prestressing and to confirm the experimental results.

9.2 BACK ANALYSIS OF LOCAL REINFORCEMENT

The extended back analysis of the local reinforcement is described in this section. In order to include the effect of the location of the reinforcement, the back analyses were extended with three different cases, the case CR with the plane pipe (without reinforcements), the case RE1 with the reinforcements near to the external pipe surface as used in the experimental tests and the case RE2 with the reinforcements near to the internal surface of the pipe. In the analysis, 8-node brick elements and 3-node bar elements were used. The finite element meshes are shown in Figure 9.2(a), 9.2(b) and 9.2(c) for the CR, RE1 and RE2 respectively. The quarter of the pipe used in the analysis was between $\theta = 90^0$ and $\theta = 180^0$ as shown in Figure 9.2(d). The reinforcements were modelled by elastic bar elements (refer to Section 2.5 in Chapter 2). A typical steel Young's modulus E_{st} = 200GPa was used for the steel bars and the cross sectional area of the bar was $A = 6.28\text{mm}^2$ as shown in Figure 8.7 in Chapter 8. For simplicity, the bond between the reinforcing bars and the concrete was considered to be perfect. The analysis was carried out using the modified Newton-Raphson method described in Chapter 2. The number of calculation steps was 400.

To examine the pipe performance, only the stresses in the concrete pipe are discussed and presented in this chapter with the stresses in the reinforcing steel bars excluded. The most tensile principal stresses within the concrete pipe are shown in Figures 9.3(a), 9.3(b) and 9.3(c) for the cases CR, RE1 and RE2 respectively. From the figure, it is clearly seen that the tensile stresses in all three cases have similar distribution patterns and reach the tensile strength (5MPa) in the region of $\theta = 90^0$ on the internal surface at first (the tensile stresses are mainly in the hoop direction). This possibly explains why there are many cracks found on the internal surface of the pipe after failure. However, the size of the domain with high tensile stresses in the cases of RE1 and RE2 is smaller than that in the case of CR because the reinforcing bars have undertaken some of the tensile stresses, especially in the case of RE2.

The most tensile principal stresses within the pipe viewed from the opposite direction are shown in Figures 9.4(a), 9.4(b) and 9.4(c) for the cases CR, RE1 and RE2 respectively (the region of $\theta = 180^0$ is at the right side in Figure 9.4). Again, the figure shows that the stress distribution patterns are similar to some extent in all three cases and the high tensile stresses are mainly located at or near the pipe joint, where the pipe usually failed during the laboratory tests. Moreover, the results indicate that with the reinforcements at the pipe joint, cracks may first appear in the region of $\theta=180^0$ below the reinforcement on the external surface as found during the tests (refer to Section 8.7 in Chapter 8). The maximum tensile stress reduces in the cases of RE1 and RE2 compared with that in the case of CR due to the effect of the reinforcing steel bars.

From the discussion above, the back analysis clearly shows that the tensile stresses first reach the tensile strength on the internal surface in the region $\theta = 90^0$ at the right top corner of the pipe, then the tensile stresses redistribute into the adjacent region and across the pipe thickness towards the external surface of the pipe due to the failure of the concrete (in the current material model, this means the concrete cannot take more tensile stresses); and that the reinforcements take some tensile stresses over from the failed concrete and improve the pipe's performance. Moreover, the reinforcements in the case RE2 have a greater effect than those in the case RE1 because the high tensile stresses are mainly located on the internal surface of the pipe. In practice, due to the cracking (which is not considered in the current project), the concrete would soon lose its capacity to sustain tensile stresses after reaching the tensile strength (Jiang and Feng 1991, Neville 1981), and the stress redistribution would be quicker and larger than that predicted in this back analysis. This means the effect of the reinforcements could be bigger than that shown in Figures 9.3 and 9.4 especially in the case of RE1. In order to examine the detailed failure mechanism in the reinforced concrete pipe, a complex material model is needed.

9.3 BACK ANALYSIS OF LOCAL PRESTRESSING

The extended back analysis of the local prestressing is described in this section. The prestressing was applied at the pipe joint by a steel band as shown in Figure 9.5(a) before the pipe was fixed on the bottom steel block (refer to Section 8.6 in Chapter 8). To model this problem, there were two analysis stages in the back analysis. At first, a uniform pressure from the prestressed steel band was applied on the external surface of the plain concrete pipe at the joint with the pipe simply supported at the bottom as shown in Figure 9.5(c); the finite element mesh was the same as shown in Figure 9.2(a) for the plain pipe; and the boundary conditions included the nodes pinned at the pipe bottom and the symmetrical conditions on the plane of $x = 0$ and $y = 0$. In the second analysis stage, for simplicity the prestressed steel band was modelled as elastic reinforcing bars at the external surface of the pipe as shown in Figure 9.5(b), and the applied load and boundary conditions were the same as those described in Section 9.2. The cross sectional area of the steel band was $A = 18\text{mm}^2$ as shown in Figure 9.5(a) (the middle reinforcing bar had a cross sectional area of 9mm^2 and the cross sectional area for the other two bars was 4.5mm^2). The bond between the reinforcing bars and the concrete was again treated as perfect and the steel Young's modulus was $E_{st} = 200\text{GPa}$. Only a quarter of the pipe was used in the analysis due to the symmetry of the pipe, the loading condition and the constraint conditions. To examine the influence of the magnitude of the local prestressing, the back analyses were also extended with two cases, the case PR1 with q = 5MPa which was calculated from the experimental data and the case PR2 with q = 1MPa. Again, the analysis was carried out using the modified Newton-Raphson method. The number of calculation steps was 50 for the first analysis stage and 400 for the second stage.

The most tensile principal stresses within the concrete pipe (the stresses in the steel band are not included) are shown in Figures 9.6(a) and 9.6(b) for the case of PR1 and PR2 respectively, while Figures 9.6(c) and 9.6(d) show the most tensile principal stresses viewed from the opposite direction (that is, the region of $\theta = 180^0$ is at the right side in Figures 9.6(c) and 9.6(d)). Comparing with the stresses in Figure 9.3(a) in Section 9.2, it is clear that the stress distribution patterns on the internal surface are somewhat similar in the cases of CR, PR1 and PR2. However, the high stress domains in the case of PR1 and PR2 are smaller than that in the case of CR, especially in the case of PR1. On the external surface of the pipe, the high stresses are located below the steel band which is the region in which cracks were first spotted during the tests. The maximum tensile stress in the case of PR2 is lower that that in the case of CR, however, in the case of PR1, the maximum tensile stress is higher.

From the discussion above, it is clear that the local prestressing is very effective to reduce the tensile stresses on the internal surface of the pipe at the pipe joint due to the compressive stresses produced by the prestresses on the external pipe surface (Timoshenko and Goodier 1970). Furthermore, the steel band also reduces the tensile stresses on the external surface of the pipe acting as reinforced steel bars. However, the magnitude of the prestress should be controlled well to avoid a worse situation on the external surface of the pipe due to the local effect. The results in the back analysis also show that the magnitude of the prestresses used in the experiment in Chapter 8 are slightly higher than necessary because it worsens the tensile stresses on the external surface of the pipe. This is possibly the reason why the local reinforcement gives a better improvement in the pipe performance than the local prestressing in the experiment.

9.4 DISCUSSION

From the discussion above, the back analysis described in this chapter demonstrates the improvement of the stresses in the concrete pipe with the local reinforcement and the local prestressing using a simple modified Matsuoka model. In general, the location of early cracks spotted during the test agree well with the region of high tensile stress in the analysis. The results in this chapter confirm the improvement of the use of local reinforcement and local prestressing. This means that the local reinforcement and the local prestressing can be applied to improve the design of prototype concrete pipe. Due to the complicated nature of the problem, the final failure mechanism and the failure load are out of the scope of this back analysis. Further research is needed to examine the cracking behaviour of the concrete in order to have a better understanding of the pipe's performance in practice.

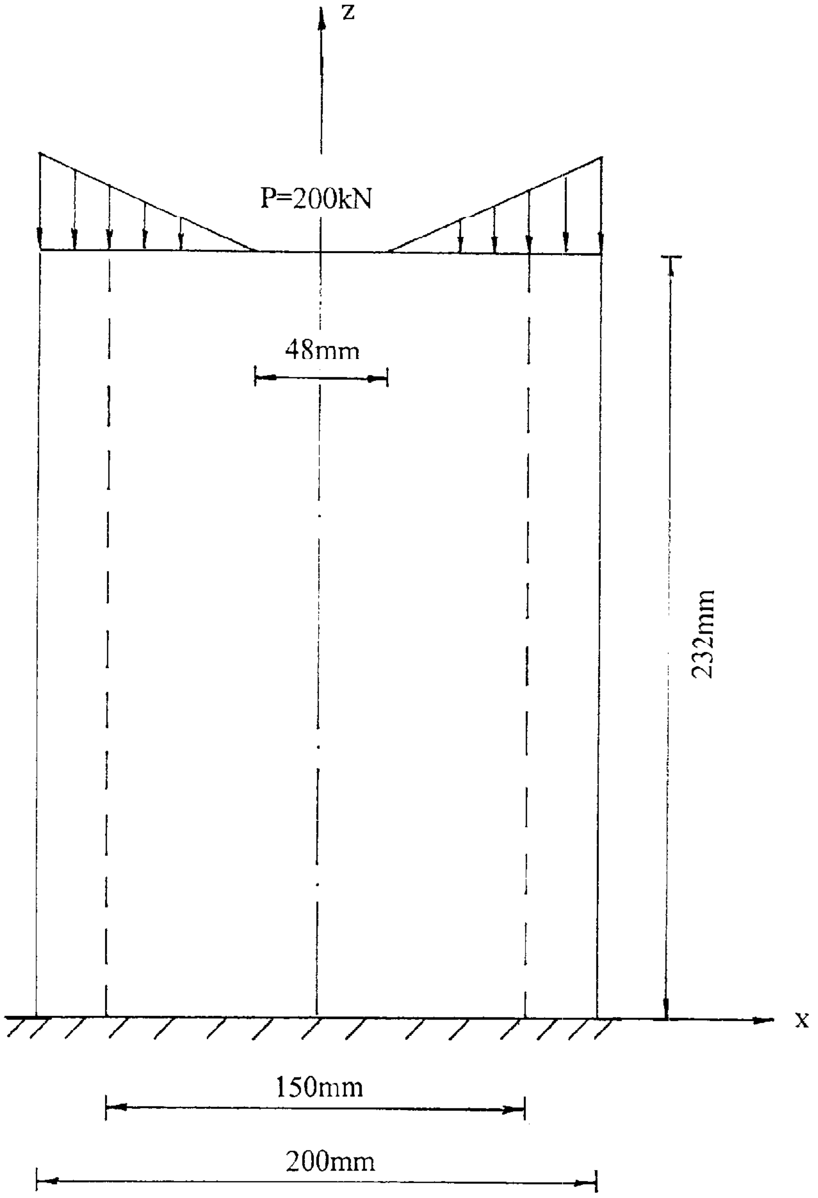

Figure 9.1 Loading and boundary condition of the tests

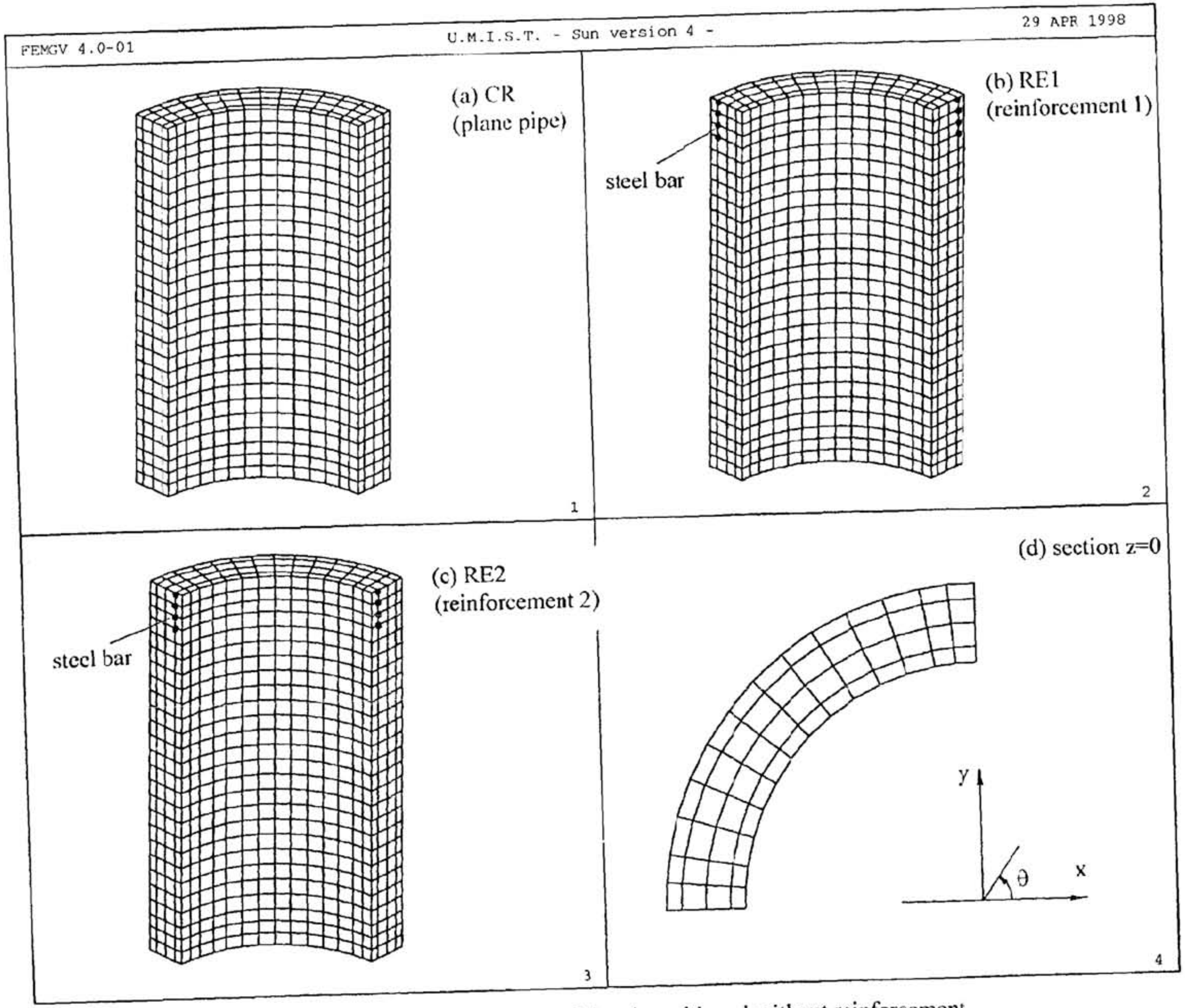

Figure 9.2 Finite element meshes of the pipe with and without reinforcement

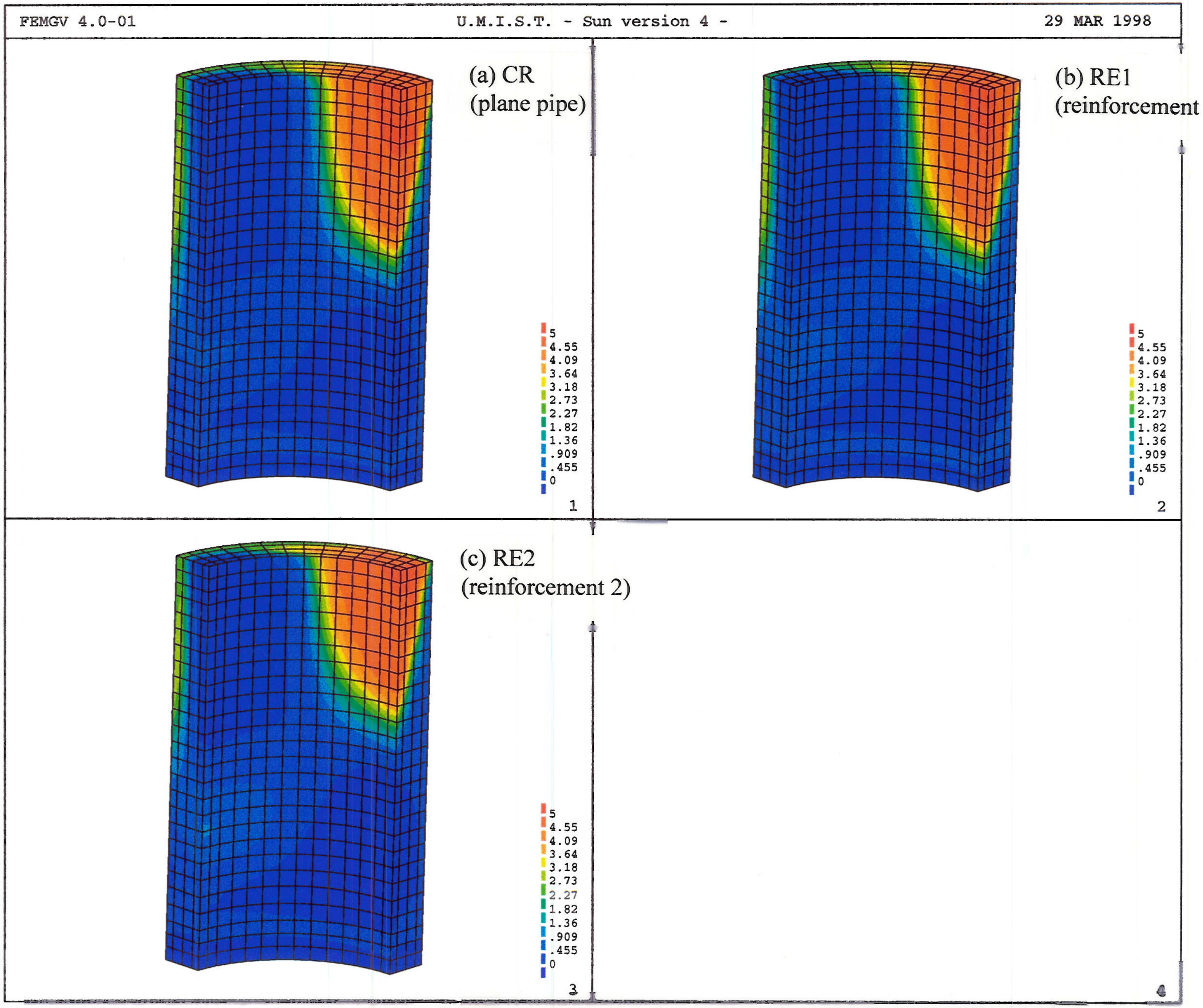

Figure 9.3 Most tensile principal stresses in the concrete pipe with and without reinforcement (MPa)

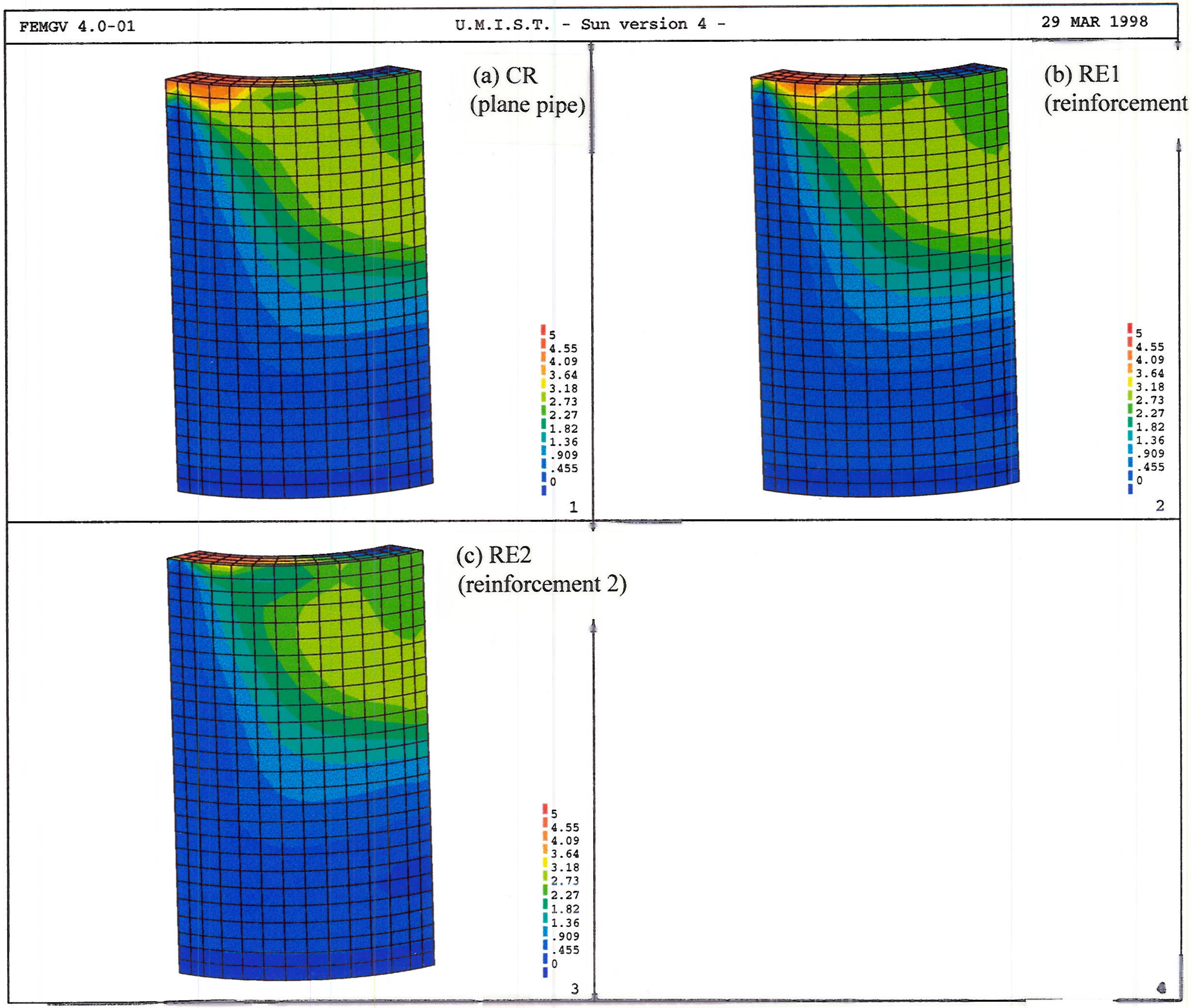

(a) CR
(plane pipe)

(b) RE1
(reinforcement 1)

(c) RE2
(reinforcement 2)

Figure 9.4 Most tensile principal stresses in the pipe viewed from the opposite direction (MPa)

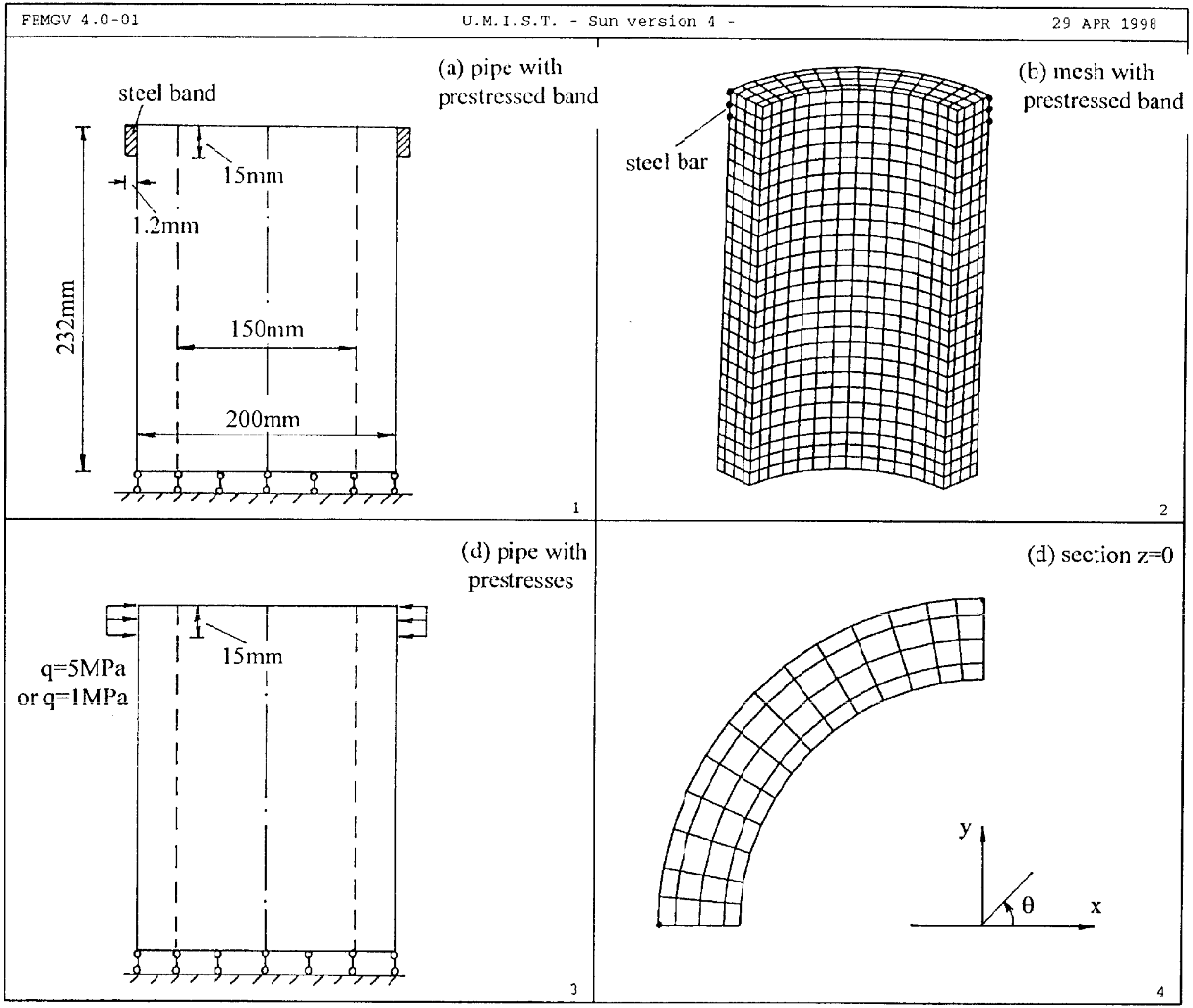

Figure 9.5 Local prestressing and the corresponding finite element mesh

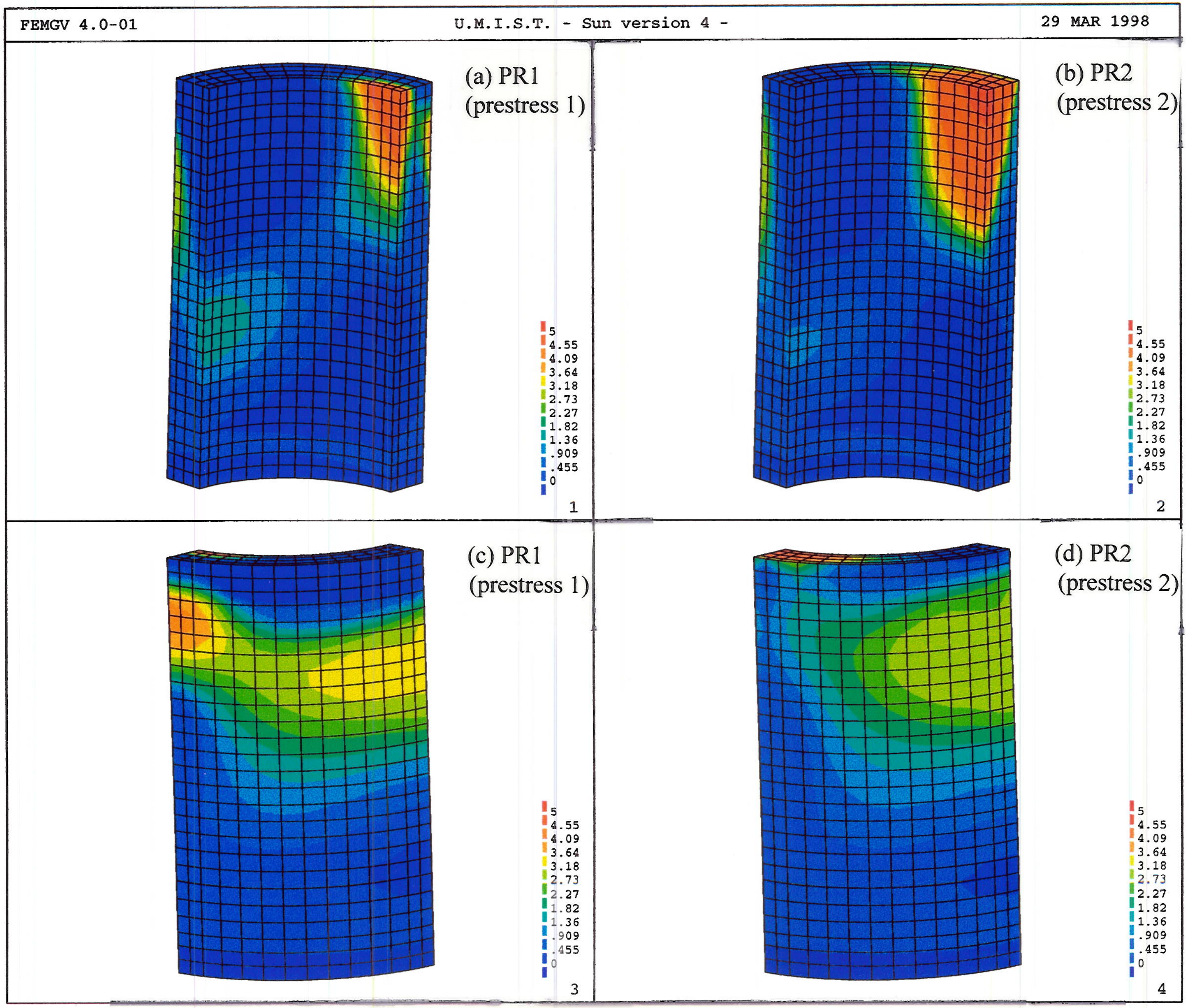

Figure 9.6 Most tensile principal stresses in the concrete pipe with prestressing (MPa)

CHAPTER 10 SUMMARISATION AND RECOMMENDATIONS

The purpose of this research is to understand the performance of concrete jacking pipes under working conditions and to suggest improvements to the design of pipes and pipe joints. There are many factors affecting the performance of concrete pipes during jacking, and it is therefore impractical to conduct an extensive study of these factors by experiment. From the previous research (Ripley 1989, Milligan and Norris 1993b, Norris 1992, Boot and Husein 1991, Husein 1989), the performance of concrete pipes is determined by local cracking due to high tensile stresses at the pipe joint and within the concrete pipe induced by the pipeline misalignment. This makes the problem complicated and difficult for analytical methods to examine in detail. In this research, the finite element method was used to examine the pipe performance with limited laboratory tests. After some developments of the finite element model as described in Chapter 2, an extensive parametric study was carried out in this research to examine the influence of several factors affecting the pipe performance.

10.1 PIPELINE MISALIGNMENT

Previous research (Concrete Pipe Association of Australia 1982, Haslem 1996, Ripley 1989, Milligan and Norris 1993b, Norris 1992, Boot and Husein 1991, Husein 1989) shows that pipeline misalignment causes high stress localization at pipe joints (on the interface between jacking pipe and packing material). These localized stresses induce high tensile stresses within the pipe, which would damage the pipe under severe conditions. However, the interaction mechanism between the pipe and the packing material is still not very clear. To improve the design of the pipe, it is necessary to investigate the distribution patterns of the localized stresses at the pipe joint (on the interface) and within the pipe. In this research, the influence of the pipeline misalignment was examined with the simplified two-dimensional plane strain model and the symmetrical three-pipe system, numerical model C, as discussed in Chapter 3 and Chapter 6 respectively. Both numerical models were used to simulate the 'edge' loading condition under different misalignment angles (refer to Figures 3.1 and 6.2).

In this research, the analyses were carried out assuming the concrete pipe was linearly elastic since the purpose of the research is to understand the pipe performance under working conditions. However, due to the pipeline misalignment, the pipe may separate from the packing material. To model the interaction between the pipe and the packing material, the Mohr-Coulomb frictional model was extended to include a gap zone as described in Chapter 2. This makes the problem highly non-linear when a big gap forms on the interface between the pipe and the packing material (refer to Section 6.4 in Chapter 6).

The numerical results show that the pipeline misalignment induces some shear stresses and high localization of normal stresses on the interface between the pipe and the packing material, which in turn cause high tensile stresses within the concrete pipe (mainly in the hoop direction and in the region of the pipe joint under 'edge' loading). The higher the misalignment angle at the joint, the higher the tensile stresses within the concrete pipe. The results also show that the displacements and the normal stresses at the pipe joint are almost linearly distributed over the joint when the misalignment angle is small (no gap between the pipe and the packing material). However, when the misalignment angle is high, there exists a big gap between the concrete pipe and the packing material, and the displacements and the normal stresses are highly non-linear over the joint. The result comparison under the 'edge' loading condition between the numerical model and the analytical models suggest that under a small misalignment angle (without a gap) both the Australian model and Haslem's (1996) flexible pipe model give good predictions of the displacements and the normal stresses at the joint. When under a high misalignment angle (with a big gap on the interface), the Australian model gives good predictions of the maximum normal stress and the diametrical contact width on the joint, and the predictions from Haslem's (1996) model are poor due to the assumption of tensile stresses in the axial direction within the concrete pipe since the tensile stresses are mainly localized in the region of pipe joint and in the hoop direction.

10.2 PACKING MATERIAL

The packing material plays an important role in the practice of pipe jacking by increasing the contact area over the pipe joint which in turn reduces the stress localization. Previous research by Ripley (1989), Milligan and Ripley (1989), Boot and Husein (1991) and Husein (1989) shows that the packing material with low Poisson's ratio and low stiffness is a good packing material, such as chipboard and plywood. However, its influence on the stresses on the interface between the pipe and the packer and within the pipe still needs to be examined for a better understanding of its working mechanism. In this research, an extensive parametric study of the influence of the properties of the packing material was carried out using both the two-dimensional model and the three-dimensional model as described in Chapter 3 and Chapter 6 respectively (refer to Figures 3.1 and 6.2). The analysis was carried out with three typical Poisson's ratios and three typical shear moduli (two shear moduli in the three-dimensional analysis) under different misalignment angles. In the analysis, both the pipe and the packing material were linear elastic, and the interaction between the pipe and the packing material was modelled by a layer of interface elements as discussed in Section 10.1. The influence of two extremely different packing materials, plywood packing with an almost zero Poisson's ratio and rubber packing which is considered as almost incompressible, was also examined by laboratory tests in this research.

The results confirm that a good packing material should have a low Poisson's ratio and a low stiffness (or a low shear modulus). The numerical results show that the packing material with a higher shear modulus and a higher Poisson's ratio generates higher stress localization on the interface between the pipe and the packing material. The shear stresses on the interface between the pipe and the packing material are mainly due to a high Poisson's ratio of the packing material. Unlike the normal stresses, the shear stresses are always non-linearly distributed on the interface. The shear stresses and the localized normal stresses on the interface induce high tensile stresses in the concrete pipe as discussed in Chapters 3 and 6. The influence of the Poisson's ratio of the packing material on these stresses is significant. There is no analytical model to deal with the shear stresses on the interface.

10.3 SURROUNDING SOIL

The interaction between the concrete pipe and the surrounding soil is another important factor affecting the pipe performance during pipe jacking. In practice, there may be an initial gap between the pipe and the surrounding soil due to overcut, or the pipe is squeezed by the surrounding soil due to the swelling of surrounding overconsolidated clay or the collapse of surrounding sand (Thomson 1993). However, in this research, the effort was on the interaction between the pipe and the surrounding soil caused by the pipeline misalignment. It was assumed that there was no initial gap between the pipe and the surrounding soil and that there was no initial pressure on the pipe from the soil. The parametric study was carried out using a three-dimensional model, Numerical model B, as described in Chapter 5 (refer to Figure 5.1). Three cases were examined, that is, the pipe and elastic surrounding soil with and without an interface between them, and the pipe with plastic surrounding soil. In each case, the analysis was carried out with three different soil stiffnesses under both 'edge' loading and 'diagonal' loading conditions.

The numerical results show that the high tensile stresses are mainly located at the pipe joint in the hoop direction under the 'edge' loading condition, and that under 'diagonal' loading the high tensile stresses are located on the external surface of the pipe in the normal direction of the line connecting the two loaded corners. The numerical results with interface elements show that the pipe separates from the surrounding soil over a large part of the interface and the reaction stresses from the surrounding soil are mainly located in the region adjacent to the loaded area. The results with elastic soil without an interface are considered to be unreliable due to the unrealistic tensile stresses acting on the pipe from the surrounding soil. The research results also demonstrate that the displacements at the pipe end under the 'diagonal' loading condition are mainly due to the rigid body rotation of the pipe in the soil and that the surrounding soil has a significant effect on the stresses in the pipe under the 'diagonal' loading condition due to the rigid body rotation of the pipe in the soil as discussed in Chapter 7. (In practice, prediction of the rigid body rotation of the pipe under the 'diagonal' loading condition is difficult because the load distribution at the pipe end is affected by the rotation of the pipe. There is no analytical model for the 'diagonal' loading condition). Under the loading condition in the research the soil seems to reduce the stresses at the pipe joint and in the pipe in both 'edge' loading and 'diagonal' loading cases, especially with stiff soil (It should be stressed here that the frictional force from the surrounding soil will increase the jacking load in practice. This aspect is not included in the current project).

10.4 PIPE WALL THICKNESS AND LOAD DISTRIBUTION

The analysis in this research also included the influence of the pipe wall thickness and the influence of the load distribution on the pipe end. The analysis was carried out with a single small scaled model pipe, Numerical model A, as discussed in Chapter 4 (refer to Figure 4.1). The numerical results show that the more localized the applied load on the pipe end, the higher the tensile stresses at the pipe joint and within the concrete pipe. Due to the local bending effects in the pipe wall, the stresses within the thin wall pipe exceed those in the thick wall pipe by more than the thickness ratio. The results also show that the constraints under the 'diagonal' loading condition have a great effect on the stresses in the pipe. Husein (1989) has found a similar effect of the hoop geometry, as discussed in Chapter One. This means that laboratory tests of pipe jacking without surrounding soil should be carefully designed in order to simulate the situation in practice.

10.5 IMPROVEMENT OF PIPE DESIGN

A few proposed design improvements, based on the numerical results in this research, were investigated by laboratory tests. An extended numerical back analysis of the experiments was also carried with a simple modified Matsuoka model proposed in this research. The reinforcements were modelled by curved bar elements as discussed in Chapter 9 (refer to Figure 9.2). Both the experiments and the back analysis demonstrate the effectiveness of the local reinforcement and local prestressing on the improvement of the pipe strength. The experimental results show that the local reinforcement and local prestressing also prevent the spalling problem at the pipe joint. The results from the extended back analysis suggest that the reinforcement located near the internal surface of the pipe may produce better results because the high tensile stresses are mainly located on the internal surface under the 'edge' loading condition, and that the magnitude of the prestress should be well controlled to produce good results.

10.6 RECOMMENDATIONS

The current research has demonstrated that the finite element method is very effective in the analysis of pipe jacking. Many interesting results have been obtained. However, due to the complex nature of the problem, some subjects are not included in this research, such as the cracking behaviour of the pipe and the influence of the lubricant on the frictional force. To improve the current understanding of pipe jacking and to make better design of pipe and pipe joint, further research is still needed. A few of important research topics are recommended as following:

(1) Numerical analysis with a complex concrete model including crack failure,

(2) Numerical analysis with a generalized numerical model, three pipes including two pipe joints with packing material and surrounding soil, under both 'edge' loading and 'diagonal' loading condition,

(3) Numerical analysis with different material constants of the interface between the pipe and the soil to model the influence of the use of lubricant in practice,

(4) Laboratory tests of the 'diagonal' loading condition with local reinforcement at the pipe joint and at the middle pipe length,

(5) Laboratory tests with instrumented pipe to examine the load distribution on the pipe end under different pipeline misalignment angles.

REFERENCES

Adhikary, D. P. and Dysin, A. V.(1998), 'A Continuum model of Layered Rock Masses with Non-associative Joint Plasticity', Int. J. Num. Analy. Meth. Geomech., Vol. 22, P245-261.

American Concrete Pipe Association (1960), 'Jacking Reinforced Concrete Pipelines', Virginia, USA.

Anon(1978), 'State of The Art Review of Tunnel Linings in The UK', Tunnels and Tunnelling, Vol. 10, No. 9.

Anon(1987), 'Making an Impact in Switzerland', Tunnels and Tunnelling, Vol. 19, No. 9.

Atkin, R. (1993), 'Resewering Cambridge by Pipe Jacking', Proc. 2nd Int. Conf. on Pipe Jacking and Microtunnelling, p8.1-8.8, Pipe Jacking Association, London.

Atkinson, J.(1993), 'An Introduction to The Mechanics of Soils and Foundations', McGraw-Hill Book Company, London.

Auld, F. A. (1982), 'Determination of Pipe Jacking Loads', Paper presented at Pipe Jacking Conference, Manchester.

Bangash, M. Y. H.(1989), 'Concrete and Concrete Structures: Numerical Modelling and Applications', Elsvier Applied Science, London.

Bazant, Z. P.(1976), 'Instability, Ductility and Size Effect in Strain Softening Concrete', J. Eng. Mech. Div., ASCE, 102(2), p331-344.

Bazant, Z. P. and Cedolin, L. (1979), 'Blunt Crackband Propagation in Finite Element Analysis', J. Eng. Mech. Div., ASCE, 105(2), p297-315.

Bazant, Z. P. and Gambarova, P. (1980), 'Rough Cracks in Reinforced Concrete', J. Struc. Div. 106(ST4), 819-842.

Bazant, Z. P. and Tsubaki, T. (1980), 'Slip-dilatancy Model for Cracked Reinforced Concrete', J. Struc. Div. 106(ST9), 1947-1966.

Beer, G.(1985), 'An Isoparametric Joint / Interface Element for Finite Element Analysis', Int. J. Num. Meth. Eng., Vol. 21, p585-600.

Bigelow, C. A., Johnson, W. S. and Naik, R. A. (1989), 'A Comparison of Various Micromechanics Models for Metal Matrix Composites', Mechanics of Composite Materials and Structures, AMD-vol 100 (Edited by Reddy, J. N. and Teply, J. L.).

Bolton, M. D.(1979), 'A Guide to Soil Mechanics', MacMillan, London.

Boot, J. C. and Husein, N. M.(1991), 'Vitrified Clay Pipes Subject to Jacking Forces', Proc. 1st Int. Conf. on Pipe Jacking and Microtunnelling, p6.1-6.9, Pipe Jacking Association, London.

Boswell, L. F. and Chen, Z. (1987), 'A General Failure Criterion for Plain Concrete', Int. J. Solids Structures, 23(5), 621-630.

British Standard 5911: Part 120. (1989), 'Precast Concrete Pipes, fittings and ancillary products: Specification for reinforced Jacking Pipes with Flexible Joints', British Standards Institution, London.

Burd, H. J. (1986), 'A Large Displacement Finite Element Analysis of A Reinforced Unpaved Road', D.Phil Thesis, Oxford University.

Burd, H. J. and Brocklehurst, C. J. (1992), 'Parametric Studies of a Soil Reinforcement Problem Using Finite Element Analysis', Computer Methods and Advances in Geomechanics (ed. Beer, Booker and Carter), Balkema, Rotterdam.

Burd, H. J., Yu, H.-S. and Houlsby, G. T.(1989), 'Finite Element Implementation of Frictional Plasticity Models with Dilation', Proc. Int. Conf. Constitutive Laws for Engineering Materials, Chongqing, China, 11-13.

Burd, H. J. (1993), ' OXFEM1.4', Research Report, Dept. of Eng. Science, Oxford University.

Chen, A. C. T. and Chen, W.-F. (1975), 'Constitutive Relations for Concrete', J. Eng. Mech. Div., 101(EM4), 465-481.

Clarke, N. W. H. (1968), 'Buried Pipelines: A Manual of Structural Design and Installation', McLaren and Sons, London.

Cole, B. J. and Lees, H. J. (1993), 'Mechanised Pipejacking and Microtunnelling Development in North West Water', Proc. 2nd Int. Conf. on Pipe Jacking and Microtunnelling, p13.1-13.9, Pipe Jacking Association, London.

Concrete Pipe Association of Australia (1983), Pipe Jacking Bulletin.

Craig, R. N. and Muir Wood, A. M. (1978), 'A Review of Tunnel Lining Practice in The United Kingdom', TRRL Supplementary Report 335, Crowthrorne.

Craig, R. N. (1983), 'Pipe Jacking : A State-of-the-Art-Review', Technical Note No. 112, CIRIA, London.

Damjanic, F. B., Mihanovic, A. and Jaramaz, B. (1987), 'A Two-dimensional Finite Element Model for Seismic Analysis of Reinforced Concrete Structures', Computational Plasticity (Edited by Owen, D. R. J., Hinton, E. and Onate, E.)

Das, B. M.(1983), 'Advanced Soil Mechanics', Hemisphere Publishing Corporation.

de Boer, R. and Dresenkamp, H. T.(1989), 'Constitutive Equation for Concrete in Failure State', J. Eng. Mech., ASCE, Vol.103, p1591-1608.

Durden, J. A.(1982), 'Overcoming Jacking Pressures', Conference Proceedings, Pipe Jacking Association, Manchester.

Frantzskakis, C. and Theillout, J. N. (1989), 'Nonlinear Finite Element Analysis of Reinforced Concrete Structures with a Particular Strategy Following the Cracking Process', Computers & Structures, 31(3), 395-412.

Goodman, R. E., Taylor, R. L. and Brekke, T. L.(1968), 'A Model for the Mechanics of Joint Rock', J. Soil Mechanics and Foundation Div., ASCE, 94(SM3), P637-659.

Gudehus, G., editor (1977). 'Finite Elements in Geomechanics', Wiley and Sons.

Haslem, R. F.(1986), ' Pipe Jacking Forces: from Theory to Practice', Proceedings of Infrastructure, Renovation and Waste Control Centenary Conference, N. W. Association, Institute of Civil Engineers, p173-180.

Haslem, R. F.(1996), 'Structural Interaction at Joints in Pipe Jacked Tunnels', The Structural Engineer, Vol. 74, No. 10.

Hayes, N. F. (1993), 'Mechanised Excavation and Muck Removal Systems for Pipe Jacking', Proc. 2nd Int. Conf. on Pipe Jacking and Microtunnelling, p12.1-12.5, Pipe Jacking Association, London.

Hillerborg, A., Modeer, M. and Peterson, P. E. (1976), 'Analysis of Crack Formation and Crack Growth in Concrete by Means of Fracture Mechanics and Finite Elements', Cem. Concr. Res. Vol. 6, No. 6, p773-782.

Holt, C. C., Milligan, G. W. E. and Burd, H. J.(1997), 'Prototype testing of Improved Microtunnelling Pipes', Report OUEL 2151/97, Dept. of Engineering Science, University of Oxford.

Hough, C. M.(1974), 'Concrete Pipe jacking in the UK', Tunnels and Tunnelling, Vol. 6, No. 3.

Houlsby, G. T.(1988), 'Finite Element Mesh Generation Program OXMESH', Research Report, Dept. of Engineering Science, Oxford University.

Hornung, K., Karlsruhe, K. S., Waldbronn, R. L. and Villmar, A. P. (1987), ' Berechnung und Konstruktion von Vortiebsrohren nach DVDW GW 312 / ATV A 161', Beton-und Stahlbetonbau No. 10 and 11, Berlin.

Husein, N. M. (1989), 'Vitrified Clay Pipes Installed by Trenchless Techniques', PhD Thesis, Univ. of Bradford.

Jiang, J. and Feng, L (1991), 'Concrete Mechanics', Chinese Railway Publisher (in Chinese).

Jones, M.(1990), 'From Jacking to Segments in the Same Drive', Tunnels and Tunnelling, Vol. 22, No. 12.

Kirkland, C. J. (1982), 'The Need for Research', Conference Proceedings, Pipe Jacking Association, Manchester.

Kosowatz, J. J.(1987), 'Thrust-Bore Keeps Traffic Moving - New Soft-ground Mole Jacks Pipe under Congested Intersection', Engineering News-Record, Vol. 218, No. 2.

Krieg, R. D. and Krieg, D. B.(1977), 'Accuracies of Numerical Solution methods for the Elastic-perfectly Plastic Model', ASME J. Pressure Vessel Tech., Vol. 99, p510-515.

Kupfer, H. B. and Gerstle, K. H. (1973), 'Behaviour of Concrete under Biaxial Stress', J. Eng. Mech. Div., 99(EM4), 853-866.

Lauritzsen, R., Sande O. K. and Slatten, A. (1996), 'Europipe Landfall Tunnel', Publikasjon - Norges Geotekniske Institutt/Norwegian Geotechnical Institute, No. 197, Norwegian Geotechnical Inst., Oslo, Norway.

Lin C. S. and Scordelis, C. (1975), 'Nonlinear Analysis of RC Shells of General Form', J. Struc. Div. ASCE, 101(ST3), 523-538.

Liao, H. J. and Cheng M.(1996), ' Construction of a Piperoofed Underpass below Groundwater Table', Proc. of the Institution of Civil Engineers Geotechnical Engineering, Vol. 119, No. 4.

Lock, J.(1988), 'Computerised Laser-aided Guidance Systems', Tunnels and Tunnelling, Vol. 20., No. 12.

Matsuoka, H.(1976), ' On the Significance of the Spatial Mobilised Plane', Soil and Foundations, Vol. 16, p91-100.

Milligan, G. W. E. (1995), ' Practical Examinations', Ground Engineering, Vol. 28, No. 10.

Milligan, G. W. E. and Norris, P. (1991), 'Concrete Jacking Pipes - The Oxford Research Project', Proc. 1st Int. Conf. on Pipe Jacking and Microtunnelling, p3.1-3.7, Pipe Jacking Association, London.

Milligan, G. W. E. and Norris, P. (1993a), 'Oxford Research in Pipe Jacking - Research Gathers Pace', Proc. 2nd Int. Conf. on Pipe Jacking and Microtunnelling, p2.1-2.7, Pipe Jacking Association, London.

Milligan, G. W. E. and Norris, P. (1993b), 'The Performance of Concrete Jacking Pipes During Installation', Oxford University Research Report, Report No. OUEL 1986/93.

Milligan, G. W. E. and Norris, P. (1995), 'Pipe Jacking - Research Results and Recommendations', Pipe Jacking Association, London.

Milligan, G. W. E. and Norris, P. (1996), 'Site-based Research in Pipe Jacking - Objectives, Procedures and a case history', Tunnelling and Underground Space Technology, Vol. 11, No. Suppl. 1.

Milligan, G. W. E. and Ripley, K. J.(1989), 'Packing Material in Jacked Pipe Joints', No-Dig 89, Proc. 4nd Int. Conf. on Trenchless Technology, p2.1.1-2.1.10, ISTT, London.

Morcos, S. S. and Jorhovde, R. B. (1992), 'Fracture Criterion of Concrete', Fracture Mechanics of Concrete Structures (Edited by Bazant, Z. P.), Elsevier Applied Science, p5.1-5.4, PJA, London.

Moss, A. F. (1993), 'First Time Sewerage by Pipe Jacking in Major Cities', Proc. 2nd Int. Conf. on Pipe Jacking and Microtunnelling, London.

Neville, A. M.(1981), 'Properties of Concrete', Longman Scientific & Technical, UK.

Ngo-Tran, C. L.(1996), 'The Analysis of Offshore Foundations Subjected to Combined Loading', D.Phil. Thesis, Oxford University.

Nomura, Y., Hoshina, H., Shiomi, H. and Umezu, T.(1985), 'Pipe jacking Method for Long Curve Construction', Journal of Construction Engineering and Management, Vol. 111, No. 2.

Norris, P. (1992), 'The Behaviour of Jacked Concrete Pipes During Site Installation', D.Phil Thesis, Univ. of Oxford.

Norris, P. and Milligan, G. W. E.(1991), 'Pipe and Load Transfer Mechanisms During Pipe Jacking', Proc. Int. Conf. on Trenchless Construction, No-Dig 92, Paper H3, p1-15, Washington.

Norris, P. and Milligan G. W. E.(1992), 'Frictional Resistance of Jacked Concrete Pipes at Full Scale', Proc. Int. Conf. on Trenchless Construction, p121-128, No-Dig 92, Paris.

O'Reilly, M. P. and Rogers, C. D. F. (1987), ' Pipe Jacking Forces', Proceedings of the International Conference on Foundations and Tunnels, Vol. 2, Edited M. C. Forde, Edinburgh Engineering Technics Press.

Ortiz, M, Pinsky P. M. and Taylor, R. L.(1983), 'Operator Split Methods for the Numerical Solution of the Elasticoplastic Dynamic Problem', Comp. Meth. Appl. Mech. Eng., Vol.39, p137-157.

Ortiz, M. and Simo, J. C.(1986), 'An Analysis of a New Class of Integration Algorithms for Elastoplastic Constitutive Relations', Int. J. Num. Meth. Eng. Vol. 23, p353-366.

Owen, D. R. J., Figueiras, J. A. and Damjanic (1983), 'Finite Element Analysis of Reinforced and Prestressed Concrete Structures Including Thermal Loading', Comp. Mech. Appl. Mech. Eng., 323-366.

Phillips, D. V. (1987), 'Three-dimensional Non-linear Analysis of Reinforced Concrete with Application to Torsion', Computational Plasticity (Edited by Owen, D. R. J., Hinton, E. and Onate, E.)

Pau, S. H., Chau, K. W. and Wong, W. G.(1993), ' Prospects for No-dig Technology in Hong Kong Construction Industry', J. Constru. Eng. Manag., Vol 119., No. 3.

Pipe Jacking Association (1981), 'A Guide to Pipe Jacking Design', Pipe Jacking Association, London.

Pipe Jacking Association (1986), 'Jacking Concrete Pipes', Pipe Jacking Association Design and Specification Bulletin No. 1, Pipe Jacking Association, London.

Pipe Jacking Association (1995a), 'Guide to Best Practice for the Installation of Pipe Jacks and Microtunnels', Pipe Jacking Association, London.

Pipe Jacking Association (1995b), 'An Introduction to Pipe Jacking and Microtunnelling Design', Pipe Jacking Association, London.

Read, G.(1986), 'New Construction Techniques in Sewers', Civil Engineering (London), Oct. 1986.

Remmer, F. (1995), ' North See Gas Pipe Jacking Pushes Technology to the Limit', Tunnels and Tunnelling, Vol. 27, No. 6.

Richardson, M. A.(1970), 'Pipeforcing: An Appraisal of Ten Years of Operation', Tunnels and Tunnelling, July 1970, p215-219.

Richardson, H. W. and Mayo, R. S. (1941), 'Practical Tunnel Driving', McGraw-Hill, New York and London.

Ripley, K. J.(1989), 'The Performance of Jacked Pipes', D.Phil Thesis, Univ. of Oxford.

Rogers, C. D. F. and Yonan, S. J. S.(1992), 'Experimental Study of a Jacked Pipeline in Sand', Tunnels and Tunnelling, Vol. 24, No. 6, p35-38.

Roison, V.(1989), 'Innovation at the Cross-roads of Europe', Tunnels and Tunnelling, Vol. 21, No. 5.

Schreyer, H. L., Kulak, R. F. and Kramer, M. M.(1979), 'Accurate Numerical Solutions for Elastic-plastic Models', ASME J. Pressure Vessel Tech., Vol. 101, p226-234.

Sharp, J. D. and Turner, M.(1989), 'Pipe Jacking Through Hazardous Ground in St. Helens', Tunnels and Tunnelling, Vol. 21, No. 3.

Shullock, S. H. (1982), 'Problems in Tunnelling by Pipe Jacking at Tilehurst', Journal of the Institution of Water Engineers and Scientists, April, p151-153.

Simo, J. C. and Taylor, R. L.(1985), 'Consistent Tangent Operators for Rate-independent Elastoplasticity', Comp. Meth. Appli. Mech. Eng., Vol. 48, p101-118.

Sloan, S. W.(1981), 'Numerical Analysis of Incompressible and Plastic Solids Using Finite Elements', PhD Thesis, Cambridge University.

Smith, I. M., editor (1994), 'Numerical Methods in Geotechnical Engineering', Balkema, Rotterdam.

Spiegel, M. R.(1959), 'Theory and Problems of Vector Analysis and An Introduction to Tensor Analysis', Schaum Publishing Company, New York.

Strang, G. and Fix G. J.(1973), 'Analysis of the Finite Element Method', Prentice-Hall.

Thomson, J. (1993), 'Pipejacking and Microtunnelling', Black Academic & Professional.

Timoshenko, S. P. and Goodier, J. N.(1970), 'Theory of Elasticity', McGraw-Hill.

Vidosa, F. G., Kotoves, M. D. and Pavlovic, M. N. (1991a), 'Three-dimensional Non-linear Finite Element Model for Structural Concrete, Part 1: Main Features and Objective Study', Proc. of the Institution of Civil Engineers, 517-544.

Vidosa, F. G., Kotsovos, M. D. and Pavlovic, M. N. (1991b), 'Three-dimensional Non-linear Finite Element Model for Structural Concrete, Part 2: Generality Study', Proc. of the Institution of Civil Engineers, 545-560.

Wallis, S.(1984), 'German Put Bends into Pressurised Pipe Jacking', Tunnels and Tunnelling, Vol. 16, No. 9.

Wang, Z.(1982) 'Shanghai Tunnel Projects Spur Construction Innovations', Civil Engineering (New York), Vol. 52, No. 12.

Washbourne, J. (1986), 'Use of Thixotropic Slurries in the Tunnelling Industry', Ground Engineering, Vol. 19., No. 2.

Yamaguchi, E. and Chen, W.-F. (1990), 'Cracking Model for Finite Element Analysis of Concrete Materials', J. Eng. Mech., ASCE, 116(6), 1243-1260.

Zhou, J.-Q.(1997), ' User's Manual of FEPS', Personal Document.

Zienkiewicz, O. C.(1977), 'The Finite Element Method (third edition)', McGraw-Hill.